Theoretical studies of multi-state and multi-mode dynamics of polyatomic molecular systems

Thesis submitted in partial fulfilment
of the requirements for the degree of

Doctor of Philosophy

by

Arun Kumar Kanakati
Reg. No. 15CHPH25
arunkumarkanakati@gmail.com

School of Chemistry
University of Hyderabad
Hyderabad - 500 046, INDIA
December 2022

Declaration of Authorship

I hereby declare that the matter embodied in the thesis entitled "**Theoretical studies of multi-state and multi-mode dynamics of polyatomic molecular systems**" is the result of investigations carried out by me in the School of Chemistry, University of Hyderabad, India under the supervision of Prof. Susanta Mahapatra.

I also confirm that this thesis is free from plagiarism. In keeping with the general practice of reporting scientific investigations, acknowledgements have been made wherever the work described is based on the finding of other investigators.

23/12/2022

Date

Hyderabad 500046

K. Arunkumar

Signature of the candidate

Certificate

School of Chemistry
University of Hyderabad
Hyderabad-500 046
India

It is certified that the work contained in this thesis, titled "**Theoretical studies of multi-state and multi-mode dynamics of polyatomic molecular systems**"by **Arun Kumar Kanakati (Reg.No. 15CHPH25)**, has been carried out under my supervision and is not submitted elsewhere for a degree.

This thesis is free from plagiarism and has not been submitted previously in part or in full to this or any other University or Institution for award of any degree or diploma.

Parts of this thesis have been published in the following publications:

1. **Arun Kumar Kanakati**, V. Jhansi Rani, R. Sarkar and S. Mahapatra*, J. Chem. Phys. **157**, 204304 (2022), **Chap. 3**.
2. **Arun Kumar Kanakati** and S. Mahapatra*, J. Chem. Phys. **154**, 054313 (2021), **Chap. 4**.
3. **Arun Kumar Kanakati**, V. Jhansi Rani and S. Mahapatra*, Phys. Chem. Chem. Phys. **24**, 16522 (2022), **Chap. 6**.

and presented in following conferences :

1. A Tributary Symposium on 100 Years of Chemical Bonding-2016, 4-5 August, 2016, at CSIR-Indian Institute of Chemical Technology, Hyderabad (National).
2. 15^{th} Indian Theoretical Chemistry Symposium (TCS-2016), 14-17 December, 2016, at University of Hyderabad, Hyderabad (National).
3. 8^{th} International Collaborative and Cooperative Chemistry Symposium, 18-19 December, 2017, at University of Hyderabad, Hyderabad, India (International).
4. 16^{th} Indian Theoretical Chemistry Symposium (TCS-2019), 13-16 February, 2019, at BITS Pilani, Pilani campus, Rajasthan (National).

Further, the student has passed the following courses towards fulfilment of coursework requirement for Ph.D.

Course code	Name	Credits	Pass/Fail
1. CY-801	Research Proposal	3	Pass
2. CY-802	Chemistry Pedagogy (CY507: Instrumentation and Computer Applications Lab)	3	Pass
3. CY-805	Instrumental Methods A	3	Pass
4. CY-403	Quantum Chemistry	3	Pass

S Mahapatra

23/12/2022

Date

Hyderabad 500046

Advisor: Prof. Susanta Mahapatra

Susanta Mahapatra
Professor
School of Chemistry
University of Hyderabad
Hyderabad-500 046 A.P India

Dean

School of Chemistry

University of Hyderabad

Dean
SCHOOL OF CHEMISTRY
University of Hyderabad
Hyderabad-500 046

Acknowledgements

First and foremost, I would like to express my great gratitude to my advisor, Prof. Susanta Mahapatra, for his guidance, support and inspiration of my work. I am indebted to him for the values he taught me in approaching a research problem and the work freedom which he has given me, which made me stronger and more independent.

I thank the present and former Deans, School of Chemistry for their support and encouragement in creating a wonderful work environment throughout the years. I am equally grateful to the faculties of our department who have taught me and helped me at various stages of my MSc and doctoral days. Also thanks to my doctoral committe members Prof. M. Durga Prasad and Dr. Debashis Barik. A special thanks to Prof. M. Durga Prasad, Prof. T. P. Radhakrishnan, Prof. K. D. Sen, Prof. D. Basavaiah, Prof. K. C. Kumaraswamy and Prof. Anunay Samanta for their wonderful lectures are indeed my role models and have inspired me in learning and appreciating the basic sciences. I thank to Prof. Harjinder Singh (IIIT Hyderabad), Prof. Zhengang Lan (China), Prof. S. K. Das, Prof. G. Aravind (IIT Madras) and Dr. V. Madhu (Karunya University) for fruitful discussions on collaborative projects. I also thanks to all the non-teaching staff of the School of Chemistry for their assistance in various occasions. A special thanks to Venkatesh, Swetha, Radhika and Geetha.

I am thankful to my labmates Jayakrushna, Daradhi, Nitai, Ajay Rawat, Jhansi, Rani, Alamgir, Ajay, Dr. Manjusha, Dr. Arpita, Dr. Sugata, Dr. Rudra, Dr. Krishna, Dr. Karunamoy, Dr. Sundarayya, Dr. Satyendra Gupta, Dr. Rajagopala Reddy, Dr. Nagaprasad Reddy, Dr. Rajagopala Rao, Dr. Tanmoy Roy and Dr. Sundarayya for maintaining a very supportive and friendly environment to work. Also, a very special thanks to Krishna anna, Sugata da, Rajanna (Reddy), Napa anna, Dr. Tanmoy Mondal, Jhansi and Anjana for various scientific and non-scientific discussions and I learned a lot through their invaluble suggestions in various occasions. Also thanks to Sarithakka, Sridharanna (late), Dinesh anna, Lalitha di, Subrato da of MDP sir's group for their warm company in various occasions.

Also, I want to thankful to all the MSc project students and summer intenship students who worked with me. Start with Saumya and Raghi (Kannur University), Samragni, Akhil Chakravarthy, Hardik K Desai (Sardar Patel University), Yenugu Nikhil (IISER-K), Calvinshijo (Bharathidasan University), Shiv Prakash Mishra (University of Lucknow), Parag (Assam), Arpan Chowdary, Gnana Spoorthy (IIT-KGP), Supriyo Santra. I truley appriciate their dedication and curiosity on their project work.

Apart from my labmates, I would like to extend my special thanks to University of Hyderabad friends and my seniors, Sashanna, Pavananna, Obanna, Vikranthanna, Sathish

anna (PKP lab), Nanda Kishore anna, Ashok anna, Chandu anna, Konda Reddy, Billa Narsimha, Shakthivel anna, Suman da, Naveen anna, Pon Sathish anna, Shiva Reddy anna, Suresh anna, Ramakrishna anna, Sathish anna, Surender, Chandahas, Rangu Prasad, Rambabu, Suryanarayana, Venky anna, Nagamaih, Umamaheshwer, Jada Ravi, Narsimha, Ravi Nayak, Vinay, Vinod, Sai, Sunny, Rajesh, Ashok, Srinu, Praveen, Sasi, Laxman, Naresh, Jishu, Irfan, Ishfaq, Akram, Gora, Vamshi, Ali, Somnath, Sumantha, Suman Mondal, Shubham, Sachin, Alim, Suman, Ravinder, Arumugam, Santhosh, Ramnaidu, Ranadeep, Pritham, Basha, Arun, Shyam, Satyam, Narsimha anna, Anupam, Soutrik, Hafizur, Premakumar, Ramesh Palibabu, Ganesh, Lasya, Srujana, Anjana, Divya, Santhi, Kirthi, Prasannatha, Kamala, Sneha, Navaneetha, Archana, Sridhatri, Gunjan, Shampita, Nisha and Prachi.
My MSc friends: Shiva, Suresh, Sable, Chandu, Dileep, Adi, Anand Roy, Thiru, Jaipal, Azhar, Mani, Thallapa Reddy, Maka, Chaitanya, Prakash, Srikanth, Manoj, Lakkireddy, Rajireddy, Suryanarayana, Hemanth, Anand, Rabinarayan, Veeresh, Venkataramana, Arjun, Umashankar, Swamy, Harish Reddy, Yadava Rao.
From school of physics: Rasi, Naresh, Vinod, Prem, Nisha and Pooja with whom I have shared many wonderful moments to cherish in my life.

I also thanks to all of my PhD batchmates Srinu, Ramesh, Ankit, Senthil, Sandeep, Apurba, Saddam, Tanmay, Shankar, Manzur, Sameeta, Sipra, Harilal, Venky anna, Anif and Manish. We shared many memories, academic and non-academic discussions. A special thanks to Ramesh and Srinu.

A special thanks to my BSc teacher Srinivas sir for his encouragement and support during my BSc days.

I thank Mrs. Gitashree Mahapatra (madam), Anusha and Anish for providing me a homely atmosphere in several occasions during my initial days of my PhD.

Financial support from the Council of Scientific and Industrial Research (CSIR), New Dlehi, is greatly acknowledged. For computational facilities CMSD and HPCUPE-II are also greatly acknowledged.

Also, I would like to thaks to village friends and well wishers, especially, Bhasker, Yadi, Nagaraju, Venkatesh, Kittigadu, Bhaskeranna, Krishna Gavvala, Veeraiah mama, Ashok anna, Sathish anna (Kummari), Saibaba and Pabba Srinu.

My family mean the primary world to me and it is beyond words to express gratitude to my Bapu (Narsaiah), Amma (Padma), Anna (Anil Kumar), Vadina (Lavanya), Vishu, Vedansh, Tambi (Harish Kumar) and Bapamma (Prameela) who stood by me in all times of life; be it good or bad. Whatever I have achieved so far is all of their love, sacrifice and endless support. They always proud of me all the time, while I really regret

that I could not spend sufficient time with them since the beginning of my university time. In addition to my family members, my close relatives are also gave me so much of support since my schooling, Mamayya (Mallaiah), Athamma (Vijaya), Kavithakka, Venky, Sumathi and at last my thatha (Ramulu), I inspired many things from him about the life.

December 2022 (**Arun Kumar Kanakati**)
Hyderabad - 500046

Contents

List of Figures

List of Tables

Abbreviations

aug-cc-pVDZ	augmented correlation-consistent polarized Valence Double-ζ
aug-cc-pVTZ	augmented correlation-consistent polarized Valence Triple-ζ
aug-cc-pVQZ	augmented correlation-consistent polarized Valence Quadrapule-ζ
ADT	adiabatic to diabatic transformation
B3LYP	Becke 3-Parameter, Lee, Yang and Parr
BO	Born-Oppenheimer
BH	Born-Haung
Bz	Benzene
CASSCF	complete active space self consistent field
CCSD	coupled cluster singles and doubles
cc-pVDZ	correlation-consistent polarized Valence Double-ζ
CG	Clebsch-Gordon
CIs	conical intersections
DOF	degrees of freedom
DVR	discrete variable representation
ECP	effective core potentials
EOM-CCSD	equation of motion-coupled cluster singles and doubles
EOMIP-CCSD	equation of motion ionization potential-coupled cluster singles and doubles
FC	Franck-Condon
FWHM	full width at the half maximum
HFBz	hexafluorobenzene
HO	Harmonic oscillator
HOMO	highest occupied molecular orbital
IRREP	irreducible representation
JT	Jahn-Teller
LIF	laser-induced fluorescence
LVC	linear vibronic coupling
m-DFBz	meta-difluorobenzene
MCTDH	multi-configuration time-dependent Hartree
MFBz	monofluorobenzene
MO	molecular orbital
MP2	Møller-Plesset perturbation theory
MRCI	multi-reference configuration interaction
o-DFBz	ortho-difluorobenzene
OVGF	outer valence Greens function
PAHs	polycyclic aromatic hydrocarbons
PESs	potential energy surfaces

PFBz	pentafluorobenzene
PJT	pseudo-Jahn-Teller
QVC	quadratic vibronic coupling
RT	Renner-Teller
REMPI	resonance enhanced multiphoton ionization
SPFs	single particle functions
TDDFT	time-dependent density functional theory
TFBz	1,3,5 trifluorobenzene
VC	vibronic coupling
VIEs	vertical ionization energies
VEEs	vertical excitation energies
WP	wave packet

Dedicated

to

my family members

Chapter 1

Introduction

"Theoretical studies of multi-state and multi-mode dynamics of polyatomic molecules" is a topic of current interest, covering many essential topics in modern theoretical chemistry. It is imperative to provide the reader with an introduction that elucidates exactly what it is that this thesis will attempt to cover. An excellent place to start is with the title.

As a chemist (especially as a theoretician), we always think about how molecules behave when they are exposed to light. That is, all about the dance of atoms and molecules happening in a tiny fraction of seconds, the movement that we shine light on them. We use all kinds of mathematics, physics and chemistry tools to understand the molecular electronic spectroscopy of molecules in detail. When it is exposed to light, a molecule in a ground equilibrium state goes to a higher energy state called an excited state. Different types of responses can be relayed by the excited molecule depending on the topography of excited state potential energy surfaces (PESs). For example, fluorescence (biomarkers) [1, 2] and radiationless relaxation (DNA photo-stability) [3, 4] to the ground state. Things can also happen in excited states, such as excited state electron transfer (DNA photo-repair) [5, 6], excited state energy transfer is used for optoelectronics [7] and chemistry can also happen in the excited state. That is, photoisomerization of retinal in rhodopsin protein (visual response) [8, 9] and proton transfer (green fluorescent protein) [10–12]. In order to study these complicated systems, new method developments and understanding of dynamics on multiple surfaces are needed. In polyatomics, the electronic ground state is typically well separated energetically from other (excited) electronic states. The latter states are very close in energy, and there may be a strong coupling between them along suitable nuclear degrees of freedom (DOFs). One requires to establish all required excited states relative to a reference ground electronic state. In principle, it is not very simple.

A common approach to facilitate the study of molecular dynamics is to use the Born-Oppenheimer (BO) or adiabatic approximation [13]. Vibronic coupling, i.e., coupling between electronic and nuclear motion, is ubiquitous in polyatomic molecules. Such coupling causes a breakdown of the BO approximation [13] and electronic transition occurs during nuclear motion. A generic feature of vibronic coupling is the occurrence of conical intersections (CIs) of PESs [14–22], the signature of which is often imprinted in the molecular electronic spectrum and the absence of radiative emission of excited molecular states. The standard vibronic coupling theory [14, 23, 24] has successfully treated molecular processes in the non-BO situation. It relies on the concept of a diabatic electronic basis, symmetry selection rule, and a Taylor series expansion of the electronic Hamiltonian [14].

1.1 Current state of research

Electron spectroscopy of benzene (Bz) and benzene radical cation (Bz^+) and their fluoro derivatives have been extensively studied experimentally [25–46] and also, to a large extent, theoretically [47–58] in the past decades. Fluorination of the benzene ring stabilizes the states arising out of σ-type orbitals of Bz in its fluoro derivatives. The extent of stabilization increases with increasing fluorination. This is a consequence of the electronic effect of a fluorine atom and is termed a perfluoro effect [34]. Stabilizing electronic states in the fluoro Bz and Bz^+ causes their energetic re-ordering. As a result, the vibronic coupling becomes a crucial mechanism and largely governs the mechanistic details of the spectroscopy and dynamics of electronically excited states of these molecules.

The optically dark $\pi\sigma^*$ state becomes lower in energy and often mixes with the optically bright $\pi\pi^*$ state [34, 52–54, 57–60]. It was found that the lowest $\pi\sigma^*$ state is significantly higher in energy than the lowest $\pi\pi^*$ state, when the number of fluorine atom substitutions in the Bz is four or less. These molecules exhibit structured $S_1 \leftarrow S_0$ absorption band, large quantum yield and nanosecond fluorescence lifetime. Whereas, penta- and hexa-fluorinated Bz molecules exhibit structureless $S_1 \leftarrow S_0$ absorption band, low quantum yield and picosecond lifetimes of fluorescence emission [61–64]. Recent ultra-violet (UV) absorption experiments [59, 60, 65–67] on pentafluorobenzene (PFBz) and hexafluorobenzene (HFBz) indicate that the lowest $\pi\pi^*$ and $\pi\sigma^*$ states become energetically very close with each other which results into a broad and structureless profile of the first absorption band. The first four excited electronic states of PFBz are reported to be of $\pi\pi^*$ (S_1), $\pi\sigma^*$ (S_2), $\pi\sigma^*$ (S_3) and $\pi\pi^*$ (S_4) type [60]. While a transition from the S_0 to the $\pi\pi^*$state is optically allowed, the same to the $\pi\sigma^*$ state is forbidden. The signature of the latter can only appear in the spectrum when it interacts vibronically

with the optically bright $\pi\pi^*$ state. These $\pi\pi^*$ and $\pi\sigma^*$ states are also energetically very close. Therefore, a detailed systematic theoretical investigation of the vibronic coupling between these $\pi\pi^*$ and $\pi\sigma^*$ states is worthwhile to understand the structureless absorption bands of PFBz (see Chapter 3).

Moreover, the observation of radiative emission and structureless electronic bands in fluoro Bz^+, in particular, motivated detailed theoretical studies of the structure and dynamics of their electronic excited states. It was found that less than three-fold fluorination of Bz^+ does not give rise to fluorescence emission [43, 44]. Köppel and coworkers carried out benchmark theoretical studies for the first time on Bz^+ and its mono- and difluoro derivatives [47–51]. They devised multi-state and multi-mode vibronic coupling models through extensive electronic structure calculations and carried out detailed nuclear dynamics studies. It turned out from these studies that energetically accessible CIs among states drives the nonradiative decay of excited states in Bz^+, F-Bz^+ and F_2-Bz^+. Among the three isomers [ortho (o), meta (m) and para (p)] of the latter, the m-isomer is weakly emissive [51]. It was found that the energetic minimum of its $\widetilde{C}$ state occurs at higher energy as compared to the two other isomers. Therefore, the nonradiative decay of this state becomes partially feasible. In a later study on 1,3,5-trifluoro Bz^+ we found that its excited electronic state of $\widetilde{A}\,^2A_2''$ symmetry is energetically well separated from the other states. Therefore, the observed radiative emission of this radical cation is explained to be arising out of this state [55]. The radiative emission and nonradiative decay were also studied recently both experimentally and theoretically for phenol and pentafluoro phenol [68, 69]. In this case the coupling between optically bright $^1\pi\pi^*$ and optically dark $^1\pi\sigma^*$ states governs the radiative emission. In phenol these states are energetically apart whereas, in pentafluoro phenol they are energetically close. Therefore, while radiative emission of the $^1\pi\pi^*$ state dominates in phenol, it is significantly quenched in pentafluoro phenol owing to a large nonradiative population transfer to the optically dark $^1\pi\sigma^*$ state [69]. As part of this thesis, the radiative emission and photoelectron spectrum of both PFBz and HFBz is studied theoretically by *ab initio* quantum dynamical methods (see Chapters 4 and 5).

Allene (H_2CCCH_2, propadiene), propyne (H_3CCCH, methyl acetylene) and cyclopropene are the three stable isomers of C_3H_4. The former two isomers are important intermediates in combustion and astrochemistry [70–74]. They are members of the cumulene series with odd number of carbon atoms. The radical cation of these isomers possesses degenerate electronic states and vibrational modes. Therefore, they provide a unique platform to investigate multi-mode Jahn-Teller (JT) and pseudo-Jahn-Teller (PJT) effects [75–77] in their ionic states. While the equilibrium configuration of allene belongs to less common D_{2d} symmetry point group, that of propyne belongs to the more common C_{3v} symmetry point group. The non-degenerate vibrational modes of b_1 and b_2

symmetry are JT active in the degenerate ionic states of allene. On the other hand, the degenerate vibrational modes of e symmetry causes PJT coupling among the degenerate and non-degenerate ionic states of allene. Multi-mode JT and PJT interactions in the ionic states of allene have been extensively studied theoretically [78–85] and also probed experimentally through photoelectron spectroscopy measurements [86–91]. To the best of our knowledge, it is the first example treated with a higher-order vibronic coupling model in the literature [83]. The PJT coupling in its $\widetilde{\mathrm{A}}\ ^2\mathrm{E}$-$\widetilde{B}^2B_2$ electronic manifold was found to be extremely strong which leads to a broad and diffuse vibronic band structure at higher energies. As stated above, the JT and PJT effects in the ionic states of propyne are not rigorously studied in the literature. It would therefore be interesting to study how these effects in propyne radical cation differ as compared to those in allene radical cation since they are isomeric in nature and have different JT and PJT coupling mechanisms (see Chapter 6).

1.2 Our goal and outline of the thesis

The work presented in this thesis explores the vibronic interactions in photo-induced polyatomic molecular systems: of particular importance are the molecules PFBz, HFBz and Propyne (their structures are shown in Fig. 1.1) are investigated by employing the quantum dynamical methods. Among these, HFBz (D_{6h}) and Propyne (C_{3v}) are highly symmetric molecules. The radical cations of them possess degenerate electronic states and degenerate vibrational modes. Therefore, they provide a unique platform to investigate multi-mode JT and PJT effects in their ionic states.

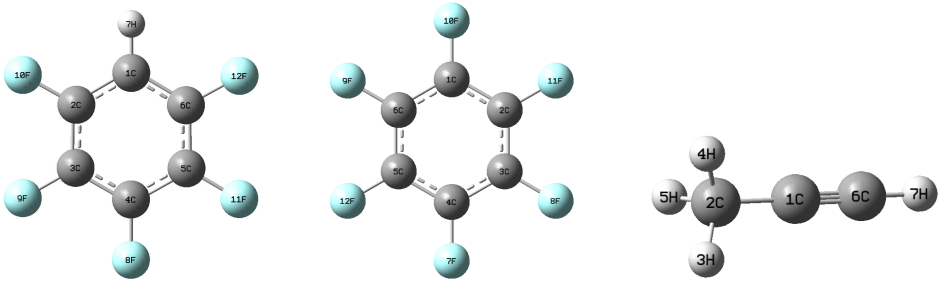

(a) PFBz (b) HFBz (c) Propyne

FIGURE 1.1: Schematic representation of the equilibrium minimum structure of the electronic ground state of PFBz (a), HFBz (b) and Propyne (c) molecules discussed in detail in this thesis.

The theoretical investigation of complex vibronic spectra and ultrafast nonradiative decay dynamics through CIs are carried out with the aid of *ab initio* electronic structure

calculations and quantum dynamical simulations of nuclear motion on multi-sheeted coupled electronic states. Vibronic coupling is established to be an important mechanism in the dynamics of excited electronic states of these molecules. The complex vibronic spectra, dominant vibrational progressions, electronic population transfer process at the CIs, nonradiative decay rate and the effect of fluorination on the broadening of the spectra and emission properties are investigated in detail. The theoretical findings are compared with the available experimental results. The diabatic electronic representation has been introduced and used to deal with the PESs crossings and to avoid the singular nature of the nuclear kinetic coupling term of the adiabatic electronic representation. Model vibronic Hamiltonian is devised in this basis using elementary symmetry selection rules and the relevant coupling parameters of the Hamiltonian are extracted from *ab initio* electronic structure results. The spectroscopic implications of JT and PJT effects and vibronic interactions are probed through photoelectron/absorption spectroscopic experiments. The vibronic bands are calculated by solving both time-independent and time-dependent Schrödinger equations using the multi-configuration time-dependent Hartree (MCTDH) program module.

Chapter 2 gives a systematic essential theoretical background of the present studies. In particular, an outline of the concept of BO (or adiabatic) approximation and the necessity of a diabatic electronic basis to investigate the static and dynamic aspects of multi-mode vibronic coupling effects. In this regard, at first, a simple linear vibronic coupling (LVC) scheme augmented with diagonal quadratic terms is discussed. The vibronic coupling involving degenerate modes and degenerate electronic states (i.e., the JT Hamiltonian) is also discussed in this chapter. Technical details of the first principles of quantum dynamics calculations (i.e., the time-independent and time-dependent approaches for solving the quantum eigenvalue equation to calculate vibronic spectra) using the MCTDH program module are also illustrated.

Chapter 3 presents a comprehensive theoretical study of the electronically excited eight states and the related absorption spectrum of PFBz molecule. Accurate *ab initio* computations and modern WP propagation techniques are combined to give a detailed picture of the electronic bands, multi-dimensional PESs and vibrational assignments. The vibronic coupling in the eight electronic excited states of PFBz is investigated. In particular, the vibronic coupling between the optically bright $\pi\pi^*$ state and optically dark $\pi\sigma^*$ state of PFBz is considered. A model 8×8 diabatic Hamiltonian is constructed in terms of normal coordinates of vibrational modes using standard vibronic coupling theory and symmetry selection rule. The Hamiltonian parameters are estimated with extensive *ab initio* quantum chemistry calculations. The topography of the first eight electronic states of PFBz is examined at length, and multiple multi-state CIs are established. The nuclear dynamics calculations on the coupled electronic surfaces are carried

out from the first principles of the WP propagation method. Theoretical results are found to be in good accord with the available experimental optical absorption spectrum of PFBz.

Chapter 4 contributes to the studies of fluorinated benzene derivatives, which represent an important field of organic and theoretical chemistry, providing new insights into the trends in molecular structure and spectroscopy of benzene related aromatic compounds. In this work, the first six low-lying electronic states of pentafluorobenzene radical cation ($PFBz^+$) are treated using a state-of-the-art theoretical approach. The respective PESs are computed using the equation of motion ionization potential-coupled cluster singles and doubles (EOMIP-CCSD) and complete active space self-consistent field - multi reference configuration interaction (CASSCF-MRCI) methods. Their vibronic coupling is studied using the diabatic model Hamiltonian comprising all six electronic states and including terms up to fourth-order Taylor expansion of the diagonal potential energy terms. Finally, the nuclear dynamics are treated using the highly efficient MCTDH approach. All vibronic interactions of the states belonging to the manifold under consideration have been established and characterized in terms of their CIs and vibronic coupling constants. The simulated spectrum results are in good agreement with the available experimental data. The population dynamics have been studied, allowing for discussion of nonradiative decay channels. Finally, the results were used to analyze the radiative emission trends in the fluorobenzene radical cations series.

In continuation with Chapter 4, the theoretical photoelectron spectroscopy of hexafluorobenzene (HFBz) and its radiative emission and nonradiative decay dynamics are explored in detail in Chapter 5. Due to the highly symmetric structure of the HFBz (D_{6h}) molecule, the radical cation of this molecule possesses degenerate electronic states and vibrational modes. Therefore, this provided a unique platform to investigate multimode JT and PJT effects in its ionic states. In this work, the first four low-lying $\widetilde{\mathrm{X}}\ ^2\mathrm{E}_{1g}$, $\widetilde{\mathrm{A}}\ ^2\mathrm{A}_{2u}$, $\widetilde{\mathrm{B}}\ ^2\mathrm{B}_{2u}$, and $\widetilde{\mathrm{C}}\ ^2\mathrm{E}_{2g}$ electronic states of $HFBz^+$ are considered and the high-level *ab initio* EOMIP-CCSD method is used for this purpose. Among these electronic states, $\widetilde{\mathrm{X}}\ ^2\mathrm{E}_{1g}$ and $\widetilde{\mathrm{C}}\ ^2\mathrm{E}_{2g}$ states are doubly degenerate, and the $\widetilde{\mathrm{X}}\ ^2\mathrm{E}_{1g}$ state is energetically well separated from the other excited states. However, the latter states are closer in energy, and among them, the states forms low energy CIs underlying the JT and PJT interactions. The $E\otimes e$ model Hamiltonian is expanded up to fourth-order to investigate the static and dynamics JT effects. The Hamiltonian model is constructed in terms of dimensionless normal displacement coordinates using standard vibronic coupling theory and symmetry selection rule. Both time-independent and time-dependent quantal methods carried out the nuclear dynamical calculations. Theoretical results are found to be in good agreement with the available experimental data. The impact of the fluorination

effects on the structure and dynamics of excited states is discussed with the parent Bz radical cation.

The JT and PJT effects in the $\widetilde{X}\ ^2E$, $\widetilde{A}\ ^2E$ and $\widetilde{B}\ ^2A_1$ electronic states of the propyne radical cation are investigated with the aid of *ab initio* quantum chemistry calculations and first-principles quantum dynamics simulations. For the latter, both time-independent and time-dependent quantum mechanical methods are employed. Standard vibronic coupling theory is used to construct a symmetry-consistent vibronic Hamiltonian on a diabatic electronic basis. Taylor series expansion of the elements of the diabatic electronic Hamiltonian is carried out and the parameters that appear in the expansion are derived from the *ab initio* calculated adiabatic electronic energies. It is found that the JT effect is weak in the $\widetilde{X}\ ^2E$ state as compared to that in the $\widetilde{A}\ ^2E$ state. Because of the large energy separation, the PJT coupling among the JT-split components of the $\widetilde{X}\ ^2E$ state with the neighboring states is also very weak. However, the PJT coupling of the $\widetilde{B}\ ^2A_1$ state with the JT-split components of the $\widetilde{A}\ ^2E$ state has some impact on the dynamics in the coupled $\widetilde{A}\ ^2E$-$\widetilde{B}\ ^2A_1$ electronic states. The vibronic spectrum of each of these states is calculated and compared with the experimental results. The nonradiative internal conversion dynamics of excited cationic states is examined. An interesting comparison is made with the JT and PJT coupling effects in the nuclear dynamics of the $\widetilde{X}\ ^2E$-$\widetilde{A}\ ^2E$-$\widetilde{B}\ ^2B_2$ electronic states of the isomeric Allene radical cation. These results are discussed in detail in Chapter 6.

Finally, Chapter 7 summarizes the theoretical results presented in this thesis and new concepts emerged from them in relation to the experimental observations. A brief outlook on the future challenges is also ennumerated.

Chapter 2

Theoretical methodology

In this chapter, the basic theoretical background of the present work is discussed. The Born-Oppenheimer (BO) approximation [13], plays a key role in the description of molecular chemistry.

2.1 The BO approximation

The BO approximation is a crucial part of the quantum description molecules [13]. The basic idea of this approximation is the separation of the electronic and nuclear motions. Since the mass of an electron is smaller (∼1836 times) compared to that of the nuclei, the electrons move quickly, the change in the nuclear positions can be considered to be negligible when calculating the electronic wave functions. Therefore, the BO approximation allows the calculation of molecular processes in two steps. In the first step, the electronic problem is solved keeping the nuclei fixed. For each fixed nuclear position, the electronic energies are calculated by quantum chemical methods, and thus the PESs are obtained. The nuclear dynamics on one or several predetermined PESs are performed in the second stage.

The time-independent molecular Schrödinger equation in the whole space of electronic $\{q\}$ and nuclear $\{Q\}$ coordinates can be written as

$$\hat{H}(q,Q)\Psi(q,Q) = E\Psi(q,Q), \tag{2.1}$$

where $\Psi(q,Q)$ is an energy eigenfunction, E is the associated energy eigenvalue, and $\hat{H}(q,Q)$ is the molecular Hamiltonian, which is defined as (at the non-relativistic level

of theory)

$$\hat{H} = -\frac{\hbar^2}{2}\sum_{\alpha}\frac{\nabla_{\alpha}^2}{m_{\alpha}} - \frac{\hbar^2}{2m_e}\sum_{i}\nabla_i^2 + \sum_{\alpha}\sum_{\beta>\alpha}\frac{Z_{\alpha}Z_{\beta}e'^2}{r_{\alpha\beta}} - \sum_{\alpha}\sum_{i}\frac{Z_{\alpha}e'^2}{r_{i\alpha}} + \sum_{i}\sum_{j>i}\frac{e'^2}{r_{ij}}, \quad (2.2)$$

where α and β refer to nuclei and i and j refer to electrons. The first and second terms in Eq. 2.2 are the operators for the KE of the nuclei and electrons, respectively. The third term is the PE of the repulsions between the nuclei, $r_{\alpha\beta}$ being the distance between the nuclei α and β with atomic numbers Z_{α} and Z_{β}. The fourth term is the PE of the attractions between the electrons and the nuclei, $r_{i\alpha}$ being the distance between electron i and nucleus α. The last term is the PE of the repulsions between the electrons, r_{ij} is the distance between electrons i and j. In abbreviated form, the above equation can be represented as

$$\hat{H} \equiv \hat{T}_N + \hat{T}_e + \hat{V}_{NN} + \hat{V}_{eN} + \hat{V}_{ee}. \quad (2.3)$$

The molecular wave function Ψ_i can be expanded using the following ansatz

$$\Psi_i(q,Q) = \sum_{i=1}^{N}\Phi_i(q,Q)\chi_i(Q). \quad (2.4)$$

where $\Phi_i(q,Q)$ and $\chi_i(Q)$ are electronic and nuclear wave functions, respectively. For a complete set of eigenstates (i.e., $N \to \infty$), the ansatz Eq. 2.4 is exact. In most applications in chemistry, N is restricted to a small number of close-lying electronic states, and the effect of other electronic states is ignored. While the nuclear wave functions exclusively depend on the nuclear coordinate Q, the electronic wave functions depend on both the electronic (q) and the nuclear coordinates. The electron-nuclear interaction term $\hat{V}_{eN}$ [cf., Eq. 2.3] in the molecular Hamiltonian is the main obstacle for a full separation of the electronic wave function from the nuclear wave function. In the BO approximation, the electronic wave function $\Phi_i(q,Q)$ depends parametrically on the nuclear coordinates and which is denoted as $\Phi_i(q;Q)$. In the BO approximation, the *ab initio* electronic structure algorithms solve the fixed nuclei electronic Schrödinger equation

$$\hat{H}_e\Phi_i(q;Q) = V_i(Q)\Phi_i(q;Q), \quad (2.5)$$

where the electronic Hamiltonian $\hat{H}_e = \hat{T}_e + \hat{V}_{eN} + \hat{V}_{ee}$. $V_i(Q)$ is the PE obtained by solving the eigenvalue equation 2.5 for a fixed position of the nuclei. The PES can be obtained by varying the nuclear positions parametrically and solving Eq. (2.5) in each case.

Using the basis defined in Eq. 2.4 and the solution of the electronic Schrödinger equation 2.5, one can derive the coupled nuclear differential equation [13, 14]

$$\left[\hat{T}_N I + \hat{V}_j(Q) - E\right] \chi_j(Q) = \sum_{i=1}^{\infty} \hat{\Lambda}_{ij} \chi_i(Q). \tag{2.6}$$

In the above equation, I represent the identity matrix. The quantity, $\hat{\Lambda}_{ij}$ are the elements of nonadiabatic coupling operator and are defined as

$$\hat{\Lambda}_{ij} = -\int dr \Phi_i^* \left[T_N, \Phi_j\right] \tag{2.7}$$

where $[A, B] = AB - BA$. Using the general form of nuclear kinetic energy operator (KEO) as differential operator [92], the nonadiabatic operator ($\hat{\Lambda}_{ij}$) decomposes into a differential operator and a constant number in Q-space [14, 93].

$$\hat{\Lambda}_{ij} = \sum_{n=1}^{M} F_{ij}^{(n)} \nabla - G_{ij}, \tag{2.8}$$

with

$$F_{ij}^{(n)} = \langle \Phi_i | \nabla | \Phi_j \rangle; G_{ij} = \langle \Phi_i | \nabla^2 | \Phi_j \rangle \tag{2.9}$$

It can be seen from Eq. 2.9 that the electronic states i and j are coupled through the derivative operators representing the nuclear motion. The elements $F_{ij}^{(n)}$ and G_{ij} represents vector coupling and scalar coupling, respectively. The solution of the nuclear Schrödinger equation is complicated by this nonadiabatic operator ($\hat{\Lambda}_{ij}$), especially for polyatomic molecules where several nuclear coordinates have to be considered. The nonadiabatic operators are ignored ($\hat{\Lambda}_{ij} = 0$) in the so-called adiabatic approximation. The adiabatic approximation is based on the assumption that the KEO of the nuclei can be considered as a small perturbation to the electronic motion. A more useful approximation, which is known as the Born-Huang approximation [94], is obtained by neglecting only the off-diagonal terms of nonadiabatic operators $\hat{\Lambda}_{ij}$. Using the Hellmann-Feynman theorem [95–98], the vector coupling term can be written as [14]

$$F_{ij}^{(n)} = \frac{\langle \Phi_i(q;Q) | \nabla_n H_e(q;Q) | \Phi_j(q;Q) \rangle}{V_i(Q) - V_j(Q)} \tag{2.10}$$

The adiabatic approximation may fail in many cases, especially when different electronic states are energetically close together. When two electronic states are exactly degenerate ($i = j$ at the point of CI), the derivative coupling terms of the electronic wave function ($F_{ij}^{(n)}$ in Eq. 2.9) diverge and the adiabatic approximation fails in the vicinity of CI. Because of this singularity the electronic states and their energies no longer remain an analytic function of nuclear coordinates, and states change their electronic character.

Their energy surfaces exhibit a cusp at the degeneracy [99].

The singularity of the derivative coupling mentioned above makes the adiabatic electronic basis unsuitable for a numerical solution of the nuclear Schrödinger equation. In practice, this is circumvented by defining a new electronic basis, called a diabatic electronic basis, in which the diverging kinetic coupling of the adiabatic electronic basis is transformed into smooth potential coupling by a suitable unitary transformation [14, 100–102]. In a diabatic electronic basis, the nuclear Schrödinger equation (Eq. (2.6)) reads [103]

$$\left[\hat{T}_N I + \hat{U}_j(Q) - E\right] \chi_j(Q) = \sum_{i=1(i\neq j)}^{\infty} \hat{U}_{ij}(Q)\chi_i(Q), \tag{2.11}$$

with

$$\hat{U}_{ij}(Q) = \langle \phi_i(q;Q)|\hat{H}_e(q;Q)|\phi_j(q;Q)\rangle. \tag{2.12}$$

The quantity $|\phi_i(q;Q)\rangle$ above defines the diabatic electronic wave function. The integration is carried out over electronic coordinates q. The sole difference between Eqs. 2.6 and 2.11 is the diverging kinetic coupling of Eq. 2.6 is transformed into smooth potential coupling in $\hat{U}_{ij}$. Since the diverging kinetic coupling can be "ideally" removed (entirely) on a diabatic basis, both the wave function and energy restore the analytic continuation as a function of Q in this basis. The diagonal elements, $\hat{U}_j(Q)$ of the U matrix, describe the diabatic electronic states, and the off-diagonal elements, $\hat{U}_{ij}(Q)$, define the coupling among them. As a result of analytic continuation, the states become smooth in the entire nuclear coordinate space, and the electronic character of the states is preserved in this representation. The preceding discussion revealed that the adiabatic electronic representation, although more realistic, cannot be used to study the dynamics. Therefore, although not unique, a diabatic electronic representation is restored for all practical purposes, ranging from atom-atom collisions to molecular spectroscopy [14, 101, 104].

Let us consider the following two-states diabatic electronic Hamiltonian

$$\hat{H}_e^d(Q) = \begin{bmatrix} \hat{U}_{11}(Q) & \hat{U}_{12}(Q) \\ \hat{U}_{21}(Q) & \hat{U}_{22}(Q) \end{bmatrix}, \tag{2.13}$$

where $\hat{U}_{11}(Q)$ and $\hat{U}_{22}(Q)$ represent the diabatic PESs, and $\hat{U}_{12}(Q)$=$\hat{U}_{21}(Q)$ describe their coupling surface. All the elements of the above matrix depend on the set of nuclear coordinates Q. Upon similarity transformation [14, 100–102, 104–107] through a suitable unitary matrix, $\mathbf{S}$, one obtains the adiabatic electronic Hamiltonian

$$\hat{H}_e^{ad}(Q) = \mathbf{S}^\dagger \hat{H}_e^d(Q)\mathbf{S}, \tag{2.14}$$

the transformation matrix is given by

$$\mathbf{S} = \begin{pmatrix} \cos\theta(Q) & \sin\theta(Q) \\ -\sin\theta(Q) & \cos\theta(Q) \end{pmatrix}. \tag{2.15}$$

The quantity $\theta(Q)$ defines the adiabatic-to-diabatic transformation angle and is given by [14]

$$\theta(Q) = \frac{1}{2}\tan^{-1}\left[\frac{2\hat{U}_{12}(Q)}{\hat{U}_{22}(Q) - \hat{U}_{11}(Q)}\right], \tag{2.16}$$

and $\Phi^{ad} = \mathbf{S}^{\dagger}\Phi^{d}$, († represents the adjoint). The adiabatic PESs are expressed as:

$$V_{1,2}(Q) = \frac{1}{2}\left[(\hat{U}_{11} + \hat{U}_{22}) \pm \sqrt{(\hat{U}_{11} - \hat{U}_{22})^2 + (2\hat{U}_{12})^2}\right]. \tag{2.17}$$

From this equation, one can see the possibility of their intersection. The separation between the two potentials (V_1 and V_2) is given by

$$\Delta V = V_1 - V_2 = \pm\sqrt{(\hat{U}_{11} - \hat{U}_{22})^2 + (2\hat{U}_{12})^2}. \tag{2.18}$$

The two adiabatic curves become degenerate (cross) when the argument of the two terms under the square root in Eq. 2.18 vanishes independently, and thus

$$\hat{U}_{11}(Q) = \hat{U}_{22}(Q) \tag{2.19}$$

$$\hat{U}_{12}(Q) = 0. \tag{2.20}$$

Thus, two equations must be satisfied with only one independent parameter, the internuclear separation, Q. In general, there is no reason why a single unknown should satisfy any two equations. Hence, in one dimension, the potentials cannot cross. This is called the "non-crossing rule". When stated more clearly for diatomics with only one degree of freedom (DOF), two adiabatic curves belonging to electronic states of the same symmetry generally do not cross but exhibit avoided crossings [108]. However, in molecular systems with three or more atoms (i.e., polyatomic), on the other hand, there are enough independent DOFs that can be varied to satisfy Eqs. 2.19 and 2.20. Therefore, we should expect degeneracies, or surface crossings, to be typical for polyatomic systems [16].

In two-dimensional space, these generally occur as isolated points where the PESs can touch. These points are referred to as "conical intersections"(CIs). Equation 2.17 describes a double cone topography of the two adiabatic PESs (V_1 and V_2) intersecting at the vertex [16, 17, 75]. If the number of dimensions (N) is more significant than two,

the space in which all the intersections that form CIs lie is N-2 dimensional space, with Eqs. 2.19 and 2.20 act as two constraints.

2.2 The model diabatic Hamiltonian

2.2.1 Vibronic coupling Hamiltonian

We assume that a diabatic basis is already constructed, and it is used in all the theoretical studies presented in this thesis. On this basis, the nuclear KEO is in the diagonal form, and the coupling between the electronic states is described by the off-diagonal elements of the PE operator. Also, the PESs are smooth, crossing curves on a diabatic basis in contrast to the adiabatic basis in which the PESs are non-crossing and exhibit a discontinuity (singularity) at the avoided crossing. In order to express the elements of the model diabatic Hamiltonian, a suitable coordinate system is needed first. An obvious choice is internal coordinate (bond length and bond angle) system which is best suited for the description of PESs. However, such a choice is not suitable for large molecular systems. This choice leads to a highly complex expression of the nuclear KEO and cannot be evaluated trivially for large systems in a numerical application. The normal coordinate representation of nuclear vibrations has become the obvious choice to treat small amplitude nuclear motion. In these coordinates, the nuclear KEO assumes a simple form. So, the vibronic Hamiltonian of the final states of the excited/ionized species is constructed in terms the normal dimensionless coordinates of the electronic ground state of the corresponding (reference) neutral species. From now onwards, the electronic states and vibrational modes are designated with n, m and i, j, respectively. The mass-weighted normal coordinates (q_i) are obtained by diagonalizing the force field and are converted into dimensionless form [92] by

$$Q_i = (\omega_i/\hbar)^{\frac{1}{2}} q_i, \tag{2.21}$$

where, ω_i is the harmonic frequency of the ith vibrational mode, and throughout the thesis, we consider $\hbar = 1$. These vibrational frequencies describe the above-mentioned normal displacement coordinates of the reference (equilibrium) geometry at $\mathbf{Q} = 0$. The vibronic Hamiltonian describing the photo-induced molecular process can be written as [14]

$$\hat{H} = H_0 \mathbf{1_n} + \Delta H \tag{2.22}$$

In the above equation, H_0 ($=\mathcal{T}_N + \mathcal{V}_0$) defines the reference electronic ground state zero-order (or unperturbed) Hamiltonian. In terms of the dimensionless normal displacement

coordinates of the vibrational modes, the KE and PE operators of the reference Hamiltonian H_0, within the harmonic approximation are given by

$$\mathcal{T}_N = -\frac{1}{2}\sum_i \omega_i \left[\frac{\partial^2}{\partial Q_i^2}\right], \tag{2.23}$$

$$\mathcal{V}_0 = \frac{1}{2}\sum_i \omega_i Q_i^2. \tag{2.24}$$

The quantity $\mathbf{1_n}$ in Eq. 2.22 describes a $n \times n$ diagonal unit matrix (where n depends on the total number of electronic states considered in the nuclear dynamics study), and ΔH is the change in electronic energy upon excitation/ionization from the reference Hamiltonian (H_0). The elements in this electronic Hamiltonian ΔH describe the diabatic PESs ($\hat{U}_{nn}$) and their coupling PESs ($\hat{U}_{nm}$) with the neighboring electronic states. Mainly, the $\hat{U}_{nm}$ elements take care of the nonadiabaticity in molecules. All these elements are expanded in a Taylor series expansion in terms of Q_i as

$$\hat{U}_{nn} = E_n + \sum_i \kappa_i^{(n)} Q_i + \frac{1}{2!}\sum_{i,j} \gamma_{ij}^{(n)} Q_i Q_j + \cdots \tag{2.25}$$

$$\hat{U}_{nm} = \sum_i \lambda_i^{(nm)} Q_i + \cdots, (n \neq m) \tag{2.26}$$

with

$$\kappa_i^{(n)} = \left(\frac{\partial \hat{U}_{nn}}{\partial Q_i}\right)\Bigg|_{\mathbf{Q}=0} \tag{2.27}$$

$$\lambda_i^{(nm)} = \left(\frac{\partial \hat{U}_{nm}}{\partial Q_i}\right)\Bigg|_{\mathbf{Q}=0} \tag{2.28}$$

$$\gamma_{ij}^{(n)} = \frac{1}{2}\left[\frac{\partial^2 \hat{U}_{nn}}{\partial Q_i \partial Q_j}\right]\Bigg|_{\mathbf{Q}=0}. \tag{2.29}$$

The E_n describes the vertical excitation/ionization energies (i.e., the vertical energy difference between the ground state PES and the corresponding surface of the nth number of the vibronically interacting electronic manifold at **Q=0**) of the system. The $\kappa_i^{(n)}$ (represents the forces acting within an electronic state (n) and determines the change in the structural arrangement of the molecule in this excited state compared to the ground state potential along the ith vibrational mode) and $\gamma_{ij}^{(n)}$ (is responsible for the change in the frequency in the excited state as compared to the ground state) are, respectively, the linear and quadratic (are responsible for the Duschinsky rotation) intra-state coupling constants for the nth electronic state. The $\lambda_i^{(nm)}$ represent the linear inter-state coupling constant between the nth and mth electronic states. For highly symmetric molecules, many of the terms appearing in Eqs. 2.25 and 2.26 vanish by symmetry. The symmetry

selection rule for non-vanishing linear terms fulfill

$$\Gamma_n \otimes \Gamma_{Q_i} \otimes \Gamma_m \supset \Gamma_A, \tag{2.30}$$

where Γ_n and Γ_{Q_i} denotes the irreducible representations (IRREPs) of the nth electronic state and of the ith vibrational mode, respectively. Similarly, the non-vanishing quadratic terms fulfill

$$\Gamma_n \otimes \Gamma_{Q_i} \otimes \Gamma_{Q_j} \otimes \Gamma_m \supset \Gamma_A. \tag{2.31}$$

Similar expressions hold for higher-order terms.

2.2.2 Vibronic coupling involving degenerate modes and degenerate states: The Jahn-Teller Hamiltonian

All symmetric non-linear polyatomic molecules with a main rotational axis C_n with $n \geq 3$-fold symmetry (high symmetry), result in multiple degenerate electronic states and vibrational modes. In the case of linear molecules, the vibronic coupling problem is known as the RT effect [109]; otherwise, it is known as the JT effect [75, 99]. In the JT case, the symmetry-induced degeneracy of an electronic state is lifted by distortions along modes of the appropriate symmetry and thus a CI is formed. A CI is characterized by the breakdown of the adiabatic or BO approximation because the adiabatic wave functions of the interacting states cease to be continuously differentiable functions with respect to the nuclear coordinates and the symmetry point constitutes a pole of the nonadiabatic coupling elements [15]. As we discussed in Sec. 2.1 that, even without the existence of a CI, the BO approximation may be invalid if two states become sufficiently close in energy and the nonadiabatic coupling elements become large. Besides the countless cases of generally avoided crossings, the so-called PJT effect is particularly interesting for analyzing such nonadiabatic interactions. The PJT interaction is characterized by coupling of a JT-split degenerate state with either a non-degenerate or the components of another JT-split state [14, 76, 77].

The JT theorem says that a configuration of a polyatomic molecule for an electronic state having orbital degeneracy cannot be stable for all displacements of the nuclei unless in the original configuration the nuclei all lie on a straight line [75]. The "orbital degeneracy" refers to E (for doubly) or T (for triply) symmetry electronic states. That is, Jahn and Teller have shown that a non-totally symmetric vibrational mode can always lift the orbital degeneracy in the first-order [75, 110]. The symmetries of the JT-active vibrational modes are determined by the requirement that the IRREP of the vibrational

mode (Γ_{vib}) must be included in the symmetrized direct product of the IRREP (Γ_{el}) of the degenerate electronic manifold

$$[\Gamma_{el}]^2 \supset \Gamma_{vib}. \tag{2.32}$$

The so-called $E\otimes e$-JT effect is the most well-studied JT problem in the literature [14, 76, 77, 99, 111, 112]. This JT model demonstrates that the two-fold electronic degeneracy (E) is lifted in first-order in displacements along the vibrational modes of e symmetry if the molecule contains at least one three-fold principle axis of rotation. Trigonal molecules are, therefore, systems of the lowest symmetry that exhibit the JT effect and have attracted continuous interest. Molecules of C_3, C_{3v}, D_3, C_{3h}, D_{3h}, D_{3d}, D_{6h} and O_h, etc., symmetries belong to this class. That is, most of the JT-active modes are degenerate. The tetragonal point groups (with two- or four-fold principle rotational axes of symmetry) are, however, exceptions: C_4, C_{4v}, C_{4h}, D_4, S_4, D_{2d}, D_{4h} and D_{4d}. For them, there are non-degenerate modes that are JT-active, the so-called $E\otimes b$-JT effect [14, 79, 81, 83, 99, 113]. The latter is due to the symmetry selection rules and not to the lack of degenerate normal modes. We mention here that the symmetry of the electronic states and the vibrational modes is denoted by upper and lower case letters, respectively, throughout this thesis.

Now let us consider a general molecule with a C_3 main rotational axis, a doubly degenerate E state and a nondegenerate A electronic state. The $E\otimes e$-JT and $(E+A)\otimes e$-PJT (i.e., an E state can couple a close lying nondegenerate A state through the same JT-active e vibrational mode) Hamiltonian may conveniently be expressed in the real representation as [14, 114, 115]

$$\begin{aligned}\Delta H =& \sum_{n=0}^{2} \frac{1}{n!} \left\{ \begin{pmatrix} \mathcal{V}_{E_x}^{(n)} & 0 & 0 \\ 0 & \mathcal{V}_{E_y}^{(n)} & 0 \\ 0 & 0 & \mathcal{V}_{A}^{(n)} \end{pmatrix} \right. \\ &\left. + \begin{pmatrix} \mathcal{W}_{JT}^{(n)} & \mathcal{Z}_{JT}^{(n)} & 0 \\ \mathcal{Z}_{JT}^{(n)} & -\mathcal{W}_{JT}^{(n)} & 0 \\ 0 & 0 & 0 \end{pmatrix} + \begin{pmatrix} 0 & 0 & \mathcal{W}_{PJT}^{(n)} \\ 0 & 0 & -\mathcal{Z}_{PJT}^{(n)} \\ \mathcal{W}_{PJT}^{(n)} & -\mathcal{Z}_{PJT}^{(n)} & 0 \end{pmatrix} \right\} \\ =& \sum_{n=0}^{2} \frac{1}{n!} \left\{ V_{diag}^{(n)} + V_{JT}^{(n)} + V_{PJT}^{(n)} \right\}. \end{aligned} \tag{2.33}$$

In the above equation, the diagonal matrices $V_{diag}^{(n)}$ represent the potentials of the corresponding states in absence of any coupling. The matrices $V_{JT}^{(n)}$ are responsible for the splitting of the degenerate electronic state due to the JT effect whereas $V_{PJT}^{(n)}$ are the

PJT coupling matrices. The degenerate e vibrational mode of the real coordinates are Q_x and Q_y. The explicit parametrized expressions for the diagonal $\mathcal{V}^{(n)}$ elements and the coupling elements $\mathcal{W}^{(n)}$ and $\mathcal{Z}^{(n)}$ are given by

$$\mathcal{V}^{(0)} = a_1^{(0)}, \tag{2.34a}$$
$$\mathcal{V}^{(1)} = 0, \tag{2.34b}$$
$$\mathcal{V}^{(2)} = a_1^{(2)} \left[Q_x^2 + Q_y^2\right], \tag{2.34c}$$
$$\mathcal{W}^{(0)} = 0, \tag{2.34d}$$
$$\mathcal{W}^{(1)} = \lambda_1^{(1)} Q_x, \tag{2.34e}$$
$$\mathcal{W}^{(2)} = \lambda_1^{(2)} \left[Q_x^2 - Q_y^2\right], \tag{2.34f}$$
$$\mathcal{Z}^{(0)} = 0, \tag{2.34g}$$
$$\mathcal{Z}^{(1)} = \lambda_1^{(1)} Q_y, \tag{2.34h}$$
$$\mathcal{Z}^{(2)} = -2\lambda_1^{(2)} Q_x Q_y. \tag{2.34i}$$

It is worth noting that the elements of the JT and PJT coupling matrices are of identical form and are only distinguished by different coupling constants $\lambda_m^{(n)}$. In the standard model of JT theory, the non-vanishing coupling terms are truncated, in most cases, after linear or quadratic terms [14, 77, 116, 117]. From the dynamical point of view, the limitation to quadratic terms and using HO basis sets for the nuclear motion has the advantage that all terms of the Hamiltonian matrix can be evaluated analytically. However, the disadvantage is that for systems displaying strong anharmonicity, this method will give poor results for properties determined by more extended regions of the PESs. The complete derivation of the Jahn-Teller model Hamiltonian, the selection rules for the higher-order JT- and PJT-coupling terms are given in the Appendix A.

2.3 Nuclear dynamics and simulation of electronic spectra

The vibronic coupling strongly influences the nuclear dynamics of molecular systems. Some attempts include vibronic effects in a classical treatment of dynamics, such as the surface hoping approach [118]. However, in this thesis work, we aim for a fully quantum treatment of nuclear motion. Full quantum dynamics simulations necessitate the solution of the nuclear Schrödinger equation. This can be conveniently achieved in both time-independent and time-dependent approaches. A straightforward approach is to develop the total wave function based on time-independent basis functions with time-dependent coefficients. This method is, however, only feasible for a small number of DOFs due to exponential scaling for computational time and memory requirements. One way to overcome this problem is the MCTDH method introduced by Meyer, Manthe,

and Cederbaum in 1990 [119]. It represents a powerful tool that is based on a multi-configurational wave function ansatz to solve the time-dependent Schrödinger equation.

The nuclear dynamics study is carried out from first principles using time-independent and time-dependent quantum mechanical methods. In the time-independent method, the vibronic spectrum is calculated by Fermi's golden rule equation of spectral intensity [14, 120]

$$P(E) = \sum_{n} |\langle \Psi_n^f | \hat{T} | \Psi_0^i \rangle|^2 \delta(E - E_n^f + E_0^i). \tag{2.35}$$

In the above equation, $|\Psi_0^i\rangle$ and $|\Psi_n^f\rangle$ are the initial and final vibronic states with energy E_0^i and E_n^f, respectively. The quantity $\hat{T}$ is the transition dipole operator. The reference electronic ground state, $|\Psi_0^i\rangle$, is assumed to be vibronically decoupled from the excited electronic states and is given by

$$|\Psi_0^i\rangle = |\Phi_0^i\rangle |\chi_0^i\rangle, \tag{2.36}$$

where $|\Phi_0^i\rangle$ is the diabatic electronic part and $|\chi_0^i\rangle$ is the nuclear part of this state. The nuclear component of the wave function in Eq. (2.36) is given by the product of eigenfunction of the reference harmonic Hamiltonian $\mathcal{H}_0$, as a function of the normal coordinates of the vibrational modes. The final vibronic state can be expressed as

$$|\Psi_n^f\rangle = \sum_{m} |\Phi^m\rangle |\chi_n^m\rangle. \tag{2.37}$$

In the above equation m and n are electronic and vibrational index, respectively. With the above definitions the spectral intensity of Eq. (2.35) assumes the form [14]

$$P(E) = \sum_{n,m} |\tau^m \langle \chi_n^m | \chi_0 \rangle|^2 \delta(E - E_n^f + E_0^i), \tag{2.38}$$

where,

$$\tau^m = \langle \Phi^m | \hat{T} | \Phi^0 \rangle, \tag{2.39}$$

represents the transition dipole matrix elements in the diabatic electronic basis. These are treated as constants assuming the validity of Condon approximation in this basis [121].

2.3.1 Time-independent approach

The time-independent Schrödinger equation of the vibronically coupled states is solved by representing the Hamiltonian [cf., Eq. (2.22)] in the direct product HO basis of the

reference state. The vibrational wave function, $|\chi_n^m\rangle$, on this basis, is given by

$$|\chi_n^m\rangle = \sum_{n_1,n_2,\ldots,n_k} a^m_{n_1,n_2\ldots,n_k}|n_1\rangle|n_2\rangle\ldots|n_k\rangle. \tag{2.40}$$

In the above equation, n_l is the quantum number associated with the lth vibrational mode, and k is the total number of such modes. The summation runs over all possible combinations of quantum numbers and diabatic states. The vibrational basis is suitably truncated for each vibrational mode depending on its excitation strength, $\left(\kappa^2/2\omega^2\right)$ and $\left(\lambda^2/2\omega^2\right)$ for the totally symmetric and non-totally symmetric vibrational modes, respectively. The Hamiltonian matrix acquires a sparse structure when expressed in a direct product HO basis. This sparse matrix is tridiagonalized employing the Lanczos algorithm [122] prior to its diagonalization. The eigenvalues of this matrix yield the location of the vibronic energy levels, and the intensity is calculated by squaring the first component of the eigenvector matrix [123].

In order to facilitate comparison with the experiment, the vibronic eigenvalue spectrum calculated with the prescription demonstrated above is convoluted with a line shape function to generate the spectral envelope.

$$P_\Gamma(E) = P(E)\otimes\mathcal{L}_\Gamma(E) \tag{2.41}$$

For example, the $\mathcal{L}_\Gamma(E)$ can be taken as Lorentzian function with full width at the half maximum (FWHM) Γ

$$\mathcal{L}_\Gamma(E) = \frac{1}{\pi}\frac{\Gamma/2}{E^2+(\Gamma/2)^2}. \tag{2.42}$$

2.3.2 Time-dependent approach

In a time-dependent picture, the spectral intensity defined in Eq. (2.35) translates to a Fourier transform of the time autocorrelation function of the WP evolving on the final electronic state [14, 120]

$$P(E) \approx 2Re\sum_{m=1}^{N}\int_0^\infty e^{iEt/\hbar}\langle\chi_0|\tau^\dagger e^{-i\hat{H}t/\hbar}\tau|\chi_0\rangle dt, \tag{2.43}$$

$$\approx 2Re\sum_{m=1}^{N}\int_0^\infty e^{iEt/\hbar}C^m(t)dt, \tag{2.44}$$

where, $C^m = \langle\Psi^m(0)|\Psi^m(t)\rangle$, represents the time autocorrelation function of the WP initially prepared on the mth electronic state. Finally, the composite spectrum is calculated by combining the partial spectra obtained by propagating WP on each electronic state.

2.4 The Multi-configuration time-dependent Hartree method

Despite the high numerical accuracy and simplicity of the implementation, the straightforward numerical solution of the time-dependent Schrödinger equation (TDSE), which may be called the standard method, suffers from the exponential scaling of the computational effort with the number of electronic and nuclear DOFs. An alternative to the standard method is the time-dependent Hartree (TDH) method which expresses the wave function as a Hartree product of time-dependent single-particle-functions (SPFs) or orbitals and the time-dependent expansion coefficients are determined variationally by solving the TDSE using the Dirac-Frenkel variational principle [124, 125]

$$\langle \delta\Psi \left| \hat{H} - i\frac{\partial}{\partial t} \right| \Psi \rangle. \tag{2.45}$$

As a single reference method, TDH often performs poorly and misses a large part of the correlation between different DOFs [126]. The MCTDH method has been developed as a trade-off between the accuracy of the numerically exact method and the efficiency of the TDH method [119, 127, 128]. The flexibility in the number of DOFs and in choosing the number of SPFs allows MCTDH to cover a full range of approximations between TDH (single reference) to numerically exact (analogous to the full CI treatment in electronic structure theory). Importantly, due to the variational character, small sets of SPFs are usually sufficient in many cases to yield good results which makes the MCTDH method appealing, especially when the number of DOFs is large.

The MCTDH wave function allows to combine of several DOFs in its multi-set formulation, and it is defined by the following ansatz [119, 127, 128]

$$\begin{aligned} \Psi(Q_1, Q_2, ..., Q_f, t) &= \Psi(q_1, q_2, ..., t) && (2.46)\\ &= \sum_m \sum_{j_l=1}^{n_l^{(m)}} ... \sum_{j_p=1}^{n_k^{(m)}} A^{(m)}_{j_l,...,j_p}(t) \prod_{k=1}^{p} \phi^{(m,k)}_{jk}(q_k, t)|m\rangle, && (2.47)\\ &= \sum_m \sum_J A^{(m)}_J \Phi^{(m)}_J |m\rangle. && (2.48) \end{aligned}$$

In the above equation, m, f, and p are the indices for the electronic state, number of vibrational DOFs, and MCTDH particles, respectively. The particles are formed by combining DOFs. For example, the particles coordinate can be given as, q_k=$[Q_1, Q_2, ...]$. The $A^{(m)}_{j_l,...,j_p}$ denotes the MCTDH expansion coefficients and the $\phi^{(m,k)}_{jk}$ are the n_k time-dependent expansion functions (SPFs) for each DOF k associated with the electronic state m. The latter is the multidimensional function of the set of particle coordinates. Since $p < f$, the computational overhead is drastically reduced for systems with large

DOFs. The variables for the p sets of SPFs are defined in terms of one- or multi-dimensional coordinates of a particle. $\Phi_J^{(m)}$ is the f-dimensional Hartree product of the SPFs represented by the composite index J=$(j_l, ..., j_p)$. For practical purposes, the SPFs have to be represented in terms of an underlying time-independent primitive basis set

$$\phi_{jk}^{(m,k)}(q_k, t) = \sum_{l=1}^{N_k} c_{lj_k}^{(k)}(t)\chi_l^{(k)}(q_k). \tag{2.49}$$

The primitive basis functions are often replaced by a discrete variable representation (DVR) grid. MCTDH is of advantage in comparison to the numerically exact method only if $n_k < N_k (k = 1, ..., f)$. The method uses DVR, the fast Fourier transform algorithm and robust integrators to evaluate the WP on the grid. For more technical details the readers are referred to the URL https://www.pci.uni-heidelberg.de/cms/mctdh.html.

The limiting factor in quantum dynamical calculations is often the memory consumption, so here we provide a brief overview of the memory requirement for the MCTDH calculations. In comparison with the N^f numbers required to describe the standard method, the MCTDH wave functions require

$$memory \sim fnN + n^f, \tag{2.50}$$

where, f, n, and N represent the total number of DOFs, SPFs, and total number of grid points or primitive basis functions, respectively. The first part in the sum (fnN) accounts for the space needed to store the SPFs, and the second term (n^f), accounts for the storage of the coefficient vector [129]. The base can be further reduced by grouping DOFs together in combined modes or logical coordinates [129]. One obtains a smaller number of effective DOFs, d (i.e., d DOFs are combined). There are hence $p = f/d$ particles; the grid size increases to $\tilde{N} = N^d$, and the number of combined SPFs increases to $\tilde{n} = dn$. The memory requirement changes to

$$memory \sim p\tilde{n}\tilde{N} = \tilde{n}^p \tag{2.51}$$

$$\sim fnN^d + \tilde{n}^{f/d}, \tag{2.52}$$

which leads to huge saving in memory when the dimensionality of the problem is high [129, 130]. For the details of this method and algorithm, the readers are referred to the original research papers [119, 127, 128, 131].

In this thesis, the Heidelberg MCTDH program package [131] will be consistently used for all the quantum dynamical calculations.

Chapter 3

Elucidation of vibronic structure and dynamics of first eight excited electronic states of pentafluorobenzene

In this chapter the vibronic coupling in the first eight electronic excited states of pentafluorobenzene (PFBz) is examined. Benzene (Bz), benzene radical cation (Bz^+) and their fluorinated derivatives have received renewed attention in different contexts in the literature in connection to their novel electronic structure and spectroscopic properties. Fundamentally, the change of photophysical properties of Bz upon fluorination is an interesting subject and investigated by various researchers [52–54, 59–67, 132–142]. A detailed study of the spectroscopic and dynamical properties of the excited electronic states of their radical cations have been explored in the recent past [47–51, 55–57, 143, 144]. It is well established that the stabilization of σ-orbital increases with an increased fluorination of Bz. This phenomenon is termed as perfluoro effect in the literature [34]. As a result of this, the optically dark $\pi\sigma^*$ state becomes lower in energy and often mixes with optically bright $\pi\pi^*$ state [34, 52–54, 59, 60]. It was found that the lowest $\pi\sigma^*$ state is significantly higher in energy than the lowest $\pi\pi^*$ state, when the number of fluorine atom substitution in the Bz is four or less. These molecules exhibit structured $S_1 \leftarrow S_0$ absorption band, large quantum yield and nanosecond lifetime of fluorescence. Whereas penta and hexa fluorinated Bz molecules exhibit structureless $S_1 \leftarrow S_0$ absorption band, low quantum yield and picosecond lifetimes of fluorescence emission [61–64].

Recent ultra-violet (UV) absorption experiments [59, 60, 65–67] on pentafluorobenzene (PFBz) and hexafluorobenzene (HFBz) indicate that the lowest $\pi\pi^*$ and $\pi\sigma^*$ states

become energetically very close with each other which results into a broad and structureless profile of the first absorption band. The first four excited electronic states of PFBz are reported to be of $\pi\pi^*$ (S_1), $\pi\sigma^*$ (S_2), $\pi\sigma^*$ (S_3) and $\pi\pi^*$ (S_4) type [60]. While a transition from the S_0 to the $\pi\pi^*$state is optically allowed, the same to the $\pi\sigma^*$ state is forbidden. The signature of the latter can only appear in the spectrum when it interacts vibronically with the optically bright $\pi\pi^*$ state. These $\pi\pi^*$ and $\pi\sigma^*$ states are also energetically very close. Therefore, a detailed systematic theoretical investigation of the vibronic coupling between these $\pi\pi^*$ and $\pi\sigma^*$ states is worthwhile to understand the structureless absorption bands of PFBz.

Numerous experimental and theoretical studies have been carried out on the structure and spectroscopy of PFBz [52, 53, 60–65, 132–142]. We in the recent past developed a vibronic coupling model and studied its optical absorption spectrum [52, 53]. Recent femtosecond time-resolved time-of-flight mass spectroscopy measurements and theoretical vibronic coupling calculations indicated the involvement of a second $\pi\sigma^*$ state in the detailed vibronic structure of the $\pi\pi^*$ state [60]. Although we found such a state in our previous study, it was dropped from the theoretical model owing to its zero oscillator strength. In the present contribution we develop a complete model by including low-lying eight excited electronic states and all relevant nuclear degrees of freedom (DOF). Detailed electronic structure calculations are performed and multiple curve crossings leading to conical intersections (CIs) are established. This "complete"model is employed to study nuclear dynamics and the impact of nonadiabatic coupling effects due to CIs on the vibronic band structures. The present results are compared with our earlier theoretical results of Refs. [52, 53] as well as the available experimental results of Refs. [60, 63] and discussed.

3.1 Theoretical Framework

3.1.1 Vibronic Hamiltonian

Energetically low-lying eight singlet electronic states of PFBz molecule are considered in this study. A vibronic Hamiltonian is constructed in a diabatic electronic basis in terms of dimensionless normal displacement coordinates of vibrational modes of the electronic ground state of PFBz and symmetry selection rules. Thirty vibrational modes of PFBz transform according to the following irreducible representations (IRREPs) of the C_{2v} equilibrium symmetry point group.

$$\Gamma_{\text{vib}} = 11a_1 + 6b_1 + 10b_2 + 3a_2. \tag{3.1}$$

Employing the elementary symmetry selection rule and standard vibronic coupling theory, the Hamiltonian can be written in a diabatic electronic basis as [14, 21]

$$\mathcal{H} = \mathcal{H}_0 \mathbf{1_8} + \mathbf{\Delta}\mathcal{H}, \tag{3.2}$$

with

$$\mathcal{H}_0 = \mathcal{T}_N + \mathcal{V}_0. \tag{3.3}$$

In the above, $\mathcal{H}_0$ is the unperturbed Hamiltonian of the reference electronic ground state of PFBz, $\Delta\mathcal{H}$ represents the change in energy upon electronic excitation and $\mathbf{1}$ represents a (8×8) unit matrix. In terms of the dimensionless normal displacement coordinates of the vibrational modes, the components of the reference Hamiltonian of Eq. (3.3) within the harmonic approximation are given by

$$\mathcal{T}_N = -\frac{1}{2}\sum_i \omega_i \left(\frac{\partial^2}{\partial Q_i^2}\right); i \in a_1, b_1, b_2, a_2 \tag{3.4}$$

$$\mathcal{V}_0 = \frac{1}{2}\sum_i \omega_i Q_i^2 \; ; i \in a_1, b_1, b_2, a_2. \tag{3.5}$$

The first eight singlet excited states of PFBz belong to the $^1\mathrm{B}_2(S_1)$, $^1\mathrm{A}_2(S_2)$, $^1\mathrm{B}_1(S_3)$, $^1\mathrm{A}_1(S_4)$, $^1\mathrm{A}_2(S_5)$, $^1\mathrm{B}_1(S_6)$, $^1\mathrm{A}_1(S_7)$ and $^1\mathrm{B}_2(S_8)$ electronic terms of the C_{2v} symmetry point group. The quantity $\Delta\mathcal{H}$ in Eq. (3.2) can be symbolically written as

$$\Delta\mathcal{H} = \begin{bmatrix} H_{11} & H_{12} & H_{13} & H_{14} & H_{15} & H_{16} & 0 & 0 \\ & H_{22} & H_{23} & H_{24} & 0 & H_{26} & H_{27} & 0 \\ & & H_{33} & H_{34} & H_{35} & 0 & H_{37} & H_{38} \\ & & & H_{44} & H_{45} & H_{46} & 0 & H_{48} \\ & & & & H_{55} & H_{56} & H_{57} & H_{58} \\ & & & & & H_{66} & H_{67} & H_{68} \\ & h.c. & & & & & H_{77} & H_{78} \\ & & & & & & & H_{88} \end{bmatrix}. \tag{3.6}$$

The elements of this electronic Hamiltonian matrix are expanded in a Taylor series around the equilibrium geometry of the reference state (**Q**=0) as

$$\begin{aligned} H_{nn} = E_0^n &+ \sum_{i \in a_1} \kappa_i^n Q_i + \frac{1}{2!} \sum_{i,j \in a_1,a_2,b_1,b_2} \gamma_{ij}^n Q_i Q_j \\ &+ \frac{1}{3!} \sum_{i,j>i \in a_1} \left[\eta_{ii}^n Q_i^3 + \eta_{jj}^n Q_j^3 + \eta_{ij}^n Q_i^2 Q_j + \eta_{ij}^{'n} Q_i Q_j^2 \right] \\ &+ \frac{1}{4!} \sum_{i,j \in a_1,a_2,b_1,b_2} \zeta_{ij}^n Q_i^2 Q_j^2 + \frac{1}{4!} \sum_{i,j>i \in a_1,\ b_1} \left[\zeta_{ij}^{'n} Q_i^3 Q_j + \zeta_{ij}^{''n} Q_i Q_j^3 \right] \\ &+ \sum_{i \in a_1(\nu_2)} \left[\frac{1}{5!} \theta_i Q_i^5 + \frac{1}{6!} \delta_i Q_i^6 + \frac{1}{7!} \rho_i Q_i^7 + \frac{1}{8!} \xi_i Q_i^8 \right] \end{aligned} \tag{3.7}$$

and

$$H_{nm} = \sum_{i \in a_2,\ b_1,\ b_2} \lambda_i^{nm} Q_i, \tag{3.8}$$

where, n and m, are the electronic state indices and i, j represents the vibrational modes. The vertical excitation energy (VEE) of the nth electronic state is defined as E_0^n, where, $n \in S_1$ to S_8 electronic states, respectively. The quantity κ_i^n is linear intra-state coupling parameter related to the relative shift of the equilibrium minimum (i.e., change in the structural arrangement of the molecule) of the excited state with respect to that of the reference state. The quantity γ_{ij}^n is the diagonal second-order, η_{ij}^n and $\eta_{ij}^{'n}$ are the third-order, ζ_{ij}^n, $\zeta_{ij}^{'n}$ and $\zeta_{ij}^{''n}$ are the fourth-order intra-state bilinear coupling parameters of the vibrational modes i and j in the nth electronic state. The change in the curvature (i.e., frequency) of the excited state is described by γ and the higher-order coupling parameters (η, ζ, θ, δ, ρ and ξ) describe the anharmonicity of the potentials. The quantity, λ_i^{nm} is linear inter-state coupling parameter between the states n and m, coupled through the ith vibrational mode, and this term is approximated within the linear vibronic coupling approach [14]. All these vibronic coupling parameters are determined by fitting the electronic energies calculated *ab initio* to the adiabatic form of the Hamiltonian of Eqs. (3.7) and (3.8) as discussed below.

The parameters appearing in the Taylor expansion of the elements of the diabatic Hamiltonian matrix are derived from a non-linear least squares fitting to the corresponding adiabatic electronic energies calculated *ab initio*. The fitting is done by using the Levenberg Marquardt algorithm [145, 146] as implemented in MATLAB [147]. The linear inter-state coupling parameter (λ_i^{nm}) of Eq. (3.8) is evaluated from a separate two-state model calculations and is given by

$$\lambda_i^{nm} = \sqrt{\frac{1}{8} \frac{\partial^2 \left(|V_m - V_n|^2 \right)}{\partial Q_i^2}} \Bigg|_{Q_0}. \tag{3.9}$$

3.1.2 Details of electronic structure calculations

The optimized equilibrium geometry of the electronic ground state of PFBz is calculated by using the second-order Møller-Plesset perturbation (MP2) theory [148] employing the augmented correlation-consistent polarized valence double zeta (aug-cc-pVDZ) basis set of Dunning [149]. GAUSSIAN-09 [150] suite of program is used for this purpose. The optimized equilibrium structure of the PFBz in the electronic ground state ($^1A_1$) belongs to C_{2v} symmetry point group. The harmonic vibrational frequency of ith vibrational mode (ω_i) of the reference equilibrium structure is calculated by diagonalizing the kinematic and *ab initio* force constant matrix at the same level of theory. The eigenvectors of the force constant matrix yield the mass-weighted normal coordinates of the vibrational modes. The latter is transformed to the dimensionless form $\mathbf{Q}$ by multiplying with $\sqrt{\omega_i}$ (in a_0; $\hbar$=1) [92]. The adiabatic electronic energies of these electronic states are calculated in the range -5.00 to +5.00 with an increment of 0.25, along Q_i using the equation-of-motion coupled cluster singles and doubles (EOM-CCSD) method [151–153] and aug-cc-pVDZ basis set, with the aid of MOLPRO suite of program [154].

3.2 Results and Discussion

3.2.1 Hamiltonian parameters

The parameters of the vibronic Hamiltonian discussed in Sec. 3.1.1 are extracted from the calculated adiabatic electronic energies discussed in Sec. 3.1.2. The Harmonic vibrational frequencies of the electronic ground state of PFBz calculated at the MP2 level of theory using the aug-cc-pVDZ basis set are given in Table 3.1 along with the literature data [155, 156] for comparison. The molecular orbitals which are involved to form the low-lying eight excited singlet electronic states of PFBz are schematically represented in Fig. 3.1. It can be seen from the figure that, they are of $\pi\pi^*(S_1)$, $\pi\sigma^*(S_2)$, $\pi\sigma^*(S_3)$, $\pi\pi^*(S_4)$, $\pi\sigma^*(S_5)$, $\pi\pi^*(S_6)$, $\pi\pi^*(S_7)$ and $\pi\pi^*(S_8)$ type (hear after they will be designated as S_1, S_2, S_3, S_4, S_5, S_6, S_7 and S_8), respectively. A transition to the first (S_2) and third (S_5) $\pi\sigma^*$ states from the S_0 state is optically forbidden. However, these states can be coupled with the optically bright $\pi\pi^*$ states through non-totally symmetric vibrational modes and can have their impact in the spectrum through intensity borrowing mechanism.

The VEEs of the above mentioned electronic states are given in Table 3.2, along with their oscillator strengths (f) and the available experimental data [138]. The f values are consistent with the nature of the optical transitions discussed above. In order to

TABLE 3.1: Symmetry designation and harmonic frequency (in cm^{-1}) of vibrational modes of the electronic ground state of PFBz calculated at the MP2 level of theory.

Sym.	Mode	This work aug-cc-pVDZ	Expt. Ref. [155]	Expt. Ref. [156]	Description of the modes
a_1	ν_1	3257	3103	3105	C-H stretching in plane
	ν_2	1682	1648	1648	C-C-C bending
	ν_3	1533	1516	1514	C-C and C-F stretching
	ν_4	1422	1413	1410	C-C stretching
	ν_5	1268	1291	1286	C-C stretching (Kekule)
	ν_6	1063	1078	1082	C-F stretching
	ν_7	716	719	718	C-C-C trigonal bending
	ν_8	574	577	580	ring breathing
	ν_9	467	474	469	C-C-C in plane bending
	ν_{10}	324	327	325	C-F in plane bending
	ν_{11}	267	272	272	C-F in plane bending
a_2	ν_{12}	632	661	-	C-C-C out-of-plane
	ν_{13}	384	387	391	C-F out-of-plane bending
	ν_{14}	132	142	171	C-F out-of-plane
b_1	ν_{15}	841	837	838	C-H out-of-plane bending
	ν_{16}	591	715	689	C-H and C-F out of plane trigonal
	ν_{17}	543	556	556	C-H and C-C-C out of plane
	ν_{18}	317	321	-	C-F out-of-plane bending
	ν_{19}	204	206	-	C-F out-of-plane bending, in phase
	ν_{20}	158	158	-	C-F out-of-plane bending
b_2	ν_{21}	1679	1648	1648	C-C stretching
	ν_{22}	1552	1540	1535	C-C stretching
	ν_{23}	1478	1269	1268	C-C stretching
	ν_{24}	1185	1182	1182	C-H bending, in plane
	ν_{25}	1129	1143	1138	C-F stretching, in plane
	ν_{26}	947	958	953	C-F stretching and C-H bending, in plane
	ν_{27}	684	692	662	C-F in plane bending
	ν_{28}	429	433	436	C-C-C in plane bending
	ν_{29}	300	303	300	C-F in plane bending
	ν_{30}	272	256	-	C-F in plane bending

extract the Hamiltonian parameters, the calculated adiabatic *ab initio* electronic energies along each vibrational mode are fitted with the analytical adiabatic form of the diabatic electronic Hamiltonian of Eq. (3.6). The estimated Hamiltonian parameters of the eight excited electronic states are given in Tables B1-B10 of Appendix B. The inter-state coupling parameters between the given electronic states and their excitation strength ($\lambda^2/2\omega^2$) are given in the parentheses along the suitable non-totally symmetric vibrational modes are given in Table B11 of the Appendix B.

TABLE 3.2: State symmetry and VEEs (in eV) of the first eight excited singlet states of PFBz calculated at the ground state equilibrium geometry. Oscillator strengths are given in the parenthesis.

State symmetry	EOM-CCSD	TD-DFT	Theory [52]	Theory [60]	Expt. [138]
S_1 ($^1B_2, \pi\pi^*$)	5.139 (0.0087)	5.178 (0.0125)	5.111	4.85	4.79
S_2 ($^1A_2, \pi\sigma^*$)	5.936 (0.0000)	5.345 (0.0000)	-	5.93	-
S_3 ($^1B_1, \pi\sigma^*$)	6.235 (0.0011)	5.643 (0.0008)	6.314	6.20	5.85
S_4 ($^1A_1, \pi\pi^*$)	6.615 (0.0042)	5.981 (0.0009)	6.597	6.29	6.36
S_5 ($^1A_2, \pi\sigma^*$)	7.315 (0.0000)	6.756 (0.0000)	-	-	7.12
S_6 ($^1B_1, \pi\pi^*$)	7.396 (0.0173)	6.796 (0.0082)	-	-	7.12
S_7 ($^1A_1, \pi\pi^*$)	7.492 (0.6702)	6.832 (0.5406)	7.475	-	-
S_8 ($^1B_2, \pi\pi^*$)	7.535 (0.6527)	6.882 (0.5164)	7.509	-	-

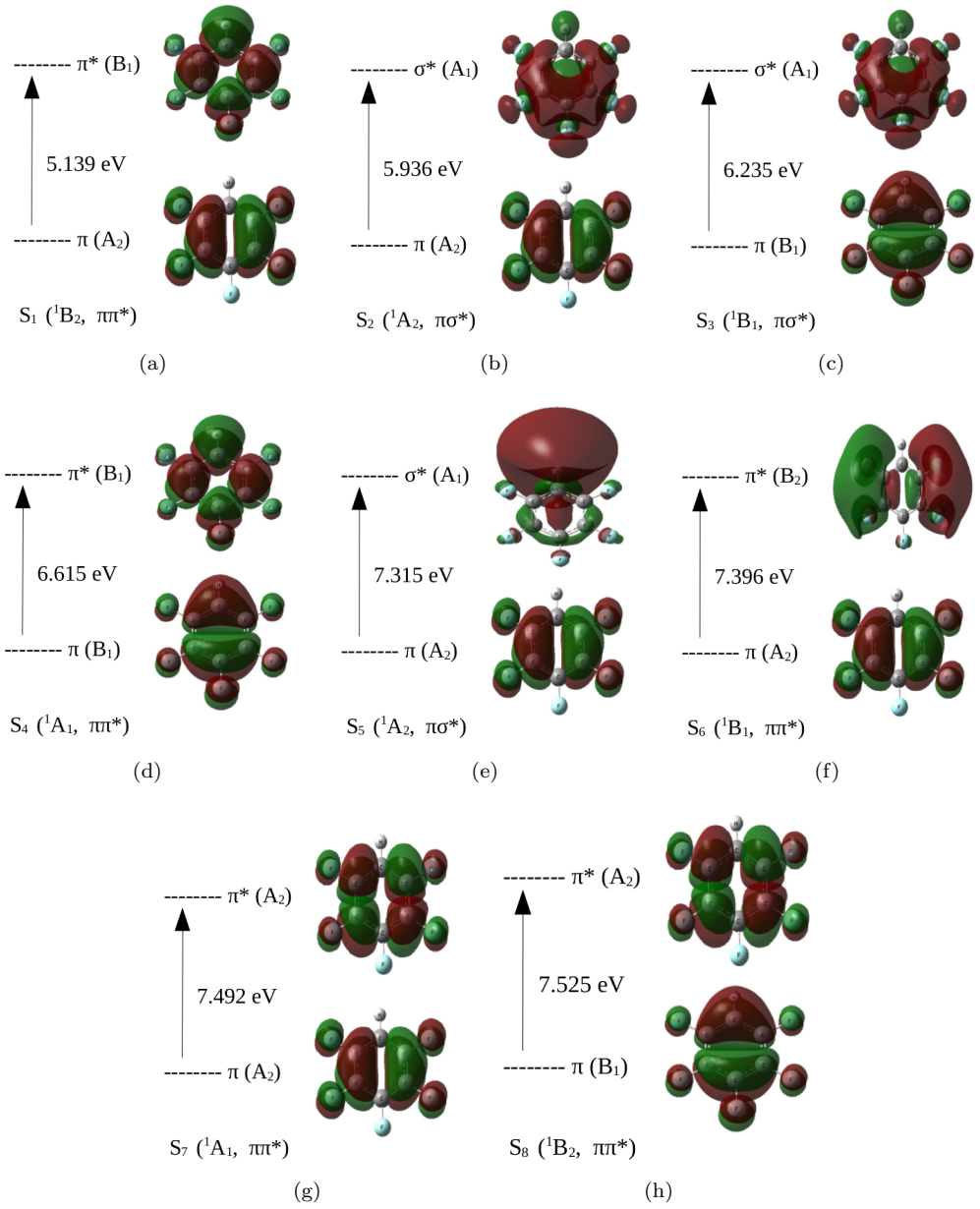

FIGURE 3.1: Molecular orbitals (MOs) involved in the first eight (S_1 to S_8) excited singlet electronic states of PFBz are shown in panels (a)-(h), respectively.

3.2.2 Potential energy surfaces and conical intersections

It is well known that the totally symmetric vibrational modes tune the energy gap between the electronic states [14]. One-dimensional cuts of the PESs of the first eight excited singlet electronic states of PFBz along the totally symmetric vibrational modes (ν_2-ν_4, ν_7-ν_9 and ν_{11}) are shown in Fig. 3.2. Solid lines in each panel represent the PESs obtained from the constructed vibronic coupling model [cf., Sec. 3.1.1] and the parameters of Tables 3.1, 3.2 and B1-B5 of the Appendix B. The asterisks represent the electronic energies obtained from the *ab initio* calculations. It can be seen from Fig. 3.2

that the calculated energies are well reproduced by the present vibronic coupling model. Among the eleven totally symmetric vibrational modes, the Condon activity of the ν_8 is highest in the S_1, S_4, S_7 and S_8 electronic states, whereas, the Condon activity of the ν_{11} and ν_9 is highest in the S_2, S_6 and S_3, S_5 electronic states, respectively. Based on the coupling strengths, we have considered seven (ν_2-ν_4, ν_7-ν_9 and ν_{11}) totally symmetric vibrational modes for the nuclear dynamics study.

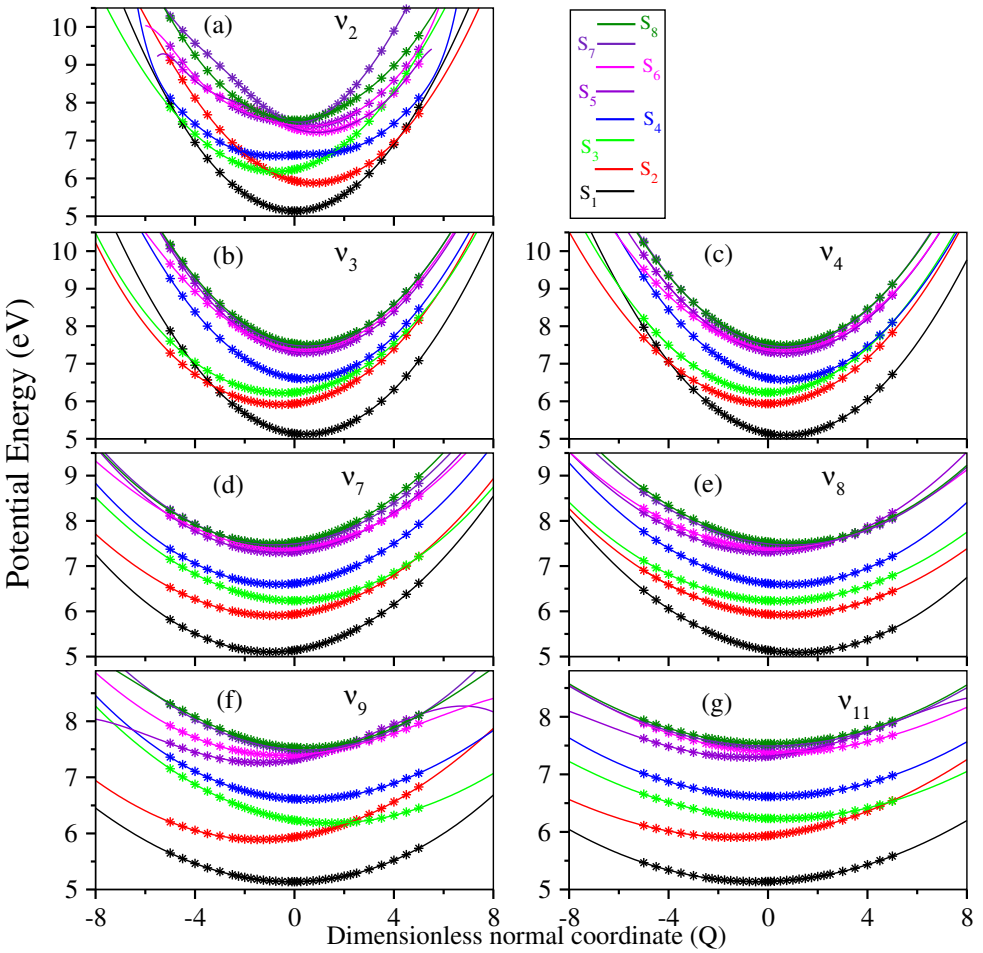

FIGURE 3.2: Adiabatic potential energies of the first eight low-lying excited singlet electronic states of PFBz along the normal coordinates of the totally symmetric vibrational modes ν_2, ν_3, ν_4, ν_8, ν_9, and ν_{11} shown in panels (a)-(g), respectively. The potential energies obtained from the present model and the computed *ab initio* energies are shown by solid lines and asterisks, respectively.

The energetic locations of the minimum of these eight electronic states in the subspace of totally symmetric vibrational modes are given in the diagonal entries of the Table 3.3. Several crossings between the PESs which acquire the topography of CIs in multi-dimensions [cf., Fig. 3.3] can be seen in Fig. 3.2. The estimated energetic minimum of the CIs among eight excited electronic states are given in Table 3.3 in the off-diagonal entries. The energetic locations of the minimum of CIs are estimated with

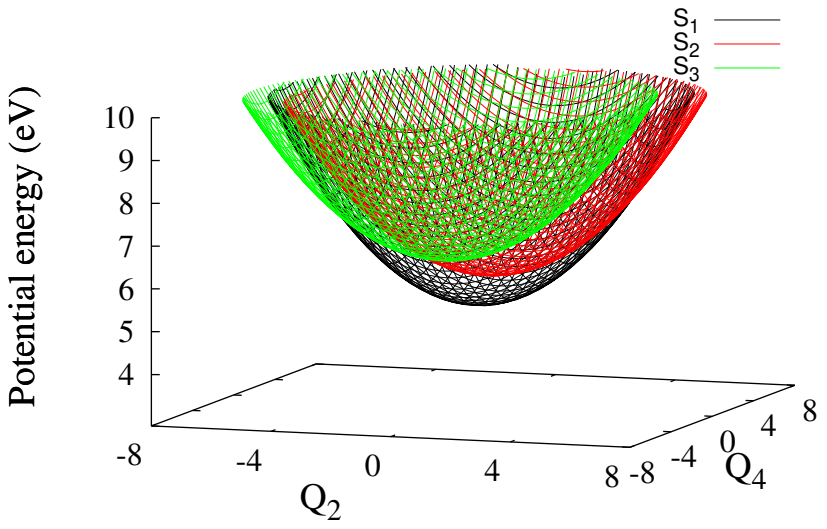

FIGURE 3.3: Adiabatic potential energies of the first three low-lying excited singlet electronic states of PFBz are plotted along the dimensionless normal displacement coordinates of the ν_2 and ν_4 totally symmetric vibrational modes.

the quadratic vibronic coupling model employing a constrained minimization procedure using Lagrangian multipliers as implemented in Mathematica program module [157]. It can be seen from Fig. 3.2 that the S_1 state is energetically well separated from the other states at the Franck-Condon (FC) region, whereas beyond this region, intersection between S_1 and S_2 electronic states along the ν_2, ν_3 and ν_4 vibrational modes are found [cf., panels a, b and c of Fig. 3.2]. This indicates that S_2 ($\pi\sigma^*$) state may have considerable impact on the dynamics of S_1 state of PFBz. The data given in Table 3.3 reveals that the S_1-S_2 intersection minimum occurs at ∼0.88 eV and ∼0.14 eV above the minimum of the S_1 and S_2 electronic states, respectively. Hence, an excitation to the S_2 state would readily allow the WP to access the S_1-S_2 CIs and it may have crucial impact on the nuclear dynamics in the S_1-S_2 interacting electronic state of PFBz. The minimum of S_2-S_3 CIs occurs at ∼6.10 eV, which is only ∼0.38 eV above the S_2 minimum and it nearly coincides with the S_3 minimum. The minimum of S_3-S_4 CIs occurs at ∼0.45 eV and ∼0.07 eV above the minimum of the S_3 and S_4 states, respectively. The S_4 and S_5 states are quasi-degenerate and their CIs occur at ∼0.22 eV and ∼0.20 eV above their equilibrium minimum, respectively. The minimum of the S_6, S_7 and S_8 states occurs at ∼7.30 eV, ∼7.37 eV and ∼7.40 eV, respectively. These three electronic states are also quasi-degenerate and their CIs occur very close to their equilibrium minimum.

At the FC region, the VEE difference between the S_1 and S_2 is ∼0.80 eV, whereas the same between S_1-S_3 and S_1-S_4 are ∼1.10 eV and ∼1.48 eV, respectively. The energy

TABLE 3.3: Energy (in eV) of the equilibrium minimum of the state (diagonal entries) and the minimum of its intersection seam with its neighbors (off-diagonal entries) of PFBz calculated within a second-order coupling model.

	S_1	S_2	S_3	S_4	S_5	S_6	S_7	S_8
S_1	4.98	5.86	6.41	6.49	6.59	8.97	-	-
S_2	-	5.72	6.10	6.48	-	8.81	13.60	-
S_3	-	-	6.09	6.54	6.87	-	12.61	10.36
S_4	-	-	-	6.47	6.69	8.67	-	30.94
S_5	-	-	-	-	6.49	7.35	7.38	7.40
S_6	-	-	-	-	-	7.30	7.37	7.40
S_7	-	-	-	-	-	-	7.37	7.40
S_8	-	-	-	-	-	-	-	7.40

difference between S_1 and S_2 states decreases beyond the FC region. Therefore, it would be expected that the totally symmetric vibrational modes that modulate the energy gap between the S_1 and S_2 states and the electronic nonadiabatic effects mediated through b_1 vibrational modes would be vary due to the tuning activities of the totally symmetric modes. It is therefore, worthwhile to examine the modulation of electronic nonadiabatic effects through vibrational modes of b_1 symmetry in addition to the tuning activity of totally symmetric vibrational modes.

The out-of-plane bending vibrational modes of b_1 symmetry couples the $S_1(^1B_2)$ and $S_2(^1A_2)$ states and the topography of these coupling surfaces is shown in Fig. 3.4. The lower adiabatic potential energy surface exhibits a symmetric double well shape along the Q_{20}, Q_{18}, Q_{17} and Q_{16} normal coordinates with two symmetric minimum at distorted geometry compared to the reference equilibrium C_{2v} geometry at, **Q=0**. This symmetry breaking [14], known as pseudo-Jahn-Teller (PJT) effect [158], occurs due to strong nonadiabatic coupling (interstate coupling) through b_1 symmetry vibrational modes [cf., Table S11 of the ESI] between the energetically close lying S_1 ($\pi\pi^*$) and S_2 ($\pi\sigma^*$) electronic states. Therefore, it appears that the vibronic coupling through b_1 vibrational modes stabilizes the PFBz molecule in its S_1 state at various distorted out-of-plane geometries. It can be seen from Table 3.2 that the S_1 state is vertically $\sim$0.80 eV below the S_2 state whereas, the S_3 and S_4 states occur more than 1 eV above it. On the other hand, the S_3 and S_4 states are vertically close in energy, therefore, it is also possible that the S_3 and S_4 states can have some indirect impact on the dynamics of the S_1 state.

To understand the tuning activity of the totally symmetric vibrational modes on the S_1-S_2 coupled surfaces, we plotted the potential energies of these two states along the dimensionless normal coordinate of the strongest coupling mode, Q_{20}, at some fixed values of the coordinate of totally symmetric modes (Q_2, Q_3 and Q_4) in Fig. 3.5. It

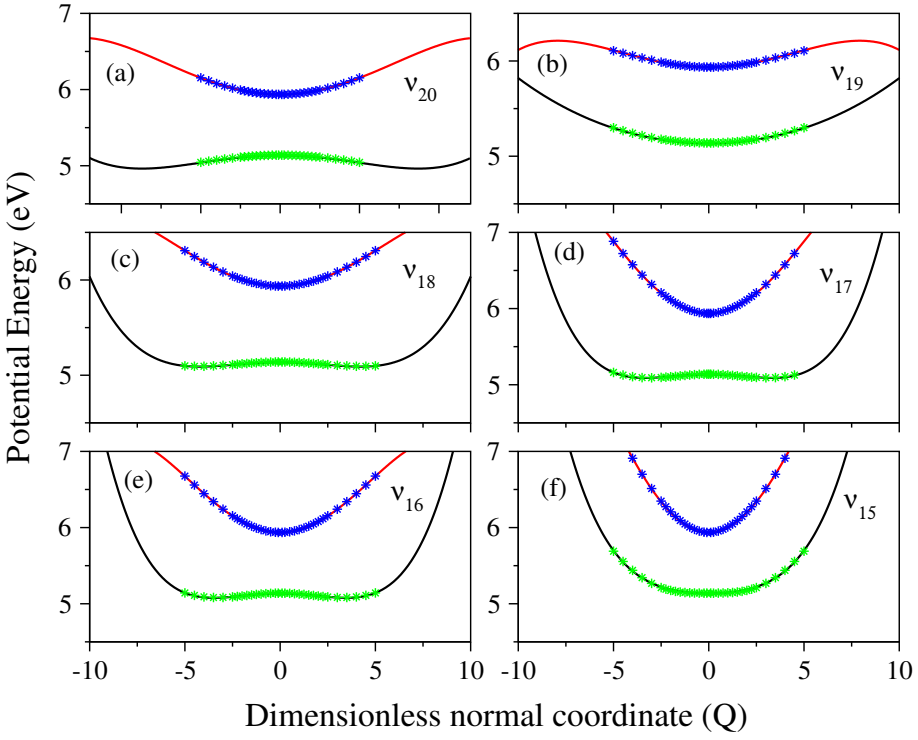

FIGURE 3.4: Adiabatic potential energy curves of the first two lowest excited singlet electronic states (S_1 and S_2) of PFBz along the normal mode displacement coordinate of out-of-plane bending (b_1) symmetry vibrational modes of b_1 symmetry ν_{20}, ν_{19}, ν_{18}, ν_{17}, ν_{16}, and ν_{15} shown in panels (a)-(f), respectively. The potential energies obtained from this model and the computed *ab initio* energies are shown by solid lines and asterisks, respectively.

can be seen from panels a, b and c of Fig. 3.2 that the S_1-S_2 intersection occurs at $\sim$4.11, $\sim$ -3.25 and $\sim$ -3.97 along Q_2, Q_3 and Q_4, respectively, and the potential energy difference between these states increases beyond the point of intersection [cf., panels a, b and c of Fig. 3.2]. For example, the potential energy gap between the S_1 and S_2 states along Q_{20} and at Q_2= -4.109 [cf., panel c1 of Fig. 3.5] is higher than the same at Q_2=0.0 [cf., panel b1 of Fig. 3.5], which is in accordance with the trend observed in panel b of Fig. 3.2. Finally, at Q_2= 4.109, at the intersection point of the S_1 and S_2 states along Q_2, these states become degenerate [cf., panel a1 of Fig. 3.5]. Similar observations can be made for simultaneous distortions along (Q_3, Q_{20}) and (Q_4, Q_{20}) dimensionless normal coordinates [cf., panels (a2, b2, c2) and (a3, b3, c3) of Fig. 3.5]. Therefore, it is obvious that the topography and the extent of nonadiabaticity of the S_1-S_2 coupled PESs are governed by the tuning and coupling vibrational modes of a_1

and b_1 symmetry, respectively.

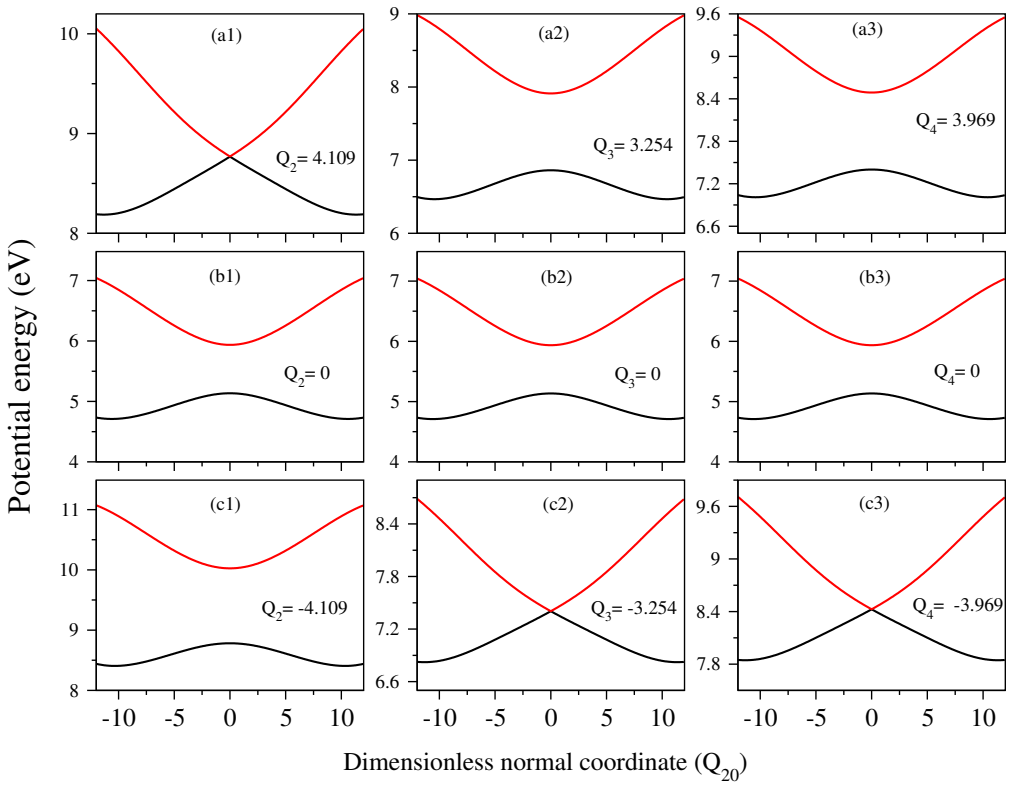

FIGURE 3.5: Potential energy profiles along the coordinate Q_{20} of the vibrational mode of ν_{20} of b_1 symmetry at different values of the coordinates Q_2, Q_3 and Q_4 of the totally symmetric vibrational modes ν_2, ν_3, and ν_4 shown in panels (a1)-(c1), (a2)-(c2), and (a3)-(c3), respectively.

3.2.3 Electronic absorption spectrum

The vibronic band structure of the electronic absorption spectrum of PFBz is calculated and compared with the experimental gas-phase UV absorption spectrum of Philis *et al.* [63] and Hüter *et al.* [60]. The vibronic Hamiltonian constructed in Sec. 3.1.1, the parameters of Tables 3.1-3.2 and B1-B11 of Appendix B and both time-independent and time-depended methods within the MCTDH framework [131] have been utilized for the purpose. As stated in the introduction, when the number of fluorine substitution in the Bz is four or less, the lowest $\pi\sigma^*$ state is significantly higher in energy than the lowest $\pi\pi^*$ state and they exhibit structured $S_1 \leftarrow S_0$ absorption band. In the case of five and six fluorine atom substitution on the Bz ring, both the lowest $\pi\sigma^*$ and $\pi\pi^*$ states become energetically very close with each other and hence, leads to a structureless

$S_1 \leftarrow S_0$ absorption band. As a result, the seam of S_1-S_2 CI is expected to be more readily accessible to the nuclear motion on the S_1 electronic state. Therefore, one can expect that there should be a much profound effect of coupling on the spectral envelope of the first and second absorption bands of PFBz. All these details are already established in our previous work [52–54]. To further confirm this, we first construct various reduced dimensional models and examine the vibrational energy levels of each of these electronic states by excluding the inter-state (λ_i) coupling with their neighbors. These results help to understand the role of various vibrational modes and electronic states in the complex vibronic structures of PFBz. For this, a time-independent matrix diagonalization method is used to calculate the precise location of the energy levels of the uncoupled electronic states. The final simulation of nuclear dynamics is carried out by including all relevant vibronic couplings of the Hamiltonian. The time-dependent WP propagation method is used to accomplish the latter task. The two methods mentioned above are implemented in the Heidelberg MCTDH program module [131] and are used for this purpose.

Precise location of the vibrational energy levels of the uncoupled electronic states is calculated by the time-independent matrix diagonalization approach using the Lanczos algorithm [122]. The optical absorption spectrum of the S_1 electronic state is shown in Fig. 3.6. The vibronic spectra shown in panels c and d of this figure are calculated with uncoupled S_1 state and by including its coupling with the S_2 electronic state, respectively. The experimental S_1 band reproduced from Philis *et al.* [63] and Hüter *et al.* [60], are shown in panels a and b, respectively. Both uncoupled and coupled S_1-S_2 electronic states stick spectrum and the convoluted envelopes are, respectively, shown in panels c and d of Fig. 3.6. The stick spectrum is converged with respect to the size of the vibrational basis as well as the number of Lanczos iterations. The theoretical stick spectrum is convoluted with a 20 meV full width at the half maximum (FWHM) Lorentzian line shape function to generate the spectral envelopes shown in panels c and d [cf., Fig. 3.6]. The same convolution procedure is used for all the later stick data presented in this article. Among the eleven totally symmetric vibrational modes, seven vibrational modes ν_2-ν_4, ν_7-ν_9 and ν_{11} have large excitation strength ($\kappa^2/2\omega^2$) in all the electronic states. Therefore, these seven totally symmetric modes are included in the present investigations. It can be seen from panel c of Fig. 3.6 that, the diffused $S_1 \leftarrow S_0$ absorption band is not in agreement with the observed experimental results [cf., panels a and b of Fig. 3.6]. So, to assess the nonadiabatic coupling effects on the spectral envelope we included the coupling between the S_1 and S_2 states in the dynamics. According to the symmetry selection rules, the inter-state coupling (λ) between S_1 and S_2 states is caused by the six vibrational modes of b_1 symmetry. In coupled S_1-S_2 states dynamical treatment, we included total thirteen (i.e., $7a_1$+$6b_1$) nuclear DOFs. The

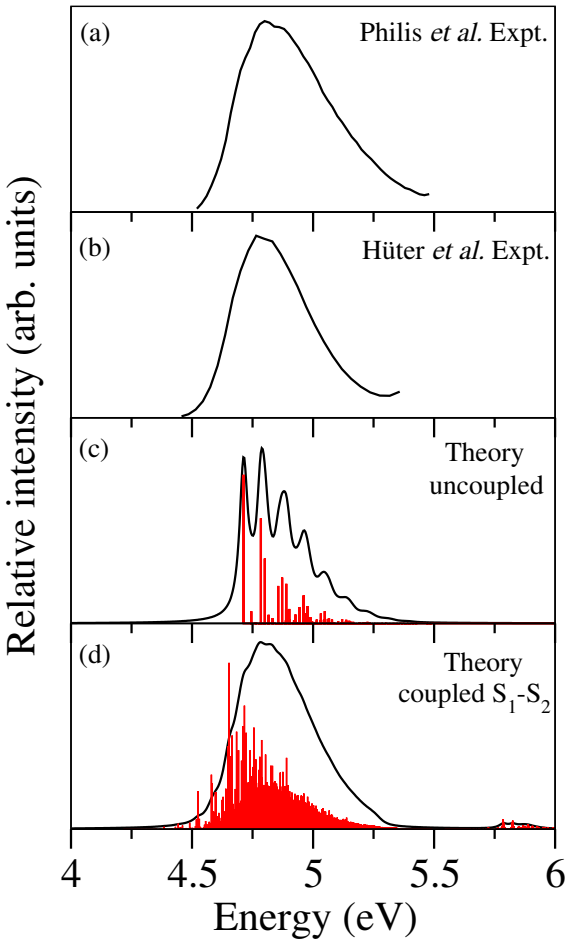

FIGURE 3.6: Vibronic energy levels of S_1 electronic state of PFBz: The experimental [60, 63] and theoretical (uncoupled and coupled S_1-S_2 states) results are shown in panels (a)-(d), respectively. The relative intensity is plotted along the energy of the final vibronic state.

spectrum obtained by diagonalizing two-state vibronic Hamiltonian show a huge increase of spectral line density [cf., Fig. 3.6(d)] and its convoluted envelope is in good accord with the experiment. It is to be noted here that the EOM-CCSD method overestimates the VEE of the S_1 state as compared to the experiment [cf., Table 3.2]. Therefore, the theoretical spectra of panels c and d of Fig. 3.6 are shifted down (by ∼0.35 eV) along the abscissa to reproduce the center-of-gravity of the bands at the experimental VEE. The HO basis functions used along each mode in these calculations are given in Table B12 of the Appendix B.

The vibronic structure of the uncoupled S_1 electronic state [cf., Fig. 3.6(c)] reveals that all seven totally symmetric vibrational modes (ν_2-ν_4, ν_7-ν_9 and ν_{11}) are excited. Peak spacings of ∼1738 cm^{-1}, ∼1522 cm^{-1}, ∼1422 cm^{-1}, ∼707 cm^{-1}, ∼576 cm^{-1}, ∼407 cm^{-1} and ∼257 cm^{-1} due to the progression of ν_2, ν_3, ν_4, ν_7, ν_8, ν_9 and ν_{11} vibrational

modes, respectively, are found. Among the seven symmetric vibrational modes, ν_4, ν_7, and ν_8 form dominant progression in the S_1 state. The ν_3, ν_{11} modes are moderately and ν_2, ν_9 modes are weakly excited in accord with their excitation strength [cf., Table B1]. The vibronic structure of the S_1 electronic state [cf., Fig. 3.6(d)] from the coupled S_1-S_2 matrix diagonalization calculations show a highly dense spectral line structure. In this case identification of individual vibrational progression is cumbersome and ambiguous. However, its convoluted spectrum is in good accord with the broad band experimental spectrum.

A few observations on the S_1 band structure are discussed here. It was stated before that the S_1 state is vertically well separated from the rest of the states. The S_1-S_2 intersection minimum occurs ∼0.80 eV above the S_1 minimum. Therefore, it is counterintuitive on energetic ground to observe such a huge line structure of the S_1 state. The population dynamics of the S_1 state in the S_1-S_2 coupled states situation shown in Fig. B1 (panels b and d) also supports this puzzle.

It can be seen from Table B11 that the coupling of the S_1-S_2 states along out-of-plane b_1 vibrational modes is fairly strong, particularly along ν_{17}, ν_{18} and ν_{20} modes. In order to assess the effect of b_1 vibrational modes on the vibronic structure of the uncoupled S_1 state we carried out reduced dimensional calculations by systematically including them in the S_1-S_2 coupled states calculations. It can be seen from the results presented in Fig. B2 that vibronic line density increases to some extent as compared to the uncoupled spectrum [cf., Fig. 3.6c] when one b_1 mode is included at a time. The increase is somewhat more when two b_1 modes are included [cf., Fig. B3]. The surprising results obtained when all six b_1 modes are considered. These results are shown in Fig. B4(a-d). In panel c of this figure results are shown when only six b_1 modes are included in the dynamics. The huge line density obtained appears to be a collective effect of all out-of-plane b_1 modes. Note that the results of Fig. B4 are obtained by placing the S_1 VEE at its experimental value of ∼4.79 eV. This increases the S_1-S_2 vertical gap by ∼1.11 eV. However, this increase seems to have only negligible impact on the overall structure of the S_1 band and the corresponding population dynamics, as shown in Fig. B1. The potentials are neither strongly bound nor unstable along the b_1 vibrational modes. Interestingly, shallow minima appears on the potential energy surface at large internuclear distances (see the potential curves plotted along ν_{20} vibrational modes, for example, in Fig. 3.7). The WP therefore spreads out over large internuclear distances and causes the observed broadening of the S_1 band.

The vibrational energy level spectrum of the uncoupled S_3, S_4, S_6, S_7 and S_8 electronic states is shown in panels a-e of Fig. 3.8. As mentioned above, the theoretical calculations are carried out with seven relevant symmetric vibrational modes. The HO basis functions

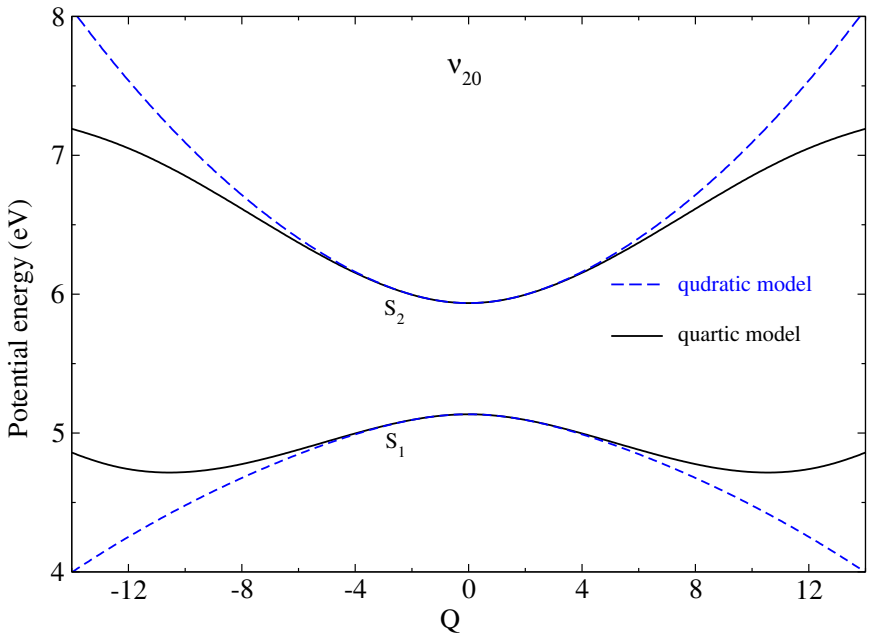

FIGURE 3.7: Adiabatic potential energy curves of the first two lowest excited singlet electronic states (mentioned in the panel) of PFBz along ν_{20} mode.

used along each mode in these calculations are given in Table B12 of the Appendix B. The energy eigenvalues and their assignments of the above mentioned electronic states are given in Table B13 of the Appendix B. This system has a broad band at about 5.85 eV (marked as C-band [63]) and it is attributed to a $\pi \rightarrow \sigma^*$ transition. This vibronic band results from the $\pi\sigma^*$ character of S_2 (optically dark) and S_3 electronic states of PFBz. The vibronic band structure of S_3 state reveals the dominant progression of ν_9 vibrational mode with peak spacing of $\sim$408 cm^{-1}.

The second vibronic band solely originates from the S_4 electronic state. It reveals dominant excitation of ν_8, ν_7 and ν_4 vibrational modes. The peaks are $\sim$568 cm^{-1}, $\sim$692 cm^{-1}, and $\sim$1348 cm^{-1} spaced in energy corresponding to the frequencies of these vibrational modes, respectively. The third vibrational band results from the S_5 (optically dark), S_6, S_7, and S_8 electronic states of PFBz. It can be seen from panels b-e of Fig. 3.8 that the vibronic band structures of the S_6, S_7 and S_8 states are highly overlapping. They together form the third vibronic band and at the Franck-Condon geometry, S_6 to S_8 states are energetically very close to each other. The corresponding vibrational progressions are given in Table B13.

In addition to the energetic location and excitation strength analysis, the assignment of the peaks is also confirmed by examining the nodal pattern of the vibrational wave functions. These wave functions are calculated using a block-improved relaxation method implemented in the MCTDH program module [129, 159, 160]. To save space and for brevity, we show a few vibrational wave functions of the S_1, S_3, and S_4 electronic states,

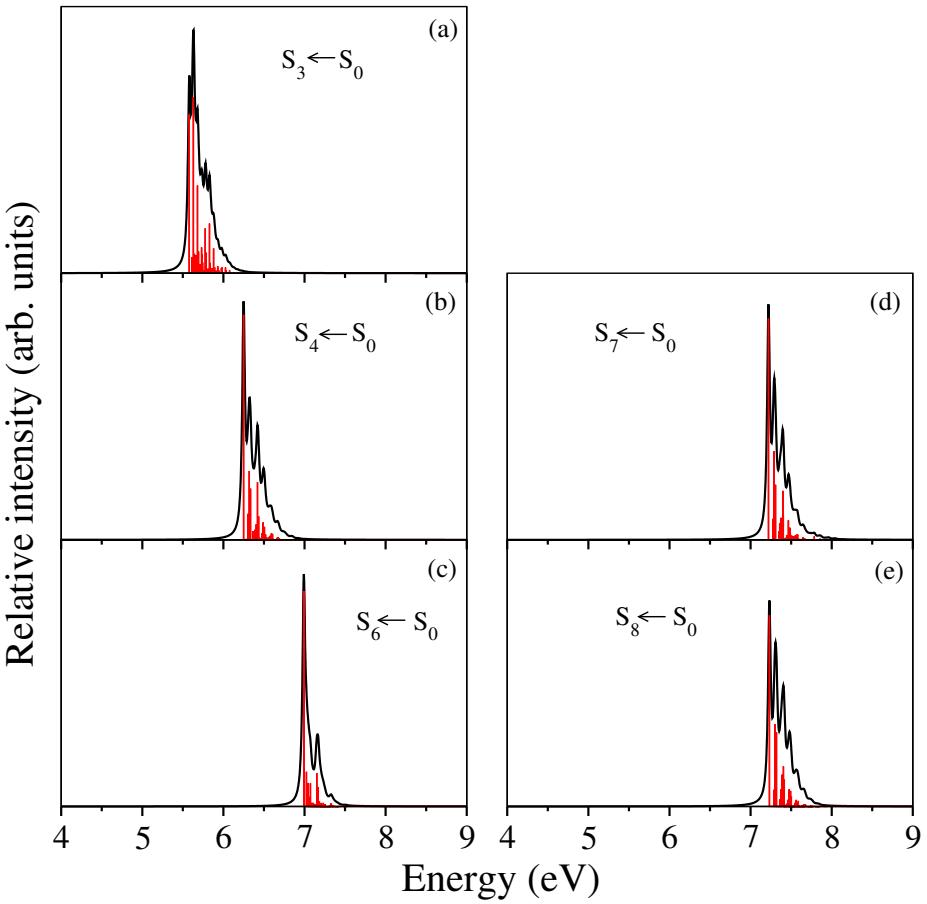

FIGURE 3.8: Stick spectrum and its convoluted envelope of the uncoupled S_3, S_4, S_6, S_7 and S_8 electronic states of PFBz are shown in panels (a)-(e), respectively. The relative intensity is plotted along the energy (relative to the minimum of the S_0 state of PFBz) of the final vibronic states.

in Figs. B5-B7 of Appendix B. The wave function probability density is plotted in these figures in a suitable reduced dimensional space of the dimensionless normal displacement coordinates. As can be seen from the Fig. B5 of the Appendix B that in panels a-c, the wave function of the fundamental of ν_9, ν_8 and ν_7 are shown, respectively. These wave functions acquire a node along the coordinate of the respective mode. Panels d-f of Fig. B5 show the vibrationally excited wave functions with multiple nodes. Along with these some of the combination peaks are also shown in panels g-l of Fig. B5. Similarly, the vibrational wave functions of the other states (S_3 and S_4) are shown in Figs. B6 and B7 of the Appendix B, respectively.

The vibronic bands of the uncoupled electronic states presented above in Fig. 3.8 are structured and contain rich information on the excitation of various vibrational modes. However, they are quite different from the spectral envelopes recorded in the experiment [60, 63]. The experimental spectral envelopes are broad and structureless. So, a detailed interpretation of the experimental data requires inclusion of twenty two relevant vibrational modes ($7a_1$+$3a_2$+$6b_1$+$6b_2$) and all relevant vibronic (nonadiabatic) couplings of

the Hamiltonian in the dynamical calculations. The vibrational modes are chosen according to their excitation strength [cf., Tables B1 and B11]. The totally symmetric ν_2-ν_4, ν_7-ν_9 and ν_{11} and non-totally symmetric ν_{12}-ν_{14} (a_2), ν_{15}-ν_{20} (b_1), ν_{21}-ν_{23} and ν_{28}-ν_{30} (b_2) vibrational modes are included in the nuclear dynamics calculations of eight coupled electronic states. Such a consideration leads to a huge increase of the dimension of the secular matrix. The matrix diagonalization approach could not be used further to carry out the nuclear dynamics on the coupled manifold of eight electronic states. Therefore, we resort to the time-dependent WP propagation calculations with the help of Heidelberg MCTDH program modules [119, 127, 128, 131].

An initial WP pertinent to the vibronic ground state (S_0) of PFBz is vertically promoted to the excited state and then propagated up to 200 fs in the coupled manifold of S_1 to S_8 electronic states. Eight separate calculations are carried out by initially promoting the WP to each of the eight excited electronic states of PFBz. During the propagation, the autocorrelation function of the WP is recorded in time. Later, we perform a Fourier transformation of the time-autocorrelation function to calculate the spectrum. The numerical details of the mode combination, sizes of the primitive and single-particle basis functions used in the WP propagations are given in Table B.13 of the Appendix B.

The composite vibronic band structure is generated by combining the autocorrelation function obtained from eight calculations with equal weightage, damping with an exponential function, $e^{-\frac{-t}{\tau_r}}$ (with τ_r=22 fs) and Fourier transforming to the energy domain. Due to zero oscillator strength, the transition from the ground ^{1}A$_1$ (S_0) to the ^{1}A$_2$ ($\pi\sigma^*$) (S_2 and S_5) states are forbidden in C_{2v} point group symmetry. The effect of the S_2 and S_5 states in the dynamics are included through their coupling with the remaining states. The calculated vibronic band structures of the coupled S_1 to S_8 electronic states of PFBz is plotted in Figs. 3.9 and 3.10 along with the experimental results in panel a reproduced from Refs. [63] and [60], respectively. In Figs. 3.9 and 3.10 relative intensity (in arbitrary units) is plotted as a function of the energy of the final vibronic levels. It can be seen from Figs. 3.9 and 3.10 that the theoretical results of panel b are in good accord with the old and recent experimental recordings [60, 63].

The structured absorption band of the uncoupled S_1 state [cf., panel c of Fig. 3.6] becomes essentially structureless upon considering its coupling with other states. As noted above the collective effect of the out-of-plane b_1 vibrational modes plays a major role in this band structure in addition to the coupling of S_1 with the remaining states. Shallow minima on the potential appear at large internuclear displacements along the b_1 vibrational modes [cf., Fig. 3.7]. This causes a spreading of the WP and a huge broadening of the S_1 band. Data given in the Table 3.3 indicates that the S_2 ($\pi\sigma^*$) state

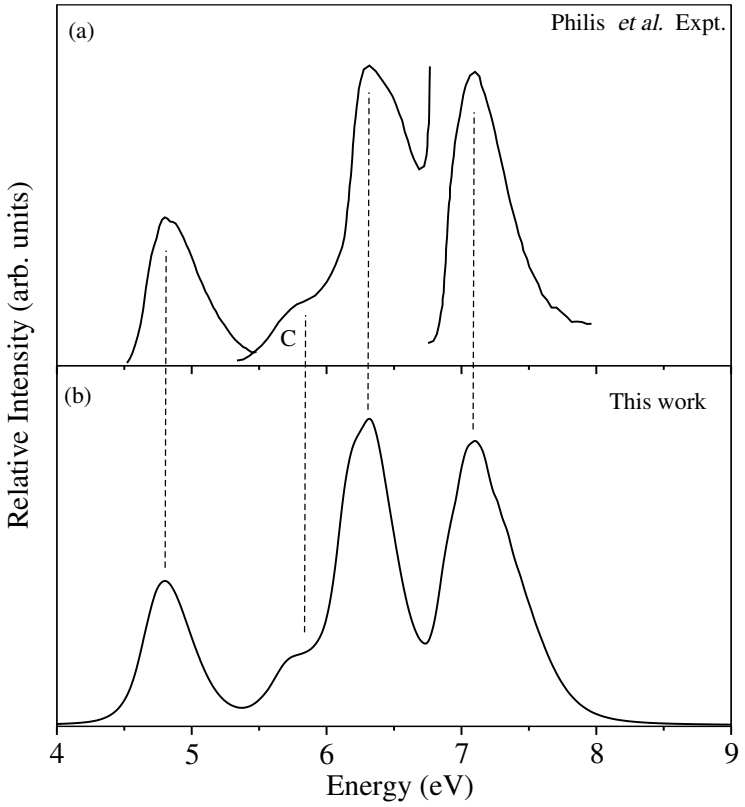

FIGURE 3.9: The absorption spectra of the coupled S_1-S_8 electronic states of PFBz. Experimental spectrum is reproduced from Ref. [63] is shown in panel a and the present theoretical results shown in panel b.

is energetically close to the S_1 ($\pi\pi^*$) state compared to the other excited electronic states in the Franck-Condon region. A strong inter-state coupling between the S_1 and S_2 states via the vibrational modes of b_1 symmetry is found [cf., Table B11). Inclusion of these inter-state couplings in the S_1 state dynamics of PFBz yields an improved broadening of the first absorption band shown in panel b of Figs. 3.9 and 3.10.

As discussed for the uncoupled state situation above, this system has a additional broad band at about 5.85 eV (marked as C-band [63]) near the onset of the second band [cf., panel b of Figs. 3.9 and 3.10]. This new band is absent in the parent Bz and in the lower fluoroderivatives [52–54, 63]. The new additional band can certainly be attributed to a $\pi \rightarrow \sigma^*$ transition to both S_2 and S_3 electronic states from the electronic structure data. According to our theoretical results, this suggestion is in accordance with the prediction of Philis *et al.* [63]. Also, there is strong vibronic coupling between S_1-S_2, S_2-S_3 and S_3-S_4 electronic states via the vibrational modes of b_1, b_2 and b_1 symmetry, respectively. The minimum of the seam of S_1-S_2 and S_2-S_3 CIs is located only 0.14 eV and 0.37 eV above the S_2 equilibrium minimum, respectively. In addition, the minimum of S_2-S_3 and S_3-S_4 CIs is located only 0.01 eV and 0.45 eV above the S_3 minimum, respectively.

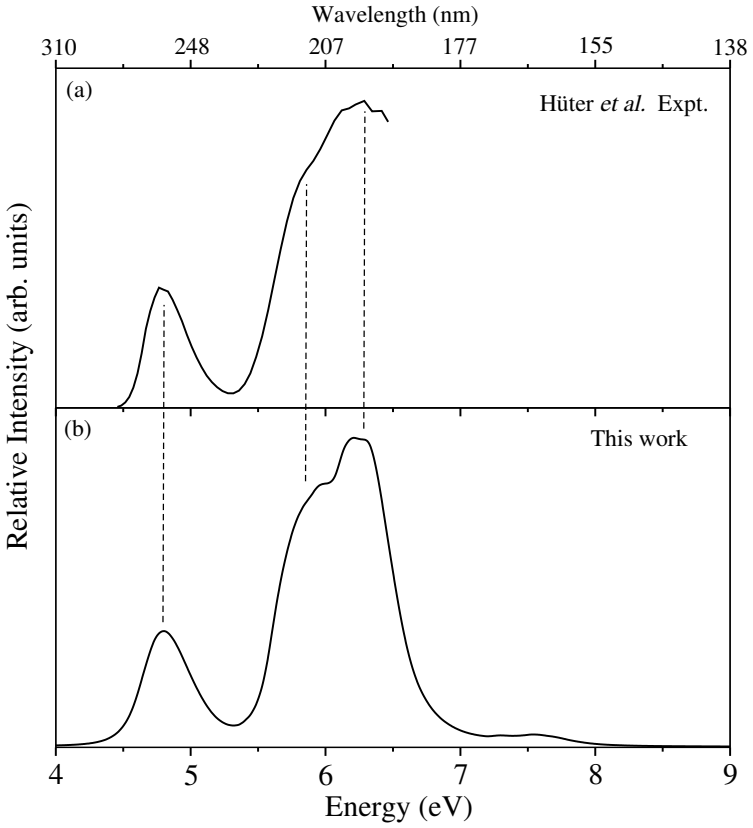

FIGURE 3.10: The absorption spectra of the coupled S_1-S_4 electronic states of PFBz. Experimental spectrum is reproduced from Ref. [60] is shown in panel a and the present theoretical results shown in panel b.

All these considerations explain that this additional band originates from both S_2 and S_3 electronic states through a $\pi \rightarrow \sigma^*$ transition. Since a transition to these states is optically forbidden, they gain small intensity through their coupling with optically bright $\pi\pi^*$ states. This gives rise to the small hump in the overall band structure at $\sim$5.85 eV.

As discussed above, the S_4 ($\pi\pi^*$) electronic state form the second absorption band and it strongly overlaps with the new additional band (marked as C-band as discussed above) [cf., panel b of Figs. 3.9 and 3.10]. This is because of strong vibronic coupling between the S_2, S_3 and S_4 electronic states [cf., Table B11]. Similarly, the third absorption band is formed by the highly overlapping S_5, S_6, S_7 and S_8 electronic states. Among these states S_5 ($\pi\sigma^*$) state is optically dark and other three states are optically bright ($\pi\pi^*$). All these states are energetically close to each other at the Franck-Condon geometry and also their CIs are quasi-degenerate with their equilibrium minimum [cf., Table 3.3]. Finally, the results from the eight different calculations are combined with equal weightage to generate the composite theoretical band structure shown in Figs. 3.9 and 3.10 along with the available experimental results reproduced from Philis *et al.* [63] and Hüter *et*

al. [60]. It can be seen from the figures that the present theoretical results are in very good accord with the experimental findings [60, 63].

The optically dark S_2 and S_5 states of $^1A_2$ symmetry were not included in an earlier theoretical study [52, 53]. Therefore, it appears to be important here to discuss on the effect of these states on the overall structure of the observed spectrum. In Fig. B8(a and b) the band structure of individual states is shown with (panel a) and without (panel b) inclusion of S_2 and S_5 states. It is clear from the comparison that the C-band gains intensity from both the S_2 and S_3 states. The S_3 band becomes somewhat broad in panel a as compared to panel b. The S_4 band also becomes broad when $^1A_2$ states are included. Additionally, the S_5 band appears at the same location of the S_6 band and makes significant contribution to the third band of the recorded spectrum. The details of the population dynamics is examined in the above situations and discussed later in the text.

3.2.4 Internal conversion dynamics

Time-dependent diabatic electronic populations of coupled S_1 to S_8 excited electronic states of PFBz are examined here in order to understand the impact of various nonadiabatic coupling effects in this complex situation. The results obtained for transition of the initial WP to the S_1, S_2, S_3, S_4, S_5, S_6, S_7, and S_8 electronic states are shown in panels a-h of Fig. 3.11, respectively. The electronic populations are color-coded (online version) in the same way in all panels of the respective figures. Following the vertical transition to the S_1 ($\pi\pi^*$) state, the population of this state decreases in time whereas, the population of the optically dark S_2 ($\pi\sigma^*$) and S_5 ($\pi\sigma^*$) electronic states increases very little as can be seen from Fig. 3.11(a). This is owing to the vibronic coupling between the S_1-S_2 and S_1-S_5 electronic states [cf., Table B11]. In addition, the minimum of these CIs occurs at ∼0.88 eV and ∼1.61 eV above the minimum of the S_1 state, respectively. It appears that the collective effect of the b_1 vibrational modes is the bottleneck underlying the broadening of the $S_1 \leftarrow S_0$ absorption band. The vertical transition to the S_2 ($\pi\sigma^*$) state [cf., Fig. 3.11(b)] on the other hand induces a fast population transfer to the optically active S_1 ($\pi\pi^*$) state. In ∼16 fs, the population of the two states becomes equal (∼0.42), and after ∼40 fs, the S_2 state population depletes to ∼0.37, whereas the S_1 state population becomes ∼0.47. The remaining population of ∼0.16 flows to all other electronic states. It appears from the above discussion that the strong vibronic coupling between the S_1-S_2 states drives the population dynamics discussed above. This remark is in accordance with the observation that the energetic minimum of the S_1-S_2 CIs is only ∼0.14 eV above the minimum of the S_2 state of PFBz.

A decay rate of ∼27 fs can be estimated from the initial fast decay of the population of the S_2 state.

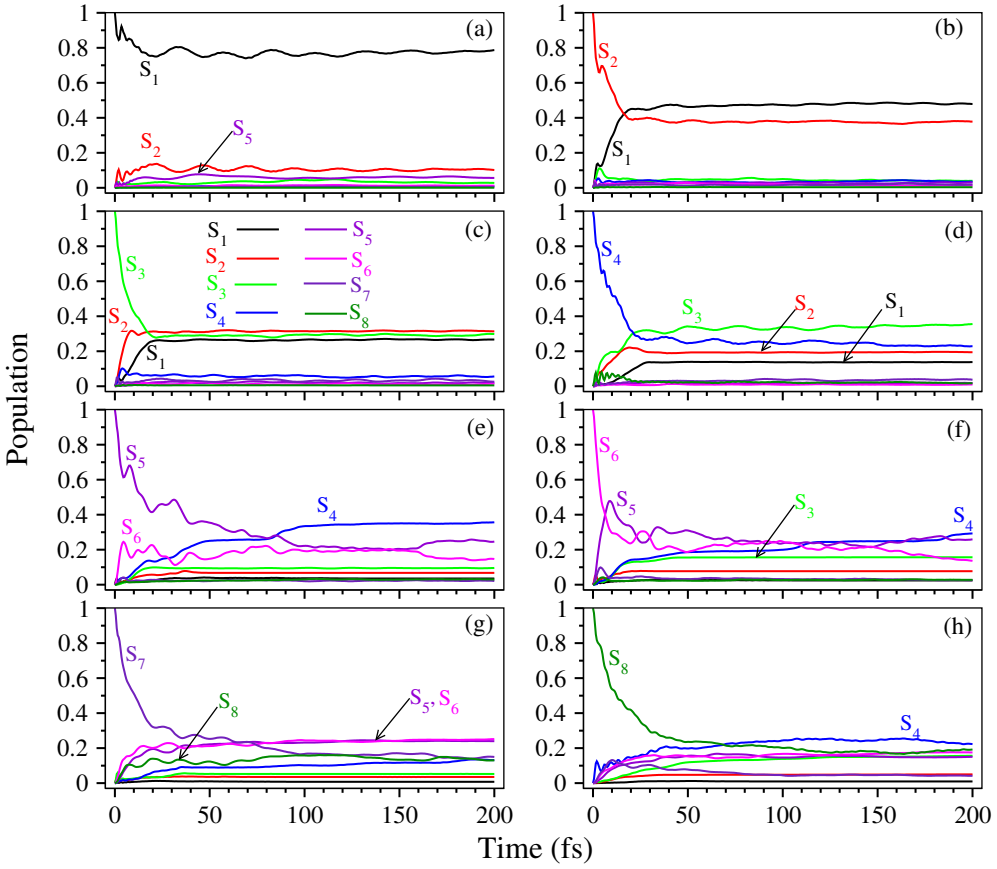

FIGURE 3.11: Time-dependence of diabatic electronic populations for an initial location of the WP on the S_1-S_8 electronic states in the full coupled states dynamics are shown in panels (a)-(h), respectively.

The electronic state population shown in panel c of Fig. 3.11 represents the initial excitation of the WP to the S_3 ($\pi\sigma^*$) state. In this case, two decay channels predominantly open up through S_3 ($\pi\sigma^*$)-S_2 ($\pi\sigma^*$) and S_3 ($\pi\sigma^*$)-S_1 ($\pi\pi^*$) CIs. The S_2 and S_1 states are populated predominantly [cf., Fig. 3.11(c)], due to the fact that the energetic minimum of the S_3-S_2 and S_3-S_1 CIs occurs ∼0.01 eV and ∼0.32 eV above the minimum of the S_3 state, respectively. It can be seen that at ∼17 fs, both S_3 and S_2 electronic states population become equal (∼0.31). Within ∼22 fs, the S_3 state population decays rapidly and reaches a value of ∼0.28, while the population of the S_2 and S_1 states approaches a maximum value of ∼0.31 and ∼0.26, respectively. The remaining population of ∼0.15 flows to all other electronic states, and after ∼50 fs, the populations of all the electronic states reach a constant value. A nonradiative decay rate of ∼17 fs can be estimated from the population curve of the S_3 state [cf., Fig. 3.11(c)].

When the WP is initially prepared on the S_4 ($\pi\pi^*$) electronic state, the electron population dynamics appears to be more complex, and it is shown in panel d of Fig. 3.11. In this case, most of the population flows to the S_3, S_2, and S_1 electronic states. At ∼21 fs, both S_4 and S_3 states population becomes equal (∼0.30), and S_2 state population reaches a maximum value of ∼0.22 at ∼19 fs. After ∼50 fs, the population moves back and forth between the S_4 and S_3 electronic states. The population of S_1 and S_2 states saturates at a value of ∼0.13 and ∼0.19, respectively. The complex behavior of population dynamics in this case originates from strong nonadiabatic coupling among S_1, S_2, S_3, and S_4 electronic states. In addition, a large population transfer is facilitated by the energetic proximity of the equilibrium minimum and the minimum of various intersection seams in the S_1-S_2-S_3-S_4 states as given in Table 3.3. The initial fast decay of S_4 ($\pi\pi^*$) state population relates to a decay rate of ∼20 fs.

Fig. 3.11(e) portrays the population dynamics for an initial excitation of the WP to the optically dark S_5 ($\pi\sigma^*$) state. It can be seen from the figure that the S_5 state population rapidly decreases to a value of ∼0.61, whereas the S_6 state population increases to a maximum value of ∼0.24 within ∼5 fs. The S_4 state population increases slowly in a step-wise manner and reaches a maximum value of ∼0.33 within ∼100 fs. Also, the population moves back and forth between the S_5 and S_6 state throughout the entire duration. This complex behavior of population dynamics arises from strong nonadiabatic coupling between S_4, S_5, and S_6 electronic states [cf., Table B11] and quasi-degeneracy of S_4 and S_5 states [cf., Table 3.3]. A nonradiative decay rate of ∼98 fs can be estimated from the population curve of the S_5 ($\pi\sigma^*$) state of Fig. 3.11(e).

The electronic population dynamics for an initial excitation of the WP to the S_6 ($\pi\pi^*$), S_7 ($\pi\pi^*$), and S_8 ($\pi\pi^*$) electronic states is shown in panels f-h of Fig. 3.11, respectively. Upon excitation to the S_6 state, the WP accesses S_5-S_6 CIs and a fast transfer of population takes place to the optically dark S_5 ($\pi\sigma^*$) state. Since the latter state intersects with S_3 and S_4 electronic states, further population transfer occurs from the S_5 state to the S_3 and S_4 electronic states [cf., panel f of Fig. 3.11]. Also, due to relatively strong nonadiabatic coupling between the S_6 and S_4 states, the S_4 state population increases more than the S_3 state [cf., panel f of Fig. 3.11]. In about 6 fs, the populations of the S_6 and S_5 states become equal (∼0.4). At longer times, the S_4 state population increases slowly and reaches a maximum value of ∼0.29. The population of S_5 and S_6 states moves back and forth between a value of ∼0.2 to ∼0.3. The populations of all other states remain steady. A nonradiative decay rate of ∼10 fs can be estimated from the population curve of the S_6 state given in panel f. In the case of S_7 and S_8 electronic states, the electronic population dynamics becomes more complex than the S_6 state [cf., panels f-h of Fig. 3.11]. In these cases, most of the population flows to all the lower excited electronic states. This is because of strong nonadiabatic coupling among

them and the seam minima of these states are quasi-degenerate with their equilibrium minimum [cf., Table 3.3]. The initial sharp decay of the populations in panels g and h of Fig. 3.11 relates to a nonradiative decay rate of ∼19 fs and ∼31 fs of the S_7 and S_8 states, respectively. Overall, it appears that the nonadiabatic coupling effects in the electronically excited PFBz molecule are strong. This leads to the appearance of much broader and diffuse electronic absorption bands in PFBz.

To this end we note that the population dynamics of S_3 and S_6 states is much affected when the S_2 and S_5 states of $^1A_2$ symmetry are included in the calculation. For comparison, the population dynamics without S_2 and S_5 states is shown in Fig. B9 of Appendix B. A rapid decay of population of S_3 and S_6 states [cf., Fig. 3.11] contributes much to the spectral broadening when S_2 and S_5 states are included in the calculations [cf., Fig. B8].

3.3 Summary and conclusion

A detailed theoretical account of vibronic coupling among the energetically lowest eight singlet excited electronic states of PFBz is presented in this chapter. The computed optical absorption spectrum of PFBz is compared with the available experimental results of Philis *et al.* [63] and Hüter *et al.* [60]. Along with this, we examined the role of optically dark $\pi\sigma^*$ states on the quantum dynamics of optically bright $\pi\pi^*$ states of PFBz. The equilibrium geometry of the electronic reference ground (S_0) state of the PFBz is optimized at the MP2/aug-cc-pVDZ level of theory. The adiabatic electronic energies of the lowest eight excited electronic states are calculated along the dimensionless normal displacement coordinates using the EOM-CCSD method and aug-cc-pVDZ basis set with the aid of the MOLPRO suite of programs. A detailed topographical analysis of the eight adiabatic electronic states is carried out and multiple conical intersections among them are established. With electronic structure results, a higher-order model vibronic Hamiltonian of the eight coupled electronic states is developed in a diabatic electronic representation in terms of the dimensionless normal displacement coordinate of vibrational modes. It is found that the vibronic coupling between optically active ($\pi\pi^*$) and optically dark ($\pi\sigma^*$) states is quite strong. The strong vibronic coupling between the S_1 ($\pi\pi^*$) and S_2 ($\pi\sigma^*$) states causes the lowering of symmetry of the lowest excited adiabatic S_1-S_2 coupled potential energy surface and leads to a symmetric double-well type of potential, which stabilizes the molecule along with the out-of-plane modes of b_1 symmetry. The minimum of the last four (S_5, S_6, S_7, and S_8) excited electronic states is quasi-degenerate with their intersection minimum.

The nuclear dynamics calculations are carried out from the first principles. Both time-independent and time-dependent WP propagation methods are explored. The individual vibronic energy level structure of the eight lowest excited electronic states is systematically investigated and assigned. The assignment of the peaks is also confirmed by examining the nodal pattern of the vibrational wave functions. For a detailed interpretation of the experimental results, twenty two relevant vibrational modes ($7a_1$+$3a_2$+$6b_1$+$6b_2$), and all possible nonadiabatic couplings between the eight electronic states of the Hamiltonian are considered in the dynamical calculations.

The results show that the first absorption band, $S_1 \leftarrow S_0$, is structureless due to collective effect of the out-of-plane b_1 vibrational modes in addition to strong S_1-S_2 nonadiabatic coupling. Shallow minima on the potential are found at large internuclear displacements along the b_1 modes. This causes a spreading of the WP and the broadening of the S_1 band. A new additional broad band appears at about 5.85 eV (marked as C-band in the literature [63]) near the onset of the second band [cf., Figs. 3.9 and 3.10]. This is attributed to the $\pi \rightarrow \sigma^*$ type transition to both S_2 and S_3 states. Also, the strong vibronic coupling between S_1-S_2, S_2-S_3, and S_3-S_4 states contributes to the observed diffused and broad structure of this additional band in PFBz. In the recent experiment [60], this additional new band strongly overlaps with the second band [cf., Fig. 3.10]. This new band is absent in the parent Bz and the lower fluoroderivatives. The second band in figures 3.9 and 3.10 originates from the S_4 ($\pi\pi^*$) electronic state. It strongly overlaps with the additional C-band. The third absorption band is formed by energetically close-lying S_5, S_6, S_7, and S_8 electronic states. Because of energetic proximity, these bands are strongly overlapping, and occurrence of multiple CIs between these electronic states contributes significantly to the complex structureless pattern of this band. The theoretical results are shown to be in good accord with the available experimental results.

Chapter 4

Vibronic coupling in the first six electronic states of Pentafluorobenzene radical cation: Radiative emission and nonradiative decay

In this chapter the vibronic coupling in the $\widetilde{\mathrm{X}}\ ^2\mathrm{A}_2$, $\widetilde{\mathrm{A}}\ ^2\mathrm{B}_1$, $\widetilde{\mathrm{B}}\ ^2\mathrm{B}_1$, $\widetilde{\mathrm{C}}\ ^2\mathrm{B}_2$, $\widetilde{\mathrm{D}}\ ^2\mathrm{A}_1$, and $\widetilde{\mathrm{E}}\ ^2\mathrm{B}_2$ electronic states of Pentafluorobenzene radical cation (PFBz^+) is examined. The photoelectron spectrum of PFBz has been recorded by Bieri *et al.*[25] using He II radiation as ionization source. Four distinct bands observed in the ∼9-16 eV energy range were attributed to result from an ionization from the six valence MOs of neutral PFBz. Among the four electronic bands of PFBz^+, the first, third and fourth band revealed overlapping vibronic structure and therefore carries the signature of vibronic coupling in the energetically low-lying electronic states of PFBz^+.

Radiative emission and highly overlapping electronic band structure motivated us to investigate vibronic coupling and nuclear dynamics in the energetically low-lying electronic states of PFBz^+. In the following, vibronic interactions in the energetically lowest six electronic states of PFBz^+ have been investigated. These states result from ionization from the occupied valence MOs of PFBz. The MO configuration of the latter is: $(\mathrm{core})(13b_2)^2(19a_1)^2(14b_2)^2(4b_1)^2(5b_1)^2(3a_2)^2$. Ionization from the highest occupied MO and the inner ones gives rise to $\widetilde{\mathrm{X}}\ ^2\mathrm{A}_2$, $\widetilde{\mathrm{A}}\ ^2\mathrm{B}_1$, $\widetilde{\mathrm{B}}\ ^2\mathrm{B}_1$, $\widetilde{\mathrm{C}}\ ^2\mathrm{B}_2$, $\widetilde{\mathrm{D}}\ ^2\mathrm{A}_1$ and $\widetilde{\mathrm{E}}\ ^2\mathrm{B}_2$ electronic states of PFBz^+ in the order of increasing energy. Hereafter, these states will be identified as $\widetilde{\mathrm{X}}$, $\widetilde{\mathrm{A}}$, $\widetilde{\mathrm{B}}$, $\widetilde{\mathrm{C}}$, $\widetilde{\mathrm{D}}$ and $\widetilde{\mathrm{E}}$ in the rest of this chapter.

A vibronic coupling model is developed here to investigate the nuclear dynamics in the mentioned six electronic states. The electronic PESs are calculated *ab initio*, by both complete active space self-consistent field (CASSCF) [161, 162]-multi reference configuration interaction (MRCI) [163, 164] and equation of motion ionization potential coupled cluster singles and doubles (EOMIP-CCSD) [165, 166] methods. The coupling strength of all vibrational modes on six electronic states are calculated and the relevant vibrational modes are included in the study based on the coupling strength. First principles nuclear dynamics study is carried out by both time-independent and time-dependent quantum mechanical methods.

The vibronic coupling model developed here with the aid of the standard vibronic coupling theory [14]. The latter relies on the concept of diabatic electronic state, Taylor expansion of the elements of the diabatic electronic matrix in terms of normal coordinate of vibrational mode and elementary symmetry rules. The dynamics study is carried out by a matrix diagonalization method in the time-independent framework [14]. This enables to determine the precise location of the vibronic energy levels and aids in their assignments. The time-dependent calculations are carried out by propagating WPs with the aid of the MCTDH method developed at Heidelberg [119, 127, 128, 131]. This exercise enables us to calculate the broad band electronic spectra and to study the mechanistic details of radiative and nonradiative decay of excited electronic states. The results of this study are shown to be in good accord with the available experimental results.

4.0.1 Quantum chemistry calculations

The optimized equilibrium geometry of the electronic ground state of PFBz molecule is calculated at the MP2 level employing both aug-cc-pVDZ basis set of Dunning [149] and def2-TZVPPD [167–169] basis set. Gaussian-09 [150] suite of program is used for the calculations. The electronic ground term of PFBz is $^1A_1$ and the equilibrium geometry possesses C_{2v} point group symmetry. This is the reference state in this study and the vibrational motions in this state are treated as harmonic. The frequency (ω_i) of the thirty vibrational modes at the optimized equilibrium geometry is calculated by diagonalizing the kinematic (**G**) and *ab initio* force constant (**F**) matrix at the same level of theory. The mass-weighted normal displacement coordinates are derived from the eigenvectors of the **GF** matrix, and are transformed to the dimensionless form (**Q**) [92] as discussed in the Sec. 2.2.1.

The optimized equilibrium geometry of PFBz is shown in Fig. 4.1 with atom numbering and the equilibrium geometry parameters are given in Table 4.1. The harmonic frequency of the vibrational modes and their symmetry are given in Table 4.2 along with the

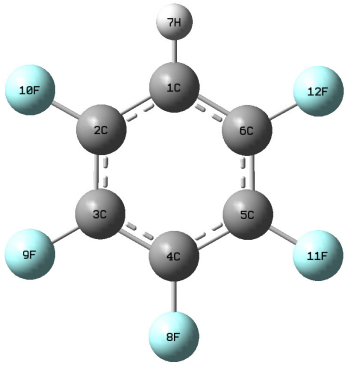

FIGURE 4.1: Schematic representation of the equilibrium minimum structure of the electronic ground state of PFBz.

literature data [155, 156] for comparison. It can be seen from Table 4.2 that the present data compare well with the experimental as well as the theoretical results available in the literature.

TABLE 4.1: Optimized equilibrium geometry of the electronic ground state of PFBz. The bond length (R) and bond angle (∠) are given in of Å and degrees, respectively.

Parameters	aug-cc-pVDZ	def2-TZVPPD
R(C1-C2,C1-C6)	1.40	1.38
R(C2-C3,C5-C6)	1.40	1.39
R(C3-C4,C4-C5)	1.40	1.39
R(C1-H7)	1.09	1.08
R(C2-F10,C6-F12)	1.35	1.33
R(C3-F9,C5-F11)	1.35	1.33
R(C4-F8)	1.35	1.33
∠(C1-C2-C3,C1-C6-C5)	121.48	121.28
∠(C2-C3-C4,C4-C5-C6)	119.15	119.20
∠(C3-C4-C5)	120.39	120.37
∠(C2-C1-C6)	118.34	118.68
∠(H7-C1-C2,H7-C1-C6)	120.83	120.66
∠(F10-C2-C1,F12-C6-C1)	119.97	120.11
∠(F10-C2-C3,F12-C6-C5)	118.55	118.61
∠(F9-C3-C2,F11-C5-C6)	120.94	120.94
∠(F9-C3-C4,F11-C5-C4)	119.90	119.86
∠(F8-C4-C3,F8-C4-C5)	119.81	119.81

In order to study the nuclear dynamics, the PESs of the six electronic states of $PFBz^+$ are calculated along the dimensionless normal displacement coordinates of the reference electronic ground state of PFBz. The adiabatic potential energies are calculated both by the CASSCF-MRCI and EOMIP-CCSD methods employing the aug-cc-pVDZ basis set. The CASSCF-MRCI and EOMIP-CCSD calculations are carried out using MOLPRO [154] and CFOUR [171] suite of programs, respectively. The vertical ionization energies

TABLE 4.2: Symmetry designation and harmonic frequency (in cm^{-1}) of vibrational modes of the electronic ground state of PFBz calculated at the MP2 level of theory.

		This work		Expt.		Description of the modes
Sym.	Mode	aug-cc-pVDZ	def2-TZVPPD	Ref. [155]	Ref. [156]	
a_1	ν_1	3257	3262	3103	3105	C-H stretching in plane
	ν_2	1682	1683	1648	1648	C-C-C bending
	ν_3	1533	1552	1516	1514	C-C and C-F stretching
	ν_4	1422	1444	1413	1410	C-C stretching
	ν_5	1268	1302	1291	1286	C-C stretching (Kekule)
	ν_6	1063	1092	1078	1082	C-F stretching
	ν_7	716	729	719	718	C-C-C trigonal bending
	ν_8	574	584	577	580	ring breathing
	ν_9	467	474	474	469	C-C-C in plane bending
	ν_{10}	324	329	327	325	C-F in plane bending
	ν_{11}	267	269	272	272	C-F in plane bending
a_2	ν_{12}	632	671	661	-	C-C-C out-of-plane
	ν_{13}	384	398	387	391	C-F out-of-plane bending
	ν_{14}	132	132	142	171	C-F out-of-plane
b_1	ν_{15}	841	840	837	838	C-H out-of-plane bending
	ν_{16}	591	636	715	689	C-H and C-F out of plane trigonal
	ν_{17}	543	560	556	556	C-H and C-C-C out of plane
	ν_{18}	317	323	321	-	C-F out-of-plane bending
	ν_{19}	204	208	206	-	C-F out-of-plane bending, in phase
	ν_{20}	158	155	158	-	C-F out-of-plane bending
b_2	ν_{21}	1679	1685	1648	1648	C-C stretching
	ν_{22}	1552	1570	1540	1535	C-C stretching
	ν_{23}	1478	1455	1269	1268	C-C stretching
	ν_{24}	1185	1207	1182	1182	C-H bending, in plane
	ν_{25}	1129	1163	1143	1138	C-F stretching, in plane
	ν_{26}	947	969	958	953	C-F stretching and C-H bending, in plane
	ν_{27}	684	694	692	662	C-F in plane bending
	ν_{28}	429	436	433	436	C-C-C in plane bending
	ν_{29}	300	303	303	300	C-F in plane bending
	ν_{30}	272	274	256	-	C-F in plane bending

TABLE 4.3: Vertical ionization energy (in eV) of the energetically lowest six electronic states of $PFBz^+$ calculated at the equilibrium geometry of the electronic ground state of PFBz (reference).

State	OVGF	CASSCF-MRCI	EOMIP-CCSD	RI-SCS-CC2[a]	Expt.
$\widetilde{X}\ ^2A_2$	9.63	10.42	9.91	9.86	9.9[b]
$\widetilde{A}\ ^2B_1$	9.94	10.69	10.27	10.49	10.1[a]/10.06[c]
$\widetilde{B}\ ^2B_1$	12.89	13.54	13.07	12.63	12.7[a]/12.74[d]
$\widetilde{C}\ ^2B_2$	14.26	15.72	13.98	-	13.9[a]
$\widetilde{D}\ ^2A_1$	14.53	16.08	14.39	-	-
$\widetilde{E}\ ^2B_2$	15.20	17.00	14.93	-	14.9[a]

[a]Ref. [25] [b]Ref. [40] [c]Ref. [60] [d]Ref. [170]

(VIEs) are calculated along the dimensionless normal displacement coordinates of each vibrational mode. The CASSCF-MRCI calculations are carried out with a (12e,10o) active space, which includes six valence occupied orbitals and four virtual orbitals with twelve electrons for PFBz. The electronic states of $PFBz^+$ have open shell configuration and a (11e,10o) active space is used. We note that many test calculations are carried out with varying active space and the chosen ones yield the best result with an affordable computational cost.

The VIEs calculated at the equilibrium geometry of the reference state are given in Table

4.3 along with the literature data. In addition to the CASSCF-MRCI and EOMIP-CCSD results, the VIEs calculated by the outer valence Green's function (OVGF) method are also given in Table 4.3. It can be seen from Table 4.3 that both the OVGF and EOMIP-CCSD results are closer to the experimental data as compared to the CASSCF-MRCI results. The EOMIP-CCSD results appear to be closest to the experimental data. A close look at the data given in Table 4.3 reveal that the $\widetilde{\mathrm{X}}$ and $\widetilde{\mathrm{A}}$ states are energetically close at the vertical configuration. A similar observation can also be made for the $\widetilde{\mathrm{B}}$-$\widetilde{\mathrm{C}}$-$\widetilde{\mathrm{D}}$-$\widetilde{\mathrm{E}}$ electronic states. Therefore, vibronic coupling appears to be an important mechanism to govern nuclear dynamics in these states.

4.0.2 The vibronic model

In this section a vibronic coupling model of the six energetically lowest electronic states $\widetilde{\mathrm{X}}$, $\widetilde{\mathrm{A}}$, $\widetilde{\mathrm{B}}$, $\widetilde{\mathrm{C}}$, $\widetilde{\mathrm{D}}$ and $\widetilde{\mathrm{E}}$ of PFBz$^+$ is developed. As noted in the thoery and methodology [cf., Sec. 2.2 in Chapter 2], the model is based on the framework of standard vibronic coupling theory, symmetry selection rules, a diabatic electronic basis and dimensionless normal displacement coordinates of the vibrational modes [14]. The thirty vibrational modes of the electronic ground state of PFBz transform to the following IREPs of the C_{2v} symmetry point group.

$$\Gamma_{vib} = 11a_1 \oplus 6b_1 \oplus 10b_2 \oplus 3a_2. \tag{4.1}$$

Using symmetry selection rules and standard vibronic coupling theory, the Hamiltonian can be written in a diabatic electronic basis as [14]

$$\mathcal{H} = \mathcal{H}_0 \mathbf{1_6} + \mathbf{\Delta}\mathcal{H}, \tag{4.2}$$

with

$$\mathcal{H}_0 = -\frac{1}{2} \sum_{i \in a_1,a_2,b_1,b_2} \omega_i \left(\frac{\partial^2}{\partial Q_i^2} \right) + \frac{1}{2} \sum_{i \in a_1,a_2,b_1,b_2} \omega_i Q_i^2, \tag{4.3}$$

and

$$\Delta\mathcal{H} = \begin{pmatrix} \mathcal{W}_{XX} & \mathcal{W}_{XA} & \mathcal{W}_{XB} & \mathcal{W}_{XC} & \mathcal{W}_{XD} & \mathcal{W}_{XE} \\ & \mathcal{W}_{AA} & \mathcal{W}_{AB} & \mathcal{W}_{AC} & \mathcal{W}_{AD} & \mathcal{W}_{AE} \\ & & \mathcal{W}_{BB} & \mathcal{W}_{BC} & \mathcal{W}_{BD} & \mathcal{W}_{BE} \\ & & & \mathcal{W}_{CC} & \mathcal{W}_{CD} & \mathcal{W}_{CE} \\ h.c. & & & & \mathcal{W}_{DD} & \mathcal{W}_{DE} \\ & & & & & \mathcal{W}_{EE} \end{pmatrix}. \tag{4.4}$$

In Eq. (4.2), the quantity **1** represents a (6 × 6) unit matrix. The Hamiltonian of the harmonic reference electronic ground state of PFBz is denoted by $\mathcal{H}_0$ and is defined in Eq. (4.3). The quantity $\Delta\mathcal{H}$ defines the change in electronic energy upon ionization to PFBz$^+$.

The elements of the matrix Hamiltonian $\Delta\mathcal{H}$ are expanded in a Taylor series around the equilibrium geometry of the reference state at **Q**=0 as

$$\mathcal{W}_{\alpha\alpha} = E^0_\alpha + \sum_{i\in a_1} \kappa_i^{(\alpha)} Q_i + \frac{1}{2!} \sum_{i,j\in a_1,a_2,b_1,b_2} \gamma_{ij}^{(\alpha)} Q_i Q_j + \frac{1}{3!} \sum_{i\in a_1} \eta_i^{(\alpha)} Q_i^3 + \frac{1}{4!} \sum_{i\in a_1,a_2,b_1,b_2} \zeta_i^{(\alpha)} Q_i^4 \quad (4.5)$$

and

$$\mathcal{W}_{\alpha\alpha'} = \mathcal{W}^*_{\alpha'\alpha} = \sum_i \lambda_i^{\alpha\alpha'} Q_i. \quad (4.6)$$

In the above equations, α and α', are the electronic state indices and i, j are the indices representing vibrational modes. The VIE of the α^{th} electronic state is denoted by E^0_α. The quantities κ_i^α, γ_{ij}^α, η_i^α, and ζ_i^α represent the linear, quadratic, cubic and quartic coupling parameters, respectively, within the α^{th} electronic state. The quantity, $\lambda_i^{\alpha\alpha'}$ denote the linear inter-state coupling parameter between the states α and α', coupled through i^{th} vibrational mode. The numerical values of the above parameters are derived by fitting the adiabatic electronic energies calculated *ab initio* to the diabatic electronic Hamiltonian introduced above. The Hamiltonian parameters of all six electronic states calculated in that way are given in Tables C1-C7 of the Appendix C. We note that while a second-order Taylor expansion resulted a good fit (along the totally symmetric modes) of the electronic energies calculated by the EOMIP-CCSD method, the CASSCF-MRCI energies required a higher order fit. Along with this, we have estimated the diagonal bilinear coupling parameters along the five (ν_2, ν_3, ν_4, ν_9 and ν_{11}) totally symmetric vibrational modes by a two-dimensional fit (using Levenberg Marquardt algorithm as implemented in MATLAB [147]). The diagonal bilinear parameters are given in Table C8 of the Appendix C. We also estimated the third-order coupling parameters along the coupling modes. The magnitude of these parameters is of the order of 10^{-3} eV or less. Therefore, a linear expansion of the coupling elements is retained in Eq. (4.6) and are tabulated in Tables C9 and C10 of the Appendix C.

4.0.3 Potential energy surfaces and Conical intersections

The topography of the adiabatic potential energy surfaces of the $\widetilde{\text{X}}$, $\widetilde{\text{A}}$, $\widetilde{\text{B}}$, $\widetilde{\text{C}}$, $\widetilde{\text{D}}$ and $\widetilde{\text{E}}$ electronic states of PFBz$^+$ is discussed in this section. One dimensional cuts of the multidimensional potential energy hypersurface of the electronic states are presented. These are plotted along the normal displacement coordinates of some selected totally

symmetric vibrational modes (ν_2-ν_4, ν_9 and ν_{11}) in Fig. 4.2. The points in the figure represent the adiabatic electronic energies calculated by the CASSCF-MRCI (Fig. 4.2a) and EOMIP-CCSD (Fig. 4.2b) methods. The superimposed solid curves represent the analytic fit of the corresponding points. The parameters derived from the fits are reported in Tables C1-C7 of the Appendix C, respectively.

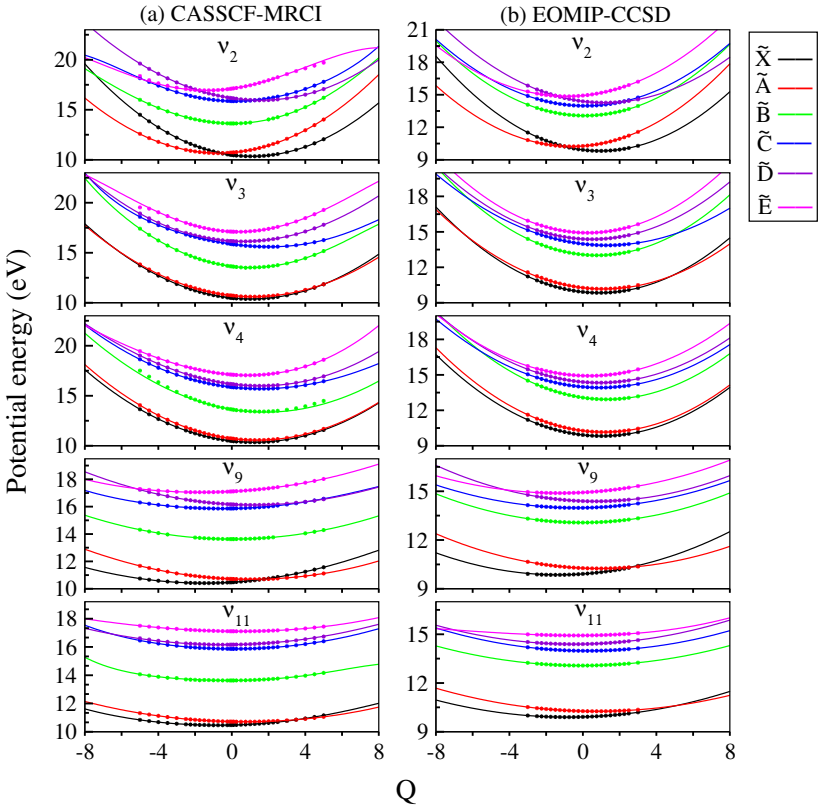

FIGURE 4.2: One dimensional cuts of the adiabatic potential energy surface of the $\widetilde{\mathrm{X}}$, $\widetilde{\mathrm{A}}$, $\widetilde{\mathrm{B}}$, $\widetilde{\mathrm{C}}$, $\widetilde{\mathrm{D}}$ and $\widetilde{\mathrm{E}}$ electronic states of PFBz^+ along the dimensionless normal displacement coordinate of the totally symmetric vibrational modes mentioned in the panel. The potential energies obtained from the present theoretical model and calculated *ab initio* (column (a): CASSCF-MRCI, column (b): EOMIP-CCSD) are shown by the solid lines and points, respectively.

It can be seen from Fig. 4.2 that the $\widetilde{\mathrm{X}}$ and $\widetilde{\mathrm{A}}$ states are energetically very close in the entire range of nuclear coordinates in both sets of data. The crossing of these states can be clearly seen along ν_2 and ν_9 vibrational modes. Such curve crossings acquire the topography of CIs in multi-dimensional space. The location of the $\widetilde{\mathrm{B}}$ state is energetically closer to the $\widetilde{\mathrm{C}}$-$\widetilde{\mathrm{D}}$-$\widetilde{\mathrm{E}}$ electronic states in the EOMIP-CCSD energy data [cf., Table 4.3]. In both (CASSCF-MRCI and EOMIP-CCSD) energy data the entanglement of $\widetilde{\mathrm{C}}$-$\widetilde{\mathrm{D}}$-$\widetilde{\mathrm{E}}$ states can be seen [cf., Fig. 4.2]. Multiple crossings of these states lead to multiple multi-dimensional CIs. The greater anharmonicity of the CASSCF-MRCI energies is also revealed by the data plotted in Fig. 4.2. Various stationary points viz., the energy of the minimum of the seam of CIs and the minimum of the states are calculated with

the EOMIP-CCSD potential energy curves using a minimization algorithm employing Lagrange multipliers. The numerical tools available in MATHEMATICA [157] are used for this purpose. The results are tabulated in a matrix array in Table 6.8. In the latter, the energies in the diagonal represent the minimum of a state and those in the off-diagonal are the minimum of the intersection seam.

TABLE 4.4: Energy (in eV) of the equilibrium minimum of the state (diagonal entries) and the minimum of its intersection seam with its neighbors (off-diagonal entries) of PFBz$^+$ calculated within a second-order coupling model and the EOMIP-CCSD electronic energy data.

	$\widetilde{X}^2A_2$	$\widetilde{A}^2B_1$	$\widetilde{B}^2B_1$	$\widetilde{C}^2B_2$	$\widetilde{D}^2A_1$	$\widetilde{E}^2B_2$
$\widetilde{X}^2A_2$	9.74	10.13	32.90	27.42	-	21.29
$\widetilde{A}^2B_1$	-	10.12	-	26.71	22.60	23.25
$\widetilde{B}^2B_1$	-	-	12.97	15.22	15.62	17.00
$\widetilde{C}^2B_2$	-	-	-	13.89	14.37	-
$\widetilde{D}^2A_1$	-	-	-	-	14.26	14.89
$\widetilde{E}^2B_2$	-	-	-	-	-	14.84

The following remarks can be readily made by examining the data given in Table 6.8. The energetic minimum of the $\widetilde{\text{B}}$ state occurs well above its minimum of intersections with the other states. The energetically closest one is the $\widetilde{\text{B}}$-$\widetilde{\text{C}}$ intersection minimum occurring ∼2.25 eV above the minimum of the $\widetilde{\text{B}}$ state. The minimum of the $\widetilde{\text{C}}$ state is however closer, ∼1.33 eV lower than the $\widetilde{\text{B}}$-$\widetilde{\text{C}}$ intersection minimum. The $\widetilde{\text{C}}$-$\widetilde{\text{D}}$-$\widetilde{\text{E}}$ electronic states of PFBz$^+$ are energetically close. The $\widetilde{\text{C}}$-$\widetilde{\text{D}}$ intersection minimum is closer to their respective equilibrium minimum. This is also true for the $\widetilde{\text{D}}$-$\widetilde{\text{E}}$ intersection minimum. The latter is almost quasi-degenerate with the minimum of the $\widetilde{\text{E}}$ state.

It emerges from the above results and also from the potential energy curves of Fig. 4.2 that, $\widetilde{\text{X}}$-$\widetilde{\text{A}}$ states of PFBz$^+$ form an isolated pair and are energetically well separated from the rest of their neighbors. The excitation strength of the vibrational modes is also similar in both these states [cf., Table C1 and C3], except the vibrational mode ν_8 has somewhat larger coupling strength in the $\tilde{A}$ state.

The $\widetilde{\text{X}}$-$\widetilde{\text{A}}$ coupling is fairly strong along the ν_{28} mode of b_2 symmetry and the coupling is moderate along the vibrational modes ν_{21} and ν_{30} of b_2 symmetry [cf., Tables C9 and C10]. Although the $\widetilde{\text{C}}$-$\widetilde{\text{D}}$-$\widetilde{\text{E}}$ states are energetically close and their respective equilibrium minimum is closer to various intersection minimum [cf., Table 6.8] the coupling of $\widetilde{\text{C}}$-$\widetilde{\text{D}}$ and $\widetilde{\text{D}}$-$\widetilde{\text{E}}$ states is not very strong. As can be seen from Tables C9 and C10 that $\widetilde{\text{C}}$-$\widetilde{\text{D}}$ states are moderately coupled through vibrational modes ν_{22} and ν_{29} and weakly coupled through ν_{26} of b_2 symmetry. Likewise, $\widetilde{\text{D}}$-$\widetilde{\text{E}}$ states are moderately coupled through ν_{21} and ν_{28} and weakly coupled through ν_{24}, ν_{27} and ν_{30} vibrational modes of b_2 symmetry.

The impact of these couplings on the nuclear dynamics is examined below. For nuclear dynamics formalism readers are referred to Ref. [14].

4.0.4 Results and Discussion

The vibronic band structure of the $\widetilde{\text{X}}$-$\widetilde{\text{A}}$-$\widetilde{\text{B}}$-$\widetilde{\text{C}}$-$\widetilde{\text{D}}$-$\widetilde{\text{E}}$ coupled electronic manifold of PFBz$^+$ is calculated and compared with the experimental photoionization spectroscopy results of Ref. [25]. In order to develop a systematic understanding of the details, we in the following examine the vibronic energy level structure of the uncoupled electronic states first and include the coupling between states subsequently to reveal its impact on the energy level structure. A time-independent matrix diagonalization method is used to calculate the precise location of the energy levels of the uncoupled electronic states and coupled two electronic states. Because of the dimensionality problem (as mentioned above) this method could not be used in the complete coupled states situation. The final spectral envelope for the entire coupled states situation is therefore calculated by a time-dependent WP propagation method employing the Heidelberg MCTDH [131] program modules.

4.0.4.1 Vibrational energy level spectrum of the uncoupled $\widetilde{\text{X}}$, $\widetilde{\text{A}}$, $\widetilde{\text{B}}$, $\widetilde{\text{C}}$, $\widetilde{\text{D}}$ and $\widetilde{\text{E}}$ electronic states of PFBz$^+$

The vibrational energy level spectrum of the uncoupled $\widetilde{\text{X}}$, $\widetilde{\text{A}}$, $\widetilde{\text{B}}$, $\widetilde{\text{C}}$, $\widetilde{\text{D}}$ and $\widetilde{\text{E}}$ electronic states of PFBz$^+$ is calculated by a matrix diagonalization approach [14] using the Lanczos algorithm. The theoretical calculations are carried out with ten totally symmetric vibrational modes (ν_2-ν_{11}) and the vibronic Hamiltonian of Sec. 4.0.2 and the parameters of Tables C1, C3, and C5. Both set of parameters derived from the CASSCF-MRCI and EOMIP-CCSD electronic energies are used for these calculations and the corresponding results are shown in panels a and b of Fig. 4.3, respectively. The HO basis functions used along each mode in these calculations are given in Table C11 Appendix C. The Hamiltonian of each state represented in the HO basis is diagonalized using 10,000 Lanczos iterations. The theoretical stick spectrum obtained from the diagonalization of the Hamiltonian matrix is convoluted with the Lorentzian line shape function of 40 meV FWHM to generate the spectral envelopes shown in Fig. 4.3.

The excitation of the fundamental of vibrational modes ν_8, ν_9 and ν_{11} is found in the $\tilde{X}$ state of PFBz$^+$ calculated with both the CASSCF-MRCI and EOMIP-CCSD Hamiltonian parameters. The peaks are ∼578, ∼465, ∼303 cm^{-1} (CASSCF-MRCI) and ∼577, ∼488, ∼298 cm^{-1} (EOMIP-CCSD) spaced in energy and correspond to the frequency of the vibrational modes ν_8, ν_9 and ν_{11}, respectively. Peak spacings of ∼572, ∼458, ∼285

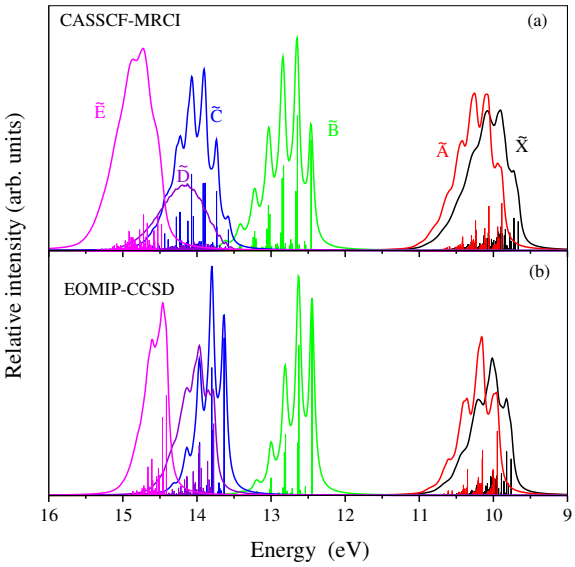

FIGURE 4.3: The stick vibrational spectrum and the convoluted envelope of the uncoupled $\widetilde{\mathrm{X}}$, $\widetilde{\mathrm{A}}$, $\widetilde{\mathrm{B}}$, $\widetilde{\mathrm{C}}$, $\widetilde{\mathrm{D}}$ and $\widetilde{\mathrm{E}}$ electronic states of $PFBz^+$, calculated with totally symmetric vibrational modes using the CASSCF-MRCI (panel a) and EOMIP-CCSD (panel b) Hamiltonian parameters.

cm^{-1} (CASSCF-MRCI) and ∼572, ∼460, ∼285 cm^{-1} (EOMIP-CCSD) corresponding to the excitation of ν_8, ν_9 and ν_{11} vibrational modes, respectively, are found in the $\widetilde{\mathrm{A}}$ state. The extended progression of all the modes excited in both the $\widetilde{\mathrm{X}}$ and $\widetilde{\mathrm{A}}$ states is assigned and given in Tables C12 and C13 Appendix C, respectively.

In addition to the energetic location and excitation strength analysis, the assignment of the peaks is also confirmed by examining the nodal pattern of the vibrational wave functions. These wave functions are calculated by a block improved-relaxation method as implemented in the MCTDH program module [129, 159, 160]. In Figs. C1 - C4 we present a few vibrational eigenfunctions of the $\widetilde{\mathrm{X}}$ and $\widetilde{\mathrm{A}}$ states. In these figures, the wave function probability density is plotted in a suitable reduced dimensional space of normal coordinates. In panels a-c, the wave function of the fundamental of ν_8, ν_9 and ν_{11} are shown, respectively. It can be seen from these plots that the wave function develops a node along the respective normal coordinate. The wave function for the overtone peaks of the excited vibrational modes are shown in panels d-f. Two, three and four quantum excitations along the first, second and third overtones, respectively, can be seen from the plots. Some combination peaks are shown in panels g-l of Figs. C1 - C4.

4.0.4.2 Coupled two-states results

In order to assess the impact of nonadiabatic coupling on the vibronic structure of an individual state, we performed several coupled two states calculations. The overall structure of the spectrum of the $\widetilde{\text{X}}$ state does not change upon inclusion of its coupling with the other states (i.e., $\widetilde{\text{A}}$, $\widetilde{\text{B}}$, $\widetilde{\text{C}}$ and $\widetilde{\text{E}}$) eventhough the coupling strength is moderate [cf., Table C10]. This is because except $\widetilde{\text{A}}$, the other states are energetically (vertically) well separated from the $\widetilde{\text{X}}$ state [cf., Table 4.3] and the energetic minimum of the seam of its intersection with them lies well above its equilibrium minimum [cf., Table 6.8].

The WP initially prepared on the $\widetilde{\text{X}}$ state does reaches the $\widetilde{\text{X}}$-$\widetilde{\text{A}}$ crossing seam and some population flows to the $\widetilde{\text{A}}$ state [cf., panel a of Fig. 4.4]. In this case the energetic minimum of the intersection seam occurs ∼0.39 eV and ∼0.01 eV above the minimum of the $\widetilde{\text{X}}$ and $\widetilde{\text{A}}$ electronic states, respectively [cf., Table 6.8]. As a result, the impact of the coupling is significant on the $\widetilde{\text{A}}$ state. The vibronic structure of the $\widetilde{\text{A}}$ state and its electronic population dynamics bears the signature of this coupling effect. The WP initially prepared on the $\widetilde{\text{A}}$ state accesses the $\widetilde{\text{X}}$-$\widetilde{\text{A}}$ intersection seam and more than ∼80% electronic population flows to the $\widetilde{\text{X}}$ state within ∼22 fs [cf., panel b of Fig. 4.4]. Such a huge population exchange causes a large increase in the spectral line density and broadening of the vibronic spectrum of the $\widetilde{\text{A}}$ state. The $\widetilde{\text{X}}$ and $\widetilde{\text{A}}$ electronic bands resulting from these coupled $\widetilde{\text{X}}$-$\widetilde{\text{A}}$ states calculations are shown in panels a and b of Fig. 4.5, respectively. In addition to this, we examined the $\widetilde{\text{X}}$-$\widetilde{\text{A}}$ coupled states results obtained by the matrix diagonalization method. Based on the excitation strength [cf., Tables C1, C3, C9 and C10] five totally symmetric vibrational modes (ν_2, ν_3, ν_4, ν_9, ν_{11}) and five coupling vibrational modes (ν_{21}, ν_{24}, ν_{28}, ν_{29}, ν_{30}) of b_2 symmetry are included in the calculation. The composite vibronic spectra of the $\widetilde{\text{X}}$-$\widetilde{\text{A}}$ coupled states of PFBz$^+$ are shown in panels b and c of Fig. 4.6 and compared with the experimental band plotted in panel a. The results of the panel b and c are obtained with CASSCF-MRCI and EOMIP-CCSD Hamiltonian parameters, respectively. The theoretical spectral envelope is obtained by convoluting the vibronic stick lines with a Lorentzian line shape function of 40 meV FWHM. The theoretical spectrum of of the $\widetilde{\text{X}}$ state given in panel b and c is shifted by ∼0.9 eV and ∼0.6 eV, respectively, along the abscissa to reproduce the experimental [25] adiabatic ionization energy. Because of reduced dimensional calculations such shifts were necessary to account for the zero-point energy. We also calculated the adiabatic ionization energy of the $\widetilde{\text{X}}$ state by the CCSD method. We obtained a value of ∼9.56 eV as compared to its experimental value of ∼9.64 eV [25]. It can be seen from Fig. 4.6 that the theoretical results are in very good accord with the experimental band structure of the $\widetilde{\text{X}}$-$\widetilde{\text{A}}$ coupled states.

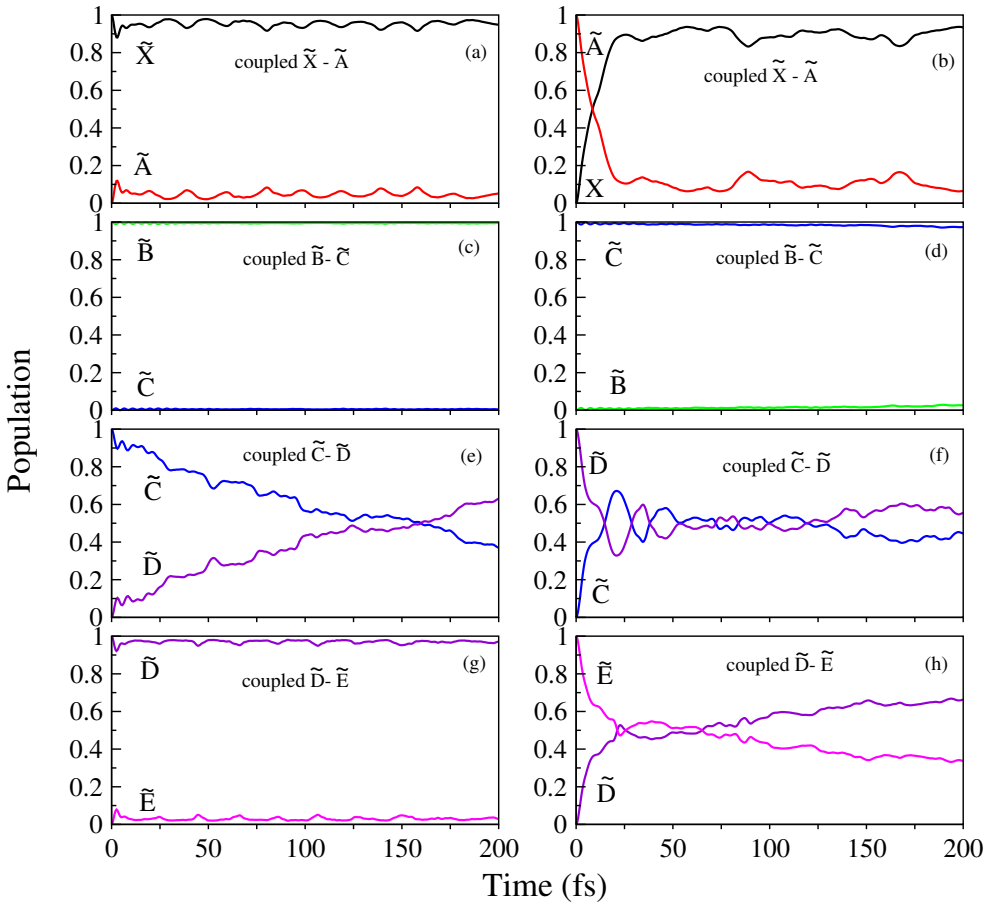

FIGURE 4.4: Time-dependence of the diabatic electronic populations in the coupled $\widetilde{X}$-$\widetilde{A}$, $\widetilde{B}$-$\widetilde{C}$, $\widetilde{C}$-$\widetilde{D}$ and $\widetilde{D}$-$\widetilde{E}$ states dynamics obtained by locating an initial WP on each electronic state separately are shown in the panels a-b, c-d, e-f and g-h, respectively. EOMIP-CCSD Hamiltonian parameters are used for these calculations.

The vibronic energy levels of the $\widetilde{X}$-$\widetilde{A}$ coupled states are assigned by examining the WP density plots in an analogous way as described in Sec. 5.2.2.1. The most probable assignments of vibronic energy lines are presented in Tables C14, C15 and the WP density plots of some of these assignments are shown in Figs. C5-C8 of the Appendix C. The comparison with the data presented in Tables C12 and C13 reveals a slight change of the energetic location of the fundamentals of the totally symmetric vibrational modes. In contrast to the uncoupled state spectrum, the combination peaks of the totally symmetric vibrational modes are not found in the coupled states spectrum of the $\widetilde{X}$ state. However, they are found in the $\widetilde{A}$ state both in the uncoupled state and coupled states situations. In the $\widetilde{X}$-$\widetilde{A}$ coupled states spectrum excitation of the vibrational modes of b_2 symmetry is found. These vibrational modes also form combination peaks between them and also with the totally symmetric modes. Less number of combination peaks are found with the EOMIP-CCSD parameters as compared to the CASSCF-MRCI parameters.

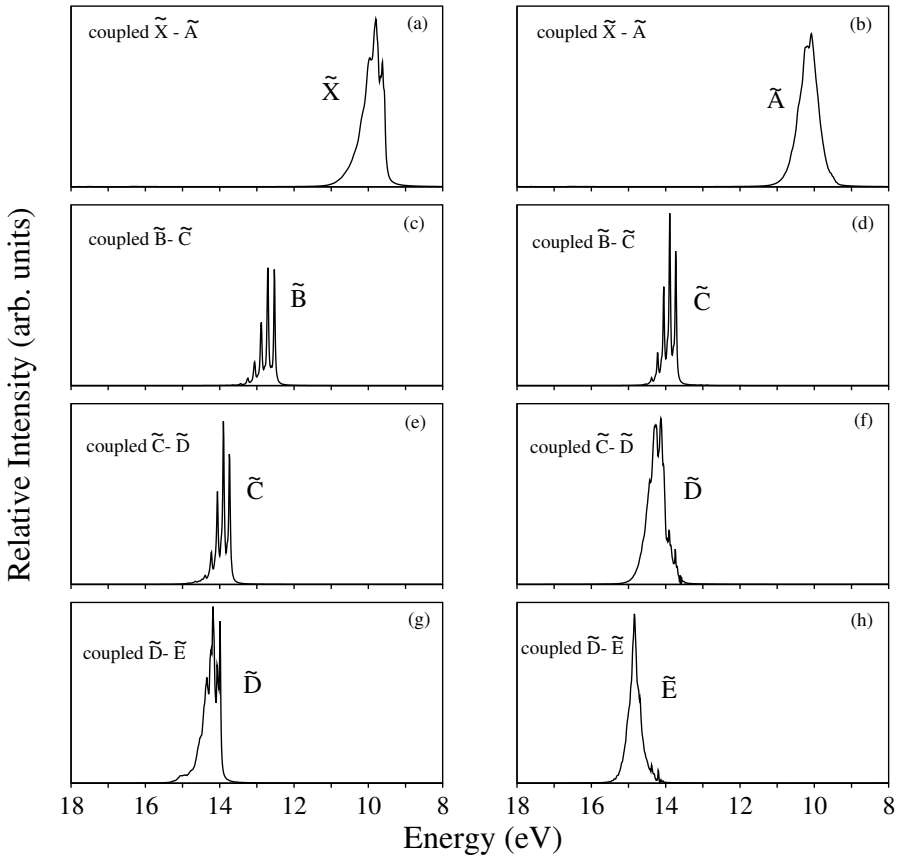

FIGURE 4.5: Composite vibronic band structure of the coupled $\widetilde{\text{X}}$-$\widetilde{\text{A}}$, $\widetilde{\text{B}}$-$\widetilde{\text{C}}$, $\widetilde{\text{C}}$-$\widetilde{\text{D}}$ and $\widetilde{\text{D}}$-$\widetilde{\text{E}}$ states of PFBz$^+$ are shown in the panels a-b, c-d, e-f and g-h, respectively. The band structures are calculated using the Hamiltonian parameters derived from the EOMIP-CCSD energy data.

It can be seen from the results presented above that, the fundamental of the totally symmetric ν_{11} and ν_9 vibrational modes appears at ∼300 cm^{-1} and ∼460 cm^{-1}, respectively [cf., Tables C14 and C15 of the Appendix C]. The latter is reported at ∼474 cm^{-1} in the experiment [60] and is reasonably in good agreement with the present result. Inclusion of $\widetilde{\text{X}}$-$\widetilde{\text{A}}$ coupling increases the vibronic line density and causes a broadening of spectral envelope. Because of large energy separation, the vibronic spectrum of the $\widetilde{\text{B}}$, $\widetilde{\text{C}}$, $\widetilde{\text{D}}$ and $\widetilde{\text{E}}$ states is not affected by their coupling with the $\widetilde{\text{X}}$ state, as significantly as the $\widetilde{\text{A}}$ state. The coupling between the $\widetilde{\text{A}}$ and $\widetilde{\text{B}}$ states is approximated to zero, due to large energy separation between them. The coupling of $\widetilde{\text{B}}$ and $\widetilde{\text{C}}$ states does not have impact on their respective vibronic structure, as indicated by very little population exchange between them [cf., panels c and d of Fig. 4.4].

In contrast to the above, the coupling between $\widetilde{\text{C}}$-$\widetilde{\text{D}}$ and $\widetilde{\text{D}}$-$\widetilde{\text{E}}$ states have strong impact on their respective vibronic structure. In case of $\widetilde{\text{C}}$-$\widetilde{\text{D}}$ coupled states, the energetic minimum of the intersection seam occurs ∼0.48 eV and ∼0.11 eV above the estimated equilibrium

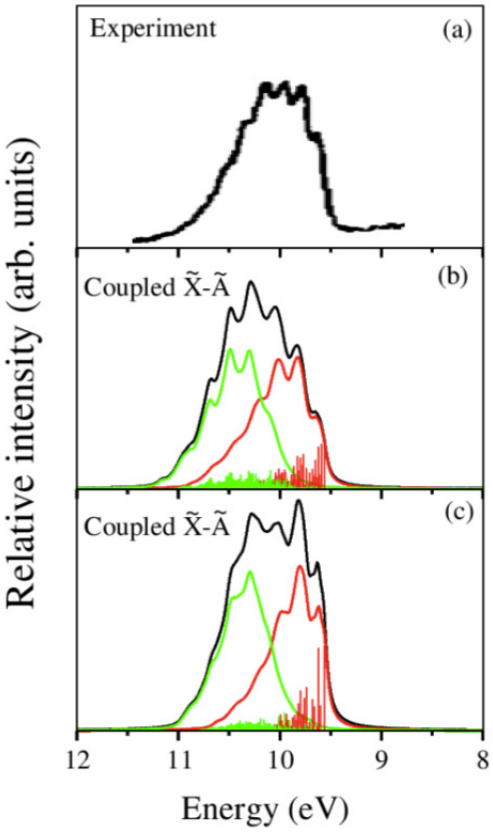

FIGURE 4.6: Stick vibronic spectrum and convoluted envelope of the $\widetilde{X}$-$\widetilde{A}$ coupled electronic states of $PFBz^+$. Panels b and c are obtained with the Hamiltonian parameters derived from the CASSCF-MRCI and EOMIP-CCSD, respectively. The experimental $\widetilde{X}$-$\widetilde{A}$ band is reproduced from Ref. [25] and shown in panel a.

minimum of the $\widetilde{C}$ and $\widetilde{D}$ states, respectively [cf., Table 6.8]. The coupling between these states is also fairly strong. As a result large population exchange occurs between them. In order to illustrate, time-dependence of the diabatic electronic population for an initial transition to the $\widetilde{C}$ and $\widetilde{D}$ states in the $\widetilde{C}$-$\widetilde{D}$ coupled states situation is shown in panels e and f of Fig. 4.4, respectively. It can be seen from the panel e of Fig. 4.4 that, the population of the $\widetilde{C}$ state monotonically decays to ∼0.37 and that of the $\widetilde{D}$ state grows to ∼0.67 in about 200 fs. As can be seen from panel f of Fig. 4.4, a large fraction of population flows to both the electronic states in this case. This is because the equilibrium minimum of the $\widetilde{D}$ state is energetically very close to the minimum of the $\widetilde{C}$-$\widetilde{D}$ CIs [cf., Table 6.8]. A sharp decay of population occurs within ∼20 fs followed by quasi-periodic recurrences at longer times.

In case of coupled $\widetilde{D}$-$\widetilde{E}$ states the energetic minimum of the intersection seam occurs ∼0.63 eV and ∼0.05 eV above the estimated equilibrium minimum of $\widetilde{D}$ and $\widetilde{E}$ states, respectively [cf., Table 6.8]. This leads to a very small amount of population transfer to the $\widetilde{E}$ state when the WP is initially launched on the $\widetilde{D}$ state [cf., panel g of Fig. 4.4]. Because of fairly strong coupling between the $\widetilde{D}$ and $\widetilde{E}$ states and the fact that the

minimum of their intersection seam is energetically very close to the minimum of the $\widetilde{\mathrm{E}}$ state [cf., Table 6.8], the coupling has strong impact on the dynamics of the $\widetilde{\mathrm{E}}$ state. The population of the $\widetilde{\mathrm{E}}$ state sharply decays to ∼0.47 and that of the $\widetilde{\mathrm{D}}$ state grows to ∼0.53 within a short time of ∼23 fs [cf., panel h of Fig. 4.4] when the WP is initially located on the $\widetilde{\mathrm{E}}$ state. At longer times $\widetilde{\mathrm{E}}$ state population decreases monotonically. The vibronic band structures resulting from the above coupled-states calculations are shown in Fig. 4.5.

4.0.4.3 Vibronic spectrum of coupled $\widetilde{\mathrm{X}}$-$\widetilde{\mathrm{A}}$-$\widetilde{\mathrm{B}}$-$\widetilde{\mathrm{C}}$-$\widetilde{\mathrm{D}}$-$\widetilde{\mathrm{E}}$ electronic states

The vibronic spectrum of the coupled $\widetilde{\mathrm{X}}$-$\widetilde{\mathrm{A}}$-$\widetilde{\mathrm{B}}$-$\widetilde{\mathrm{C}}$-$\widetilde{\mathrm{D}}$-$\widetilde{\mathrm{E}}$ is calculated and presented in this section. Because of large vertical energy separation of the $\widetilde{\mathrm{B}}$ state from all other states, we have performed nuclear dynamics calculations with two separate group of states viz., $\widetilde{\mathrm{X}}$-$\widetilde{\mathrm{A}}$-$\widetilde{\mathrm{B}}$ and $\widetilde{\mathrm{B}}$-$\widetilde{\mathrm{C}}$-$\widetilde{\mathrm{D}}$-$\widetilde{\mathrm{E}}$. Both the CASSCF-MRCI and EOMIP-CCSD Hamiltonian parameters are employed in the calculations. With the CASSCF-MRCI parameters 16 vibrational modes were necessary for both group of states and with the EOMIP-CCSD parameters 16 and 24 vibrational modes, respectively, were necessary for the two group of states noted above. Different coupling mechanism revealed by the CASSCF-MRCI and EOMIP-CCSD parameters is reflected in the electronic population dynamics discussed below. The different number of vibrational DOFs required for $\widetilde{\mathrm{B}}$-$\widetilde{\mathrm{C}}$-$\widetilde{\mathrm{D}}$-$\widetilde{\mathrm{E}}$ coupled states dynamics is assessed from the interstate coupling parameters obtained from the two sets of electronic energy data. The coupling between $\widetilde{\mathrm{B}}$-$\widetilde{\mathrm{D}}$ states is absent in case of CASSCF-MRCI [cf., Table C9] data. It can be seen from panel d of Figs. 4.7 and 4.8 that the electronic population dynamics calculated with two sets of data differs significantly when the $\widetilde{\mathrm{C}}$ state is initially populated.

The dynamics calculations are carried out by propagating WPs on the coupled electronic states using the Heidelberg MCTDH suite of program modules [131]. Six WP calculations are performed by launching the initial WP on each of the six electronic states separately. The details of the mode combination and the sizes of the basis sets are given in Table C16. In each calculation WP is propagated for 200 fs. The time autocorrelation function is damped with an exponential function of relaxation time 33 fs, and then Fourier transformed to obtain the spectrum. The results from six different calculations are combined with equal weightage to generate the composite theoretical band. The results obtained with the CASSCF-MRCI and EOMIP-CCSD Hamiltonian parameters are shown in Fig. 4.9 along with the experimental results reproduced from Ref. [25]. It can be seen from the figures [cf., panels (a)-(d) of Fig. 4.9] that the theoretical results are in good accord with the experimental band structures. While the first band originates from highly overlapping $\widetilde{\mathrm{X}}$ and $\widetilde{\mathrm{A}}$ electronic states, the third and fourth

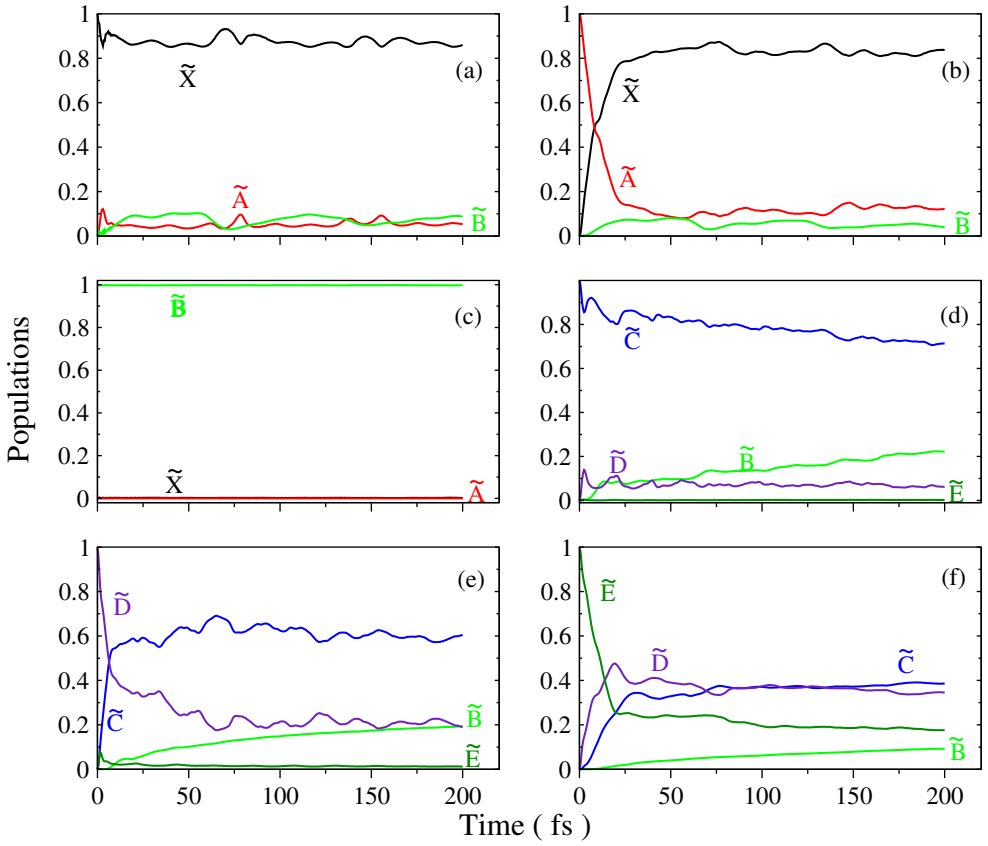

FIGURE 4.7: Time evolution of the diabatic electronic populations obtained in the coupled $\widetilde{X}\ ^2A_2$-$\widetilde{A}\ ^2B_1$-$\widetilde{B}\ ^2B_1$-$\widetilde{C}\ ^2B_2$-$\widetilde{D}\ ^2A_1$-$\widetilde{E}\ ^2B_2$ states situation (using the parameter set derived from the CASSCF-MRCI energy data) by locating an initial WP on each of the $\widetilde{X}\ ^2A_2$, $\widetilde{A}\ ^2B_1$, $\widetilde{B}\ ^2B_1$, $\widetilde{C}\ ^2B_2$, $\widetilde{D}\ ^2A_1$ and $\widetilde{E}\ ^2B_2$ electronic states separately are shown in the panels a, b, c, d, e and f, respectively.

bands are formed by highly overlapping $\widetilde{C}$, $\widetilde{D}$ and $\widetilde{E}$ electronic states. To this end, we note that the vibronic band structures remain unchanged [cf., panel d of Fig. 4.9] upon inclusion of the bilinear coupling parameters given in Table C8 of the Appendix C.

4.0.4.4 Internal conversion dynamics

The time-dependent populations of the six diabatic electronic states of $PFBz^+$ in the coupled (i.e., $\widetilde{X}$-$\widetilde{A}$-$\widetilde{B}$ and $\widetilde{B}$-$\widetilde{C}$-$\widetilde{D}$-$\widetilde{E}$) states situation are recorded and examined in this section. This is to unravel and understand the impact of various couplings on the dynamics of a given state. The results obtained by initially populating the $\widetilde{X}$, $\widetilde{A}$, $\widetilde{B}$, $\widetilde{C}$, $\widetilde{D}$ and $\widetilde{E}$ electronic states are shown in panels a-f of Figs. 4.7 and 4.8 calculated with CASSCF-MRCI and EOMIP-CCSD parameters, respectively. The electronic populations are color-coded (online version) in the same way in all panels of the respective figures. The electronic populations for an initial location of the WP on the $\widetilde{X}$ state

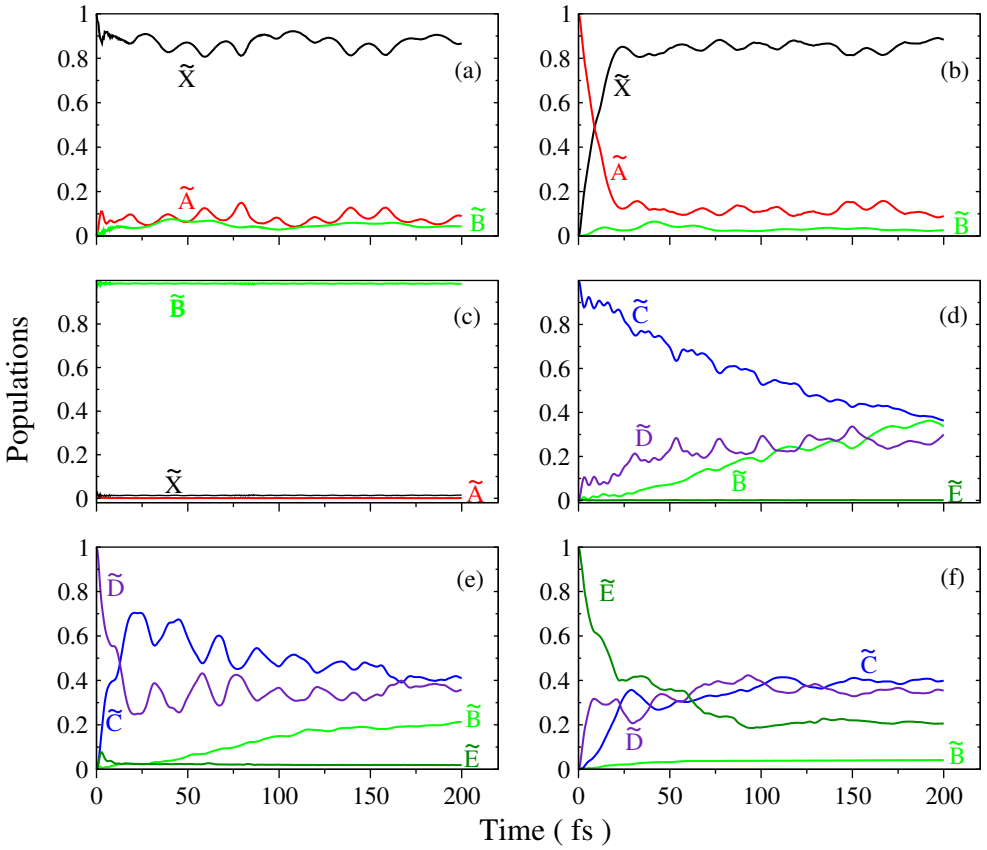

FIGURE 4.8: Same as Table 4.7 and using the parameter set derived from the EOMIP-CCSD energy data.

shown in panel a of both Fig. 4.7 and Fig. 4.8 reveal a very little amount of population transfer to the $\widetilde{\mathrm{A}}$ and $\widetilde{\mathrm{B}}$ states. The minimum of the $\widetilde{\mathrm{X}}$-$\widetilde{\mathrm{A}}$ CIs located ∼0.39 eV above the minimum of the $\widetilde{\mathrm{X}}$ state and therefore the population transfer to the $\widetilde{\mathrm{A}}$ state is not significant. Because of the large energy separation between the $\widetilde{\mathrm{X}}$ and $\widetilde{\mathrm{B}}$ states, the population transfer to the $\widetilde{\mathrm{B}}$ state is also negligible. On the other hand, a large amount of population flows to the $\widetilde{\mathrm{X}}$ state when the WP initially placed on the $\widetilde{\mathrm{A}}$ state [cf., panel b of Figs. 4.7 and 4.8]. A decay rate of ∼15 fs can be estimated from the initial fast decay of the population of the $\widetilde{\mathrm{A}}$ state. The energetic minimum of the $\widetilde{\mathrm{X}}$-$\widetilde{\mathrm{A}}$ CIs occurs ∼0.01 eV above the minimum of the $\widetilde{\mathrm{A}}$ state and therefore causes such a rapid decay of the $\widetilde{\mathrm{A}}$ state population.

The population for an initial excitation of the WP to the $\widetilde{\mathrm{B}}$ state is shown in panel c of Figs. 4.7 and 4.8. It can be seen that practically no population flows to all other states when the WP is initially prepared on the $\widetilde{\mathrm{B}}$ state. This is due to the fact that the $\widetilde{\mathrm{B}}$ state is vertically well separated from all other states and the CIs of the $\widetilde{\mathrm{B}}$ state with all other states are located at high energies and are not accessible to the WP during its evolution on this state. This results into the observed sharp vibrational level structure

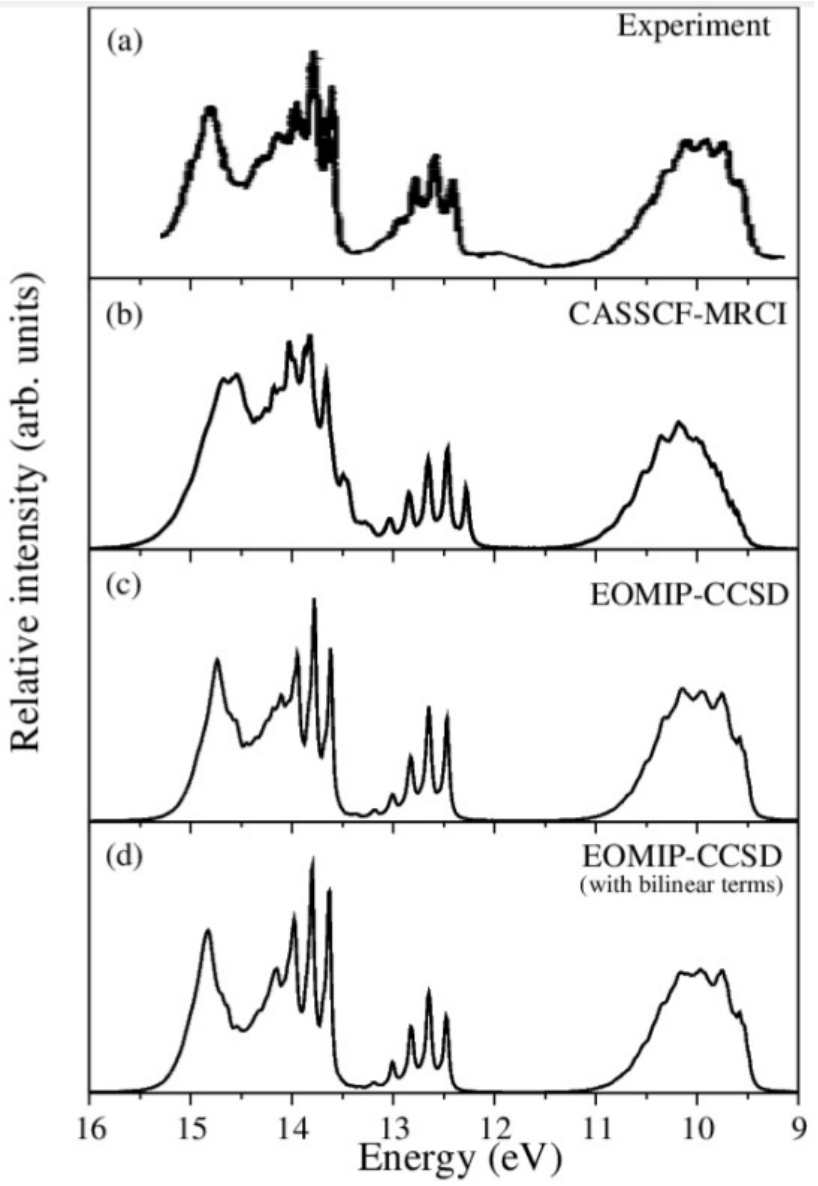

FIGURE 4.9: Composite vibronic band structure of the coupled $\widetilde{\text{X}}$-$\widetilde{\text{A}}$-$\widetilde{\text{B}}$-$\widetilde{\text{C}}$-$\widetilde{\text{D}}$-$\widetilde{\text{E}}$ electronic states of PFBz$^+$. The band structures calculated using the Hamiltonian parameters derived from the CASSCF-MRCI and EOMIP-CCSD energy data are, respectively, shown in panels b, c. The band structures obtained by including the bilinear coupling parameters of Table C8 are plotted in panel d. The experimental result reproduced from Ref. [25] is shown in panel a. The intensity in arbitrary units is plotted as a function of the energy of the cationic vibronic states. The zero of the energy scale corresponds to the energy of the equilibrium minimum of the electronic ground state of neutral PFBz.

of the $\widetilde{\text{B}}$ band [cf., panels a and b of Fig. 4.3]. This implies a long-lived nature of the $\widetilde{\text{B}}$ state and gives rise to the observed emission of PFBz$^+$. We will return to this point again later in the text.

Time-dependence of electronic populations for an initial location of the WP on the $\widetilde{\text{C}}$ state is shown in panel d of Figs. 4.7 and 4.8. In this case the internal conversion takes

place to both $\widetilde{\mathrm{D}}$ and $\widetilde{\mathrm{B}}$ states via the low-lying $\widetilde{\mathrm{C}}$-$\widetilde{\mathrm{D}}$ and $\widetilde{\mathrm{B}}$-$\widetilde{\mathrm{D}}$ CIs, respectively. At longer times the WP from the $\widetilde{\mathrm{D}}$ state moves to the $\widetilde{\mathrm{B}}$ state via $\widetilde{\mathrm{B}}$-$\widetilde{\mathrm{D}}$ CIs, minimum of which occurs ∼1.36 eV above the minimum of the $\widetilde{\mathrm{D}}$ state. Although the overall picture remains similar, the extent of population transfer obtained with the EOMIP-CCSD parameters is far greater [cf., panel d of Fig. 4.8].

The WP initially prepared on the $\widetilde{\mathrm{D}}$ state quickly flows to the $\widetilde{\mathrm{C}}$ state (shown in panel e of Figs. 4.7 and 4.8) via the energetically low-lying $\widetilde{\mathrm{C}}$-$\widetilde{\mathrm{D}}$ CIs. The minimum of the $\widetilde{\mathrm{D}}$ state is only ∼0.11 eV below the minimum of $\widetilde{\mathrm{C}}$-$\widetilde{\mathrm{D}}$ intersections. The internal conversion to the $\widetilde{\mathrm{B}}$ state appears to occur through the $\widetilde{\mathrm{C}}$ state as these states are strongly coupled via the ν_{13} mode of a_2 symmetry [cf., Tables C9 and C10 of the Appendix C]. A nonradiative decay rate of ∼16 fs can be estimated from the population curve of $\widetilde{\mathrm{D}}$ state given in panel e of Figs. 4.7 and 4.8.

The electron population dynamics becomes more complex and involved when the WP is initially prepared on the $\widetilde{\mathrm{E}}$ electronic state (shown in panel f of Figs. 4.7 and 4.8). In this case, most of the population flows to the $\widetilde{\mathrm{C}}$ and $\widetilde{\mathrm{D}}$ electronic states. This is because of strong nonadiabatic coupling among $\widetilde{\mathrm{C}}$, $\widetilde{\mathrm{D}}$ and $\widetilde{\mathrm{E}}$ electronic states. Also, a large population transfer is facilitated by the energetic proximity of the equilibrium minimum and the minimum of various intersection seams in the $\widetilde{\mathrm{C}}$-$\widetilde{\mathrm{D}}$-$\widetilde{\mathrm{E}}$ states. The initial fast decay of the population relates to a life-time of ∼64 fs of the $\widetilde{\mathrm{E}}$ state.

In summary, the results presented above show that the observed broad band photoionization spectrum of PFBz$^+$ is better reproduced with the Hamiltonian parameters extracted from the EOMIP-CCSD electronic structure data, as compared to the same with the CASSCF-MRCI data. The overall dynamical mechanism is qualitatively same in both the cases as discussed in relation to the population dynamics. The superiority of the EOMIP-CCSD data can not be judged in the present work, it requires more resolved experimental data to be available in order to make a conclusive remark.

4.0.4.5 Radiative emission

The radiative emission of Bz$^+$ and its fluoro derivatives was studied both experimentally [25–46] and theoretically [47–51, 55, 143]. A clear radiative emission was observed for three-fold fluorination or more of Bz$^+$. It was found that Bz$^+$, its monofluoro, difluoro (abbreviated as MFBz$^+$ and DFBz$^+$, respectively) derivatives are non-emissive, except the *m*-DFBz$^+$ (the meta isomer) which emits weakly [39, 51]. Fluorescence emission was observed for 1,3,5-trifluorobenzene radical cation (TFBz$^+$). In the recent past some of the experimental observations were explained in several extensive theoretical studies on the electronically excited fluorobenzene radical cations [47–56, 143]. Vibronic coupling

among electronic states was established to be the crucial mechanism that governs the nonradiative decay and radiative emission in fluorinated Bz$^+$.

Fluorination of Bz causes a stabilization of its σ-type of MOs. The stabilization increases with increasing fluorination and causes an energetic re-ordering of the cationic states. To understand the energetic ordering of electronic states of the fluorobenzene cations more clearly, we have calculated the six lowest valence MOs of Bz, monofluorobenzene (MFBz), difluorobenzene (DFBz) (o, m and p), trifluorobenzene (TFBz), PFBz and Hexafluorobenzene (HFBz) and plotted their energies in Fig. 4.10. It can be seen from

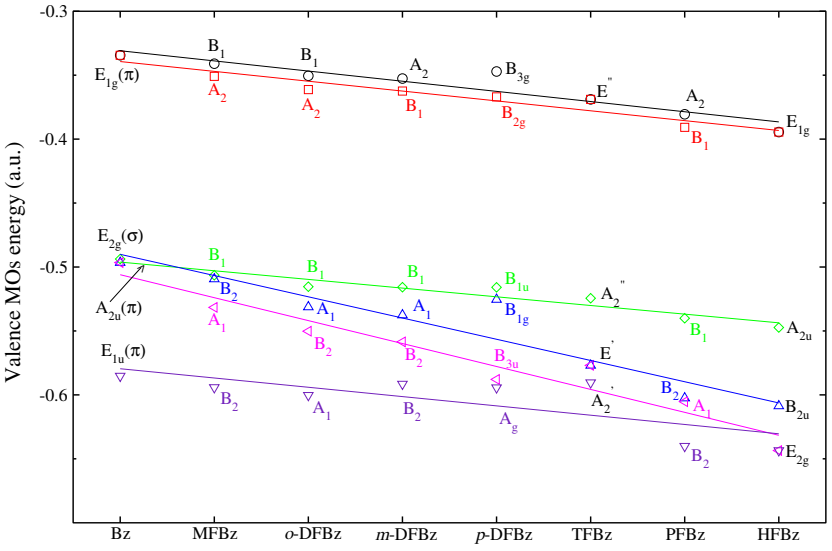

FIGURE 4.10: Energy location of the valence MOs of Bz and its fluroderivatives.

the figure that the HOMO of all molecules is of π type. Fluorination causes a reduction of symmetry of Bz (D_{6h}) which is restored again in HFBz. Due to this symmetry reduction the degenerate E_{1g} MO transforms to two non-degenerate MOs in MFBz and DFBz. Because of high symmetry of 1,3,5-TFBz (D_{3h}) the degeneracy of MOs is restored. The degeneracy is again split in PFBz (C_{2v}). It can be seen that the σ-type E_{2g} MO of Bz (HOMO-1) undergoes considerable energy shift upon fluorination, as compared to the E_{1g} (π) MO. The electronic states of the radical cations originating from ionization of an electron from the above MOs are portrayed in Fig. 4.11. In this figure the VIEs of the cationic states are calculated with the EOMIP-CCSD/aug-cc-pVDZ level of theory and plotted. First of all it can be seen that the cationic states form two groups, $\widetilde{\text{X}}$-$\widetilde{\text{A}}$ and $\widetilde{\text{B}}$-$\widetilde{\text{C}}$-$\widetilde{\text{D}}$-$\widetilde{\text{E}}$. These two groups are fairly well separated in energy. The nonradiative decay is governed by the interactions within and between the two groups. A second observation that can be clearly made from the plot is that the states arising from the $^2E_{2g}$ (σ) MO of Bz are all shifted to higher energies in the fluorinated Bz$^+$. This is due

to a stabilization of the corresponding orbitals in the neutral molecules [cf., Fig. 4.10]. A third observation that can be made from Fig. 4.11 that the states arising out of a_{2u} (π) MO of Bz remain energetically unaffected for all fluorobenzene cations.

In Bz^+ the Jahn-Teller split components of the $\widetilde{X}$ and $\widetilde{B}$ states form low energy CIs which facilitates nonradiative decay and quenching of fluorescence [143]. The interaction between the $\widetilde{X}$-$\widetilde{A}$ and $\widetilde{B}$-$\widetilde{C}$-$\widetilde{D}$ group of states gives rise to energetically accessible CIs for nonradiative decay in $MFBz^+$ and $DFBz^+$. Among the three $DFBz^+$ (o, m and p) the energetic minimum of the relevant CIs occurs relatively at higher energy in the m-isomer and gives rise to weak radiative emission of its $\widetilde{C}$ state. The degenerate $\widetilde{X}$ $^2E''$ and excited $\widetilde{B}$ $^2E'$ electronic states of 1,3,5-$TFBz^+$ are energetically well separated and the intersections of these states with its $\widetilde{A}$ $^2A_2''$ state occurring in between occurs at higher energies relative to the minimum of the latter state. As a result, minimal electronic population flows to the $\widetilde{A}$ $^2A_2''$ state when the WP initially prepared on any of the remaining states. Furthermore, the electron population dynamics of this state is not affected at all by its coupling with the other states. The population of this state remains at ∼100% for a long time and gives rise to radiative emission in 1,3,5-$TFBz^+$.

An analogous situation (as in case of 1,3,5-$TFBz^+$) can be sketched in case of $PFBz^+$ by examining the results presented in Sec. 4.0.4.4. The data presented in Table 6.8 reveal that the $\widetilde{B}$ state of $PFBz^+$ is ∼2.85 eV above the $\widetilde{A}$ state and ∼1.0 eV below the $\widetilde{C}$ state. The $\widetilde{B}$ state is not coupled with the $\widetilde{A}$ state on energy ground. However, it is coupled to the $\widetilde{C}$ state and the energetic minimum of the $\widetilde{B}$-$\widetilde{C}$ CIs occur at ∼15.22 eV which is ∼2.25 eV above the $\widetilde{B}$ state minimum. Despite strong $\widetilde{B}$-$\widetilde{C}$ coupling through ν_{13} and ν_{14} vibrational modes of a_2 symmetry [cf., Table C9], the coupling effect on the population dynamics of the $\widetilde{B}$ state is weak because of large energy gap. In fact, the electron population does not flow to the other states when the WP is initially prepared on the $\widetilde{B}$ state [cf., Figs. 4.7 and 4.8]. The population curve of the $\widetilde{B}$ state remains parallel to the time axis. This indicates a long-lived nature of the $\widetilde{B}$ state which gives rise to radiative emission in $PFBz^+$.

4.0.5 Summary

Vibronic coupling and quantum nuclear dynamics in the energetically lowest six electronic states of $PFBz^+$ is studied in this chapter. Detailed electronic structure calculations are carried out by different *ab initio* quantum chemistry methods. With the aid of the electronic structure results a model vibronic Hamiltonian is constructed in a diabatic electronic basis in terms of the dimensionless normal displacement coordinates of the vibrational modes. The coupling among different electronic states is evaluated by the standard vibronic coupling theory and elementary symmetry selection rules. The nuclear

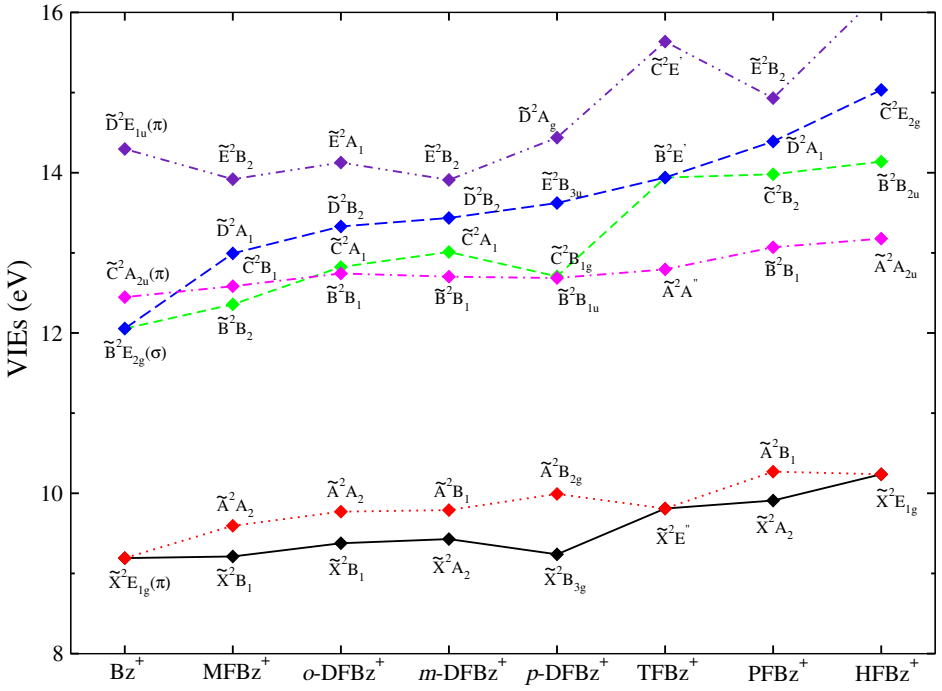

FIGURE 4.11: VIEs of Bz and its fluoro derivatives.

dynamics calculations are carried out from first principles by both time-independent and time-dependent methods. For the latter calculations the Heidelberg MCTDH suite of program modules are utilized. It appears from the electronic structure data and subsequent dynamics results that the EOMIP-CCSD method does a superior job in this case. It is by no means a conclusive remark in the absence of high resolution spectroscopy data. It is established that the energetically lowest six electronic states separates into two groups viz., $\widetilde{X}$-$\widetilde{A}$ and $\widetilde{B}$-$\widetilde{C}$-$\widetilde{D}$-$\widetilde{E}$. The $\widetilde{X}$ and $\widetilde{A}$ states form energetically accessible CIs. The effect of the latter on the dynamics of the $\widetilde{X}$ state is not as much as on the same on the $\widetilde{A}$ state. This is because the minimum of the $\widetilde{X}$ state is energetically well separated from the minimum of the $\widetilde{X}$-$\widetilde{A}$ CIs. The minimum of the $\widetilde{A}$ state on the other hand is energetically very close to the minimum of the $\widetilde{X}$-$\widetilde{A}$ intersections. Therefore, the $\widetilde{X}$-$\widetilde{A}$ coupling has a significant effect on the vibronic structure of the $\widetilde{A}$ state.

It is found that the $\widetilde{B}$ state is energetically well separated from the rest of the states. The coupling of $\widetilde{B}$ state with others therefore has no significant effect on the vibronic structure of the $\widetilde{B}$ state. The population of this state remains ∼100% for a long time when the dynamics started on it. The radiative emission in PFBz$^+$ is therefore originates from this state. The $\widetilde{C}$-$\widetilde{D}$-$\widetilde{E}$ electronic states are energetically close and therefore give rise to highly overlapping vibronic bands. The theoretical results are shown to be in

good accord with available experimental results.

Chapter 5

The Jahn-Teller and pseudo-Jahn-Teller effects in Hexafluorobenzene radical cation: Radiative emission and nonradiative decay

In continuation with Chapter 4, the theoretical photoelectron spectroscopy of Hexafluorobenzene (HFBz) and its radiative emission and nonradiative decay dynamics are examined in this chapter. HFBz is a highly symmetric molecule and its equilibrium geometry belongs to the D_{6h} symmetry point group. The radical cation $HFBz^+$ of this molecule possesses degenerate electronic states and vibrational modes. Therefore, this molecule provides a unique platform to investigate multi-mode Jahn-Teller (JT) and pseudo-Jahn-Teller (PJT) effects in its ionic states. This study helps us to understand the complexity involved in the theoretical treatment of large molecular systems.

Many previous investigations have reported the He I [26, 27, 172–178] and He II [25, 27] photoelectron spectra of HFBz. They have shown that ionization from each outermost orbital gives rise to a well-separated band located in the binding energy range of ∼9.5-15.5 eV. Each of these bands exhibits a vibrational structure. Also, the fluorobenzene radical cations have received considerable attention to unravel the effect of fluorine substitution on the emissive properties of their excited electronic states [39–46]. Laser-induced fluorescence technique was used extensively for this purpose [179, 180]. The perfluoro effect in photoelectron spectroscopy of HFBz was studied by Brundle *et al.* [34] and Decleva *et al.* [181]. The valence shell electronic structure of HFBz has been

studied both experimentally and theoretically by Holland *et al.* [182]. Despite several experimental and theoretical studies, a detailed theoretical study of multi-mode JT and PJT interactions in the electronic states of HFBz$^+$ is missing in the literature. Therefore, in this chapter we discussed the multi-mode JT and PJT interaction in the first four energetically low-lying electronic states and the mechanistic details of the radiative emission of HFBz$^+$ using *ab initio* quantum dynamical approach in a greater detail. The valence shell molecular orbital (MO) sequence of HFBz in its electronic ground state ($^1A_{1g}$) reads (core)$(4a_{1g})^2(4e_{1u})^4(4e_{2g})^4(1b_{2u})^2(5a_{1g})^2(4b_{1u})^2(1a_{1u})^2(5e_{2g})^4(5e_{1u})^4$ $(1e_{1g})^4(1e_{2u})^4(1b_{2g})^2(6e_{1u})^4(1a_{2g})^2(6e_{2g})^4(2b_{2u})^2(2a_{2u})^2(2e_{1g})^4$. Ionization from the highest occupied MO and the inner ones gives rise to $\widetilde{X}\ ^2E_{1g}$, $\widetilde{A}\ ^2A_{2u}$, $\widetilde{B}\ ^2B_{2u}$ and $\widetilde{C}\ ^2E_{2g}$ electronic states of HFBz$^+$ in the order of increasing energy.

A vibronic coupling model is developed here to investigate the nuclear dynamics in the mentioned four (altogether six states when the JT splitting is taken into consideration) electronic states. The electronic PESs are calculated *ab initio* by EOMIP-CCSD [165, 166] method. The coupling strength of all vibrational modes on four electronic states is calculated and the relevant vibrational modes are included in the study based on the coupling strength. First principles nuclear dynamics study is carried out by time-independent and time-dependent quantum mechanical methods.

The vibronic coupling model was developed using the standard vibronic coupling theory [14]. The latter relies on the concept of diabatic electronic state, Taylor expansion of the elements of the diabatic electronic matrix in terms of the normal coordinate of vibrational mode and elementary symmetry rules. The dynamics study is carried out using a time-independent matrix diagonalization method [14]. This enables to determine the precise location of the vibronic energy levels and aids in their assignments. The time-dependent calculations are carried out by propagating wave packets (WPs). The multi-configuration time-dependent Hartree (MCTDH) method developed at Heidelberg [119, 127, 128, 131] is used for this purpose. This exercise enables us to calculate the broad band electronic spectra and to study the mechanistic details of radiative and nonradiative decay of excited electronic states. The results of this study are shown to be in good accord with the available experimental results.

5.1 Theory and computational details

5.1.1 Electronic structure calculations of the HFBz

The optimized equilibrium geometry of the electronic ground state of the HFBz molecule is calculated using second-order Møller-Plesset perturbation (MP2) theory employing the

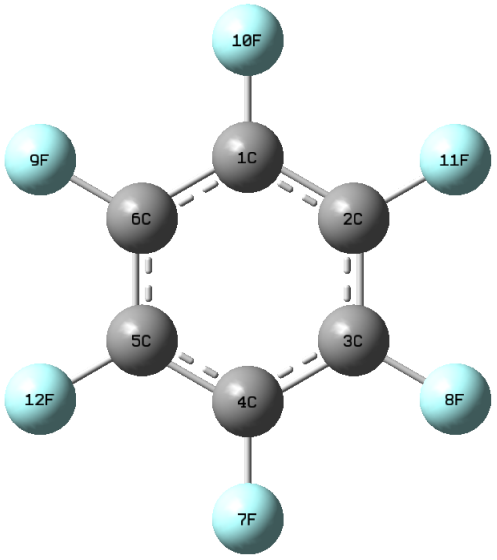

FIGURE 5.1: Schematic representation of the equilibrium minimum structure of the electronic ground state of HFBz.

augmented correlation-consistent polarized valence double zeta (aug-cc-pVDZ) basis set of Dunning [149]. Gaussian-09 [150] suite of the program is used for the calculations. The electronic ground term of HFBz is $^1A_{1g}$ and the equilibrium geometry converged to the D_{6h} point group symmetry. This is the reference state in this study and the vibrational motions in this state are treated as harmonic. The frequency (ω_i) of the thirty vibrational modes at the optimized equilibrium geometry is calculated by diagonalizing the kinematic (**G**) and *ab initio* force constant (**F**) matrix at the same level of theory. The mass-weighted normal displacement co-ordinates are derived from the eigenvectors of the **GF** matrix and are transformed to the dimensionless form (**Q**) by multiplying with $\sqrt{\omega_i}$ (in a.u. $\hbar$=1) [92].

The optimized equilibrium geometry of HFBz is shown in Fig. 5.1 with atom numbering. The experimental [183] and calculated structural constants are the following.

Experimental : C-C = 1.391 ± 0.007 Å
C-F = 1.327 ± 0.007 Å
Calculated : C-C = 1.4011 Å
C-F = 1.3461 Å

The harmonic frequency of the vibrational modes and their symmetry are given in Table 5.1 along with the literature data [155, 156] for comparison. It can be seen from Table 5.1 that the present data compare well with the experimental as well as the theoretical results available in the literature.

In order to study the nuclear dynamics, the PESs of the four electronic states of HFBz$^+$

TABLE 5.1: Symmetry designation and harmonic frequency of vibrational modes of the ground state of HFBz MP2/aug-cc-pVDZ level of theory.

Sym.	Mode	This work		Experiment [184]	Description of the modes
		eV	cm^{-1}	cm^{-1}	
a_{1g}	ν_1	0.1874	1512	1493	C-F stretching in-phase
	ν_2	0.0686	553	556	Ring breathing
a_{2g}	ν_3	0.0968	781	788	C-F in-plane bending, in-phase
a_{2u}	ν_4	0.0261	211	210	C-F out-of-plane bending, in-phase
b_{1u}	ν_5	0.1507	1276	1330	C-F trigonal stretching
	ν_6	0.0727	586	600	C-C-C trigonal bending
b_{2g}	ν_7	0.0577	465	719	C-F out-of-plane trigonal
	ν_8	0.0222	179	205	C-C-C Puckering
b_{2u}	ν_9	0.1825	1472	1252	C-C stretching (kekule)
	ν_{10}	0.0341	275	278	C-F in plane trigonal bending
e_{1g}	ν_{11}	0.0448	361	365	C-F out-of-plane bending
e_{1u}	ν_{12}	0.1921	1550	1533	C-C stretching
	ν_{13}	0.1236	997	1019	C-F stretching
	ν_{14}	0.0387	312	313	C-F in-plane bending
e_{2g}	ν_{15}	0.2093	1688	1656	C-C stretching
	ν_{16}	0.1420	1145	1162	C-F stretching
	ν_{17}	0.0541	436	440	C-C-C in-plane bending
	ν_{18}	0.0328	264	267	C-F in-plane bending
e_{2u}	ν_{19}	0.0757	611	645	C-C-C out-of-plane
	ν_{20}	0.0169	136	137	C-F out-of-plane

mentioned in the introduction are calculated along the dimensionless normal displacement coordinates of the reference electronic ground state of HFBz. The adiabatic potential energies are calculated by the EOMIP-CCSD method employing the aug-cc-pVDZ basis set. The EOMIP-CCSD calculations are carried out using the CFOUR [171] suite of programs. The vertical ionization energies (VIEs) are calculated along the dimensionless normal displacement coordinate of each vibrational mode.

The VIEs calculated at the equilibrium geometry of the reference state are given in Table 5.2, along with the literature data [25]. In addition to the EOMIP-CCSD results, the VIEs calculated by the outer valence Green's function (OVGF) method are also given in Table 5.2. It can be seen from Table 5.2 that EOMIP-CCSD results are closer to the experimental data as compared to the OVGF results. A close look at the data given in Table 5.2 reveals that the $\widetilde{X}\ ^2E_{1g}$ state is energetically well separated from all other electronic states and the $\widetilde{A}\ ^2A_{2u}$, $\widetilde{B}\ ^2B_{2u}$, $\widetilde{C}\ ^2E_{2g}$ electronic states are close in energy at the vertical configuration. Therefore, vibronic coupling appears to be an important mechanism for governing nuclear dynamics in these states.

TABLE 5.2: Vertical ionization energy (in eV) of the energetically lowest five electronic states of HFBz$^+$ calculated at the equilibrium geometry of the electronic ground state of HFBz (reference).

State	OVGF	EOMIP-CCSD	Expt. [25]
$\widetilde{\mathrm{X}}\ ^2\mathrm{E}_{1g}$	9.89	10.24	10.2
$\widetilde{\mathrm{A}}\ ^2\mathrm{A}_{2u}$	12.97	13.18	12.8
$\widetilde{\mathrm{B}}\ ^2\mathrm{B}_{2u}$	14.35	14.14	14.0
$\widetilde{\mathrm{C}}\ ^2\mathrm{E}_{2g}$	15.24	15.03	14.8
$\widetilde{\mathrm{D}}\ ^2\mathrm{A}_{2g}$	16.56	16.25	15.0

5.1.2 Theoretical approach to study the vibronic coupling

A vibronic coupling model of the four energetically lowest electronic states $\widetilde{\mathrm{X}}\ ^2\mathrm{E}_{1g}$, $\widetilde{\mathrm{A}}\ ^2\mathrm{A}_{2u}$, $\widetilde{\mathrm{B}}\ ^2\mathrm{B}_{2u}$, and $\widetilde{\mathrm{C}}\ ^2\mathrm{E}_{2g}$ of HFBz$^+$ is constructed in this section. The model is based on the framework of standard vibronic coupling theory, symmetry selection rules, a diabatic electronic basis, and dimensionless normal displacement coordinates of the vibrational modes [14]. The thirty vibrational modes of the electronic ground state of HFBz transform to the following irreducible representations (IRREPs) of the D_{6h} symmetry point group.

$$\Gamma_{vib} = 2a_{1g} + a_{2g} + a_{2u} + 2b_{1u} + 2b_{2g} + 2b_{2u} + e_{1g} + 3e_{1u} + 4e_{2g} + 2e_{2u}. \tag{5.1}$$

The symmetry selection rules are governed by the coupling constants within (intra) and between (inter) electronic states;

$$(\Gamma_j)^2 \supset \Gamma_i, \tag{5.2a}$$

$$\Gamma_j \otimes \Gamma_k \supset \Gamma_i, \tag{5.2b}$$

respectively [14]. According to Eq. (5.2a), the IRREP Γ_i of the vibrational mode i has to be contained in the symmetrized direct product of the electronic IRREP Γ_j with itself in order that the intrastate coupling constants. The analogous selection rule, Eq. (5.2b), applies to the inter-state coupling constant.

For the nondegenerate $\widetilde{\mathrm{A}}\ ^2\mathrm{A}_{2u}$ and $\widetilde{\mathrm{B}}\ ^2\mathrm{B}_{2u}$ electronic states of HFBz$^+$ according to Eq. (5.2a), only the totally symmetric (a_{1g}) vibrations ν_1 and ν_2 can couple in their respective order. For the degenerate $\widetilde{\mathrm{X}}\ ^2\mathrm{E}_{1g}$ and $\widetilde{\mathrm{C}}\ ^2\mathrm{E}_{2g}$ electronic states, one has

$$(E_{1g})^2 = (E_{2g})^2 = a_{1g} + e_{2g}. \tag{5.3}$$

In the above equation, the vibrational modes of a_{1g} symmetry cannot lift the electronic degeneracy (i.e., they are condon active), and the modes of e_{2g} symmetry can lift the

electronic degeneracy and are JT active modes. The vibrational modes active in electronically off-diagonal couplings are identified by applying Eq. (5.2b) for each pair of the four electronic states of HFBz$^+$ enumerated above. This type of interaction is called PJT activity or PJT coupling.

$$E_{1g} \otimes A_{2u} = B_{2u} \otimes E_{2g} = e_{1u}, \tag{5.4a}$$

$$E_{1g} \otimes B_{2u} = A_{2u} \otimes E_{2g} = e_{2u}. \tag{5.4b}$$

Using the above mentioned symmetry selection rules and the standard vibronic coupling theory, the Hamiltonian can be written in a diabatic electronic basis as [14]

$$\mathcal{H} = \mathcal{H}_0 \mathbf{1_6} + \mathbf{\Delta}\mathcal{H}, \tag{5.5}$$

with

$$\mathcal{H}_0 = \mathcal{T}_N + \mathcal{V}_0, \tag{5.6}$$

$$\mathcal{T}_N = -\frac{1}{2}\sum_{i\in\ a_{1g}} \omega_i \frac{\partial^2}{\partial Q_i^2} - \frac{1}{2}\sum_{i\in\ e_{1g},e_{1u},e_{2g},e_{2u}} \omega_i \left(\frac{\partial^2}{\partial Q_{ix}^2} + \frac{\partial^2}{\partial Q_{iy}^2}\right), \tag{5.7}$$

$$\mathcal{V}_0 = \frac{1}{2}\sum_{i\in\ a_{1g}} \omega_i Q_i^2 + \frac{1}{2}\sum_{i\in\ e_{1g},e_{1u},e_{2g},e_{2u}} \omega_i \left(Q_{ix}^2 + Q_{iy}^2\right), \tag{5.8}$$

and

$$\Delta\mathcal{H} = \begin{pmatrix} \mathcal{W}_{\widetilde{X}}^{x} & \mathcal{W}_{\widetilde{X}}^{xy} & \sum_{i\in e_{1u}} \lambda_i' Q_{ix} & \sum_{i\in e_{2u}} \lambda_i' Q_{ix} & 0 & 0 \\ & \mathcal{W}_{\widetilde{X}}^{y} & -\sum_{i\in e_{1u}} \lambda_i' Q_{iy} & -\sum_{i\in e_{2u}} \lambda_i' Q_{iy} & 0 & 0 \\ & & \mathcal{W}_{\widetilde{A}} & 0 & \sum_{i\in e_{2u}} \lambda_i' Q_{ix} & -\sum_{i\in e_{2u}} \lambda_i' Q_{iy} \\ & h.c. & & \mathcal{W}_{\widetilde{B}} & \sum_{i\in e_{1u}} \lambda_i' Q_{ix} & -\sum_{i\in e_{1u}} \lambda_i' Q_{iy} \\ & & & & \mathcal{W}_{\widetilde{C}}^{x} & \mathcal{W}_{\widetilde{C}}^{xy} \\ & & & & & \mathcal{W}_{\widetilde{C}}^{y} \end{pmatrix}. \tag{5.9}$$

In Eq. (5.5), the quantity $\mathbf{1}_6$ represents a 6×6 unit matrix. The Hamiltonian of the harmonic reference electronic ground state of HFBz is denoted by $\mathcal{H}_0$ and is defined in Eqs. (5.6-5.8). The quantity $\Delta\mathcal{H}$ defines the change in electronic energy upon ionization to HFBz$^+$.

The elements of the matrix Hamiltonian $\Delta\mathcal{H}$ are expanded in a Taylor series around the equilibrium geometry of the reference state at $\mathbf{Q}$=0 as

$$\begin{aligned}\mathcal{W}_j^{x/y} =& E_j^0 + \sum_{i\in a_{1g}} \kappa_i^{(1)j} Q_i + \frac{1}{2!}\sum_{i\in a_{1g}} \kappa_i^{(2)j} Q_i^2 \\ &+ \sum_{i\in e_{1g},e_{1u},e_{2g},e_{2u}} \left[\frac{1}{2!}a_i^{(2)j}\left(Q_{ix}^2+Q_{iy}^2\right) + \frac{1}{3!}a_i^{(3)j}\left(2Q_{ix}^3 - 6Q_{ix}Q_{iy}^2\right)\right] \\ &+ \sum_{i\in e_{1g},e_{1u},e_{2g},e_{2u}} \left[\frac{1}{4!}a_i^{(4)j}\left(Q_{ix}^4 + 2Q_{ix}^2Q_{iy}^2 + Q_{iy}^4\right)\right] \\ &\pm \sum_{i\in e_{1g},e_{1u},e_{2g},e_{2u}} \left[\lambda_i^{(1)j}Q_{ix} + \frac{1}{2!}\lambda_i^{(2)j}\left(Q_{ix}^2 - Q_{iy}^2\right) + \frac{1}{3!}\lambda_i^{(3)j}\left(Q_{ix}^3 + Q_{ix}Q_{iy}^2\right)\right] \\ &\pm \sum_{i\in e_{1g},e_{1u},e_{2g},e_{2u}} \left[\frac{1}{4!}\lambda_i^{(4)j}(Q_{ix}^4 - 6Q_{ix}^2Q_{iy}^2 + Q_{iy}^4) + \frac{1}{4!}\lambda_i^{(4')j}(Q_{ix}^4 - Q_{iy}^4)\right]; j \in \widetilde{X},\widetilde{C}\end{aligned} \tag{5.10}$$

$$\begin{aligned}\mathcal{W}_j^{xy} =& \sum_{i\in e_{2g}} \left[\lambda_i^{(1)j}Q_{iy} - \frac{1}{2!}2\lambda_i^{(2)j}Q_{ix}Q_{iy} + \frac{1}{3!}\lambda_i^{(3)j}\left(Q_{ix}^2Q_{iy} + Q_{iy}^3\right)\right] \\ &+\frac{1}{4!}\sum_{i\in e_{2g}} \left[\lambda_i^{(4)j}\left(4Q_{ix}^3Q_{iy} - 4Q_{ix}Q_{iy}^3\right) + \lambda_i^{(4')j}\left(-2Q_{ix}^3Q_{iy} - 2Q_{ix}Q_{iy}^3\right)\right]; j \in \widetilde{X},\widetilde{C},\end{aligned} \tag{5.11}$$

$$\begin{aligned}\mathcal{W}_j =& E_j^0 + \sum_{i\in a_{1g}} \kappa_i^{(1)j} Q_i + \frac{1}{2!}\sum_{i\in a_{1g}} \kappa_i^{(2)j} Q_i^2 \\ &+ \sum_{i\in e_{1g},e_{1u},e_{2g},e_{2u}} \left[\frac{1}{2!}a_i^{(2)j}\left(Q_{ix}^2+Q_{iy}^2\right) + \frac{1}{4!}a_i^{(4)j}\left(Q_{ix}^4 + 2Q_{ix}^2Q_{iy}^2 + Q_{iy}^4\right)\right]; j \in \widetilde{A},\widetilde{B}\end{aligned} \tag{5.12}$$

where x and y denotes the two components of the degenerate electronic states and vibrational modes. The VIEs of the jth electronic state is denoted by E_j^0. The quantities $\kappa_i^{(n)j}$ and $a_i^{(n)j}$ are the nth order intra-state coupling parameters for the totally symmetric and degenerate vibrational modes, respectively, of the jth electronic state. The quantity $\lambda_i^{(n)j}$ denote the nth order inter-state JT coupling parameter of the jth electronic state and λ_i' represent the linear PJT coupling parameter of the ith vibrational mode between the electronic states. The $\pm$ sign in Eq. (5.10) is applicable to the x (+) and y (-) components of the degenerate electronic state. All the Hamiltonian parameters are evaluated by non-linear least-squares fitting of the 6×6 diabatic potential matrix [cf., Eq. (5.9)] to the *ab initio* energies. The estimated parameters along the relevant vibrational modes are given in Tables 5.3 to 5.5. Note that the parameters of odd-order for degenerate vibrational modes do not appear in Eq. (5.12) in accordance with the symmetry selection rule. As we can see from these coupling parameters, not all 30 DOFs play significant role in the nuclear dynamics on the cationic electronic states of HFBz considered in this article. Therefore, only the relevant DOFs are retained in the nuclear dynamics study presented below.

TABLE 5.3: *Ab initio* calculated linear ($\kappa_i^{(1)}$, $\lambda_i^{(1)}$), quadratic ($\kappa_i^{(2)}$, $a_i^{(2)}$, $\lambda_i^{(2)}$) and quartic ($a_i^{(4)}$) coupling parameters for the $\widetilde{\mathrm{X}}\ ^2\mathrm{E}_{1g}$, $\widetilde{\mathrm{A}}\ ^2\mathrm{A}_{2u}$, $\widetilde{\mathrm{B}}\ ^2\mathrm{B}_{2u}$ and $\widetilde{\mathrm{C}}\ ^2\mathrm{E}_{2g}$ electronic states of HFBz$^+$. All quantities are in eV and the dimensionless Poisson parameters ($\frac{{\kappa_i}^2}{2{\omega_i}^2}$ or $\frac{{\lambda_i}^2}{2{\omega_i}^2}$) are given in the parentheses.

		$\widetilde{\mathrm{X}}\ ^2\mathrm{E}_{1g}$			$\widetilde{\mathrm{A}}\ ^2\mathrm{A}_{2u}$	
Symm.	Mode	$\kappa_i^{(1)}$	$\kappa_i^{(2)}$		$\kappa_i^{(1)}$	$\kappa_i^{(2)}$
a_{1g}	ν_1	-0.2728 (1.059545)	-0.0066		-0.2887 (1.186655)	-0.0141
	ν_2	0.0355 (0.133899)	-0.0012		-0.0147 (0.022959)	-0.0001
		$\lambda_i^{(1)}$	$a_i^{(2)}$	$\lambda_i^{(2)}$	$a_i^{(2)}$	$a_i^{(4)}$
e_{1g}	ν_{11}	-0.00005(0.000001)	0.0130	-0.0198	-0.0102	0.0003
e_{1u}	ν_{12}	0.00000(0.00000)	-0.0146	0.0081	0.0128	-0.0009
	ν_{13}	-0.00001(0.00000)	-0.0033	0.0011	-0.0030	0.0000
	ν_{14}	0.00007(0.000002)	0.0052	0.0010	0.0041	0.0000
e_{2g}	ν_{15}	0.1689 (0.3256)	0.0030	-0.00030	0.0023	-0.00010
	ν_{16}	0.0241 (0.0144)	-0.0064	0.00011	-0.0058	0.00005
	ν_{17}	0.0684 (0.7993)	-0.0036	0.00010	-0.0020	0.00100
	ν_{18}	0.0327 (0.4969)	0.0055	-0.00020	0.0049	0.00000
e_{2u}	ν_{19}	0.00008(0.000001)	0.0015	0.00340	-0.0138	0.0006
	ν_{20}	-0.00003(0.000001)	0.0024	0.00032	0.0015	0.0000

		$\widetilde{\mathrm{B}}\ ^2\mathrm{B}_{2u}$		$\widetilde{\mathrm{C}}\ ^2\mathrm{E}_{2g}$		
Symm.	Mode	$\kappa_i^{(1)}$	$\kappa_i^{(2)}$	$\kappa_i^{(1)}$	$\kappa_i^{(2)}$	
a_{1g}	ν_1	-0.2440 (0.8476)	-0.0201	-0.1325 (0.2499)	-0.0169	
	ν_2	0.0140 (0.0208)	-0.0014	0.0166 (0.0293)	-0.0019	
		$a_i^{(2)}$	$a_i^{(4)}$	$\lambda_i^{(1)}$	$a_i^{(2)}$	$\lambda_i^{(2)}$
e_{1g}	ν_{11}	0.0054	-0.0003	0.0000 (0.0000)	0.0022	0.0063
e_{1u}	ν_{12}	-0.0692	0.0063	0.0000 (0.0000)	-0.0032	0.0173
	ν_{13}	-0.0179	0.0007	0.0063 (0.0013)	-0.0035	0.0000
	ν_{14}	0.0015	0.0000	0.0000 (0.0000)	-0.0022	0.0000
e_{2g}	ν_{15}	-0.0221	0.0005	0.1482 (0.2507)	-0.0340	0.00030
	ν_{16}	-0.0096	0.0000	0.0123 (0.0037)	-0.0184	-0.00006
	ν_{17}	-0.0092	0.0000	0.0318 (0.1728)	-0.0065	0.00005
	ν_{18}	0.0085	0.0000	0.0046 (0.0098)	0.0007	0.00002
e_{2u}	ν_{19}	-0.0113	0.0000	0.0007 (0.00004)	-0.0095	0.01315
	ν_{20}	0.0025	0.0000	0.0002 (0.00007)	0.0019	0.00186

TABLE 5.4: *Ab initio* calculated higher-order coupling parameters for the $\widetilde{\mathrm{X}}\ ^2\mathrm{E}_{1g}$ and $\widetilde{\mathrm{C}}\ ^2\mathrm{E}_{2g}$ electronic states of HFBz$^+$. All quantities are in eV.

	Symm.	Mode	$a_i^{(3)}$	$\lambda_i^{(3)}$	$a_i^{(4)}$	$\lambda_i^{(4)}$	$\lambda_i^{(4')}$
$\widetilde{\mathrm{X}}\ ^2\mathrm{E}_{1g}$	e_{1g}	ν_{11}	8.5481×10^{-10}	-0.00061	-0.00090	0.00033	0.00033
	e_{2u}	ν_{19}	-3.7277×10^{-10}	-0.00009	0.00040	0.00007	0.00007
$\widetilde{\mathrm{C}}\ ^2\mathrm{E}_{2g}$	e_{1u}	ν_{12}	-0.3538×10^{-10}	-0.1635×10^{-08}	-0.004368	-0.004911	-0.3991×10^{-09}
		ν_{13}	-0.1054×10^{-08}	0.001263	-0.001207	0.4934×10^{-08}	0.2667×10^{-08}
	e_{2g}	ν_{16}	-0.3806×10^{-04}	0.003438	-	-	-
		ν_{18}	-0.1010×10^{-04}	0.002581	-	-	-

TABLE 5.5: PJT coupling ($\lambda_i^{'}$) parameters (in eV) between the electronic states. Coupling strengths are given in the parenthesis.

Sym.	Mode	$\lambda_i'^{\widetilde{\mathrm{X}}\widetilde{\mathrm{A}}}$	$\lambda_i'^{\widetilde{\mathrm{X}}\widetilde{\mathrm{B}}}$	$\lambda_i'^{\widetilde{\mathrm{X}}\widetilde{\mathrm{C}}}$	$\lambda_i'^{\widetilde{\mathrm{A}}\widetilde{\mathrm{C}}}$	$\lambda_i'^{\widetilde{\mathrm{B}}\widetilde{\mathrm{C}}}$
e_{1g}	ν_{11}	-	-	0.0000	-	-
e_{1u}	ν_{12}	0.2084(0.5884)	-	-	-	0.1902(0.4901)
	ν_{13}	0.0177(0.0102)	-	-	-	0.0641(0.1345)
	ν_{14}	0.0000(0.0000)	-	-	-	0.0346(0.3997)
e_{2u}	ν_{19}	-	0.0000(0.0000)	-	0.0562(0.2756)	-
	ν_{20}	-	0.0103(0.1857)	-	0.0220(0.8473)	-

5.2 Results and Discussion

5.2.1 Topography of the potential energy curves

One dimensional cuts of the adiabatic PESs of the four lowest cationic electronic states $\widetilde{\mathrm{X}}\ ^2\mathrm{E}_{1g}$, $\widetilde{\mathrm{A}}\ ^2\mathrm{A}_{2u}$, $\widetilde{\mathrm{B}}\ ^2\mathrm{B}_{2u}$, and $\widetilde{\mathrm{C}}\ ^2\mathrm{E}_{2g}$ of the HFBz along the dimensionless normal displacement coordinates of the totally symmetric vibrational modes (a_{1g}; ν_1 and ν_2) and the x component of the JT active degenerate vibrational modes (e_{2g}; $\nu_{15} - \nu_{18}$) keeping others at their equilibrium values at, $\mathbf{Q}$=0, are shown in Figs. 5.2(a-b) and 5.3(a-d), respectively, together with the fitted polynomial functions used in our diabatic model Hamiltonian [cf., Eq. (5.5)]. It can be seen from these figures that the calculated *ab initio* points are well reproduced by the present theoretical model constructed in Sec. 5.1.2. We note that up to a second- and fourth-order Taylor expansion of the electronic Hamiltonian along the a_{1g} and e_{2g} vibrational modes are adequate to represent the *ab initio* points extremely well, respectively. The degeneracy of the $\widetilde{\mathrm{X}}\ ^2\mathrm{E}_{1g}$ and $\widetilde{\mathrm{C}}\ ^2\mathrm{E}_{2g}$ states remains unperturbed upon distortion along the a_{1g} vibrational modes [cf., Fig. 5.2]. Also, in these figures, the ground electronic state ($\widetilde{\mathrm{X}}\ ^2\mathrm{E}_{1g}$) of the cationic HFBz is energetically well separated from the $\widetilde{\mathrm{A}}\ ^2\mathrm{A}_{2u}$, $\widetilde{\mathrm{B}}\ ^2\mathrm{B}_{2u}$, and $\widetilde{\mathrm{C}}\ ^2\mathrm{E}_{2g}$ electronic states. The latter states are energetically close in energy at the distorted geometry [cf., panel (a) of Fig. 5.2]. The displacement of the minimum of all the electronic states ($\widetilde{\mathrm{X}}\ ^2\mathrm{E}_{1g}$ to $\widetilde{\mathrm{C}}\ ^2\mathrm{E}_{2g}$) is most significant along the ν_1 (C-F stretching in-phase) vibrational mode, and it is strongly condon active. Along the ν_2 vibrational mode the minimum of the electronic states is not relatively shifted as compared to the ν_1 mode. The above distortions are in accordance with the first-order coupling strength of the given vibrational modes in the given electronic state [cf., Table 5.3].

Using the fitting parameters [cf., Table 5.3] of the $\widetilde{\mathrm{X}}\ ^2\mathrm{E}_{1g}$ to $\widetilde{\mathrm{C}}\ ^2\mathrm{E}_{2g}$ electronic states along the a_{1g} vibrational modes, the stationary points of the PESs are examined here. These stationary points are calculated within a second-order coupling model and a constrained optimization using a Lagrange multiplier [157], and the results are tabulated in a matrix array in Table 5.6. The numbers in this table, both diagonal and off-diagonal represent the equilibrium minimum of a state and energetic minimum of the seam of CIs of the PESs, respectively. It can be seen from this table that the $\widetilde{\mathrm{X}}\ ^2\mathrm{E}_{1g}$ state minimum is energetically well separated from all other electronic states, and their intersection minimum is also very high in energy [cf., Table 5.6]. The energetic minimum of the latter states are close in energy (∼1 eV) and overall the intersections between the electronic states are reasonably high in energy.

In contrast to the condon active (a_{1g}) vibrational modes, the degenerate (e_{2g}) vibrational modes are JT active (in first-order) and lift the electronic degeneracy of the $\widetilde{\mathrm{X}}\ ^2\mathrm{E}_{1g}$ and

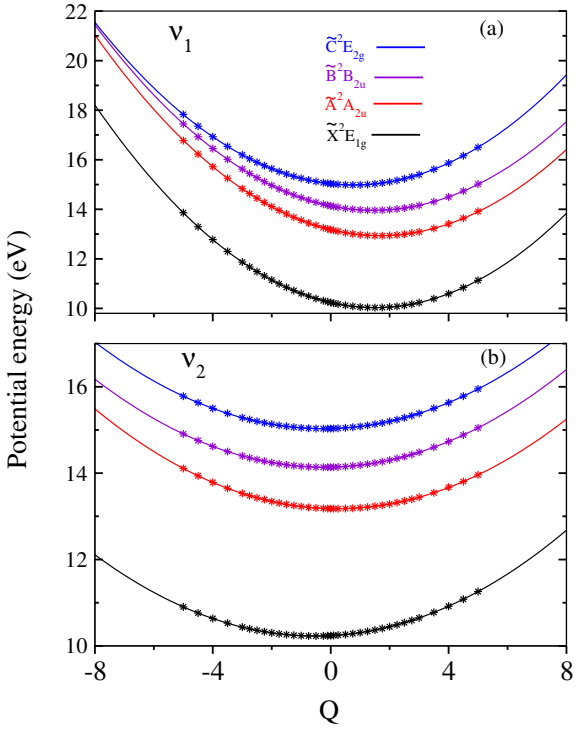

FIGURE 5.2: Adiabatic potential energy surfaces of the HFBz$^+$ along the totally symmetric modes.

TABLE 5.6: Energy (in eV) of the equilibrium minimum of the state (diagonal entries) and the minimum of its intersection seam with its neighbors (off-diagonal entries) of HFBz$^+$ calculated within a second-order coupling model.

	$\widetilde{\mathrm{X}}\ ^2\mathrm{E}_{1g}$	$\widetilde{\mathrm{A}}\ ^2\mathrm{A}_{2u}$	$\widetilde{\mathrm{B}}\ ^2\mathrm{B}_{2u}$	$\widetilde{\mathrm{C}}\ ^2\mathrm{E}_{2g}$
$\widetilde{\mathrm{X}}\ ^2\mathrm{E}_{1g}$	10.02	58.43	59.52	50.80
$\widetilde{\mathrm{A}}\ ^2\mathrm{A}_{2u}$	-	12.94	25.62	25.31
$\widetilde{\mathrm{B}}\ ^2\mathrm{B}_{2u}$	-	-	13.96	23.51
$\widetilde{\mathrm{C}}\ ^2\mathrm{E}_{2g}$	-	-	-	14.98

$\widetilde{\mathrm{C}}\ ^2\mathrm{E}_{2g}$ states of the HFBz$^+$ [cf., panels (a-d) of Fig. 5.3]. It can be seen from Fig. 5.3 that the extent of splitting of electronic degeneracy of the $\widetilde{\mathrm{X}}\ ^2\mathrm{E}_{1g}$ state is larger than the $\widetilde{\mathrm{C}}\ ^2\mathrm{E}_{2g}$ state. The extent of splitting of the degeneracy depends on the JT coupling strength ($\lambda^{(1)^2}/2\omega^2$) of the degenerate ($e_{2g}$) vibrational modes [cf., Table 5.3]. It can be seen from Table 5.3 that among the four e_{2g} vibrational modes, ν_{17} is strong, ν_{15} and ν_{18} are moderate JT coupling strengths in the $\widetilde{\mathrm{X}}\ ^2\mathrm{E}_{1g}$ state. In the $\widetilde{\mathrm{C}}\ ^2\mathrm{E}_{2g}$ electronic state, the vibrational modes of ν_{15} and ν_{17} are strong and moderate JT coupling strengths, respectively. The splitting of the JT active electronic states leads to a total of six electronic states (altogether) to be considered to treat the nuclear dynamics in the coupled $\widetilde{\mathrm{X}}\ ^2\mathrm{E}_{1g}$-$\widetilde{\mathrm{A}}\ ^2\mathrm{A}_{2u}$-$\widetilde{\mathrm{B}}\ ^2\mathrm{B}_{2u}$-$\widetilde{\mathrm{C}}\ ^2\mathrm{E}_{2g}$ electronic states of the HFBz$^+$.

It is well known that JT distortion causes symmetry breaking [14, 117]. As a result the

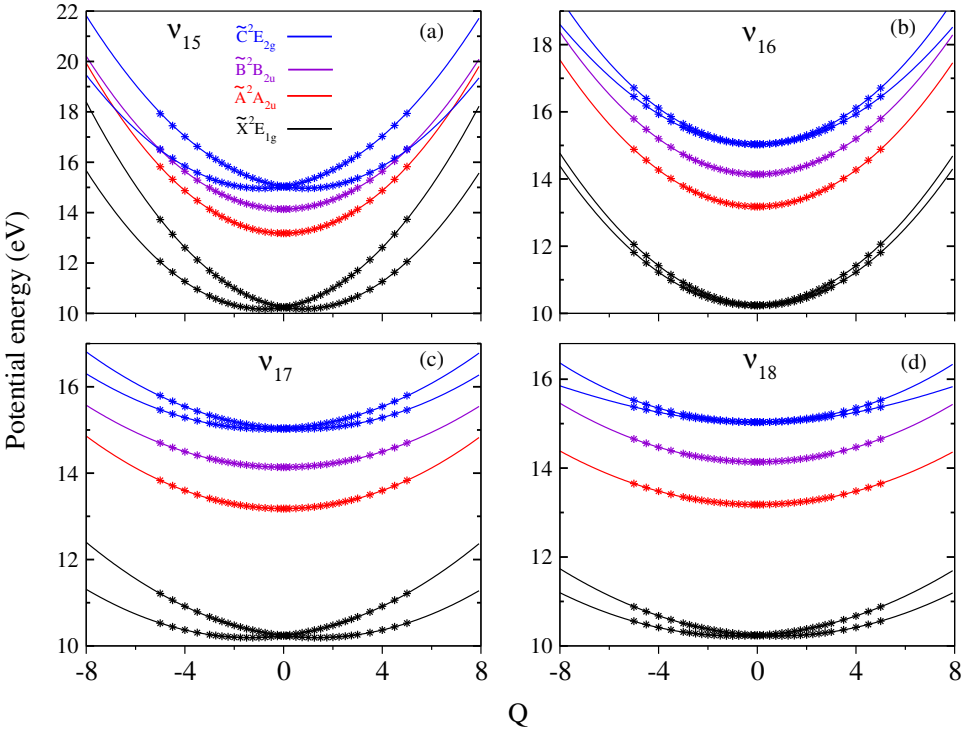

FIGURE 5.3: Adiabatic potential energy surfaces of the HFBz$^+$ along the e_{2g} vibrational modes.

lower adiabatic sheet of the JT split $\widetilde{\mathrm{X}}\ ^2\mathrm{E}_{1g}$ and $\widetilde{\mathrm{C}}\ ^2\mathrm{E}_{2g}$ electronic states develops new minima at a reduced point group symmetry. So, it is worthwhile to examine the various stationary points that appear on the JT split electronic surfaces. Using the electronic structure data and within a second-order vibronic coupling model, we calculated the energetic minimum of the JT split lower adiabatic sheets and saddle points of both $\widetilde{\mathrm{X}}\ ^2\mathrm{E}_{1g}$ and $\widetilde{\mathrm{C}}\ ^2\mathrm{E}_{2g}$ electronic states. The following equations can be derived [185, 186]

$$\mathcal{V}_{-}^{min} = E_j^0 - \frac{1}{2}\sum_{i\in a_{1g}} \frac{\left(\kappa_i^{(1)}\right)^2}{\left(\omega_i + \kappa_i^{(2)}\right)} - \frac{1}{2}\sum_{i\in e_{2g}} \frac{\left(\lambda_i^{(1)}\right)^2}{\left(\omega_i + a_i^{(2)} - |\lambda_i^{(2)}|\right)};\ j \in \widetilde{X}, \widetilde{C} \quad (5.13)$$

$$\mathcal{V}_{-}^{sp} = E_j^0 - \frac{1}{2}\sum_{i\in a_{1g}} \frac{\left(\kappa_i^{(1)}\right)^2}{\left(\omega_i + \kappa_i^{(2)}\right)} - \frac{1}{2}\sum_{i\in e_{2g}} \frac{\left(\lambda_i^{(1)}\right)^2}{\left(\omega_i + a_i^{(2)} + |\lambda_i^{(2)}|\right)};\ j \in \widetilde{X}, \widetilde{C}. \quad (5.14)$$

The minimum of the seam of CIs occurs at an energy

$$\mathcal{V}_{CI}^{min} = E_j^0 - \frac{1}{2}\sum_{i\in a_{1g}} \frac{\left(\kappa_i^{(1)}\right)^2}{\left(\omega_i + \kappa_i^{(2)}\right)};\ j \in \widetilde{X}, \widetilde{C}. \quad (5.15)$$

The JT stabilization energy is given by

$$E_{JT} = \frac{1}{2}\sum_{i\in e_{2g}} \frac{\left(\lambda_i^{(1)}\right)^2}{\left(\omega_i + a_i^{(2)} - |\lambda_i^{(2)}|\right)}. \tag{5.16}$$

The derivation of mathematical steps to arrive at the above equations are given in Appendix D. In case of the $\widetilde{\mathrm{X}}\ ^2\mathrm{E}_{1g}$ state, the energetic minimum and saddle points appear at ∼9.8908 eV and ∼9.8914 eV, respectively. On the other hand, the $\widetilde{\mathrm{C}}\ ^2\mathrm{E}_{2g}$ state energetic minimum and saddle points appear at ∼14.9052 eV and ∼14.9055 eV, respectively. These two states stationary points indicates that the barrier to pseudo rotation is low. The JT stabilization energies amounts to ∼0.13 eV and ∼0.07 eV for the $\widetilde{\mathrm{X}}\ ^2\mathrm{E}_{1g}$ and $\widetilde{\mathrm{C}}\ ^2\mathrm{E}_{2g}$ electronic states, respectively.

5.2.2 Vibronic structure in the photoelectron spectrum of HFBz

The vibronic band structure of the photoelectron spectrum of HFBz is calculated and compared with the available experimental [178] results in this section. The vibronic model Hamiltonian constructed in Sec. 5.1.2, the parameters of Tables 5.1-5.5, and both time-independent and time-dependent methods within the MCTDH framework [131] have been utilized for this purpose. In order to develop a systematic understanding of the nonadiabatic dynamics, we first construct various reduced dimensional modes and examine the vibrational energy levels of each of the considered electronic states by excluding the PJT coupling with their neighboring states. From these results, we can understand the role of various vibrational modes and electronic states in the overall vibronic band structures of the HFBz$^+$.

5.2.2.1 Vibrational energy level spectrum of the uncoupled $\widetilde{\mathrm{X}}$, $\widetilde{\mathrm{A}}$, $\widetilde{\mathrm{B}}$ and $\widetilde{\mathrm{C}}$ electronic states of HFBz$^+$

The vibrational energy level spectrum of the uncoupled $\widetilde{\mathrm{X}}\ ^2\mathrm{E}_{1g}$, $\widetilde{\mathrm{A}}\ ^2\mathrm{A}_{2u}$, $\widetilde{\mathrm{B}}\ ^2\mathrm{B}_{2u}$ and $\widetilde{\mathrm{C}}\ ^2\mathrm{E}_{2g}$ electronic states of HFBz$^+$ is calculated by time-independent matrix diagonalization approach using the Lanczos algorithm [122]. An advantage of this approach is that in addition to the spectral envelope, individual transitions (i.e., vibrational progressions) can be computed. Nevertheless, because of the dimensionality problem, this method could not be used in the complete coupled states situation.

The vibronic band structures of the uncoupled (without PJT coupling) $\widetilde{\mathrm{A}}\ ^2\mathrm{A}_{2u}$ and $\widetilde{\mathrm{B}}\ ^2\mathrm{B}_{2u}$ electronic states are shown in Fig. 5.4. The experimental [178] band structures are shown in Fig. 5.4(a and c). The stick line spectra and the convoluted envelopes are

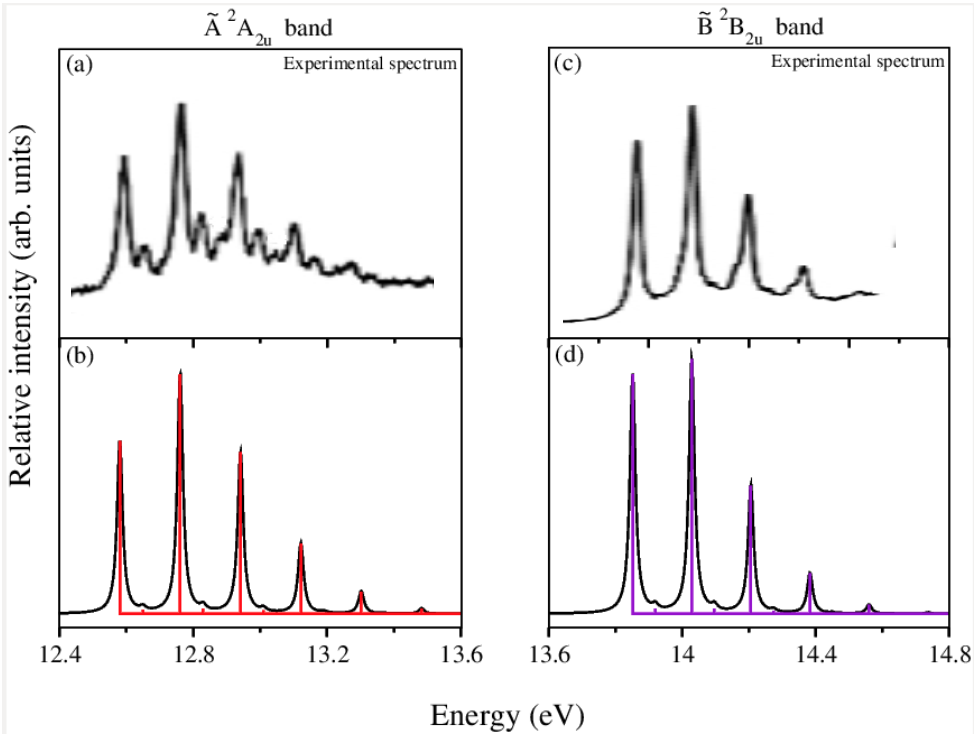

FIGURE 5.4: The $\widetilde{A}\ ^2A_{2u}$ and $\widetilde{B}\ ^2B_{2u}$ photoelectron bands of HFBz: (a) and (c) experimental spectrum [178], (b) and (d) theoretical band structures in the uncoupled states situation using the time-independent Lanczos approach.

TABLE 5.7: Vibrational energy levels (in cm^{-1}) of the $\widetilde{X}\ ^2E_{1g}$, $\widetilde{A}\ ^2A_{2u}$, $\widetilde{B}\ ^2B_{2u}$ and $\widetilde{C}\ ^2E_{2g}$ electronic states of HFBz$^+$ obtained from the uncoupled state calculations. The assignment of the levels carried out by examining the nodal pattern of the wave functions is included in the table.

$\widetilde{X}\ ^2E_{1g}$		$\widetilde{A}\ ^2A_{2u}$		$\widetilde{B}\ ^2B_{2u}$		$\widetilde{C}\ ^2E_{2g}$	
Energy	Assignment	Energy	Assignment	Energy	Assignment	Energy	Assignment
0	0_0^0	0	0_0^0	0	0_0^0	0	0_0^0
548	$\nu_{2_0}^1$	553	$\nu_{2_0}^1$	548	$\nu_{2_0}^1$	545	$\nu_{2_0}^1$
1097	$\nu_{2_0}^2$	1106	$\nu_{2_0}^2$	1095	$\nu_{2_0}^2$	1091	$\nu_{2_0}^2$
1485	$\nu_{1_0}^1$	1453	$\nu_{1_0}^1$	1428	$\nu_{1_0}^1$	1442	$\nu_{1_0}^1$
1645	$\nu_{2_0}^3$	1659	$\nu_{2_0}^3$	1643	$\nu_{2_0}^3$	1637	$\nu_{2_0}^3$
2033	$\nu_{1_0}^1+\nu_{2_0}^1$	2006	$\nu_{1_0}^1+\nu_{2_0}^1$	1976	$\nu_{1_0}^1+\nu_{2_0}^1$	1987	$\nu_{1_0}^1+\nu_{2_0}^1$
2194	$\nu_{2_0}^4$	2559	$\nu_{1_0}^1+\nu_{2_0}^2$	2523	$\nu_{1_0}^1+\nu_{2_0}^2$	2533	$\nu_{1_0}^1+\nu_{2_0}^2$
2581	$\nu_{1_0}^1+\nu_{2_0}^2$	2907	$\nu_{1_0}^2$	2856	$\nu_{1_0}^2$	2883	$\nu_{1_0}^2$
2742	$\nu_{2_0}^5$	3112	$\nu_{1_0}^1+\nu_{2_0}^3$	3071	$\nu_{1_0}^1+\nu_{2_0}^3$	3078	$\nu_{1_0}^1+\nu_{2_0}^3$
2969	$\nu_{1_0}^2$	3460	$\nu_{1_0}^2+\nu_{2_0}^1$	3404	$\nu_{1_0}^2+\nu_{2_0}^1$	3429	$\nu_{1_0}^2+\nu_{1_0}^1$
3130	$\nu_{1_0}^1+\nu_{2_0}^3$	4360	$\nu_{1_0}^3$				
3518	$\nu_{1_0}^2+\nu_{2_0}^1$						

shown in Fig. 5.4(b and d). For these the ν_1 and ν_2 a_{1g}-vibrational modes were taken into account and the maximum quantum numbers of the respective HO basis functions were 40 and 28, respectively. The resulting secular matrix is diagonalized using 10000 Lanczos iterations. The spectral envelopes were calculated by convoluting the theoretical stick lines with the Lorentzians characterized by the full width at the half maximum

(FWHM) of 0.03 eV. The same convolution procedure is used for all the later stick data presented in this chapter.

The vibronic structure of the uncoupled $\widetilde{A}\ ^2A_{2u}$ electronic state [cf., Fig. 5.4(b)] reveals that both ν_1 and ν_2 vibrational modes make progressions with peak spacings of ∼1453 and ∼553 cm^{-1}, respectively. Among these two vibrational modes, ν_1 (C-F stretching in-phase) forms the dominant progression in this state and ν_2 (ring breathing) mode is moderately excited in accord with their excitation strength [cf., Table 5.3]. Similarly, the ν_1 (∼1428 cm^{-1}) and ν_2 (∼548 cm^{-1}) modes are strongly and moderately excited, respectively, in the $\widetilde{B}\ ^2B_{2u}$ electronic state [cf., Fig. 5.4(d)]. As can be seen from Fig. 5.4 that the $\widetilde{A}\ ^2A_{2u}$ and $\widetilde{B}\ ^2B_{2u}$ bands are in good agreement with the experimental spectrum [178]. Therefore, it appears that the coupling of $\widetilde{A}\ ^2A_{2u}$ and $\widetilde{B}\ ^2B_{2u}$ states with all other states does not have any impact on their vibronic structure. We will return to this point more elaborately in the coupled state dynamics.

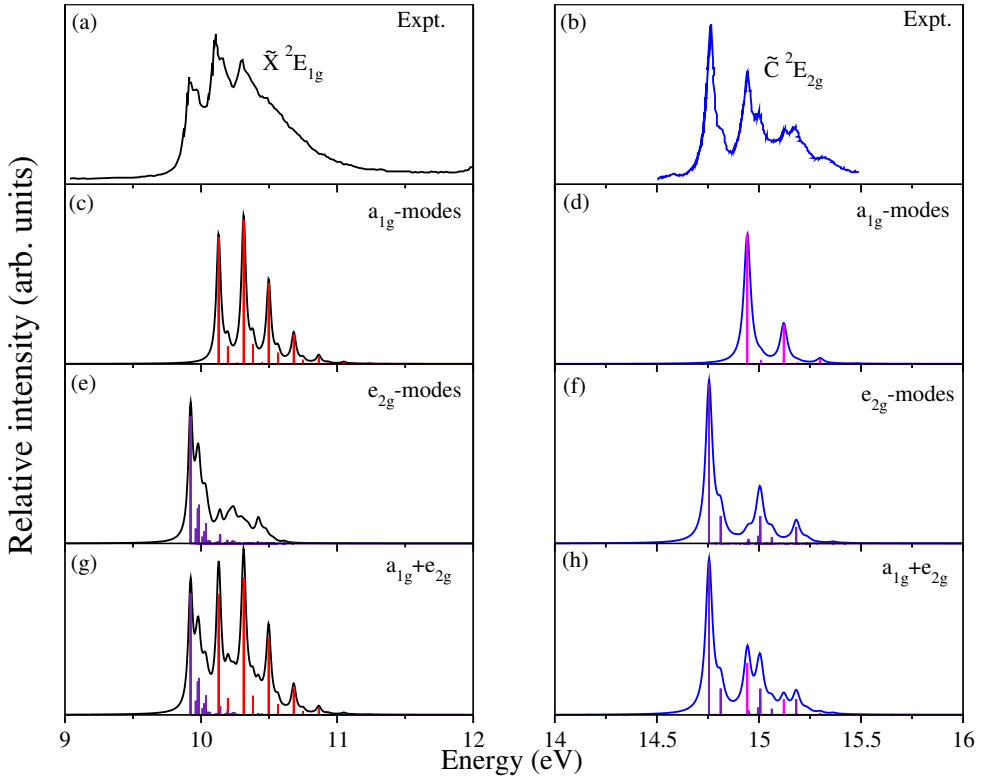

FIGURE 5.5: The $\widetilde{X}\ ^2E_{1g}$ and $\widetilde{C}\ ^2E_{2g}$ photoelectron bands of HFBz: (a) and (c) experimental spectrum [178], (b) and (d) theoretical band structures in the uncoupled states situation using the time-independent Lanczos approach.

The vibronic band structure of both $\widetilde{X}\ ^2E_{1g}$ and $\widetilde{C}\ ^2E_{2g}$ electronic states are shown in Fig. 5.5. Apart from the $\widetilde{A}\ ^2A_{2u}$ and $\widetilde{B}\ ^2B_{2u}$ electronic states, the $\widetilde{X}\ ^2E_{1g}$ and $\widetilde{C}\ ^2E_{2g}$ states are doubly degenerate. As discussed in the introduction, the electronic degeneracy will split along the doubly degenerate e_{2g} vibrational modes (i.e., JT active modes). This is

called ($E\times e$)-JT effect in the literature. The totally symmetric vibrational modes (a_{1g}) tune the PESs energy and the e_{2g} vibrational modes act as coupling coordinates between the x and y components of both $\widetilde{\mathrm{X}}\ ^2\mathrm{E}_{1g}$ and $\widetilde{\mathrm{C}}\ ^2\mathrm{E}_{2g}$ electronic states. Therefore, both a_{1g} and e_{2g} modes are considered to examine the vibronic band structures of the latter two states. We note that the Hamiltonian of these two degenerate electronic states are separable in terms of a_{1g} and e_{2g} vibrational modes, when the PJT and bilinear coupling terms are neglected. Accordingly, the partial spectrum computed with the a_{1g} [cf., Fig. 5.5(c and d)] and e_{2g} [cf., Fig. 5.5(e and f)] vibrational modes separately, and finally convoluted these two separate sets of data to generate a composite overall vibronic band structure of the $\widetilde{\mathrm{X}}\ ^2\mathrm{E}_{1g}$ and $\widetilde{\mathrm{C}}\ ^2\mathrm{E}_{2g}$ electronic states [cf., Fig. 5.5(g and h)]. The final vibronic band structure of the $\widetilde{\mathrm{X}}\ ^2\mathrm{E}_{1g}$ state shown in the panel g of Fig. 5.5 is far from the experimental [178] band structure [cf., Fig. 5.5(a)]. On the other hand, the vibronic band structure of the $\widetilde{\mathrm{C}}\ ^2\mathrm{E}_{2g}$ state [cf., Fig. 5.5(h)] is in good agreement with the experimental spectrum [178] shown in the panel (b) of Fig. 5.5. These are due to the following reasons: In case of the $\widetilde{\mathrm{X}}\ ^2\mathrm{E}_{1g}$ vibronic band, apart from the JT coupling within the degenerate electronic state, several other interstate couplings [cf., Table 5.5] are important and need to be considered to arrive at a satisfactory agreement with the experimental spectrum [178]. This can be done in the the coupled state dynamical calculations using the time-dependent WP propagation and it is discussed in more detail in the next section.

Fig. 5.5 reveals the vibrational progressions of both $\widetilde{\mathrm{X}}\ ^2\mathrm{E}_{1g}$ and $\widetilde{\mathrm{C}}\ ^2\mathrm{E}_{2g}$ electronic states. The vibronic structures of the $\widetilde{\mathrm{X}}\ ^2\mathrm{E}_{1g}$ and $\widetilde{\mathrm{C}}\ ^2\mathrm{E}_{2g}$ states [cf., Fig. 5.5(c and d)] reveal that ν_1 mode is strongly excited and the ν_2 vibrational mode is moderately excited. Peak spacings of ∼1485 and ∼548 cm^{-1} ($\widetilde{\mathrm{X}}\ ^2\mathrm{E}_{1g}$ state) and ∼1442 and ∼545 cm^{-1} ($\widetilde{\mathrm{C}}\ ^2\mathrm{E}_{2g}$ state) correspond to these vibrational modes in that order estimated from the spectrum. The symmetric vibrational modes excited in the $\widetilde{\mathrm{X}}\ ^2\mathrm{E}_{1g}$ to $\widetilde{\mathrm{C}}\ ^2\mathrm{E}_{2g}$ electronic states are assigned and given in Table 5.7. The spectrum of the $\widetilde{\mathrm{X}}\ ^2\mathrm{E}_{1g}$ and $\widetilde{\mathrm{C}}\ ^2\mathrm{E}_{2g}$ states obtained with JT active e_{2g} (degenerate) vibrational modes shown in the Fig. 5.5(e and f) reveals progressions of ν_{15}, ν_{16}, ν_{17} and ν_{18} vibrational modes. Peak spacings of ∼2033, ∼1152, ∼508, and ∼360 cm^{-1} ($\widetilde{\mathrm{X}}\ ^2\mathrm{E}_{1g}$) and ∼2026, ∼1068, ∼458, and ∼267 cm^{-1} ($\widetilde{\mathrm{C}}\ ^2\mathrm{E}_{2g}$), respectively. Based on the JT coupling strength [cf., Table 5.3], among the four degenerate vibrational modes, ν_{17} and ν_{18}, ν_{15} modes is strongly and moderately excited, and ν_{16} mode is weakly excited in the $\widetilde{\mathrm{X}}\ ^2\mathrm{E}_{1g}$ band [cf., Fig. 5.5(e)]. Due to strong JT coupling in this state, a huge increase in line density occurs along these vibrational modes. In the case of the $\widetilde{\mathrm{C}}\ ^2\mathrm{E}_{2g}$ vibronic band, ν_{15} and ν_{17} vibrational modes are excited strongly and moderately, respectively, and ν_{16} and ν_{18} modes are weakly excited.

5.2.2.2 Vibronic spectrum of coupled $\widetilde{X}$-$\widetilde{A}$-$\widetilde{B}$-$\widetilde{C}$ electronic states

In this section, the complete vibronic band structure of the coupled $\widetilde{X}\ ^2E_{1g}$-$\widetilde{A}\ ^2A_{2u}$-$\widetilde{B}\ ^2B_{2u}$-$\widetilde{C}\ ^2E_{2g}$ electronic states calculated by including 20 ($2a_{1g}$+$3e_{1u}$+$4e_{2g}$+$2e_{2u}$) relevant vibrational modes shown in Fig. 5.6. A large increase in DOF leads to a huge increase of the dimension of the vibronic secular matrix and it is beyond the capability of the matrix diagonalization method employed for the uncoupled states. Therefore, we resort to the time-dependent WP propagation calculations with the help of Heidelberg MCTDH program modules [119, 127, 128, 131]. Six WP calculations are carried out by launching the initial WP on each of the six (x and y components of the JT spit $\widetilde{X}\ ^2E_{1g}$ and $\widetilde{C}\ ^2E_{2g}$ states plus nondegenerate $\widetilde{A}\ ^2A_{2u}$ and $\widetilde{B}\ ^2B_{2u}$ states) electronic states separately. The details of the mode combination and the sizes of the basis sets are given in Table 5.8. In each calculation, the WP is propagated for 200 fs. The time autocorrelation function is damped with an exponential function of relaxation time 30 fs for all electronic states, and then Fourier transformed to generate the spectrum. The results are combined with equal weightage to obtain the composite theoretical spectrum shown in Fig. 5.6(b). The available experimental results of Mothch *et al.* [178] are also shown in Fig. 5.6(a) for comparison. It can be seen from this figure that the present theoretical results are in good accord with the experimental spectrum.

TABLE 5.8: Normal mode combinations, sizes of the primitive and single particle bases used in the MCTDH calculations. [a] The primitive basis consists of harmonic oscillator DVR functions, in the dimensionless normal coordinate required to represent the system dynamics along the relevant mode. The primitive basis for each particle is the product of the one-dimensional bases; [b] The SPF basis is the number of the single particle functions used.

Electronic state	Normal modes	Primitive basis[a]	SPF basis[b]	
$\widetilde{X}\ ^2E_{1g}$-$\widetilde{A}\ ^2A_{2u}$-$\widetilde{B}\ ^2B_{2u}$-$\widetilde{C}\ ^2E_{2g}$	ν_1, ν_{12x}, ν_{12y}, ν_{15x}, ν_{15y}	(16,6,6,12,12)	[10,10,8,8,10,10]	Fig. 5.6(b)
	ν_{13x}, ν_{13y}, ν_{16x}, ν_{16y}	(6,6,6,6)	[8,8,6,6,8,8]	
	ν_2, ν_{17x}, ν_{17y}, ν_{19x}, ν_{19y}	(8,14,14,6,6)	[10,10,8,8,10,10]	
	ν_{14x},ν_{14y},ν_{18x},ν_{18y}, ν_{20x}, ν_{20y}	(6,6,12,12,6,6)	[8,8,6,6,8,8]	

5.2.3 Population dynamics of coupled $\widetilde{X}$-$\widetilde{A}$-$\widetilde{B}$-$\widetilde{C}$ electronic states of HFBz$^+$

The time-dependence of the diabatic electronic population of coupled $\widetilde{X}\ ^2E_{1g}$-$\widetilde{A}\ ^2A_{2u}$-$\widetilde{B}\ ^2B_{2u}$-$\widetilde{C}\ ^2E_{2g}$ states of HFBz radical cation shown in Fig. 5.7 and discussed in this section. Figs. 5.7(a)-5.7(d) show how the population of the $\widetilde{X}\ ^2E_{1g}$, $\widetilde{A}\ ^2A_{2u}$, $\widetilde{B}\ ^2B_{2u}$, and $\widetilde{C}\ ^2E_{2g}$ electronic states of HFBz$^+$ changes in time after the vertical ionization of HFBz to one of these states. In Fig. 5.7(a), the population dynamics shown for an initial transition of the WP to one of the JT split components of the $\widetilde{X}\ ^2E_{1g}$ electronic state. As expected, the electronic population moves back and forth between its two components driven solely by the JT CIs and exhibits an exact mirror image behavior,

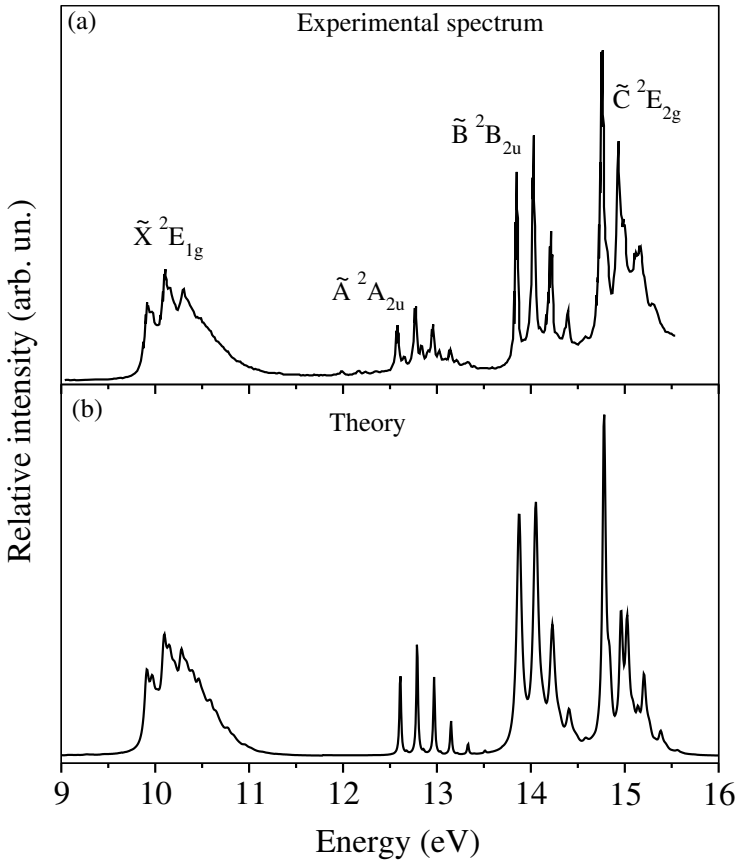

FIGURE 5.6: Vibronic spectrum of the coupled $\widetilde{X}\ ^2E_{1g}$-$\widetilde{A}\ ^2A_{2u}$-$\widetilde{B}\ ^2B_{2u}$-$\widetilde{C}\ ^2E_{2g}$ electronic states of HFBz$^+$. Relative intensity is plotted as a function of the energy of the vibronic states of HFBz$^+$. The experimental spectrum is reproduced from Ref. [178] is shown in panel (a). The present theoretical vibronic spectrum is shown in panel (b).

whereas the higher-lying population of the three higher-lying states are equal to zero [cf., Fig. 5.7(a)]. This is because the $\widetilde{X}\ ^2E_{1g}$ (ground electronic) state of the HFBz$^+$ is energetically well separated from the higher-lying states.

In case of the initial transition to the $\widetilde{A}\ ^2A_{2u}$ state, Fig. 5.7(b) shows that, practically, there is no population flow to all other states. This is due to the fact that the $\widetilde{A}\ ^2A_{2u}$ state is vertically well separated from all other states, and the CIs of the $\widetilde{A}\ ^2A_{2u}$ state with all other states are located at very high energies and are not accessible to the WP during its evolution in this state. This results in the observed sharp vibrational energy level structure of the $\widetilde{A}\ ^2A_{2u}$ band [cf., Fig. 5.6]. This implies a long-lived nature of the $\widetilde{A}\ ^2A_{2u}$ state and gives rise to the observed emission of the HFBz$^+$. We will come to this point again later in the text.

The population curve for an initial location of the WP on the $\widetilde{B}\ ^2B_{2u}$ state is shown in Fig. 5.7(c). It can be seen that a minimal amount ($\sim$2%) of the population is transferred

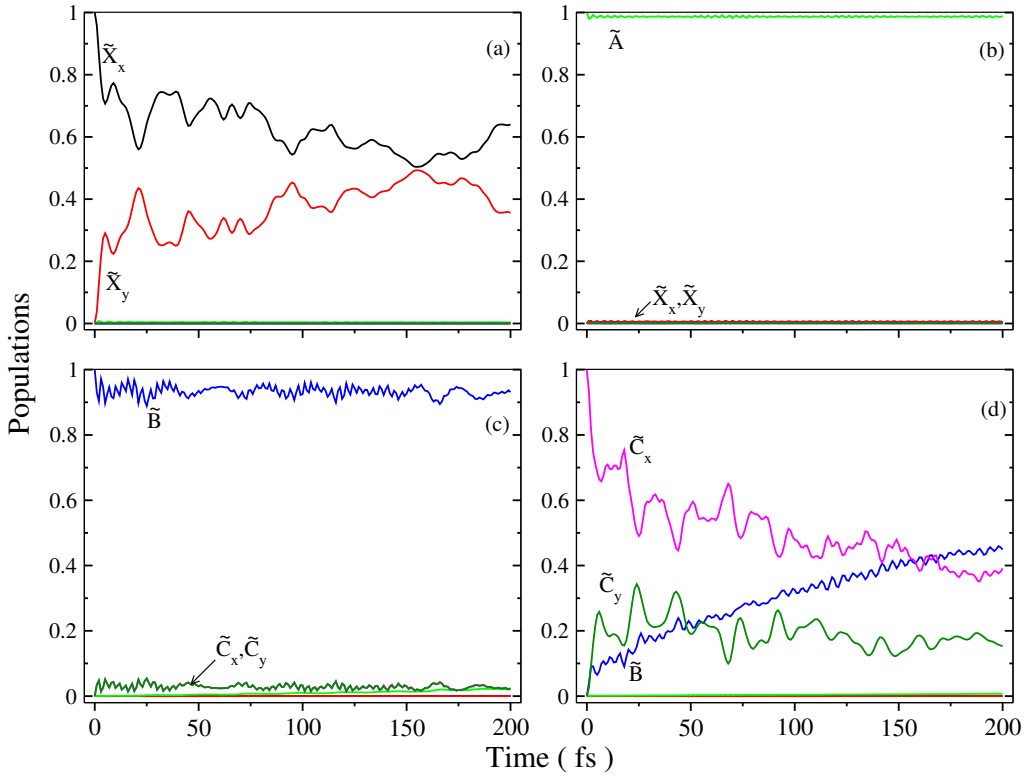

FIGURE 5.7: Time-dependence of diabatic electronic populations during the evolution of the coupled $\widetilde{X}\ ^2E_{1g}$-$\widetilde{A}\ ^2A_{2u}$-$\widetilde{B}\ ^2B_{2u}$-$\widetilde{C}\ ^2E_{2g}$ electronic states of HFBz$^+$. The population curves for the initial location of the WP on the x-component of the $\widetilde{X}\ ^2E_{1g}$ state is shown in panel (a), $\widetilde{A}\ ^2A_{2u}$ and $\widetilde{B}\ ^2B_{2u}$ states are in panels (b) and (c), the x-component of the $\widetilde{C}\ ^2E_{2g}$ state is shown in panel (d).

to the two components of the $\widetilde{C}\ ^2E_{2g}$ state only. This is because of the coupling between the $\widetilde{B}\ ^2B_{2u}$ and $\widetilde{C}\ ^2E_{2g}$ states [cf., Table 5.5], and the CIs of the $\widetilde{B}\ ^2B_{2u}$ state with all other states are located at very high energies and are not accessible to the WP during its evolution on this state. From this, we can say that similar to the $\widetilde{A}\ ^2A_{2u}$ state, $\widetilde{B}\ ^2B_{2u}$ state also may contribute to the radiative emission of the HFBz$^+$.

Fig. 5.7(d) portrays electronic population dynamics when the WP is initially prepared on the x component of the $\widetilde{C}\ ^2E_{2g}$ state. In contrast to the JT effect, the decay and growth of the population of the x and y components degenerate $\widetilde{C}\ ^2E_{2g}$ electronic state can be seen, and the population transfer to the counter (y) component is minor in the JT case. This is due to the weak JT coupling found in the $\widetilde{C}\ ^2E_{2g}$ state as compared to the $\widetilde{X}\ ^2E_{1g}$ state [cf., Table 5.5]. The PJT coupling between the $\widetilde{B}\ ^2B_{2u}$ and $\widetilde{C}\ ^2E_{2g}$ states is strong along the vibrational modes of e_{1u} symmetry (especially ν_{12} and ν_{14} vibrational modes) [cf., Table 5.5]. Hence, the population transfer to $\widetilde{B}\ ^2B_{2u}$ state is expected in this case [cf., Fig. 5.7(d)].

5.2.4 Radiative emission

As discussed in Sec. 4.0.4.5 of Chapter 4, the fluorescence emission was observed for at least three-fold fluorination of Bz^+ [43, 44]. The exception is *m*-DFBz$^+$ which emits weakly [39]. Köppel and coworkers examined the details theoretically and connected the experimental findings with the details of vibronic coupling mechanism of the underlying PESs [47–51, 143]. It was found that in Bz^+, the JT split components of the $\widetilde{X}$ and $\widetilde{B}$ states form CIs at low energies, promoting the nonradiative decay [47, 143]. In MFBz$^+$ and DFBz$^+$, the interaction between the $\widetilde{X}$-$\widetilde{A}$ and $\widetilde{B}$-$\widetilde{C}$-$\widetilde{D}$ group of electronic states gives rise to low energy CIs (except in the *m*-DFBz$^+$) and facilities the nonradiative internal conversion [49–51]. In DFBz$^+$, the two groups of states are connected through $\widetilde{A}$-$\widetilde{C}$ coupling in the orth- and meta-isomers and $\widetilde{A}$-$\widetilde{B}$ coupling in the para-isomer. The minimum energy of the corresponding crossing seams occurs at ∼0.54 and ∼0.57 eV in the ortho- and para-isomers, respectively. The minimum energy crossing seam of the meta-isomer is higher in energy than the former isomers and gives rise to weak radiative emission [39].

In case of 1,3,5 TFBz$^+$, the degenerate ground $\widetilde{X}\ ^2E''$ and excited $\widetilde{B}\ ^2E'$ electronic states are energetically well separated, and the intersections of these states with $\widetilde{A}\ ^2A''$ state occurring in between of $\widetilde{X}$ and $\widetilde{B}$ states [55]. These intersection minimums are higher in energies relative to the minimum of $\widetilde{A}\ ^2A''$ state, and the PJT coupling between these states is also weak. Therefore, hardly any WP population relaxes nonradiative to the $\widetilde{X}$ and $\widetilde{A}$ states when the WP is initially prepared on the higher excited states. Also, the $\widetilde{A}$ states electronic population dynamics are not affected by its coupling with the other states. So, when the WP is initially prepared on the $\widetilde{A}$ state, the population remains at ∼100% for a long time and gives rise to radiative emission in 1,3,5 TFBz$^+$.

In the case of PFBz$^+$, the $\widetilde{B}$ state is ∼2.25 eV above the $\widetilde{A}$ state and ∼1.0 eV below the $\widetilde{C}$ state [57]. That is, $\widetilde{B}$ state is well separated from all other states. Because of the large energy separation, the coupling effect of $\widetilde{B}$ state with all other states does not (or weak) impact the population dynamics of the $\widetilde{B}$ state. The electronic population does not flow to other states when the WP is initially prepared on the $\widetilde{B}$ state. This indicates a long-lived nature of the $\widetilde{B}$ state, which gives rise to the radiative emission in the PFBz$^+$.

In continuation with 1,3,5 TFBz$^+$ and PFBz$^+$, in the case HFBz$^+$ is sketched here by examining the results presented in Sec. 5.2.3. The data presented in Sec. 5.2.3 and Tables 5.2-5.6 revels that all the electronic states ($\widetilde{X}\ ^2E_{1g}$ to $\widetilde{C}\ ^2E_{2g}$) are well separated at the Franck-Condon geometry. Their intersection minimums are higher in energy as compared to the respective states minimum [cf., Table 5.6]. However, the inter-state

couplings between them influence the $\widetilde{\mathrm{X}}\ ^2\mathrm{E}_{1g}$ and $\widetilde{\mathrm{C}}\ ^2\mathrm{E}_{2g}$ electronic states dynamics only. On the other hand, in the case of $\widetilde{\mathrm{A}}\ ^2\mathrm{A}_{2u}$ and $\widetilde{\mathrm{B}}\ ^2\mathrm{B}_{2u}$ states, these couplings do not influence when the initial WP is prepared on these states [cf., Fig. 5.7(b and c)]. That is, the electronic population of the $\widetilde{\mathrm{A}}\ ^2\mathrm{A}_{2u}$ and $\widetilde{\mathrm{B}}\ ^2\mathrm{B}_{2u}$ states remains at ∼100% and ∼90% when the initial WP is prepared on these states, respectively. This indicates a long-lived nature of the $\widetilde{\mathrm{A}}\ ^2\mathrm{A}_{2u}$ and $\widetilde{\mathrm{B}}\ ^2\mathrm{B}_{2u}$ states, which gives rise to the fluorescence emission in the HFBz$^+$.

5.3 Summary and conclusions

A detailed theoretical account of multi-mode JT and PJT interactions in the ground and the three lowest excited states of HFBz$^+$, $\widetilde{\mathrm{X}}\ ^2\mathrm{E}_{1g}$, $\widetilde{\mathrm{A}}\ ^2\mathrm{A}_{2u}$, $\widetilde{\mathrm{B}}\ ^2\mathrm{B}_{2u}$ and $\widetilde{\mathrm{C}}\ ^2\mathrm{E}_{2g}$ were examined in this chapter. The four-state vibronic problem was treated within the framework of the model Hamiltonian in the diabatic electronic basis, and the coupling constants were derived from the *ab initio* quantum chemistry electronic structure calculations. The PESs (or ionization energies) and all the Hamiltonian coupling parameters were obtained using the EOMIP-CCSD method with aug-cc-pVDZ basis set at various nuclear configurations in terms of dimensionless normal displacement coordinates. These all are obtained from the ground-state electronic structure calculations for neutral HFBz using the MP2/aug-cc-pVDZ level of theory. It is found that all the electronic states are energetically well separated from each other at the Franck-Condon geometry. However, the couplings between them are well enough, and the curve crossing between the $\widetilde{\mathrm{B}}\ ^2\mathrm{B}_{2u}$ and $\widetilde{\mathrm{C}}\ ^2\mathrm{E}_{2g}$ states along the ν_{15} vibrational mode of the HFBz$^+$ is found.

In order to better understand the JT and PJT couplings, two sets of dynamical calculations were performed. In the first case, the individual vibronic band structures are analyzed using the time-independent matrix diagonalization method. It is observed that the JT effect due to e_{2g} vibrational modes in the $\widetilde{\mathrm{X}}\ ^2\mathrm{E}_{1g}$ state is more substantial as compared to the $\widetilde{\mathrm{C}}\ ^2\mathrm{E}_{2g}$ electronic state. In the four vibrational band structures, both a_{1g} and e_{2g} vibrational modes are excited according to their excitation strength. In the second case, the full four-state vibronic problem was treated with a time-dependent WP propagation method accounting for 20 ($2a_{1g}$+$3e_{1u}$+$4e_{2g}$+$2e_{2u}$) relevant vibrational DOF of HFBz. For these two sets of dynamical calculations, the MCTDH program module is used. The final theoretical results so obtained are in good accord with the available experimental results.

It is found that both $\widetilde{\mathrm{A}}\ ^2\mathrm{A}_{2u}$ and $\widetilde{\mathrm{B}}\ ^2\mathrm{B}_{2u}$ electronic states are well separated from the rest of the states. Therefore, the PJT coupling of these two states with others have no effect on the vibronic structures of $\widetilde{\mathrm{A}}\ ^2\mathrm{A}_{2u}$ and $\widetilde{\mathrm{B}}\ ^2\mathrm{B}_{2u}$ states. The time-dependence

of the diabatic electronic population reveals that the population of the $\widetilde{\mathrm{A}}\ ^2\mathrm{A}_{2u}$ state remains ∼100% for a long time when the dynamics started on it. Similarly, when the WP is located on the $\widetilde{\mathrm{B}}\ ^2\mathrm{B}_{2u}$ state a minimal amount (∼2%) of population is transferred to the two components of the $\widetilde{\mathrm{C}}\ ^2\mathrm{E}_{2g}$ state only. This leads to the long-lived nature of the $\widetilde{\mathrm{A}}\ ^2\mathrm{A}_{2u}$ and $\widetilde{\mathrm{B}}\ ^2\mathrm{B}_{2u}$ electronic states, and these two states contribute to the observed fluorescence emission in HFBz^+.

Chapter 6

Impact of Jahn-Teller and pseudo Jahn-Teller effect in Propyne radical cation

A detailed theoretical account on multi-mode Jahn-Teller (JT) and pseudo-Jahn-Teller (PJT) interactions in the first three low-lying doublet electronic states of Propyne radical cation is presented in this chapter. Allene (H_2CCCH_2, propadiene), propyne (H_3CCCH, methyl acetylene) and cyclopropene are the three stable isomers of C_3H_4. The former two isomers are important intermediates in combustion and astrochemistry [70–74]. They are members of the cumulene series with odd number of carbon atoms. The radical cation of these isomers possesses degenerate electronic states and vibrational modes. Therefore, they provide a unique platform to investigate multi-mode JT and PJT effects in their ionic states. While the equilibrium configuration of allene belongs to less common D_{2d} symmetry point group, that of propyne belongs to the more common C_{3v} symmetry point group. The non-degenerate vibrational modes of b_1 and b_2 symmetry are JT active in the degenerate ionic states of allene. On the other hand, the degenerate vibrational modes of e symmetry causes PJT coupling among the degenerate and non-degenerate ionic states of allene. Multi-mode JT and PJT interactions in the ionic states of allene have been extensively studied theoretically [78–85] and also probed experimentally through photoelectron spectroscopy measurements [86–91]. To the best of our knowledge, it is the first example treated with a higher-order vibronic coupling model in the literature [83]. The PJT coupling in its $\widetilde{\mathrm{A}}\ ^2\mathrm{E}$-$\widetilde{B}^2B_2$ electronic manifold was found to be extremely strong which leads to a broad and diffuse vibronic band structure at higher energies.

As stated above, the JT and PJT effects in the ionic states of propyne are not rigorously studied in the literature. It would therefore be interesting to study how these effects in

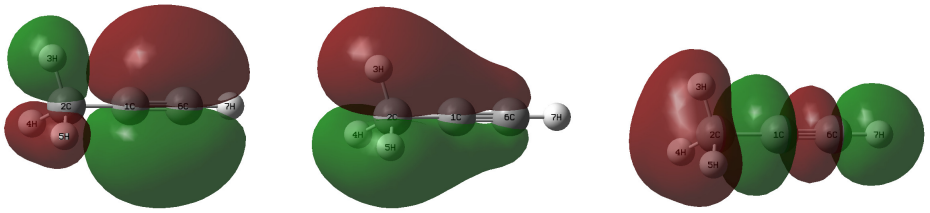

(a) HOMO (b) HOMO-1 (c) HOMO-2

FIGURE 6.1: The schematic diagram of the valence canonical molecular orbitals of the H_3CCCH molecule.

propyne radical cation differ as compared to those in allene radical cation since they are isomeric in nature and have different JT and PJT coupling mechanisms. The first two valence molecular orbitals (MO) of propyne belong to e symmetry and posses π character [cf., Fig. 6.1(a and b)]. The third valence MO is of σ type and is of a_1 symmetry [cf., Fig. 6.1(c)]. Ionization of an electron from these orbitals creates propyne radical cation ($H_3CCCH^{\cdot+}$) in its electronic ground ($\widetilde{X}\ ^2E$) and first two excited ($\widetilde{A}\ ^2E$ and $\widetilde{B}\ ^2A_1$) electronic states, respectively.

The vibronic structure of the electronic states of $H_3CCCH^{\cdot+}$ was probed in photoelectron spectroscopy experiments [187–196]. The He I and threshold photoelectron spectra [187–189] revealed that the vibrational structure of the $\widetilde{X}\ ^2E$ state consists of a strong origin band and weak progressions of C≡C and C-C stretching modes. This observation indicates that the equilibrium structure of the cationic ground state is similar to that of the neutral ground state and the JT effect is weak in the $\widetilde{X}\ ^2E$ state. The photoelectron spectrum of H_3CCCH has been recorded by Baker and Turner [187] using Helium 584 Å line. Among the first two bands in the ∼10-17 eV energy range, the second one revealed highly overlapping vibronic structure. The first photoelectron band has a simple vibronic structure and appears at ∼10.3 eV. The maxima of the second band appears at ∼14.6 and ∼15.3 eV. This band is of particular interest as it apparently bears the signature of strong JT and PJT interactions in the excited electronic manifold of $H_3CCCH^{\cdot+}$. Matsui *et al.* [193] recorded the photoelectron spectrum of H_3CCCH at higher energy resolution in a non-resonant two-photon pulsed-field ionization (PFI) Zero-Kinetic-Energy (ZEKE) measurement. They resolved spin-orbit (SO) structure in the rotational profile of the origin band of the $\widetilde{X}\ ^2E$ state.

Shieh *et al.* [191] recorded the spectrum of propyne using 2+1 resonance enhanced multi-photon ionization technique and obtained information on several Rydberg series of propyne. By extrapolating these series, they concluded that the SO splitting of the ground vibronic state of $H_3CCCH^{\cdot+}$ is less compared to that of acetylene cation (∼30.91 cm^{-1} [197]). Xing *et al.* [192] also recorded rotationally resolved spectra for $H_3CCCH^{\cdot+}$ ($\widetilde{X}\ ^2E_{3/2,1/2}$, ν_1^+=1) and estimated SO coupling ∼ -13.0±0.2 cm^{-1}, similar in magnitude

to the value determined by Shieh *et al.* [191]. This is ∼60% smaller than that of acetylene cation implying a quenching of SO coupling by strong JT effect in the $\widetilde{X}\ ^2E$ state of $H_3CCCH^{\cdot+}$ and contradicts the observation made by Matsui *et al.* [193].

In order to resolve the ambiguity of the results of Refs. [191–193], Marquez *et al.* [194] performed high level *ab initio* quantum chemistry calculations including the vibronic and SO couplings. They found that the pure electronic SO coupling of the $\widetilde{X}\ ^2E$ state of $H_3CCCH^{\cdot+}$ is ∼-28 cm^{-1}, without including the JT interaction. This coupling is ∼18 cm^{-1} when the JT interaction was included. If the sign is ignored, this result is in qualitative agreement with the results of Shieh *et al.* [191] and Xing *et al.* [192]. More recently, Jacovella *et al.* [196] recorded the single photon PFI-ZEKE photoelectron spectrum of H_3CCCH at a resolution of ∼0.8 cm^{-1} and reported partially resolved rotational structure of the origin band of the $\widetilde{X}\ ^2E$ state of $H_3CCCH^{\cdot+}$. Despite several experimental studies, a detailed theoretical study of multi-mode JT and PJT interactions in the electronic states of $H_3CCCH^{\cdot+}$ is missing in the literature. Theoretical calculations on the electronic structure and vertical ionization energies (VIEs) of H_3CCCH are reported [194, 198].

In this chapter we therefore set out to carry out a detailed investigation of multi-mode JT and PJT effects in the first three electronic states of $H_3CCCH^{\cdot+}$. Among the three low-lying electronic states, the first two electronic states are doubly degenerate, which are prone to the JT distortion [75]. The next higher electronic state is nondegenerate. The fifteen normal vibrational modes of propyne belong to the following irreducible representations of the C_{3v} symmetry point group

$$\Gamma_{vib} = 5a_1 + 5e. \tag{6.1}$$

The direct product of E electronic representation and the direct product of E with A_1 electronic representation in the C_{3v} point group yields

$$E \otimes E = a_1 + a_2 + e. \tag{6.2}$$

$$E \otimes A_1 = e. \tag{6.3}$$

We mention here that the symmetry of the electronic states and the vibrational modes are denoted by the upper and lower case letters, respectively, throughout this chapter. In case of $E\times e$-Jahn-Teller problem the equivalency of the matrix elements in the detailed selection rule reduces Eq. 6.2 to, $(E)^2 = a_1 + e$, the so-called symmetrized direct product [199]. The elementary symmetry selection rules [cf., Eqs. 6.2 and 6.3] suggest that the

degenerate $\widetilde{\mathrm{X}}\ ^2\mathrm{E}$ and $\widetilde{\mathrm{A}}\ ^2\mathrm{E}$ electronic states of $H_3CCCH^{\cdot+}$ would undergo JT splitting in first-order when distorted along the degenerate vibrational modes of e symmetry [$(E \otimes e)$-JT effect]. The JT split components of the two E states may also undergo PJT coupling through the vibrational modes of e symmetry. However, the $\widetilde{\mathrm{X}}\ ^2\mathrm{E}$ and $\widetilde{\mathrm{A}}\ ^2\mathrm{E}$ states of $H_3CCCH^{\cdot+}$ are energetically well separated and PJT coupling between them is not significant. The non-degenerate $\widetilde{\mathrm{B}}\ ^2\mathrm{A}_1$ state undergoes PJT coupling with the components of $\widetilde{\mathrm{A}}\ ^2\mathrm{E}$ state through vibrational modes of e symmetry [$(E + A) \otimes e$-PJT effect] and these states are energetically close. The PJT coupling of these states is expected to yield multiple conical intersections and consequently the nuclear motion may become predominantly nonadiabatic. The totally symmetric a_1 vibrational modes are Condon active in all three electronic states.

In the following a model Hamiltonian is constructed in a diabatic electronic basis and using the standard vibronic coupling theory [14]. The elements of the electronic Hamiltonian are expanded in a Taylor series and the parameters are derived from the adiabatic electronic energies calculated *ab initio*, by both CASSCF-MRCI [161–164] and EOMIP-CCSD [165, 166] methods. The quantum dynamical observables are calculated by solving the time-independent as well as time-dependent Schrödinger equations. In the time-independent case, Lanczos algorithm [122] is used to diagonalize the Hamiltonian matrix expressed in the basis of harmonic oscillator (HO) functions. This enables to determine the precise location of the vibronic energy levels and aids in their assignments. This method is computationally not affordable for systems with large number of electronic and vibrational degrees of freedom (DOF). To calculate the broad band spectra, the time-dependent calculations are carried out by propagating wave packets (WPs) with the aid of the multi-configuration time-dependent Hartree (MCTDH) method developed at Heidelberg [119, 127, 128, 131]. The results are compared with the experimental findings and discussed.

6.1 Theoretical framework

6.1.1 The Vibronic Hamiltonian

The photoionization to the first three low-lying $\widetilde{\mathrm{X}}\ ^2\mathrm{E}$, $\widetilde{\mathrm{A}}\ ^2\mathrm{E}$ and $\widetilde{\mathrm{B}}\ ^2\mathrm{A}_1$ electronic states (here after will be designated as $\widetilde{\mathrm{X}}$, $\widetilde{\mathrm{A}}$ and $\widetilde{\mathrm{B}}$) of $H_3CCCH^{\cdot+}$ is examined theoretically. As stated in the introduction, each of the two degenerate electronic states undergo JT splitting when $H_3CCCH^{\cdot+}$ is distorted along the degenerate vibrational modes of e symmetry. The symmetry selection rule [cf., Eqs. 6.2 and 6.3] allows the JT split component states to undergo PJT coupling among themselves or with the nondegenerate electronic state. The PJT coupling of the $\widetilde{\mathrm{X}}$ state with the $\widetilde{\mathrm{A}}$ and $\widetilde{\mathrm{B}}$ states is excluded on

the energetic ground (we discussed more about this point in Sec. 6.2.2). There are five totally symmetric a_1 vibrational modes that are Condon active in all three electronic states. In the following, we first resort to a diabatic electronic basis [100, 101, 200] to treat this vibronic coupling problem. This is to avoid the numerical difficulties [14] that arise due to the singular nature of the nonadiabatic coupling terms in an adiabatic electronic basis [13, 14]. The diabatic vibronic Hamiltonian is constructed in terms of the dimensionless normal coordinates of the vibrational modes of the electronic ground state of the neutral H_3CCCH. To a good approximation the vibrational motion in the latter state is treated as harmonic. In the following, we refer to Q_i as the dimensionless normal coordinate of the vibrational mode ν_i with a harmonic vibrational frequency ω_i. Actually, each Q_i represents the normal displacement coordinate from the equilibrium configuration of the electronic ground state of H_3CCCH occurring at $\mathbf{Q} = 0$. In the rest of the chapter the totally symmetric (a_1) vibrational modes are designated as ν_1, ν_2, ν_3, ν_4 and ν_5 and the degenerate (e) vibrational modes as ν_6, ν_7, ν_8, ν_9 and ν_{10} in the order of decreasing frequency. With this description the diabatic vibronic Hamiltonian [14] of the $\widetilde{X}$-$\widetilde{A}$-$\widetilde{B}$ coupled electronic states of $H_3CCCH^{\cdot+}$ can be written as

$$\mathcal{H} = \mathcal{H}_0 \mathbf{1_5} + \Delta\mathcal{H}. \tag{6.4}$$

In the above equation, $\mathcal{H}_0$ $(= \mathcal{T}_N + \mathcal{V}_0)$ is the unperturbed Hamiltonian of the reference ground electronic state of H_3CCCH. Within the harmonic approximation its elements are given by

$$\mathcal{T}_N = -\frac{1}{2}\sum_{i\in a_1}\omega_i\frac{\partial^2}{\partial Q_i^2} - \frac{1}{2}\sum_{i\in e}\omega_i\left(\frac{\partial^2}{\partial Q_{ix}^2} + \frac{\partial^2}{\partial Q_{iy}^2}\right), \tag{6.5}$$

$$\mathcal{V}_0 = \frac{1}{2}\sum_{i\in a_1}\omega_i Q_i^2 + \frac{1}{2}\sum_{i\in e}\omega_i\left(Q_{ix}^2 + Q_{iy}^2\right), \tag{6.6}$$

and

$$\Delta\mathcal{H} = \begin{pmatrix} u^x_{\widetilde{X}} & u^{xy}_{\widetilde{X}} & 0 & 0 & 0 \\ & u^y_{\widetilde{X}} & 0 & 0 & 0 \\ & & u^x_{\widetilde{A}} & u^{xy}_{\widetilde{A}} & u^x_{\widetilde{A}\widetilde{B}} \\ & h.c. & & u^y_{\widetilde{A}} & -u^y_{\widetilde{A}\widetilde{B}} \\ & & & & u_{\widetilde{B}} \end{pmatrix}. \tag{6.7}$$

The quantity $\mathbf{1}_5$ in Eq. 6.4 is a 5×5 diagonal unit matrix. The nuclear kinetic and potential energy operators of the reference state are denoted by $\mathcal{T}_N$ and $\mathcal{V}_0$, respectively. The change of electronic energy upon ionization from this reference state is described by the electronic Hamiltonian matrix $\Delta\mathcal{H}$ in Eq. 6.7. The diagonal elements of this matrix represent the diabatic potential energies of the electronic states and the off-diagonal

elements represent the coupling between them. The elements of $\Delta\mathcal{H}$ are expanded in a standard Taylor series around the reference equilibrium geometry at $\mathbf{Q}$=0 in the following way [114, 115, 201].

$$\begin{aligned}
u_j^{x/y} =& E_j^0 + \sum_{i\in a_1}\kappa_i^j Q_i + \frac{1}{2!}\sum_{i\in a_1}\gamma_i^j Q_i^2 + \frac{1}{3!}\sum_{i\in a_1}\sigma_i^j Q_i^3 + \frac{1}{4!}\sum_{i\in a_1}\delta_i^j Q_i^4 \\
&+\frac{1}{2!}\sum_{i\in e}\gamma_i^j\left(Q_{ix}^2+Q_{iy}^2\right) + \frac{1}{3!}\sum_{i\in e}\sigma_i^j\left(2Q_{ix}^3-6Q_{ix}Q_{iy}^2\right) + \frac{1}{4!}\sum_{i\in e}\delta_i^j\left(Q_{ix}^4+2Q_{ix}^2Q_{iy}^2+Q_{iy}^4\right) \\
&+\frac{1}{5!}\sum_{i\in e}\rho_i^j\left(2Q_{ix}^5-4Q_{ix}^3Q_{iy}^2-6Q_{ix}Q_{iy}^4\right) \pm \sum_{i\in e}\lambda_i^j Q_{ix} \pm \frac{1}{2!}\sum_{i\in e}\eta_i^j\left(Q_{ix}^2-Q_{iy}^2\right) \\
&\pm\frac{1}{3!}\sum_{i\in e}\sigma_i'^j\left(Q_{ix}^3+Q_{ix}Q_{iy}^2\right) \pm \frac{1}{4!}\sum_{i\in e}\delta_i'^j(Q_{ix}^4-6Q_{ix}^2Q_{iy}^2+Q_{iy}^4) \pm \frac{1}{4!}\sum_{i\in e}\delta_i''^j(Q_{ix}^4-Q_{iy}^4) \\
&\pm\frac{1}{5!}\sum_{i\in e}\rho_i'^j\left(Q_{ix}^5-10Q_{ix}^3Q_{iy}^2+5Q_{ix}Q_{iy}^4\right) \pm \frac{1}{5!}\sum_{i\in e}\rho_i''^j\left(Q_{ix}^5+2Q_{ix}^3Q_{iy}^2+Q_{ix}Q_{iy}^4\right);\ j\in\widetilde{X},\widetilde{A}
\end{aligned} \tag{6.8}$$

$$\begin{aligned}
u_j =& E_j^0 + \sum_{i\in a_1}\kappa_i^j Q_i + \frac{1}{2!}\sum_{i\in a_1}\gamma_i^j Q_i^2 + \frac{1}{3!}\sum_{i\in a_1}\sigma_i^j Q_i^3 \\
&+\frac{1}{2!}\sum_{i\in e}\gamma_i^j\left(Q_{ix}^2+Q_{iy}^2\right) + \frac{1}{4!}\sum_{i\in e}\delta_i^j\left(Q_{ix}^4+2Q_{ix}^2Q_{iy}^2+Q_{iy}^4\right);\quad j\in\widetilde{B}
\end{aligned} \tag{6.9}$$

$$\begin{aligned}
u_j^{xy} =& \sum_{i\in e}\lambda_i^j Q_{iy} - \frac{1}{2!}\sum_{i\in e}2\eta_i{}^j Q_{ix}Q_{iy} + \frac{1}{3!}\sum_{i\in e}\sigma_i'^j\left(Q_{ix}^2Q_{iy}+Q_{iy}^3\right) \\
&+\frac{1}{4!}\sum_{i\in e}\delta_i'^j\left(4Q_{ix}^3Q_{iy}-4Q_{ix}Q_{iy}^3\right) + \frac{1}{4!}\sum_{i\in e}\delta_i''^j\left(-2Q_{ix}^3Q_{iy}-2Q_{ix}Q_{iy}^3\right) \\
&+\frac{1}{5!}\sum_{i\in e}\rho_i'^j\left(-5Q_{ix}^4Q_{iy}+10Q_{ix}^2Q_{iy}^3-Q_{iy}^5\right) + \frac{1}{5!}\sum_{i\in e}\rho_i''^j\left(Q_{ix}^4Q_{iy}+2Q_{ix}^2Q_{iy}^3+Q_{iy}^5\right);\quad j\in\widetilde{X},\widetilde{A}
\end{aligned} \tag{6.10}$$

$$\begin{aligned}
u_{\widetilde{A}\widetilde{B}}^{x} =& \sum_{i\in e}\lambda_i'^{(1)}Q_{ix} + \frac{1}{2!}\sum_{i\in e}\lambda_i'^{(2)}\left(Q_{ix}^2-Q_{iy}^2\right) + \frac{1}{3!}\sum_{i\in e}\lambda_i'^{(3)}\left(Q_{ix}^3+Q_{ix}Q_{iy}^2\right) \\
&+\frac{1}{4!}\sum_{i\in e}\lambda_i'^{(4)}(Q_{ix}^4-6Q_{ix}^2Q_{iy}^2+Q_{iy}^4) + \frac{1}{4!}\sum_{i\in e}\lambda_i'^{(4')}(Q_{ix}^4-Q_{iy}^4) \\
&+\frac{1}{5!}\sum_{i\in e}\lambda_i'^{(5)}\left(Q_{ix}^5-10Q_{ix}^3Q_{iy}^2+5Q_{ix}Q_{iy}^4\right) + \frac{1}{5!}\sum_{i\in e}\lambda_i'^{(5')}\left(Q_{ix}^5+2Q_{ix}^3Q_{iy}^2+Q_{ix}Q_{iy}^4\right),
\end{aligned} \tag{6.11}$$

$$
\begin{aligned}
u^{y}_{\widetilde{A}\widetilde{B}} = & \sum_{i\in e} \lambda_i^{\prime(1)} Q_{iy} - \frac{1}{2!}\sum_{i\in e} 2\lambda_i^{\prime(2)} Q_{ix}Q_{iy} + \frac{1}{3!}\sum_{i\in e} \lambda_i^{\prime(3)} \left(Q_{ix}^2 Q_{iy} + Q_{iy}^3\right) \\
& + \frac{1}{4!}\sum_{i\in e} \lambda_i^{\prime(4)} \left(4Q_{ix}^3 Q_{iy} - 4Q_{ix}Q_{iy}^3\right) + \frac{1}{4!}\sum_{i\in e} \lambda_i^{\prime(4')} \left(-2Q_{ix}^3 Q_{iy} - 2Q_{ix}Q_{iy}^3\right) \\
& + \frac{1}{5!}\sum_{i\in e} \lambda_i^{\prime(5)} \left(-5Q_{ix}^4 Q_{iy} + 10Q_{ix}^2 Q_{iy}^3 - Q_{iy}^5\right) + \frac{1}{5!}\sum_{i\in e} \lambda_i^{\prime(5')} \left(Q_{ix}^4 Q_{iy} + 2Q_{ix}^2 Q_{iy}^3 + Q_{iy}^5\right).
\end{aligned}
\tag{6.12}
$$

In the above equations, two components of the degenerate electronic states and vibrational modes are identified with the labels x and y. The quantity E_j^0 denotes the vertical ionization energy of the jth electronic state. The diagonal intra-state coupling parameters of the ith vibrational mode in the jth electronic state are given by κ_i^j (linear), γ_i^j (second-order), σ_i^j (third-order), δ_i^j (fourth-order), and ρ_i^j (fifth-order). The linear, second, third, fourth and fifth-order JT coupling parameters along the degenerate vibrational modes within the jth electronic state are given by λ_i^j, η_i^j, $\sigma_i^{\prime j}$, $\delta_i^{\prime j}$ and $\delta_i^{\prime\prime j}$, $\rho_i^{\prime j}$ and $\rho_i^{\prime\prime j}$, respectively. The PJT coupling parameters between the $\widetilde{\mathrm{A}}\ ^2\mathrm{E}$ and $\widetilde{\mathrm{B}}\ ^2\mathrm{A}_1$ electronic states along the degenerate vibrational modes are given by $\lambda_i^{\prime(n)}$ (i.e., nth order inter-state coupling constant). It is worth noting that the elements of the JT and PJT coupling matrices are of identical form and are only distinguished by different coupling constants. These parameters are derived by fitting the calculated adiabatic electronic energies to the adiabatic form of $\Delta\mathcal{H}$. The summations in Eqs. 6.8-6.12 are carried out over the normal coordinate of all symmetry allowed vibrational modes. The plus and minus sign in Eq. 6.8 is applicable to the x and y components of the degenerate electronic state, respectively. Note that the parameters of odd-order for the vibrational modes of e symmetry do not appear in Eq. 6.9 in accordance with the symmetry selection rule.

6.2 Results and discussion

6.2.1 Electronic structure calculations

The equilibrium geometry of H_3CCCH molecule belongs to C_{3v} symmetry point group in its electronic ground state. This geometry is optimized with the aid of second order Møller-Plesset perturbation (MP2) method [148] employing the augmented correlation-consistent polarized valence double zeta (aug-cc-pVDZ) basis set of Dunning [149]. Gaussian-09 [150] suite of program is used for this purpose. The optimized equilibrium geometry is shown in Fig. 6.2 with atom numbering and the corresponding geometry parameters are given in Table 6.1. The harmonic vibrational frequency (ω_i), of the vibrational mode i at the reference equilibrium structure is calculated at the same level

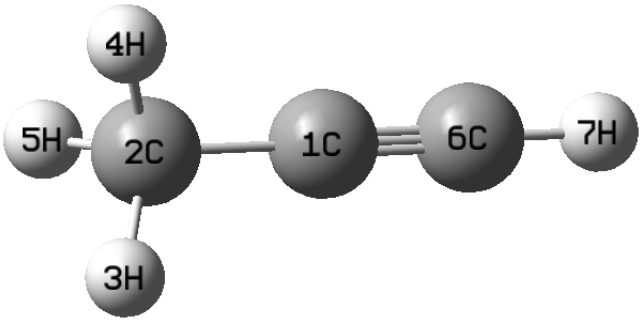

FIGURE 6.2: Optimized equilibrium geometry of the electronic ground state of H_3CCCH.

of theory. The mass-weighted normal displacement coordinate of vibrational modes is calculated and transformed to the dimensionless form Q_i by multiplying with $\sqrt{\omega_i}$ (in a.u., $\hbar$=1). The harmonic frequencies of the vibrational modes and their symmetry are given in Table 6.2 along with the available literature data [202, 203]. It can be seen from Tables 6.1 and 6.2 that the theoretical results are in good accord with the available literature data.

TABLE 6.1: Geometry parameters (distances in Å, angles in degrees) of the equilibrium structure of the electronic ground state of H_3CCCH compared with the available experimental results.

parameters	This work	Experiment [204]
R(C1-C2),	1.45	1.46
R(C1-C6)	1.20	1.20
R(C2-H3, C2-H4, C2-H5)	1.09	1.09
R(C6-H7)	1.06	1.06
∠(C1-C2-H3, C1-C2-H4, C1-C2-H5)	110	110
∠(H3-C2-H4, H3-C2-H5, H4-C2-H5)	107	108

TABLE 6.2: Symmetry, designation and harmonic frequency (in cm^{-1}) of vibrational modes of the ground electronic state of the H_3CCCH.

Symmetry	modes	This work	Theory [202]	Experiment [202]	Experiment [203]	Assignment
A_1	ν_1	3471	3502/3618	3335		acetylene C-H str.
	ν_2	3028	2941/3180	2941		symm. methyl C-H str.
	ν_3	2225	2138/2386	2138	1940	C≡C str.
	ν_4	1416	1385/1534	1385	1290	methyl deformation.
	ν_5	941	930/972	930	940	C-C str.
E	ν_6	3084	2981/3246	2981		antisymm. methyl C-H str.
	ν_7	1479	1450/1600	1450		methyl skeletal deformation.
	ν_8	1058	1036/1152	1036		methyl skeletal rock
	ν_9	672	628/792	628		C≡C-H bend
	ν_{10}	347	327/386	327		CC≡C bend

In order to study the nuclear dynamics, the PESs of the $\widetilde{X}$, $\widetilde{A}$ and $\widetilde{B}$ electronic states of $H_3CCCH^{\cdot+}$ are calculated along the dimensionless normal displacement coordinates of the reference ground state. The adiabatic potential energies of these electronic states

are calculated by both EOMIP-CCSD and CASSCF-MRCI methods using the aug-cc-pVDZ basis set. The EOMIP-CCSD and CASSCF-MRCI calculations are performed using CFOUR [171] and MOLPRO [154] suite of programs, respectively. MOLPRO has no implementation of ionization problem. So, we used the CASSCF-MRCI method for ionization potential calculations. The adiabatic energies of the electronic states are calculated along the dimensionless normal displacement coordinate of each vibrational mode. The CASSCF-MRCI calculations are carried out with a (16,8) active space, which includes 8 valence occupied orbitals with sixteen electrons for the reference electronic ground state of H_3CCCH. The electronic states of $H_3CCCH^{\cdot+}$ have open shell configuration and a (15,8) active space is used. Test calculations are carried out with varying active space and the mentioned ones are found to yield the best results with an affordable computational cost. For all these calculations it took almost three months of CPU time on a "Intel(R) Xeon(R) CPU E5-2697 v3 @ 2.60GHz model with 28 cores, 56 processors" HPC cluster. The energy difference of the cationic states with the reference neutral ground state at the equilibrium configuration (at $\mathbf{Q}$=0) representing the VIEs are given in Table 6.3 along with the available literature data for comparison. In addition to the EOMIP-CCSD and CASSCF-MRCI results, the VIEs are calculated by Outer Valence Green's function (OVGF) method [205] (using Gaussian-09 program) are also given in Table 6.3. It can be seen from Table 6.3 that our theoretical results are in good accord with the available experimental data. It can also be seen that at the vertical configuration $\widetilde{X}$ state is energetically well separated from the $\widetilde{A}$ and $\widetilde{B}$ electronic states whereas, $\widetilde{A}$ and $\widetilde{B}$ states are energetically close. Therefore, PJT coupling of the $\widetilde{X}$ state with $\widetilde{A}$ and $\widetilde{B}$ states is expected to be insignificant. On the other hand, interplay of JT and PJT coupling is expected to be strong in the $\widetilde{A}$-$\widetilde{B}$ electronic states.

TABLE 6.3: VIE (in eV) of the energetically lowest three electronic states of $H_3CCCH^{\cdot+}$ calculated at the reference equilibrium geometry of H_3CCCH and compared with the available experimental data.

states	$\widetilde{X}\ ^2E$	$\widetilde{A}\ ^2E$	$\widetilde{B}\ ^2A_1$	$\widetilde{C}\ ^2A_1$	
VIE	10.23	15.03	15.30	17.78	OVGF
	10.40	15.09	15.31	17.68	EOMIP-CCSD
	10.28	15.40	15.75	18.29	CASSCF-MRCI
	10.37	14.4	15.13	17.2	Expt.[187]
	10.37	14.6	15.3/15.5	17.4	Expt.[198]
	10.54	14.60	15.4	17.4	Expt.[190]
	10.36	13.69/14.70/15.30	15.8	17.49	Expt.[189]
	10.37	13.69	15.2	17.2	Expt.[203]
	10.37	14.70	15.50/15.80	17.49	Expt.[202]

The adiabatic form of the 5×5 diabatic electronic Hamiltonian matrix [cf., Sec. 6.1.1] is fit to the *ab initio* adiabatic electronic energies by a nonlinear least-squares procedure to estimate the various coupling parameters of Eqs. (6.8-6.12). The Levenberg-Marquardt algorithm [145, 146] is used for the purpose. These coupling parameters are given in Tables 6.4 - 6.7.

TABLE 6.4: *Ab initio* calculated linear and quadratic coupling parameters for the $\widetilde{X}\ ^2E$, $\widetilde{A}\ ^2E$ and $\widetilde{B}\ ^2A_1$ electronic states of $H_3CCCH^{\cdot+}$ derived from the EOMIP-CCSD electronic energy data. All quantities are in eV and the dimensionless Poisson parameters $\left(\frac{\kappa_i{}^2}{2\omega_i{}^2} \text{or} \frac{\lambda_i{}^2}{2\omega_i{}^2}\right)$ are given in the parentheses.

	$\widetilde{X}\ ^2E$			$\widetilde{A}\ ^2E$		
Mode	κ_i or λ_i	γ_i	η_i	κ_i or λ_i	γ_i	η_i
a_1						
ν_1	0.0003 (0.0000)	0.0020	-	0.0318 (0.0027)	0.0019	-
ν_2	-0.0320 (0.0035)	-0.0012	-	-0.3779 (0.4921)	0.0268	-
ν_3	0.2184 (0.3442)	0.0141	-	-0.0644 (0.0299)	0.0056	-
ν_4	0.0452 (0.0342)	-0.0179	-	-0.2606 (1.1359)	-0.0803	-
ν_5	-0.0194 (0.0136)	-0.0165	-	0.1027 (0.3835)	0.0219	-
e						
ν_6	0.0266 (0.0023)	0.0027	0.00011	0.2634 (0.2254)	-0.0249	-0.0004
ν_7	0.0439 (0.0289)	-0.0273	0.00004	0.4424 (2.9446)	-0.0856	0.0002
ν_8	0.0462 (0.0638)	-0.0259	0.00020	0.2163 (1.3949)	-0.0553	0.0003
ν_9	0.0101 (0.0108)	-0.0104	-0.000003	-0.0001 (0.00000)	-0.0479	-0.0010
ν_{10}	0.0119 (0.0656)	-0.0165	-0.00020	0.0010 (0.00005)	-0.0609	-0.0004

	$\widetilde{B}\ ^2A_1$				$\widetilde{A}\ ^2E \times \widetilde{B}\ ^2A_1$	
Mode	κ_i	γ_i	σ_i	δ_i	$\lambda_i'^{(1)}$	$\lambda_i'^{(2)}$
a_1						
ν_1	0.1292 (0.0446)	-0.0351	0.0093	0.0028	-	-
ν_2	-0.0757 (0.0198)	-0.0129	-0.0024	-	-	-
ν_3	-0.1311 (0.1240)	-0.0269	0.0030	-	-	-
ν_4	0.4642 (3.6038)	-0.0262	-0.0199	-	-	-
ν_5	0.1729 (1.0866)	-0.0106	-0.0023	-	-	-
e						
ν_6	-	0.05852	-	-0.0206	-0.0617 (0.0124)	0.0478
ν_7	-	0.02827	-	-0.0241	-0.0953 (0.1366)	0.0756
ν_8	-	-0.0459	-	-0.0015	-0.0201 (0.0120)	0.0210
ν_9	-	-0.0058	-	0.0036	-0.0015 (0.0002)	0.0038
ν_{10}	-	-0.0578	-	0.0049	0.0017 (0.0013)	-0.0019

6.2.2 Potential energy surfaces: The JT and PJT conical intersections

The adiabatic potential energy curves of the $\widetilde{X}$, $\widetilde{A}$ and $\widetilde{B}$ electronic states of $H_3CCCH^{\cdot+}$ are shown and discussed in this section. The adiabatic potential energies of these states are plotted along the dimensionless normal displacement coordinates of the totally symmetric a_1 vibrational modes (ν_1-ν_5) and the JT active e vibrational modes (ν_6-ν_8) in Figs. 6.3 and 6.4, respectively. The solid curves in these figures represent the potential energies obtained from the constructed theoretical model in Sec. 6.1.1 and the points superimposed on them are the computed *ab initio* adiabatic potential energies calculated by the EOMIP-CCSD (Figs. 6.3a and 6.4a) and CASSCF-MRCI (Figs. 6.3b and 6.4b) methods, discussed in Sec. 6.2.1. It can be seen that the calculated *ab initio* points are well reproduced by the present theoretical model. We note that up to a fourth- and fifth-order Taylor expansion of the electronic Hamiltonian along both a_1 and JT active e vibrational modes are found to be necessary to represent the *ab initio* points

TABLE 6.5: Same as in Table 6.4 and the parameters are derived from the CASSCF-MRCI electronic energy data.

	$\widetilde{X}\ ^2E$			$\widetilde{A}\ ^2E$		
Mode	κ_i or λ_i	γ_i	η_i	κ_i or λ_i	γ_i	η_i
a_1						
ν_1	-0.0224 (0.0013)	0.0037	-	0.0318 (0.0027)	0.0028	-
ν_2	-0.0259 (0.0023)	-0.0011	-	-0.4011 (0.5545)	0.0280	-
ν_3	0.2670 (0.5147)	0.0142	-	-0.0799 (0.0460)	0.0084	-
ν_4	0.0476 (0.0379)	-0.0148	-	-0.2721 (1.2385)	-0.0853	-
ν_5	-0.0037 (0.0005)	-0.0165	-	0.1056 (0.4050)	0.0245	-
e						
ν_6	0.0284 (0.0026)	0.0027	0.000127	0.2562 (0.2254)	-0.1080	0.0042
ν_7	0.0412 (0.0255)	-0.0248	0.000045	0.4199 (2.9446)	-0.1078	0.0001
ν_8	0.0434 (0.0563)	-0.0244	0.000205	0.1966 (1.3949)	-0.0624	0.0003
ν_9	0.0086 (0.0078)	-0.0063	-0.000002	-0.0023 (0.00000)	-0.0233	-0.0016
ν_{10}	0.0094 (0.0408)	-0.0263	-0.000123	0.0002 (0.00005)	-0.0601	-0.0004

	$\widetilde{B}\ ^2A_1$				$\widetilde{A}\ ^2E\times\widetilde{B}\ ^2A_1$	
Mode	κ_i	γ_i	σ_i	δ_i	$\lambda_i^{\prime(1)}$	$\lambda_i^{\prime(2)}$
a_1						
ν_1	0.1475 (0.0582)	-0.0467	0.0120	0.0033	-	-
ν_2	-0.0677 (0.0158)	-0.0132	-0.0028	-	-	-
ν_3	-0.1415 (0.1445)	-0.0329	0.0038	-	-	-
ν_4	0.4812 (3.8724)	-0.0272	-0.0193	-	-	-
ν_5	0.1901 (1.3136)	-0.0119	-0.0023	-	-	-
e						
ν_6	-	0.2277	-	-0.0588	-0.0024 (0.00001)	0.0515
ν_7	-	0.0650	-	-0.0389	-0.1145 (0.19724)	0.0895
ν_8	-	-0.0420	-	-0.0039	-0.0275 (0.02255)	0.0274
ν_9	-	-0.0054	-	0.0004	-0.0030 (0.00095)	0.0115
ν_{10}	-	-0.0631	-	-0.0021	0.0010 (0.00046)	0.0020

TABLE 6.6: Higher order coupling parameters of $\widetilde{X}\ ^2E$, $\widetilde{A}\ ^2E$ states and PJT coupling between $\widetilde{A}\ ^2E$-$\widetilde{B}\ ^2A_1$ electronic states are derived from EOMIP-CCSD electronic structure data.

	$\widetilde{X}\ ^2E$					
Mode	σ_i	$\sigma_i^{\prime}$	δ_i	$\delta_i^{\prime}$ ($\delta_i^{\prime\prime}$)	ρ_i	$\rho_i^{\prime}$ ($\rho_i^{\prime\prime}$)
a_1						
ν_1	0.000898		0.001036			
ν_2	-0.000691		-			
ν_3	0.002899		-			
ν_4	-0.008080		-0.000832			
ν_5	-0.001012		-			
e						
ν_6	-0.0000007	0.0004	-	-	-	-
ν_7	-0.000013	0.0060	-	-	-	-
ν_8	-0.000011	0.0057	-	-	-	-
ν_9	0.00000009	0.0014	-0.00053	0.0000004 (0.0000006)	-0.00000003	-0.000953 (-0.001846)
ν_{10}	-0.000008	0.0078	0.00348	0.0000219 (0.0000286)	-	-

	$\widetilde{A}\ ^2E$					
Mode	σ_i	$\sigma_i^{\prime}$	δ_i	$\delta_i^{\prime}$ ($\delta_i^{\prime\prime}$)	ρ_i	$\rho_i^{\prime}$ ($\rho_i^{\prime\prime}$)
a_1						
ν_1	0.000670		0.000104			
ν_2	-		-			
ν_3	-		-			
ν_4	0.018160		0.008480			
ν_5	0.002170		-			
e						
ν_6	-0.00220	0.02060	0.00890	0.00011 (0.00011)	0.00150	-0.00360 (-0.00360)
ν_7	0.00008	0.00942	0.01822	-0.00001 (-0.00001)	-0.00005	-0.00397 (-0.00397)
ν_8	-0.00024	0.01210	0.00848	-0.00002 (-0.00002)	0.00019	-0.00335 (-0.00335)
ν_9	-0.00057	0.05901	-0.01472	0.00022 (0.00022)	0.00065	-0.00244 (-0.00244)
ν_{10}	-0.00001	0.00564	0.00129	0.00004 (0.00004)	-	-

	$\widetilde{A}\ ^2E\times\widetilde{B}\ ^2A_1$(PJT parameters)				
Mode	$\lambda_i^{\prime(3)}$	$\lambda_i^{\prime(4)}$	$\lambda_i^{\prime(4^{\prime})}$	$\lambda_i^{\prime(5)}$	$\lambda_i^{\prime(5^{\prime})}$
e					
ν_6	0.0528	-0.0070	-0.0070	-0.0067	-0.0067
ν_7	0.0767	-0.0108	-0.0108	-0.0094	-0.0094
ν_8	0.0161	-0.0031	-0.0031	-0.0019	-0.0019
ν_9	-0.0017	-0.0007	-0.0007	0.0007	0.0007
ν_{10}	0.0003	0.0001	0.0001	-	-

TABLE 6.7: Same as in Table 6.6 and the parameters are derived from CASSCF-MRCI electronic structure data.

	$\widetilde{X}\ ^2E$					
Mode	σ_i	σ_i'	δ_i	δ_i' (δ_i'')	ρ_i	ρ_i' (ρ_i'')
a_1						
ν_1	0.000842		0.000785			
ν_2	-0.000850		-			
ν_3	0.002782		-			
ν_4	-0.008205		-0.001367			
ν_5	-0.001129		-			
e						
ν_6	-	-	-	-	-	-
ν_7	-0.000013	0.0060	-	-	-	-
ν_8	-0.000010	0.0059	-	-	-	-
ν_9	0.00000014	0.0025	0.000894	-0.000213 (0.000214)	-0.0000001	-0.000553 (-0.001538)
ν_{10}	-0.0000087	0.0071	0.000498	0.000010 (-0.000006)	-	-
	$\widetilde{A}\ ^2E$					
Mode	σ_i	σ_i'	δ_i	δ_i' (δ_i'')	ρ_i	ρ_i' (ρ_i'')
a_1						
ν_1	0.0005796		-			
ν_2	-		-			
ν_3	-		-			
ν_4	0.0188956		0.0090729			
ν_5	0.0024462		-			
e						
ν_6	0.00073	-0.02796	0.02753	-0.000267 (-0.000267)	-0.00042	0.00310 (0.00310)
ν_7	-0.00002	0.02677	0.02656	0.000001 (0.000001)	0.00001	-0.00601 (-0.00601)
ν_8	-0.00030	0.02306	0.01037	-0.000020 (-0.000020)	0.00023	-0.00464 (-0.00464)
ν_9	-0.00048	0.04481	-0.03453	0.000263 (0.000263)	0.00051	0.00126 (0.00126)
ν_{10}	0.00039	0.00018	0.00406	0.000019 (0.000019)	-	-
	$\widetilde{A}\ ^2E \times \widetilde{B}\ ^2A_1$(PJT parameters)					
Mode	$\lambda_i'^{(3)}$	$\lambda_i'^{(4)}$	$\lambda_i'^{(4')}$	$\lambda_i'^{(5)}$	$\lambda_i'^{(5')}$	
e						
ν_6	-0.0256	-0.0075	-0.0075	0.0080	0.0080	
ν_7	0.0866	-0.0134	-0.0134	-0.0099	-0.0099	
ν_8	0.0232	-0.0041	-0.0041	-0.0029	-0.0029	
ν_9	-0.0094	-0.0010	-0.0010	0.0018	0.0018	
ν_{10}	-0.0020	-0.0000	-0.0000	-	-	

extremely well. Also, these higher-order coupling parameters provide an accurate theoretical description of the JT split potentials and the associated vibronic spectrum. A second-order vibronic model is found to give rise an inaccurate theoretical description. The totally symmetric vibrational modes do not lift the electronic degeneracy of the $\widetilde{X}$ and $\widetilde{A}$ states. They tune the electronic energy minimum of the cationic states relative to the equilibrium minimum of the electronic ground state of H_3CCCH (**Q=0**) and therefore modify the vertical energy gap between the electronic states. It can be seen from Fig. 6.3 that the $\widetilde{X}$ state of $H_3CCCH^{\cdot+}$ is energetically well separated from the remaining two states. The latter states ($\widetilde{A}$ and $\widetilde{B}$) are vertically very close in energy [cf., Table 6.3] and undergo curve crossings in the near vicinity of reference equilibrium geometry at **Q=0** [cf., Fig. 6.3].

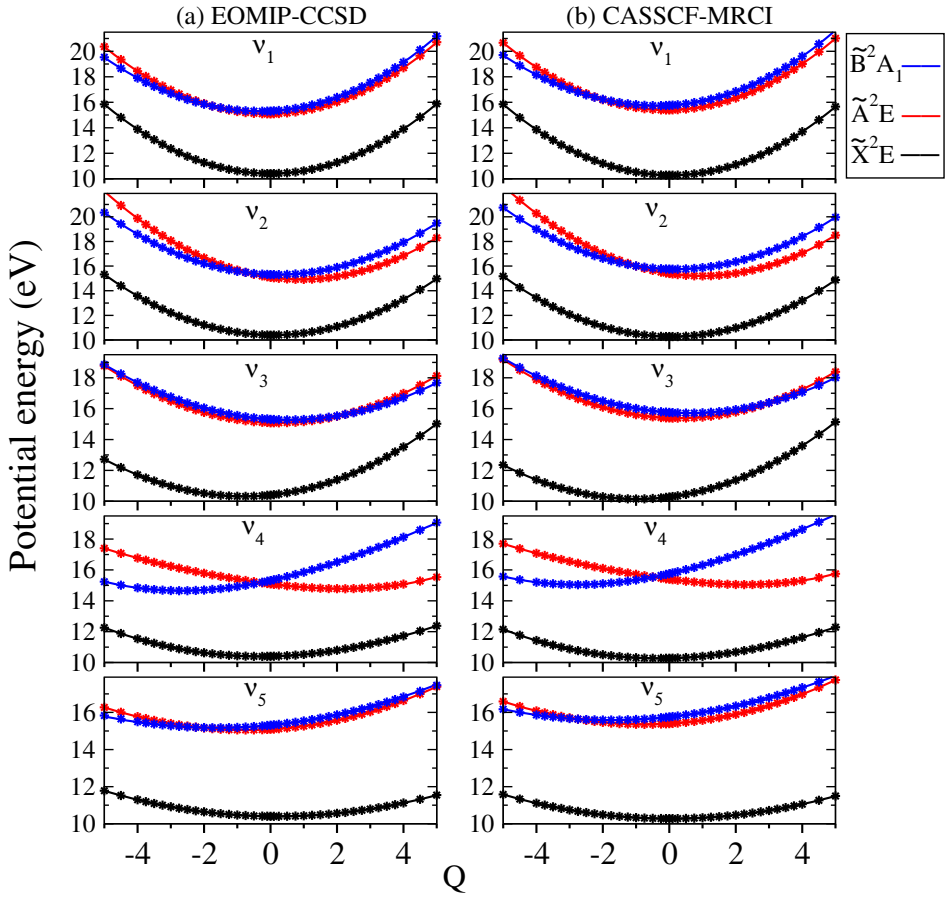

FIGURE 6.3: One dimensional viewgraph of the multi-dimensional potential energy surfaces of $\widetilde{X}\ ^2E$, $\widetilde{A}\ ^2E$ and $\widetilde{B}\ ^2A_1$ electronic states of $H_3CCCH^{\cdot+}$ plotted along the dimensionless normal displacement coordinate (Q_i) of the totally symmetric vibrational modes, ν_1-ν_5. The potential energies obtained from the theoretical model and calculated *ab initio* (column (a): EOMIP-CCSD, column (b): CASSCF-MRCI) are shown by the solid lines and points, respectively.

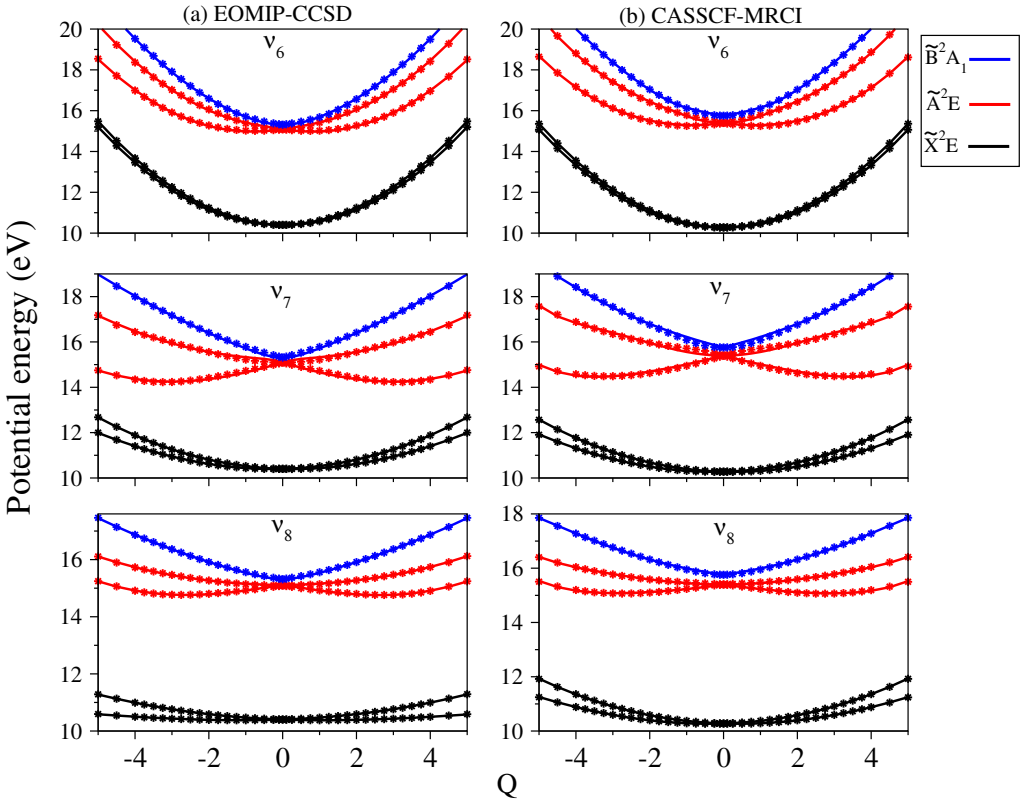

FIGURE 6.4: Adiabatic potential energy curves of the $\widetilde{X}$, $\widetilde{A}$ and $\widetilde{B}$ electronic states of $H_3CCCH^{\cdot+}$ along one component of the dimensionless normal coordinate of degenerate vibrational modes ν_6 to ν_8. The potential energies obtained from the present theoretical model and calculated *ab initio* (column (a): EOMIP-CCSD, column (b): CASSCF-MRCI) are shown by the solid lines and points, respectively.

Within a second-order coupling model and utilizing the parameters of Tables 6.2-6.5 the energetic minimum of the seam of CIs is calculated using a minimization algorithm employing Lagrange multipliers. The numerical tools available in MATHEMATICA [157] are used for this purpose. The results are tabulated in a matrix array in Table 6.8. In the latter, the numbers in the diagonal represent the minimum of a state and those in the off-diagonal are the minimum of the intersection seam. It can be seen from Table 6.8 that the minimum of the $\widetilde{X}$ state is energetically well separated from the $\widetilde{A}$ and $\widetilde{B}$ states. The intersection of the $\widetilde{X}$ state with latter states occurs at very high energies and is not relevant for the present study. Using the EOMIP-CCSD (CASSCF-MRCI) electronic structure data the $\widetilde{A}$-$\widetilde{B}$ intersection minimum is found at ∼14.80 eV (15.61 eV) and the minimum of the $\widetilde{A}$ state appears at ∼14.50 eV (14.87 eV). The energetic minimum of the $\widetilde{B}$ state appears at ∼14.37 eV (14.71 eV). Vibronic coupling between the $\widetilde{A}$ and $\widetilde{B}$ electronic states shifts the minimum of the $\widetilde{B}$ state at a distorted geometry. Among the five a_1 vibrational modes, ν_2, ν_3, ν_4 and ν_5 shift the minimum of the $\widetilde{X}$, $\widetilde{A}$ and $\widetilde{B}$ electronic states considerably away from the minimum of the neutral reference state occurring at **Q=0** [cf., Fig. 6.3].

TABLE 6.8: Estimated $\mathcal{V}_{min}$ (diagonal entries) and $\mathcal{V}^{c}_{min}$ (off-diagonal entries) of the electronic states of $H_3CCCH^{\cdot+}$ within a second-order coupling model, using the EOMIP-CCSD (CASSCF-MRCI) electronic energy data. All quantities are given in eV.

	$\widetilde{\mathrm{X}}\ ^2\mathrm{E}$	$\widetilde{\mathrm{A}}\ ^2\mathrm{E}$	$\widetilde{\mathrm{B}}\ ^2\mathrm{A}_1$
$\widetilde{\mathrm{X}}\ ^2\mathrm{E}$	10.30 (10.14)	-	-
$\widetilde{\mathrm{A}}\ ^2\mathrm{E}$	-	14.50 (14.87)	14.80 (15.53)
$\widetilde{\mathrm{B}}\ ^2\mathrm{A}_1$	-	-	14.37 (14.71)

In contrast to the vibrational modes of a_1 symmetry, the degenerate vibrational modes are JT active and lift the electronic degeneracy of $\widetilde{\mathrm{X}}$ and $\widetilde{\mathrm{A}}$ electronic states of $H_3CCCH^{\cdot+}$. The potential energy cuts along one component (say x) of a few JT active degenerate vibrational modes are shown in Fig. 6.4. It can be seen from Fig. 6.4 that the extent of splitting of electronic degeneracy of the $\widetilde{\mathrm{X}}$ state is small as compared to the $\widetilde{\mathrm{A}}$ electronic state. The extent of splitting of the degeneracy depends on the JT coupling strength ($\lambda^2/2\omega^2$) of the degenerate vibrational modes. It can be seen from Tables 6.4 and 6.5 that the vibrational modes ν_7, ν_8 and ν_{10} have moderate JT coupling strength [cf., Table 6.4 and 6.5] than the other modes in the $\widetilde{\mathrm{X}}$ state. In the case of $\widetilde{\mathrm{A}}$ electronic state, among the five degenerate vibrational modes, ν_6, ν_7 and ν_8 have relatively large coupling strength [cf., Table 6.4 and 6.5]. So, the extent of splitting of electronic degeneracy of the $\widetilde{\mathrm{A}}$ state is more as compared to that of the $\widetilde{\mathrm{X}}$ state.

Using EOMIP-CCSD electronic structure data, we calculated the energetic minimum of the JT split lower adiabatic sheets and saddle points of both $\widetilde{\mathrm{X}}\ ^2\mathrm{E}$ and $\widetilde{\mathrm{A}}\ ^2\mathrm{E}$ electronic states using the following equations [185, 206]

$$\mathcal{V}_{-}^{min} = E_j^0 - \frac{1}{2}\sum_{i\in a_1}\frac{{\kappa_i}^2}{(\omega_i+\gamma_i)} - \frac{1}{2}\sum_{i\in e}\frac{{\lambda_i}^2}{(\omega_i+\gamma_i-|\eta_i|)};\ j \in \widetilde{X},\widetilde{A} \tag{6.13}$$

$$\mathcal{V}_{-}^{sp} = E_j^0 - \frac{1}{2}\sum_{i\in a_1}\frac{{\kappa_i}^2}{(\omega_i+\gamma_i)} - \frac{1}{2}\sum_{i\in e}\frac{{\lambda_i}^2}{(\omega_i+\gamma_i+|\eta_i|)};\ j \in \widetilde{X},\widetilde{A}. \tag{6.14}$$

The minimum of the seam of CIs occurs at an energy

$$\mathcal{V}_{CI}^{min} = E_j^0 - \frac{1}{2}\sum_{i\in a_1}\frac{{\kappa_i}^2}{(\omega_i+\gamma_i)};\ j \in \widetilde{X},\widetilde{A}. \tag{6.15}$$

The JT stabilization energy is given by

$$E_{JT} = \frac{1}{2}\sum_{i\in e}\frac{{\lambda_i}^2}{(\omega_i+\gamma_i-|\eta_i|)}. \tag{6.16}$$

The mathematical steps to arrive at the above equations are discussed in the Appendix D. In the case of the $\widetilde{X}\ ^2E$ electronic state, both energetic minimum and saddle points are found at ∼10.28 eV. This shows that the barrier to pseudo rotation is low. The energetic minimum and saddle points of $\widetilde{A}\ ^2E$ state appear at ∼13.08 eV and ∼13.09 eV, respectively. The JT stabilization energies amount to ∼0.02 eV (∼160 cm^{-1}) and ∼1.42 eV (∼11,453 cm^{-1}) for the $\widetilde{X}$ and $\widetilde{A}$ electronic states, respectively. It is worthwhile to mention that the JT stabilization energy estimated above for the $\widetilde{X}$ state is in good agreement with the available theoretical data [194], ∼117 cm^{-1}.

Along with this, we have also calculated the SO coupling constant of the $\widetilde{X}\ ^2E$ electronic state. We obtained a value of ∼ -28.60 cm^{-1} and ∼ -28.83 cm^{-1}, using EOMIP-CCSD and CASSCF-MRCI methods, respectively. This is in very good agreement with the value reported by Shieh *et al.* [191], Xing *et al.* [192], Marquez *et al.* [194] and Jacovella *et al.* [196].

6.2.3 Dynamical observables: Vibronic spectra and time-dependent dynamics

The vibronic band structures of the $\widetilde{X}$, $\widetilde{A}$ and $\widetilde{B}$ electronic states of $H_3CCCH^{\cdot+}$ are calculated with the aid of the theoretical formalism discussed in Sec. 2.3 of Chapter 2. Precise location of the vibrational energy levels of the uncoupled electronic states is calculated by the time-independent matrix diagonalization approach using the Lanczos algorithm [122]. The HO basis functions used along each vibrational mode in these calculations are given in Table 6.9. The first vibronic band due to the degenerate $\widetilde{X}$ electronic state of $H_3CCCH^{\cdot+}$ is shown in Fig. 6.5. The vibronic spectra shown in panels b and c of this figure are obtained with the Hamiltonian parameters derived from the EOMIP-CCSD and CASSCF-MRCI electronic energies, respectively. The experimental $\widetilde{X}$ band is reproduced from Ref. [187] and shown in panel a. Both the stick line spectra and the convoluted envelopes are shown in Fig. 6.5(b and c). The convergence of the stick spectrum is checked with respect to the size of the vibrational basis as well as number of Lanczos iterations. The stick spectrum is convoluted with 30 meV full width at the half maximum (FWHM) Lorentzian line shape function to generate the spectral envelopes shown in panels b and c. Five totally symmetric a_1 (ν_1-ν_5) and five degenerate JT active e (ν_6-ν_{10}) vibrational modes are included in the calculation of the spectrum in Fig. 6.5(b and c).

All five symmetric vibrational modes are excited in the spectrum of the $\widetilde{X}$ state. Peak spacings of ∼3497 cm^{-1}, ∼3067 cm^{-1}, ∼2170 cm^{-1}, ∼1328 cm^{-1} and ∼876 cm^{-1} (EOMIP-CCSD) and ∼3504 cm^{-1}, ∼3067 cm^{-1}, ∼2169 cm^{-1}, ∼1341 cm^{-1} and ∼878

TABLE 6.9: The number of HO basis functions along the totally symmetric and degenerate vibrational modes and the dimension of the secular matrix used in the calculation of the stick vibrational spectra of the $\widetilde{X}\ ^2E$, $\widetilde{A}\ ^2E$ and $\widetilde{B}\ ^2A_1$ electronic states of $H_3CCCH^{\cdot+}$ shown in various figures.

Electronic states	Vibrational modes	No. of HO basis	Dimension of secular matrix	Figure(s)
$\widetilde{X}\ ^2E$	ν_1, ν_2, ν_3 ν_4, ν_5,	(10,12,20) (18,16)	691200	Figs. 6.5(b) and (c)
	ν_{6x}, ν_{6y}, ν_{7x}, ν_{7x} ν_{8x}, ν_{8y}, ν_{9x}, ν_{9y} ν_{10x}, ν_{10y}	(4,4,6,6) (8,8,4,4) (8,8)	37748736	Fig. 6.5(b) and (c)
$\widetilde{A}\ ^2E$	ν_1, ν_2, ν_3 ν_4, ν_5,	(12,18,14) (20,16)	967680	Figs. 6.6(c) and (d)
	ν_{6x}, ν_{6y}, ν_{7x}, ν_{7x} ν_{8x}, ν_{8y}, ν_{9x}, ν_{9y}	(6,6,8,8) (8,8,4,4)	2359296	Fig. 6.6(e) and (f)
$\widetilde{B}\ ^2A_1$	ν_1, ν_2, ν_3 ν_4, ν_5,	(14,12,16) (20,18)	967680	Figs. 6.5(c) and (d)

cm^{-1} (CASSCF-MRCI) due to the progression of ν_1, ν_2, ν_3, ν_4 and ν_5 vibrational modes, respectively, are found. Among the five symmetric vibrational modes, ν_3 (C≡C stretching mode) is strongly excited in the $\widetilde{X}$ state. The excitation of ν_4, ν_5 modes is weak and that of ν_1, ν_2 modes is very weak in accordance with their very low coupling strength [cf., Tables 6.4 and 6.5]. Among the JT active e vibrational modes, ν_8 and ν_{10} are very weakly excited and the appearance of a relatively small number of lines in the spectrum is indicative of very weak JT coupling effects due to all five degenerate modes, as indicated by their coupling strength [cf., Tables 6.4 and 6.5].

The overlapping second photoelectron band of H_3CCCH in the ∼14-17 eV energy range is due to a transition to the $\widetilde{A}\ ^2E$ and $\widetilde{B}\ ^2A_1$ electronic states of $H_3CCCH^{\cdot+}$ [187]. In order to systematically examine the vibronic structure of this band, we first focus on the results obtained for the JT active $\widetilde{A}\ ^2E$ electronic state. The calculations are carried out with both EOMIP-CCSD and CASSCF-MRCI Hamiltonian parameters and the resulting stick line spectra and convoluted envelopes are shown in panels (i) and (ii) of Fig. 6.6, respectively. In Fig. 6.6(a and b), the experimental $\widetilde{A}\ ^2E$-$\widetilde{B}\ ^2A_1$ band is reproduced from Ref. [187]. Panels (c) and (d) show the partial spectra of the $\widetilde{A}$ and $\widetilde{B}$ electronic states obtained with five symmetric vibrational modes, and panels (e) and (f) show the partial spectra of the $\widetilde{A}$ state obtained with four JT active degenerate vibrational modes. The symmetric mode spectrum of the $\widetilde{A}$ state in Fig. 6.6(c and d) reveals progressions of all five symmetric vibrational modes. Peak spacings of ∼3496 cm^{-1}, ∼3178 cm^{-1}, ∼2145 cm^{-1}, ∼1304 cm^{-1} and ∼1024 cm^{-1} (EOMIP-CCSD) and ∼3499 cm^{-1}, ∼3183 cm^{-1}, ∼2156 cm^{-1}, ∼1315 cm^{-1} and ∼1033 cm^{-1} (CASSCF-MRCI) due to ν_1, ν_2, ν_3,

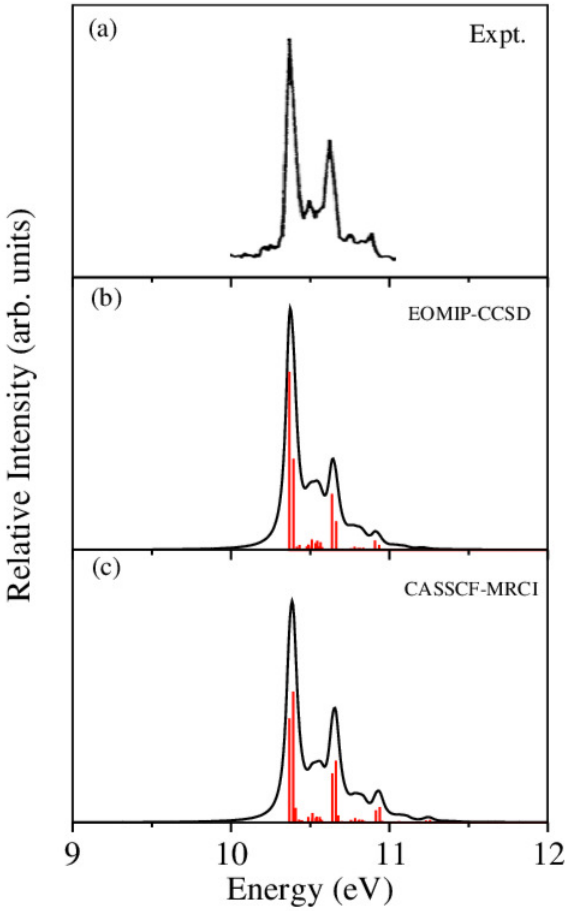

FIGURE 6.5: The vibronic energy level spectrum of the $\widetilde{X}$ electronic state of $H_3CCCH^{\cdot+}$ obtained with the Hamiltonian parameters derived from the EOMIP-CCSD and CASSCF-MRCI electronic energies shown in panels (b) and (c), respectively. The experimental $\widetilde{X}$ ^2E band is reproduced from Ref. [187] and shown in panel (a). Relative intensity (in arbitrary units) is plotted as a function of the energy (in eV).

ν_4 and ν_5, respectively, are estimated from the spectrum. Among the five symmetric vibrational modes, ν_4 (methyl deformation) is strongly excited. The excitation of ν_2 and ν_5 vibrational modes is moderate and that of ν_1 and ν_3 modes is weak. In panels (c) and (d) of Fig. 6.6 the stick line spectrum and the convoluted envelope of the uncoupled $\widetilde{B}$ electronic state is also shown. All five symmetric vibrational modes ν_1-ν_5 are found to contribute to the spectral progressions of the $\widetilde{B}$ state. Line spacings of ∼3332 cm^{-1}, ∼3017 cm^{-1}, ∼2018 cm^{-1}, ∼1497 cm^{-1} and ∼917 cm^{-1} (EOMIP-CCSD) and ∼3279 cm^{-1}, ∼3016 cm^{-1}, ∼1996 cm^{-1}, ∼1495 cm^{-1} and ∼914 cm^{-1} (CASSCF-MRCI), are obtained in this state. Dominant excitation of both ν_4 and ν_5 vibrational modes is found in this case. The symmetric vibrational modes excited in the $\widetilde{X}$, $\widetilde{A}$ and $\widetilde{B}$ electronic states are assigned and given in Tables 6.10 and 6.11. In the latter, the results of the present findings are compared to those available in the literature. It can be seen from Tables 6.10 and 6.11 that the present results compare well with various experimental findings in the literature [187, 195].

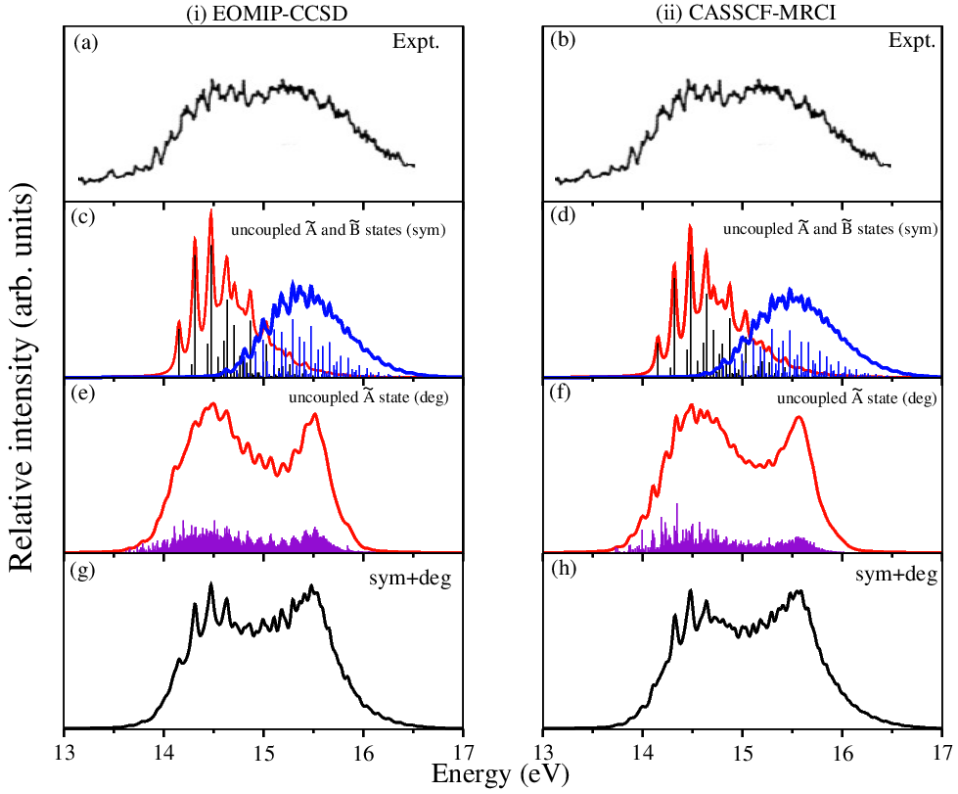

FIGURE 6.6: Vibronic energy level spectra of the $\widetilde{A}\ ^2E$ and $\widetilde{B}\ ^2A_1$ electronic states of $H_3CCCH^{\cdot+}$ obtained with the Hamiltonian parameters derived from the EOMIP-CCSD and CASSCF-MRCI electronic energies shown in column (i) and (ii), respectively. The photoelectron bands of both $\widetilde{A}\ ^2E$ and $\widetilde{B}\ ^2A_1$ electronic states computed with five totally symmetric modes ($\nu_1 - \nu_5$) are shown in panels (c) and (d). The partial spectrum of the $\widetilde{A}\ ^2E$ electronic state computed with four degenerate ($\nu_6 - \nu_9$) vibrational modes is shown in panels (e) and (f). The composite $\widetilde{A}\ ^2E$-$\widetilde{B}\ ^2A_1$ band obtained by convoluting the above two partial spectra (i.e., symmetric + degenerate) are shown in panels (g) and (h). The experimental $\widetilde{A}\ ^2E$-$\widetilde{B}\ ^2A_1$ band is reproduced from Ref. [187] and shown in panels (a) and (b).

The spectrum of the $\widetilde{A}$ state obtained with the JT active degenerate vibrational modes shown in Fig. 6.6 reveals progression of ν_6, ν_7 and ν_8 vibrational modes. Peak spacings of ∼2110 cm^{-1}, ∼711 cm^{-1} and ∼705 cm^{-1} (EOMIP-CCSD) and ∼2173 cm^{-1}, ∼1442 cm^{-1} and ∼1428 cm^{-1} (CASSCF-MRCI), respectively, corresponding to these vibrational modes (in that order) are estimated from the spectrum. It can be seen from Tables 6.4 and 6.5 that the JT coupling due to ν_7 and ν_8 vibrational modes is relatively strong in the $\widetilde{A}\ ^2E$ electronic state. Because of the strong JT coupling, a bimodal structure is obtained for the spectrum of the JT modes in this case [cf., Fig. 6.6(e and f)]. This is in good agreement with the nature of the experimental band structure. The non-degenerate $\widetilde{B}$ state is vertically located ∼0.13 and ∼0.17 eV above the $\widetilde{A}$ state in the EOMIP-CCSD and CASSCF-MRCI electronic structure data [cf., Table 6.8], respectively. As a result of this energetic proximity the spectrum of the $\widetilde{B}$ state was found to be highly overlapping with the $\widetilde{A}$ band in the experiment. The spectrum of panels

TABLE 6.10: Vibrational energy levels (in cm^{-1}) of the $\widetilde{X}\ ^2E$, $\widetilde{A}\ ^2E$ and $\widetilde{B}\ ^2A_1$ electronic states of $H_3CCCH^{\cdot+}$ obtained from the uncoupled state calculations using the EOMIP-CCSD energy data. The assignment of the levels carried out by examining the nodal pattern of the wave functions is included in the table.

$\widetilde{X}\ ^2E$				$\widetilde{A}\ ^2E$			$\widetilde{B}\ ^2A_1$	
Energy	Ref. [187]	Ref. [196]	Assignment	Energy	Ref. [187]	Assignment	Energy	Assignment
0			0^0_0	0		0^0_0	0	0^0_0
876	940	930±50	$\nu_5{}^1_0$	1024		$\nu_5{}^1_0$	917	$\nu_5{}^1_0$
1328			$\nu_4{}^1_0$	1304	1290	$\nu_4{}^1_0$	1497	$\nu_4{}^1_0$
1752			$\nu_5{}^2_0$	2048		$\nu_5{}^2_0$	1835	$\nu_5{}^2_0$
2169	1940	2000±50	$\nu_3{}^1_0$	2145		$\nu_3{}^1_0$	2018	$\nu_3{}^1_0$
2204			$\nu_4{}^1_0+\nu_5{}^1_0$	2328		$\nu_4{}^1_0+\nu_5{}^1_0$	2414	$\nu_4{}^1_0+\nu_5{}^1_0$
2628			$\nu_5{}^3_0$	2602		$\nu_4{}^2_0$	2752	$\nu_5{}^3_0$
2655			$\nu_4{}^2_0$	3073		$\nu_5{}^3_0$	2936	$\nu_3{}^1_0+\nu_5{}^1_0$
3046			$\nu_3{}^1_0+\nu_5{}^1_0$	3169		$\nu_3{}^1_0+\nu_5{}^1_0$	2991	$\nu_4{}^2_0$
3067			$\nu_2{}^1_0$	3178		$\nu_2{}^1_0$	3017	$\nu_2{}^1_0$
3080			$\nu_4{}^1_0+\nu_5{}^2_0$	3353		$\nu_4{}^1_0+\nu_5{}^2_0$	3332	$\nu_4{}^1_0+\nu_5{}^2_0$
3497			$\nu_1{}^1_0$	3449		$\nu_3{}^1_0+\nu_4{}^1_0$	3334	$\nu_1{}^1_0$
3498			$\nu_3{}^1_0+\nu_4{}^1_0$	3495		$\nu_1{}^1_0$	3515	$\nu_3{}^1_0+\nu_4{}^1_0$
3504			$\nu_4{}^5_0$	3626		$\nu_4{}^2_0+\nu_5{}^1_0$	3670	$\nu_5{}^4_0$
3531			$\nu_4{}^2_0+\nu_5{}^1_0$	3895		$\nu_4{}^3_0$	3853	$\nu_3{}^1_0+\nu_5{}^2_0$
3922			$\nu_3{}^1_0+\nu_5{}^2_0$	4097		$\nu_5{}^4_0$	3909	$\nu_4{}^2_0+\nu_5{}^1_0$
3943			$\nu_2{}^1_0+\nu_5{}^1_0$	4194		$\nu_3{}^1_0+\nu_5{}^2_0$	3935	$\nu_2{}^1_0+\nu_5{}^1_0$
3956			$\nu_4{}^1_0+\nu_5{}^3_0$	4202		$\nu_2{}^1_0+\nu_5{}^1_0$	4036	$\nu_3{}^2_0$
3980			$\nu_4{}^3_0$	4377		$\nu_4{}^1_0+\nu_5{}^3_0$	4252	$\nu_1{}^1_0+\nu_5{}^1_0$
4339			$\nu_3{}^2_0$	4482		$\nu_2{}^1_0+\nu_4{}^1_0$	5036	$\nu_2{}^1_0+\nu_3{}^1_0$
4373			$\nu_1{}^1_0+\nu_5{}^1_0$	4520		$\nu_1{}^1_0+\nu_5{}^1_0$	5352	$\nu_1{}^1_0+\nu_3{}^1_0$
4380			$\nu_5{}^5_0$	4651		$\nu_4{}^2_0+\nu_5{}^2_0$	6035	$\nu_2{}^2_0$
4395			$\nu_2{}^1_0+\nu_4{}^1_0$	4747		$\nu_3{}^1_0+\nu_4{}^2_0$		
4407			$\nu_4{}^2_0+\nu_5{}^2_0$	5218		$\nu_3{}^1_0+\nu_5{}^3_0$		
				5227		$\nu_2{}^1_0+\nu_5{}^2_0$		
				5323		$\nu_2{}^1_0+\nu_3{}^1_0$		
				5544		$\nu_1{}^1_0+\nu_5{}^2_0$		

TABLE 6.11: Same as in Table 6.10 obtained with the set of parameters derived from the CASSCF-MRCI energy data.

$\widetilde{X}\ ^2E$				$\widetilde{A}\ ^2E$			$\widetilde{B}\ ^2A_1$	
Energy	Ref. [187]	Ref. [196]	Assignment	Energy	Ref. [187]	Assignment	Energy	Assignment
0			0^0_0	0		0^0_0	0	0^0_0
876	940	930±50	$\nu_5{}^1_0$	1033		$\nu_5{}^1_0$	914	$\nu_5{}^1_0$
1341			$\nu_4{}^1_0$	1315	1290	$\nu_4{}^1_0$	1495	$\nu_4{}^1_0$
1753			$\nu_5{}^2_0$	2067		$\nu_5{}^2_0$	1828	$\nu_5{}^2_0$
2168	1940	2000±50	$\nu_3{}^1_0$	2156		$\nu_3{}^1_0$	1995	$\nu_3{}^1_0$
2218			$\nu_4{}^1_0+\nu_5{}^1_0$	2348		$\nu_4{}^1_0+\nu_5{}^1_0$	2409	$\nu_4{}^1_0+\nu_5{}^1_0$
2630			$\nu_5{}^3_0$	2622		$\nu_4{}^2_0$	2742	$\nu_5{}^3_0$
2680			$\nu_4{}^2_0$	3100		$\nu_5{}^3_0$	2909	$\nu_3{}^1_0+\nu_5{}^1_0$
3045			$\nu_3{}^1_0+\nu_5{}^1_0$	3183		$\nu_2{}^1_0$	2988	$\nu_4{}^2_0$
3067			$\nu_2{}^1_0$	3189		$\nu_3{}^1_0+\nu_5{}^1_0$	3016	$\nu_2{}^1_0$
3095			$\nu_4{}^1_0+\nu_5{}^2_0$	3382		$\nu_4{}^1_0+\nu_5{}^2_0$	3279	$\nu_1{}^1_0$
3504			$\nu_1{}^1_0$	3471		$\nu_3{}^1_0+\nu_4{}^1_0$	3323	$\nu_4{}^1_0+\nu_5{}^2_0$
3509			$\nu_3{}^1_0+\nu_4{}^1_0$	3499		$\nu_1{}^1_0$	3491	$\nu_3{}^1_0+\nu_4{}^1_0$
3557			$\nu_4{}^2_0+\nu_5{}^1_0$	3656		$\nu_4{}^2_0+\nu_5{}^1_0$	3656	$\nu_5{}^4_0$
3922			$\nu_3{}^1_0+\nu_5{}^2_0$	3922		$\nu_4{}^3_0$	3823	$\nu_3{}^1_0+\nu_5{}^2_0$
3944			$\nu_2{}^1_0+\nu_5{}^1_0$	4133		$\nu_5{}^4_0$	3902	$\nu_4{}^2_0+\nu_5{}^1_0$
3972			$\nu_4{}^1_0+\nu_5{}^3_0$	4216		$\nu_2{}^1_0+\nu_5{}^1_0$	3930	$\nu_2{}^1_0+\nu_5{}^1_0$
4017			$\nu_4{}^3_0$	4223		$\nu_3{}^1_0+\nu_5{}^2_0$	3991	$\nu_3{}^2_0$
4337			$\nu_3{}^2_0$	4312		$\nu_3{}^2_0$	4193	$\nu_1{}^1_0+\nu_5{}^1_0$
4381			$\nu_1{}^2_0+\nu_5{}^1_0$	4415		$\nu_4{}^1_0+\nu_5{}^3_0$		
4386			$\nu_5{}^5_0$	4498		$\nu_2{}^1_0+\nu_4{}^1_0$		
4408			$\nu_2{}^1_0+\nu_4{}^1_0$	4532		$\nu_1{}^1_0+\nu_5{}^1_0$		
				4689		$\nu_4{}^2_0+\nu_5{}^2_0$		
				4779		$\nu_3{}^1_0+\nu_4{}^2_0$		
				5256		$\nu_3{}^1_0+\nu_5{}^3_0$		
				5339		$\nu_2{}^1_0+\nu_3{}^1_0$		
				5346		$\nu_3{}^2_0+\nu_5{}^1_0$		

(g) and (h) of Fig. 6.6 is obtained by convoluting the partial stick spectra of uncoupled $\widetilde{A}$-$\widetilde{B}$ states along symmetric (panels (c) and (d)) and degenerate vibrational modes (panels (e) and (f)). The energetic proximity of the $\widetilde{A}$ and $\widetilde{B}$ electronic states leads to the observed complex, diffuse and overlapping $\widetilde{A}$-$\widetilde{B}$ vibronic band. The minimum of the seam of the $\widetilde{A}$-$\widetilde{B}$ CIs is located ∼0.30 (EOMIP-CCSD) and ∼0.66 eV (CASSCF-MRCI)

TABLE 6.12: Normal mode combinations, sizes of the primitive and single particle bases used in the MCTDH calculations. [a] The primitive basis consists of harmonic oscillator DVR functions, in the dimensionless normal coordinate required to represent the system dynamics along the relevant mode. The primitive basis for each particle is the product of the one-dimensional bases; [b] The SPF basis is the number of the single particle functions used.

Electronic state	Normal modes	Primitive basis[a]	SPF basis[b]	
$\widetilde{X}\ ^2E$	ν_1, ν_{6x}, ν_{6y}, ν_2	(6,10,10,8)	[8,8]	
	ν_4, ν_{7x}, ν_{7y}, ν_3	(16,14,14,14)	[8,8]	Fig. 6.10(b) and (c)
	ν_{8x}, ν_{8y}, ν_5	(16,16,10)	[8,8]	
	ν_{9x},ν_{9y},ν_{10x},ν_{10y}	(12,12,16,16)	[10,10]	
$\widetilde{A}\ ^2E$ &$\widetilde{B}\ ^2A_1$	ν_1, ν_{6x}, ν_{6y}, ν_2	(10,12,12,14)	[22,22,12]	
	ν_4, ν_{7x}, ν_{7y}, ν_3	(12,18,18,18)	[24,24,12]	Fig. 6.10(b) and (c)
	ν_{8x}, ν_{8y}, ν_5	(16,16,14)	[22,22,12]	
	ν_{9x}, ν_{9y},	(12,12)	[20,20,10]	

above the minimum of the $\widetilde{A}$ state [cf., Table 6.8]. Also, the energetic minimum of the $\widetilde{B}$ state is quasi-degenerate to that of the $\widetilde{A}$ state. This leads to a strong mixing of the vibronic levels of the $\widetilde{B}$ state with those of the $\widetilde{A}$ state. It can be seen from the bottom panels of this figure [cf., panels (g) and (h) of Fig. 6.6] that the convoluted spectrum is in good accord with the experimental spectrum.

In addition to the energetic location and excitation strength analysis, the assignment of the peaks is also confirmed by examining the nodal pattern of the vibrational wave functions. These wave functions are calculated by a block-improved relaxation method as implemented in the MCTDH program module [129, 159, 160]. In Figs. 6.7-6.9 we present a few vibrational wave functions of the $\widetilde{X}\ ^2E$, $\widetilde{A}\ ^2E$ and $\widetilde{B}\ ^2A_1$ states. In these figures, the wave function probability density is plotted in a suitable reduced dimensional space of normal coordinates.

Finally, the complete vibronic band structure of the $\widetilde{X}$-$\widetilde{A}$-$\widetilde{B}$ electronic states is calculated by including the relevant coupling among them. Understandably, this exercise is beyond the capability of the matrix diagonalization method employed for the uncoupled states. This task is therefore accomplished by the time-dependent WP propagation method employing the MCTDH suite of programs [131]. Because of large vertical energy separation of the $\widetilde{X}\ ^2E$ state from the $\widetilde{A}\ ^2E$ and $\widetilde{B}\ ^2A_1$ states, we have performed nuclear dynamical calculations for the $\widetilde{X}\ ^2E$ and $\widetilde{A}\ ^2E$-$\widetilde{B}\ ^2A_1$ electronic states separately. Both EOMIP-CCSD and CASSCF-MRCI Hamiltonian parameters are employed in the calculations. All 15 vibrational modes are included for the $\widetilde{X}\ ^2E$ state and 13 relevant vibrational modes are included for the $\widetilde{A}\ ^2E$-$\widetilde{B}\ ^2A_1$ states. Five WP calculations are carried out by launching the initial WP on each of the five (two components of the JT split $\widetilde{X}$ and $\widetilde{A}$

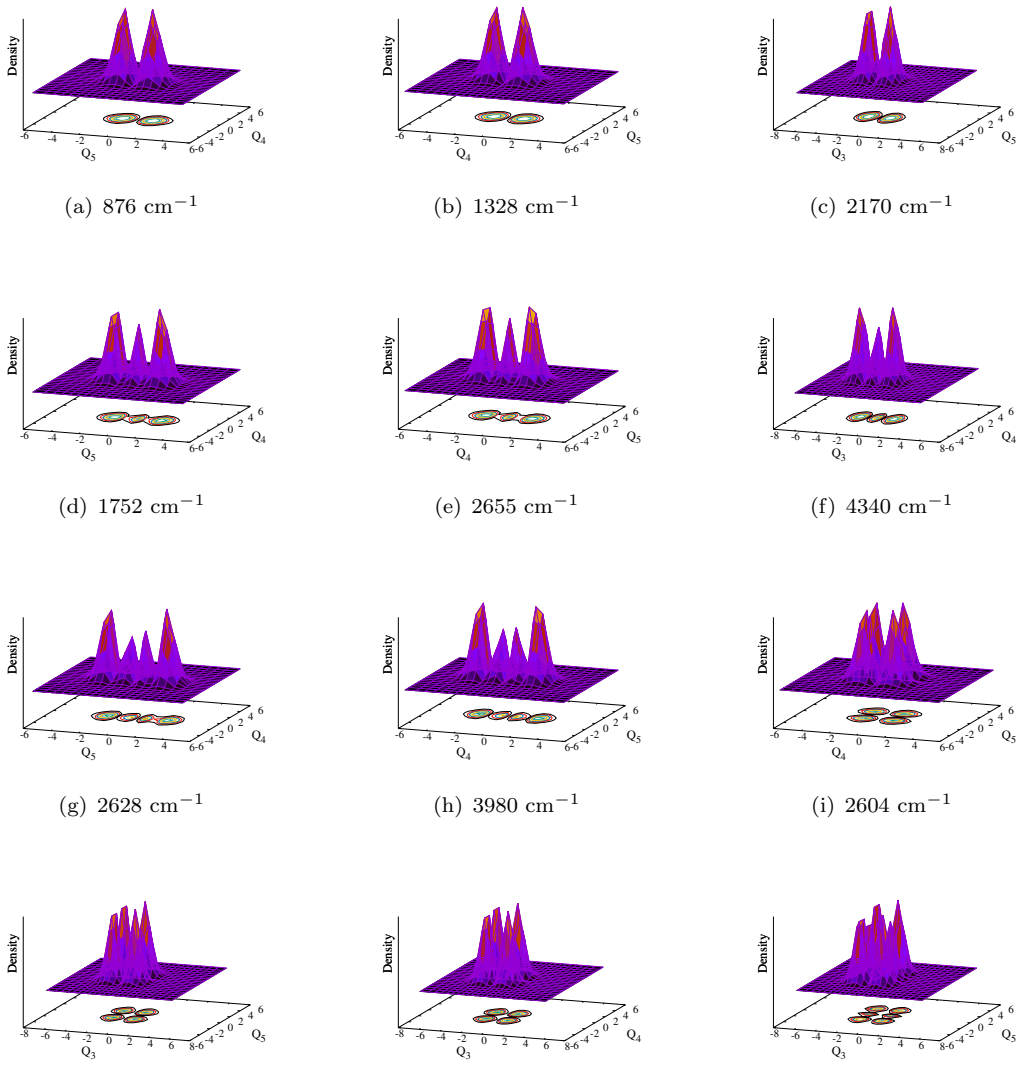

(a) 876 cm^{-1} (b) 1328 cm^{-1} (c) 2170 cm^{-1}

(d) 1752 cm^{-1} (e) 2655 cm^{-1} (f) 4340 cm^{-1}

(g) 2628 cm^{-1} (h) 3980 cm^{-1} (i) 2604 cm^{-1}

(j) 3046 cm^{-1} (k) 3498 cm^{-1} (l) 3922 cm^{-1}

FIGURE 6.7: Probability density of vibronic wave functions of the $\widetilde{X}\ ^2E$ electronic state of $H_3CCCH^{\cdot+}$ as a function of nuclear coordinate. The EOMIP-CCSD Hamiltonian parameters are used in the calculations. Panels a-c and d-f represent the fundamentals and first overtone of ν_5, ν_4 and ν_3 vibrational modes, respectively. Panels g and h represent the second overtone of ν_5 and ν_4 modes. The wave functions in panels i-l represent the combination peaks of ν_5, ν_4 andν_3 modes.

state plus the $\widetilde{B}$ state) electronic states separately. The details of the mode combination and the sizes of the basis sets are given in Table 6.12. In each calculation WP is propagated for 200 fs. The time autocorrelation function is damped with an exponential function of relaxation time 33 fs for all electronic states, and then Fourier transformed to generate the spectrum. The results from five different calculations are combined with equal weightage to generate the composite theoretical band shown in Fig. 6.10, along with the available experimental results reproduced from Ref. [187]. It can be seen from

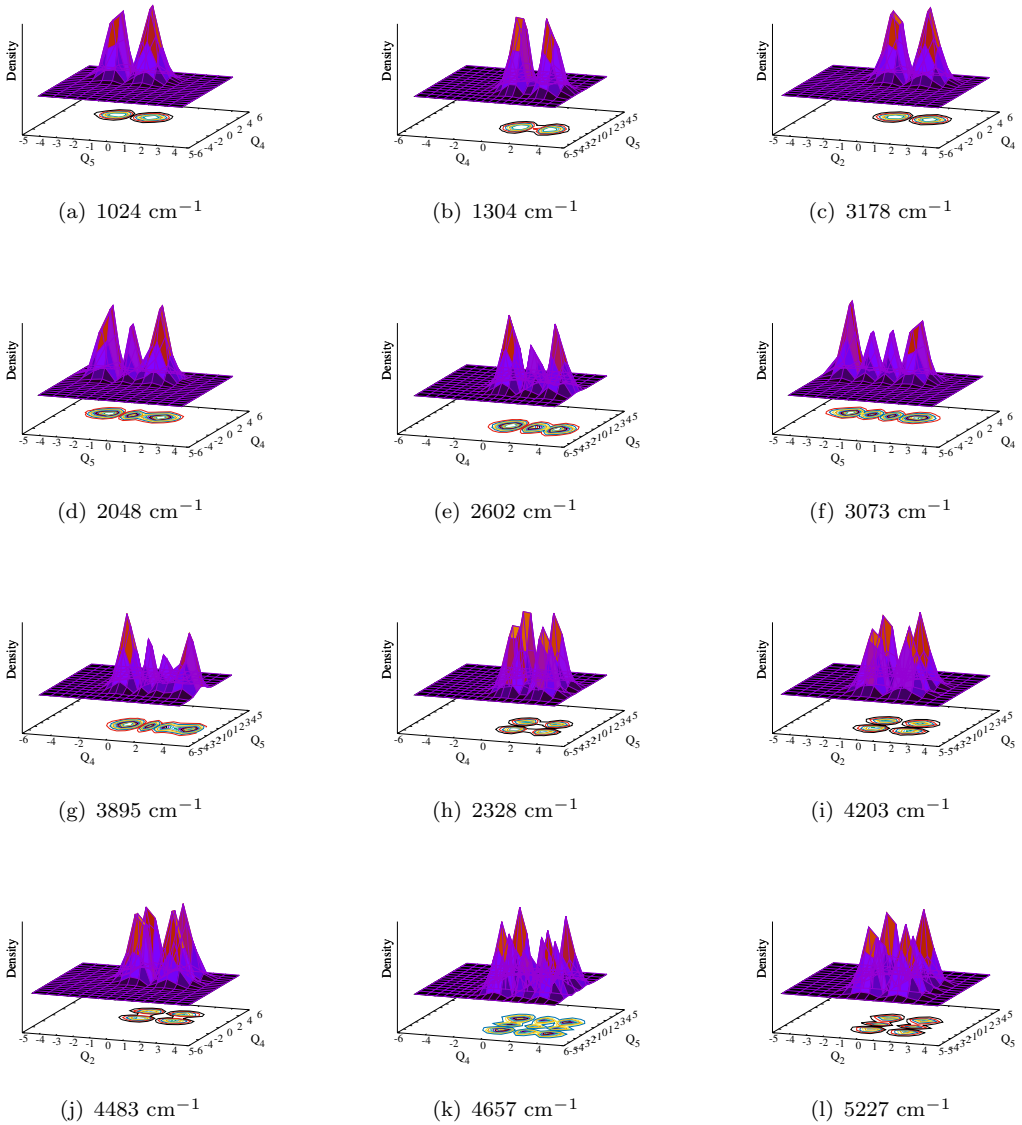

(a) 1024 cm^{-1} (b) 1304 cm^{-1} (c) 3178 cm^{-1}

(d) 2048 cm^{-1} (e) 2602 cm^{-1} (f) 3073 cm^{-1}

(g) 3895 cm^{-1} (h) 2328 cm^{-1} (i) 4203 cm^{-1}

(j) 4483 cm^{-1} (k) 4657 cm^{-1} (l) 5227 cm^{-1}

FIGURE 6.8: Probability density of vibronic wave functions of the $\widetilde{A}\ ^2E$ electronic state of $H_3CCCH^{\cdot+}$ as a function of nuclear coordinate. The EOMIP-CCSD Hamiltonian parameters are used in the calculations. Panels a-c and d-e represent the fundamentals and first overtone of ν_5, ν_4 and ν_2 vibrational modes, respectively. Panels f and g represent the second overtone of ν_5 and ν_4 modes. The wave functions in panels h-l represent the combination peaks of ν_5, ν_4 andν_2 modes.

the figure that the present theoretical results are in very good agreement with the experimental results [187]. While the first band is formed by the $\widetilde{X}\ ^2E$ state the second band is formed by highly overlapping $\widetilde{A}\ ^2E$ and $\widetilde{B}\ ^2A_1$ electronic states.

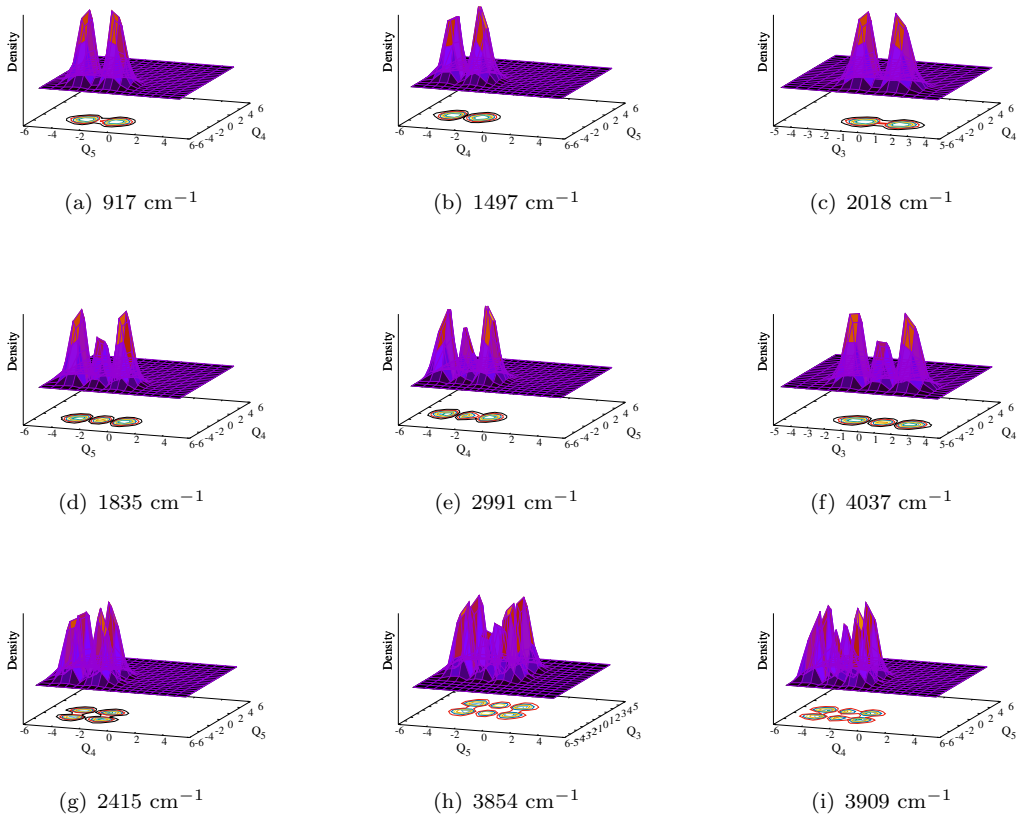

(a) 917 cm^{-1} (b) 1497 cm^{-1} (c) 2018 cm^{-1}

(d) 1835 cm^{-1} (e) 2991 cm^{-1} (f) 4037 cm^{-1}

(g) 2415 cm^{-1} (h) 3854 cm^{-1} (i) 3909 cm^{-1}

FIGURE 6.9: Probability density of vibronic wave functions of the $\widetilde{B}\ ^2A_1$ electronic state of $H_3CCCH^{\cdot+}$ as a function of nuclear coordinate. The EOMIP-CCSD Hamiltonian parameters are used in the calculations. Panels a-c and d-f represent the fundamentals and first overtone of ν_5, ν_4 and ν_3 vibrational modes, respectively. The wave functions in panels g-i represent the combination peaks of ν_5, ν_4 andν_3 modes.

6.2.4 Diabatic electronic population

In order to understand the impact of complex nonadiabatic coupling on the dynamics of the $\widetilde{X}\ ^2E$, $\widetilde{A}\ ^2E$ and $\widetilde{B}\ ^2A_1$ electronic states, the time-dependence of the diabatic electronic populations in the coupled (i.e., $\widetilde{X}\ ^2E$-$\widetilde{A}\ ^2E$-$\widetilde{B}\ ^2A_1$) electronic states of $H_3CCCH^{\cdot+}$ is recorded and discussed in this section. The electronic populations obtained by initially locating the WP on two components of the JT split $\widetilde{X}\ ^2E$, $\widetilde{A}\ ^2E$ and the $\widetilde{B}\ ^2A_1$ states are shown in columns (i) and (ii) of Fig. 6.11 calculated with the EOMIP-CCSD and CASSCF-MRCI parameters, respectively. It can be seen from panels (a) and (b) that when the WP is initially excited to the $\widetilde{X}\ ^2E$ state the electronic population moves back and forth between its two components driven solely by the JT CIs and exhibits an exact mirror image behavior.

The population curve for an initial location of the WP on the $\widetilde{A}\ ^2E$ state shown in panels (c) and (d) of Fig. 6.11. It can be seen that, a very little amount (∼1%) of population

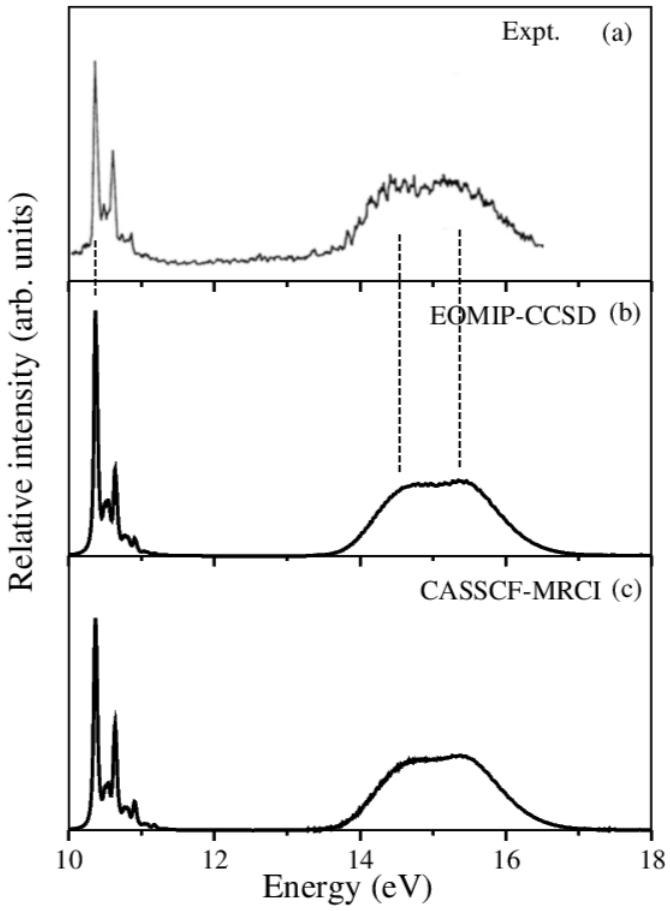

FIGURE 6.10: Vibronic band structure of the coupled $\widetilde{X}\ ^2E$-$\widetilde{A}\ ^2E$-$\widetilde{B}\ ^2A_1$ electronic states of $H_3CCCH^{\cdot+}$. Relative intensity (in arbitrary units) is plotted as a function of the energy of the vibronic states of $H_3CCCH^{\cdot+}$. Experimental spectrum reproduced from Ref. [187] is shown in panel (a). The present theoretical results obtained with the EOMIP-CCSD and CASSCF-MRCI Hamiltonian parameters are shown in panels (b) and (c), respectively.

is transferred to the $\widetilde{B}\ ^2A_1$ state in this situation. This is due to the fact that the CI of the $\widetilde{A}\ ^2E$ state with the $\widetilde{B}\ ^2A_1$ state is located at ∼0.3 eV above the minimum of the $\widetilde{A}\ ^2E$ state and it is not accessible to the WP during its evolution on this state. Most of the population moves back and forth between the x and y component of the $\widetilde{A}\ ^2E$ state. Initially, the population decreases sharply within a short time of about ∼3 fs and then increases slightly. Again it decreases to ∼0.3 within a short time of about ∼40 fs and then increases slightly up to ∼60 fs. Then after remains constant between ∼0.4 and ∼0.6 at longer times. The population profiles provided in the panels (c) and (d) of Fig. 6.11 are qualitatively same, but quantitatively very different. This is because of quantitatively different coupling parameters that result from the EOMIP-CCSD and CASSCF-MRCI methods. The time-dependence of electronic populations for an initial location of the WP on the $\widetilde{B}\ ^2A_1$ state is shown in panels (e) and (f) of Fig. 6.11. In this case ∼40% of the population is transferred to both x and y components of the $\widetilde{A}\ ^2E$

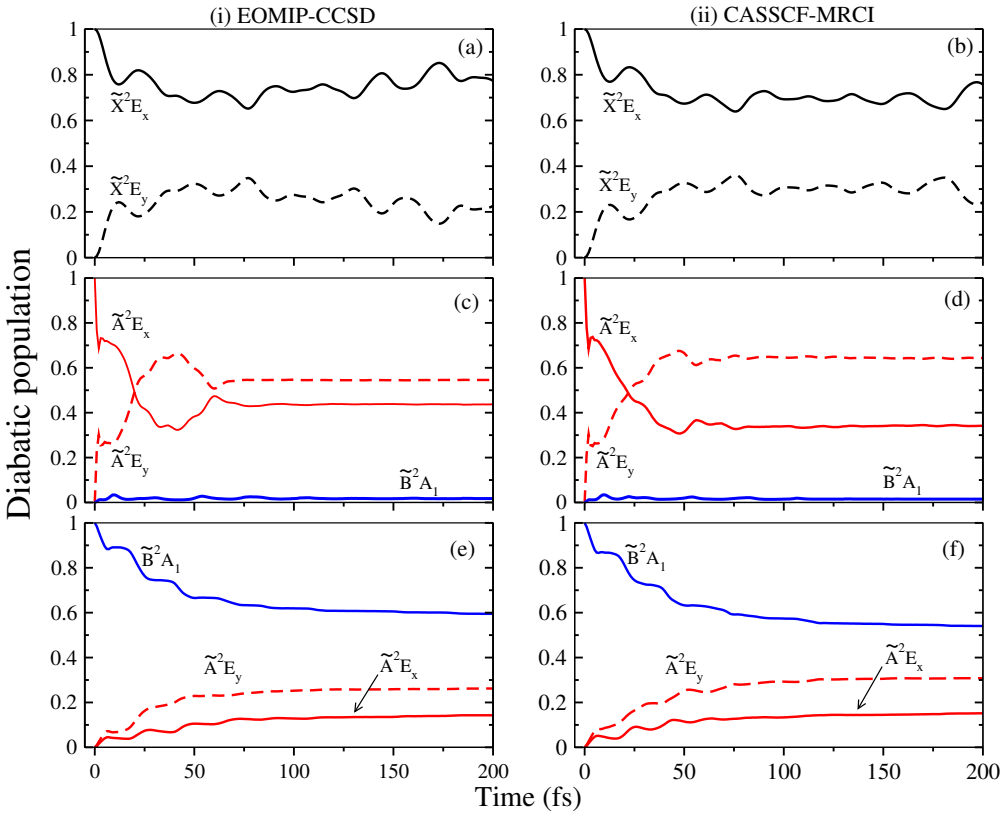

FIGURE 6.11: Time-dependence of diabatic electron populations during the evolution of the WP in the coupled $\widetilde{X}\ ^2$E-$\widetilde{A}\ ^2$E-$\widetilde{B}\ ^2A_1$ electronic states. Population curves of these states are obtained with the Hamiltonian parameters derived from both EOMIP-CCSD (column (i)) and CASSCF-MRCI (column (ii)) electronic energies. The population curve for the initial location of the WP on the x component of $\widetilde{X}$ and $\widetilde{A}$ states and on the $\widetilde{B}$ states are shown in panels (a-b), (c-d) and (e-f), respectively.

state (i.e., internal conversion) *via* the PJT coupling and CI between $\widetilde{A}\ ^2$E and $\widetilde{B}\ ^2A_1$ states. It can be seen that the PJT coupling effect between the $\widetilde{A}$ and $\widetilde{B}$ states is not particularly strong. The complex band structure of the $\widetilde{A}$ and $\widetilde{B}$ states arises solely from their energetic proximity.

The behavior mentioned above is to be contrasted with the findings on the JT and PJT coupling effects in isomeric allene radical cation [83]. In the latter the PJT coupling between the $\widetilde{A}\ ^2$E and $\widetilde{B}^2B_2$ states is very strong. Due to this, ∼50% of the $\widetilde{B}^2B_2$ state population decays within ∼5 fs when the WP is initially located on the $\widetilde{B}^2B_2$ state, and within ∼20 fs almost ∼90% of the population decays from this state [see Fig. 5 of Ref. [83]] Therefore, while the strong PJT coupling between the $\widetilde{A}\ ^2$E and $\widetilde{B}^2B_2$ states of the allene radical cation gives rise to broad and diffuse vibronic bands, the energetic proximity of the electronic states leads to the same kind of broad and diffuse vibronic bands in the isomeric propyne radical cation.

6.3 Summary

Impact of JT and PJT interactions on the photo-ionization spectroscopy of H_3CCCH is examined in this chapter. The theoretical results are compared with the experimental recording by Baker *et al.* [187]. The equilibrium geometry of the reference electronic ground state of the H_3CCCH is optimized at the MP2 level of theory. The potential energy surfaces of the $\widetilde{X}\ ^2E$, $\widetilde{A}\ ^2E$ and $\widetilde{B}\ ^2A_1$ electronic states of propyne radical cation are calculated along the dimensionless normal displacement coordinates of the electronic ground state of H_3CCCH (reference geometry) using both EOMIP-CCSD and CASSCF-MRCI *ab initio* quantum chemistry methods. With the aid of the electronic structure results, a higher-order model vibronic Hamiltonian is constructed in a diabatic electronic basis in terms of dimensionless normal displacement coordinate of vibrational modes. It is found that the $\widetilde{X}\ ^2E$ electronic state is energetically well separated from the $\widetilde{A}\ ^2E$ and $\widetilde{B}\ ^2A_1$ states at the Franck-Condon geometry. Similar results were obtained for the allene radical cation [80–83]. The curve crossings between the $\widetilde{A}\ ^2E$ and $\widetilde{B}\ ^2A_1$ electronic states along the ν_1-ν_5 vibrational modes of the propyne radical cation are found.

Nuclear dynamics calculations are carried out from first principles by time-independent and time-dependent methods. The individual vibronic bands are systematically analyzed. It is observed that the JT effect due to the e vibrational modes in the $\widetilde{A}\ ^2E$ electronic manifold of $H_3CCCH^{\cdot+}$ is stronger compared to the $\widetilde{X}\ ^2E$ state. The PJT coupling of e vibrational modes between the $\widetilde{A}\ ^2E$-$\widetilde{B}\ ^2A_1$ electronic states is weak. However, because of the energetic proximity the band structure of the $\widetilde{A}\ ^2E$-$\widetilde{B}\ ^2A_1$ electronic states is highly overlapping and diffuse. In the first vibrational band due to the $\widetilde{X}\ ^2E$ state, C≡C stretching vibrational mode ν_3 is strongly excited and excitation of ν_4 and ν_5 vibrational modes is weak. Also, among the JT active e vibrational modes, ν_8 and ν_{10} are weakly excited in this band and the JT coupling effect is weak in this band. The second photo-ionization band is due to strongly overlapping $\widetilde{A}\ ^2E$ and $\widetilde{B}\ ^2A_1$ electronic states of $H_3CCCH^{\cdot+}$. In case of the JT active $\widetilde{A}\ ^2E$ electronic state, ν_4, ν_7 and ν_8 vibrational modes are strongly excited and the excitation of ν_2, ν_5 and ν_6 modes is moderate. Because of the fairly strong JT coupling strength of the degenerate ν_7 and ν_8 vibrational modes, a bimodal structure of $\widetilde{A}\ ^2E$ vibronic band is observed. This is in good agreement with the experimental band structure. Dominant excitation of both ν_4 and ν_5 vibrational modes is found in $\widetilde{B}\ ^2A_1$ electronic state. The final theoretical results so obtained are in good agreement with the available experimental results. The close proximity of the minimum energies of both $\widetilde{A}\ ^2E$ and $\widetilde{B}\ ^2A_1$ states leads to broad, diffuse and overlapping vibronic band for the $\widetilde{A}\ ^2E$ and $\widetilde{B}\ ^2A_1$ electronic states of $H_3CCCH^{\cdot+}$.

The time-dependence of the diabatic electronic population for an initial location of the WP on the $\widetilde{B}\ ^2A_1$ state reveals that ∼40% of population is transferred to the $\widetilde{A}\ ^2E$ state

via the PJT coupling and CI between $\widetilde{\mathrm{A}}\ ^2\mathrm{E}$ and $\widetilde{\mathrm{B}}\ ^2\mathrm{A}_1$ states. It is found that the PJT coupling between these states is not so strong. The complex band structure of the $\widetilde{\mathrm{A}}\ ^2\mathrm{E}$ and $\widetilde{\mathrm{B}}\ ^2\mathrm{A}_1$ states arises solely from their energetic proximity. This is in contrast to the effects in the vibronic band structure of the $\widetilde{\mathrm{A}}\ ^2\mathrm{E}$-$\widetilde{B}^2B_2$ electronic states of the isomeric allene radical cation. In the latter, the PJT coupling among the $\widetilde{\mathrm{A}}\ ^2\mathrm{E}$-$\widetilde{B}^2B_2$ states is particularly strong leading to a very fast decay of the population of the $\widetilde{B}^2B_2$ state and diffuse vibronic bands.

Chapter 7

Summary and outlook

In this thesis, a detailed theoretical description of vibronic interactions in the photo-induced polyatomic molecular systems is presented: More specifically, the excited state dynamics of PFBz, HFBz and Propyne molecules is investigated by employing the state-art-of-the *ab initio* quantum chemistry calculations and the quantum dynamical methods. Vibronic coupling is established to be an important mechanism governing the dynamics in their excited electronic states. The complex vibronic spectra, dominant vibrational progressions, electronic population transfer process at the CIs, nonradiative decay rate and the effect of fluorination on the broadening of the spectra and emission properties are investigated in detail. The theoretical findings are compared with the available experimental results. The theoretical results are generally found to be in good accord with the experimental data. The diabatic electronic representation has been introduced and used to deal with the PESs crossings and to avoid the singular nature of the nuclear kinetic coupling term of the adiabatic electronic representation. Model vibronic Hamiltonian is devised in this basis using elementary symmetry selection rules and the relevant coupling parameters of the Hamiltonian are extracted from *ab initio* electronic structure results. The spectroscopic implications of the JT and PJT effects and vibronic interactions are probed through photoelectron/absorption spectroscopic experiments. The vibronic bands are calculated by solving the both time-independent and time-dependent Schrödinger equation using the MCTDH program module. The major findings of the present thesis are given below.

Chapter 3:
A detailed theoretical account of vibronic coupling among the energetically lowest eight singlet excited electronic states of PFBz is presented in this chapter. The computed optical absorption spectrum of PFBz is compared with the available experimental results of Philis *et al.* [63] and Hüter *et al.* [60]. Along with this, we examined the role of

optically dark $\pi\sigma^*$ states on the quantum dynamics of optically bright $\pi\pi^*$ states of PFBz. The adiabatic electronic energies of the lowest eight excited electronic states are calculated along the dimensionless normal displacement coordinates using EOM-CCSD/aug-cc-pCDZ level of theory with the aid of the MOLPRO suite of programs. A detailed topographical analysis of the eight adiabatic electronic states is carried out and multiple conical intersections among them are established. With electronic structure results, a higher-order model vibronic Hamiltonian of the eight coupled electronic states is developed in a diabatic electronic basis. It is found that the vibronic coupling between optically active ($\pi\pi^*$) and optically dark ($\pi\sigma^*$) states is quite strong. The strong vibronic coupling between the S_1 ($\pi\pi^*$) and S_2 ($\pi\sigma^*$) states causes the lowering of symmetry of the lowest excited adiabatic S_1-S_2 coupled potential energy surface and leads to a symmetric double-well type of potential, which stabilizes the molecule along with the out-of-plane modes of b_1 symmetry. The minimum of the last four (S_5, S_6, S_7, and S_8) excited electronic states is quasi-degenerate with their intersection minimum. For a detailed interpretation of the experimental results, 22 relevant vibrational modes and all possible nonadiabatic couplings between the eight electronic states of the Hamiltonian are considered in the dynamical calculations.

The results show that the first absorption band, $S_1 \leftarrow S_0$, is structureless due to collective effect of the out-of-plane b_1 vibrational modes in addition to strong S_1-S_2 nonadiabatic coupling. Shallow minima on the potential are found at large internuclear displacements along the b_1 modes. This causes a spreading of the WP and the broadening of the S_1 band. A new additional broad band appears at about 5.85 eV (marked as C-band in the literature [63]) near the onset of the second band. This is attributed to the $\pi \rightarrow \sigma^*$ type transition to both S_2 and S_3 states. This new band is absent in the parent Bz and the lower fluroderivatives.

Chapter 4:

The vibronic coupling and quantum nuclear dynamics in the coupled six electronic states of $PFBz^+$ is studied using a state-of-the-art theoretical approach. The respective PESs are computed using the EOMIP-CCSD and CASSCF-MRCI methods. It appears from the electronic structure data and subsequent dynamical results that the EOMIP-CCSD method does a superior job in this case. It is by no means a conclusive remark in the absence of high resolution spectroscopy data. It is established that the energetically lowest six electronic states separates into two groups viz., $\widetilde{X}\ ^2A_2$-$\widetilde{A}\ ^2B_1$ and $\widetilde{B}\ ^2B_1$-$\widetilde{C}\ ^2B_2$-$\widetilde{D}\ ^2A_1$-$\widetilde{E}\ ^2B_2$. The $\widetilde{X}\ ^2A_2$ and $\widetilde{A}\ ^2B_1$ states form energetically accessible CIs. The effect of the latter on the dynamics of $\widetilde{X}\ ^2A_2$ state is not as much as on the same on the $\widetilde{A}\ ^2B_1$ state. This is because the minimum of the $\widetilde{X}\ ^2A_2$ state is energetically well separated from the minimum of the $\widetilde{X}\ ^2A_2$-$\widetilde{A}\ ^2B_1$ CIs. The minimum of the $\widetilde{A}\ ^2B_1$ state on the other hand is energetically very close to the minimum of the $\widetilde{X}\ ^2A_2$-$\widetilde{A}\ ^2B_1$ intersections.

Therefore, the $\widetilde{X}\ ^2A_2$-$\widetilde{A}\ ^2B_1$ coupling has a significant effect on the vibronic structure of the $\widetilde{A}\ ^2B_1$ state.

It is found that the $\widetilde{B}\ ^2B_1$ state is energetically well separated from the rest of the states. The coupling of $\widetilde{B}\ ^2B_1$ state with others therefore has no significant effect on the vibronic structure of the $\widetilde{B}\ ^2B_1$ state. The population of this state remains ∼100% for a long time when the dynamics started on it. The radiative emission in $PFBz^+$ is therefore originates from this state. The $\widetilde{C}\ ^2B_2$-$\widetilde{D}\ ^2A_1$-$\widetilde{E}\ ^2B_2$ electronic states are energetically close and therefore give rise to highly overlapping vibronic bands. The theoretical results are shown to be in good accord with available experimental results.

Chapter 5:
In continuation with Chapter 4, the theoretical photoelectron spectroscopy of HFBz and its radiative emission and nonradiative decay dynamics are studied. That is, a detailed theoretical account of multi-mode JT and PJT interactions in the ground ($\widetilde{X}\ ^2E_{1g}$) and three lowest excited states ($\widetilde{A}\ ^2A_{2u}$, $\widetilde{B}\ ^2B_{2u}$ and $\widetilde{C}\ ^2E_{2g}$) of $HFBz^+$ were examined in this chapter. It is found that all the electronic states are energetically well separated from each other at the Franck-Condon geometry. However, the couplings between them are strong enough, and the curve crossing between the $\widetilde{B}\ ^2B_{2u}$ and $\widetilde{C}\ ^2E_{2g}$ states along the ν_{15} vibrational mode of the $HFBz^+$ is found.

It is observed that the JT effect due to e_{2g} vibrational modes in the $\widetilde{X}\ ^2E_{1g}$ state is more substantial as compared to the $\widetilde{C}\ ^2E_{2g}$ electronic state. In the four vibrational band structures, both a_{1g} and $e_{[}2g]$ vibrational modes are excited according to their excitation strength. Investigation of structure and dynamics of the $\widetilde{X}\ ^2E_{1g}$-$\widetilde{A}\ ^2A_{2u}$-$\widetilde{B}\ ^2B_{2u}$-$\widetilde{C}\ ^2E_{2g}$ electronic states of the $HFBz^+$ reveals that 20 (out of 45) vibrational modes are relevant for the dynamical calculations. It is found that both $\widetilde{A}\ ^2A_{2u}$ and $\widetilde{B}\ ^2B_{2u}$ electronic states are well separated from the rest of the states. Therefore, the PJT coupling of these states with other states have no effect on the vibronic structure of $\widetilde{A}\ ^2A_{2u}$ and $\widetilde{B}\ ^2B_{2u}$ states. The time-dependence of the diabatic electronic population reveals that the population of the $\widetilde{A}\ ^2A_{2u}$ state remains ∼100% for a long time when the dynamics started on it. Similarly, when the WP is located on the $\widetilde{B}\ ^2B_{2u}$ state a minimal amount (∼2%) of population is transferred to the two components of the $\widetilde{C}\ ^2E_{2g}$ state only. This leads to the long-lived nature of the $\widetilde{A}\ ^2A_{2u}$ and $\widetilde{B}\ ^2B_{2u}$ electronic states, and these states contribute to the observed fluorescence emission in $HFBz^+$.

Chapter 6:
The JT and PJT effects in the $\widetilde{X}\ ^2E$, $\widetilde{A}\ ^2E$ and $\widetilde{B}\ ^2A_1$ electronic states of propyne radical cation ($H_3CCCH^{\cdot+}$) are investigated with the aid of *ab initio* quantum chemistry calculations and first-principles of quantum dynamics simulations. The PESs of these states are calculated long the dimensionless normal displacement coordinates of the

electronic ground state of H_3CCCH (reference geometry) using both EOMIP-CCSD and CASSCF-MRCI *ab initio* quantum chemistry methods. With the aid of electronic structure results, a higher-order model vibronic Hamiltonian is constructed in a diabatic electronic basis. It is found that the $\widetilde{X}\ ^2E$ state is energetically well separated from the other excited states at the Franck-Condon geometry. Similar results were obtained for the allene radical cation [80–83]. The curve crossings between the $\widetilde{A}\ ^2E$ and $\widetilde{B}\ ^2A_1$ electronic states along the ν_1-ν_5 vibrational modes of the $H_3CCCH^{\cdot+}$ are found.

It is observed that the JT effect is weak in the $\widetilde{X}\ ^2E$ state as compared to that in the $\widetilde{A}\ ^2E$ state. Because of the large energy separation, the PJT coupling among the JT-split components of the $\widetilde{X}\ ^2E$ state with the neighboring states is also weak. However, the PJT coupling of the $\widetilde{B}\ ^2A_1$ state with the JT-split components of the $\widetilde{A}\ ^2E$ state has some impact of each of these states is calculated and compared with the experimental results.

The time-dependence of the diabatic electronic population for an initial location of the WP on the $\widetilde{B}\ ^2A_1$ state reveals that ∼40% of population is transferred to the $\widetilde{A}\ ^2E$ state *via* the PJT coupling and CIs between the $\widetilde{A}\ ^2E$ and $\widetilde{B}\ ^2A_1$ state. It is found that the PJT coupling between these states is not so strong. The complex band structure of the $\widetilde{A}\ ^2E$ and $\widetilde{B}\ ^2A_1$ states arises solely from their energetic proximity. This is in contrast to the effects in the vibronic band structure of the $\widetilde{A}\ ^2E$-$\widetilde{B}\ ^2B_2$ electronic states of the isomeric Allene radical cation. In the latter, the PJT coupling among the $\widetilde{A}\ ^2E$-$\widetilde{B}\ ^2B_2$ states is particularly strong leading to a very fast decay of the population of the $\widetilde{B}\ ^2B_2$ state and diffuse vibronic bands.

Future directions:

(1). The possible extension of this work necessarily requires the inclusion of rotational degree of freedom in the present vibronic coupling model Hamiltonian to obtain information on rovibronic levels of isolated molecules.

(2). The present work is restricted to vibronic coupling of electronic states with same spin multiplicities (e.g., singlet-singlet). This study can be further extended to the systematic investigation of vibronic coupling for electronic states of different spin multiplicities (e.g., singlet-triplet).

(3). It is another challenge for future research to extend the theory and *ab initio* computations to heavy-metal (especially, tetra- and octa-hedral) complexes. For these complexes higher-order vibronic coupling models are required to satisfactorily describe high-resolution measurements.

(4). With the expertise gained from the work of this thesis, study of the laser control of polyatomic molecular systems using optimal control theory (OCT) which is implemented in the MCTDH program module. In this regard a problem that we have in mind

in near future is the control of quantum yield of fluorescence from S_2 state of HFBz in the presence of CIs with S_1 along the totally symmetric vibrational modes using OCT-MCTDH.

Appendix A

Symmetry considerations for JT and PJT coupling terms

In the following, the diabatic potential matrix for the $E\otimes e$-JT and $(E + A)\otimes e$-PJT system up to sixth-order is derived for a general molecule with a $\hat{C}_3$ main rotational axis.

A.0.1 Derivation of $E\otimes e$ JT Hamiltonian

As minimum symmetry element to have the degenerate electronic state is the presence of a three fold rotational axis we can start from this point to construct the Hamiltonian. The molecule here under the study is propyne and that also falls under the same category. The components of coordinate (x,y) will be denoted as (Q_x, Q_y).
In this situation it is convenient to use polar coordinates (ρ, θ) in the x-y plane.

$$Q_x = \rho cos\theta; \quad Q_y = \rho sin\theta \tag{A.1}$$

Now we define the complex coordinates, Q_+ and Q_- as

$$Q_+ = Q_x + iQ_y = \rho(cos\theta + isin\theta) = \rho e^{i\theta} \tag{A.2}$$
$$Q_- = Q_x + iQ_y = \rho(cos\theta - isin\theta) = \rho e^{-i\theta} \tag{A.3}$$

Now introducing the effect of $\hat{C}_3$ operation on the coordinates i.e., a $2\pi/3$ rotation we get

$$\begin{aligned}\hat{C}_3 Q_x = \hat{C}_3 \rho cos\theta = \rho cos\left(\frac{2\pi}{3}+\theta\right) &= cos(2\pi/3).\rho cos\theta - sin(2\pi/3).\rho sin\theta \\ &= cos(2\pi/3)Q_x - sin(2\pi/3)Q_y \end{aligned} \tag{A.4}$$

$$\begin{aligned}\hat{C}_3 Q_y = \hat{C}_3 \rho sin\theta = \rho sin\left(\frac{2\pi}{3}+\theta\right) &= cos(2\pi/3).\rho sin\theta + sin(2\pi/3).\rho cos\theta \\ &= sin(2\pi/3)\mathcal{Q}_x + cos(2\pi/3)\mathcal{Q}_y \end{aligned} \tag{A.5}$$

$$\begin{aligned}\hat{C}_3 Q_+ &\Rightarrow \hat{C}_3(Q_x + iQ_y) \\ &\Rightarrow \hat{C}_3 Q_x + i\hat{C}_3 Q_y \\ &\Rightarrow cos(2\pi/3)Q_x - sin(2\pi/3)Q_y + i\left[sin(2\pi/3)Q_x + cos(2\pi/3)Q_y\right] \\ &\Rightarrow \left[cos(2\pi/3) + isin(2\pi/3)\right]Q_x + i\left[cos(2\pi/3) + isin(2\pi/3)\right]Q_y \\ &\Rightarrow e^{2\pi i/3}Q_x + ie^{2\pi i/3}Q_y \\ &\Rightarrow e^{2\pi i/3}[Q_x + iQ_y]. \end{aligned} \tag{A.6}$$

So, $\hat{C}_3 Q_+ = e^{+2\pi i/3}Q_+$ and similarly $\hat{C}_3 Q_- = e^{-2\pi i/3}Q_-$
Hence, a $(2\pi/3)$ rotation yields the multiplication of the complex coordinate with a complex factor $e^{\pm 2\pi i/3}$. We express the transformation in a matrix form as,

$$\hat{C}_3 \begin{pmatrix} Q_+ \\ Q_- \end{pmatrix} = \begin{pmatrix} e^{2\pi i/3} & 0 \\ 0 & e^{-2\pi i/3} \end{pmatrix} \begin{pmatrix} Q_+ \\ Q_- \end{pmatrix} \tag{A.7}$$

The components of the degenerate electronic state are also transformed (x,y) to (Φ_x, Φ_y). As done for the nuclear coordinates we define also a set of complex functions,

$$|\Phi_+\rangle = \frac{1}{\sqrt{2}}(\Phi_x + i\Phi_y), \quad |\Phi_-\rangle = \frac{1}{\sqrt{2}}(\Phi_x + i\Phi_y) \tag{A.8}$$

The electronic wave functions are transformed accordingly by the rotation as

$$\hat{C}_3\langle\Phi_+| = e^{+2\pi i/3}\langle\Phi_+| \text{ and } \hat{C}_3\langle\Phi_-| = e^{-2\pi i/3}\langle\Phi_-| \tag{A.9}$$

$$\hat{C}_3|\Phi_+\rangle = e^{-2\pi i/3}|\Phi_+\rangle \text{ and } \hat{C}_3|\Phi_-\rangle = e^{+2\pi i/3}|\Phi_-\rangle. \tag{A.10}$$

Therefore, in the complex representation the coordinates Q_+ and Q_- and the state functions $\langle\Phi_+|$ and $\langle\Phi_-|$ are eigenfunctions of the symmetry operator $\hat{C}_3$ (rotation by $2\pi/3$) with eigenvalues $e^{\pm 2\pi i/3}$. $Q_\pm$ and $\Phi_\pm$ are the most suitable coordinates and functions

to use, since they are adapted to the symmetry of the problem.

Let us now consider the matrix elements of the electronic Hamiltonian in the $\Phi_\pm$ basis set up to second order in the coordinates $Q_\pm$

$$|\Phi_+\rangle\hat{H}_{el}\langle\Phi_+| = \mathcal{D}^{(0)}+\mathcal{D}^{(1)}_+Q_+ + \mathcal{D}^{(1)}_-Q_- + \frac{1}{2!}\mathcal{D}^{(2)}_{++}Q_+Q_+ + \frac{1}{2!}\mathcal{D}^{(2)}_{--}Q_-Q_- + \frac{1}{2!}\mathcal{D}^{(2)}_{+-}Q_+Q_- + \cdots \tag{A.11}$$

If $\hat{C}_3$ is applied on this equation, then the left side is multiplied by 1 (as $e^{-2\pi i/3}.e^{+2\pi i/3} = 1$). Since $\hat{H}_{el}$ is invariant, thus the left hand side is also invariant. On the right hand side all the $\mathcal{D}$s for which the combination of the Qs are variant has to vanish, i.e.,

$$\mathcal{D}^{(1)}_+ = \mathcal{D}^{(1)}_- = \mathcal{D}^{(2)}_{++} = \mathcal{D}^{(1)}_+ = \mathcal{D}^{(2)}_{--} = 0 \tag{A.12}$$

For $\mathcal{D}^{(1)}_+Q_+$ term it can be shown that

$$\hat{C}_3(\mathcal{D}^{(1)}_+Q_+) = \mathcal{D}^{(1)}_+\hat{C}_3Q_+ = \mathcal{D}_+e^{(2\pi i/3)}Q_+ \tag{A.13}$$

So, it is not invariant with respect to the left hand side. Therefore, $\mathcal{D}^{(1)}_+ = 0$ and similarly other relations in Eq. (A.12) are true. So the terms that are not changing upon application of three fold rotations will survive in the integral. That is,

$$|\Phi_+\rangle\hat{H}_{el}\langle\Phi_+| = \mathcal{D}^{(0)} + \frac{1}{2}\mathcal{D}^{(2)}_{+-}Q_+Q_-, \tag{A.14}$$

and also

$$|\Phi_-\rangle\hat{H}_{el}\langle\Phi_-| = \mathcal{D}^{(0)} + \frac{1}{2}\mathcal{D}^{(2)}_{+-}Q_+Q_-. \tag{A.15}$$

The off-diagonal matrix elements are,

$$|\Phi_+\rangle\hat{H}_{el}\langle\Phi_-| = \mathcal{O}^{(0)}+\mathcal{O}^{(1)}_+Q_+ + \mathcal{O}^{(1)}_-Q_- + \frac{1}{2!}\mathcal{O}^{(2)}_{++}Q_+Q_+ + \frac{1}{2!}\mathcal{O}^{(2)}_{--}Q_-Q_- + \frac{1}{2!}\mathcal{O}^{(2)}_{+-}Q_+Q_- \tag{A.16}$$

If $\hat{C}_3$ is applied on this equation, then the left side is multiplied by $e^{2\pi i/3}$ (i.e., $e^{-2\pi i/3}.e^{-2\pi i/3} = e^{-4\pi i/3} = e^{2\pi i/3}$). So that we finally get,

$$\mathcal{O}^{(0)} = \mathcal{O}^{(1)}_+ = \mathcal{O}^{(2)}_{--} = \mathcal{O}^{(2)}_{(+-)} = 0 \tag{A.17}$$

Therefore, the Eq. (A.16) gives rise to

$$|\Phi_+\rangle\hat{H}_{el}\langle\Phi_-| = \mathcal{O}^{(1)}_-Q_- + \frac{1}{2!}\mathcal{O}^{(2)}_{++}Q_+Q_+ \tag{A.18}$$

The total electronic Hamiltonian can be written as

$$\hat{H}_{el} = \begin{pmatrix} \mathcal{D}^0 + \frac{1}{2!}\mathcal{D}^2_{+-}Q_+Q_- & \mathcal{O}^{(1)}_- Q_- + \frac{1}{2!}\mathcal{O}^{(2)}_{++}Q_+Q_+ \\ \mathcal{O}^{(1)}_+ Q_+ + \frac{1}{2!}\mathcal{O}^{(2)}_{--}Q_-Q_- & \mathcal{D}^0 + \frac{1}{2!}\mathcal{D}^{(2)}_{+-}Q_+Q_- \end{pmatrix} \tag{A.19}$$

Now,

$$Q_+Q_- = (Q_x + iQ_y)(Q_x - iQ_y) = Q_x^2 + Q_y^2, \tag{A.20}$$

$$Q_+Q_+ = Q_x^2 - Q_y^2 + 2iQ_xQ_y, \tag{A.21}$$

$$Q_-Q_- = Q_x^2 - Q_y^2 - 2iQ_xQ_y. \tag{A.22}$$

So in complex representation the Hamiltonian is,

$$\hat{H}_{el} = \begin{pmatrix} \mathcal{D}^0 + \frac{1}{2!}\mathcal{D}^{(2)}_{+-}(Q_x^2 + Q_y^2) & \mathcal{O}^{(1)}_+(Q_x - iQ_y) + \frac{1}{2!}\mathcal{O}^{(2)}_{++}(Q_x^2 + Q_y^2 + 2iQ_x) \\ \mathcal{O}^{(1)}_+(Q_x + iQ_y) + \frac{1}{2!}\mathcal{O}^{(2)}_{--}(Q_x^2 - Q_y^2 - 2iQ_xQ_y) & \mathcal{D}^{(0)} + \frac{1}{2!}\mathcal{D}^{(2)}_{+-}(Q_x^2 + Q_y^2) \end{pmatrix} \tag{A.23}$$

To make it real we transform it by transformation matrix as,

$$\mathcal{H}_{real} = \mathcal{U}^\dagger \hat{H}_{el} \mathcal{U} \tag{A.24}$$

where,

$$\mathcal{U} = \frac{1}{\sqrt{2}}\begin{pmatrix} 1 & -i \\ 1 & i \end{pmatrix}; \quad \mathcal{U}^\dagger = (\mathcal{U}^*)^T = \frac{1}{\sqrt{2}}\begin{pmatrix} 1 & 1 \\ i & -i \end{pmatrix}$$

By doing this transformation we get the final Hamiltonian in real space as,

$$\mathcal{H}_{real} = \begin{pmatrix} \mathcal{D}^0 + \frac{1}{2!}\mathcal{D}^{(2)}(Q_x^2 + Q_y^2) + \mathcal{O}^{(1)}Q_x + \frac{1}{2!}\mathcal{O}^{(2)}(Q_x^2 - Q_y^2) & \mathcal{O}^{(1)}Q_y - \mathcal{O}^{(2)}Q_xQ_y \\ \mathcal{O}^{(1)}Q_y - \mathcal{O}^{(2)}Q_xQ_y & \mathcal{D}^{(0)} + \frac{1}{2!}\mathcal{D}^{(2)}(Q_x^2 + Q_y^2) - \mathcal{O}^{(1)}Q_x - \frac{1}{2!}\mathcal{O}^{(2)}(Q_x^2 - Q_y^2) \end{pmatrix} \tag{A.25}$$

The coefficients appearing in the above matrix have the following definition as appeared in the Chapter 2 [cf., Sec. 2.2.2]

$$\mathcal{D}^{(0)} = a_1^{(0)}, \tag{A.26}$$

$$\mathcal{D}^{(2)} = a_1^{(2)}, \tag{A.27}$$

$$\mathcal{O}^{(1)} = \lambda_1^{(1)}, \tag{A.28}$$

$$\mathcal{O}^{(2)} = \lambda_1^{(2)} \tag{A.29}$$

This is a standard JT model Hamiltonian. When the potential energy surfaces are more anharmonic in nature, then one needs to go beyond the standard JT model. So, in the following the matrix elements are expanded in Taylor series up to sixth order in Q_+ and

Q_-. The general representation of the electronic Hamiltonian in the $\{|\Phi_+\rangle, |\Phi_-\rangle\}$ basis is given by

$$\hat{H}_{el} = \Phi_\pm^\dagger H_\pm \Phi_\pm = \sum_{i,j} |\Phi_i\rangle H_{ij} \langle\Phi_j| \quad (i,j = +,-) \tag{A.30}$$

and the matrix elements $H_{ij} = \langle\Phi_i|\hat{H}_{el}|\Phi_j\rangle$ are expanded. For example, H_{++} is expanded as (this is, a short notation of Eq. (A.11))

$$H_{++} = \sum_{p+q=0}^{6} \frac{c_{p,q}^{(++)}}{(p+q)!} Q_+^p Q_-^q. \tag{A.31}$$

Each term in the expansion of Eq. (A.31) has to fulfill the invariance condition under the symmetry operations and therefore most of the expansion coefficients are zero. For example,

$$\hat{C}_3 |\Phi_+\rangle Q_+^p Q_-^q \langle\Phi_-| = e^{-2\pi i/3} e^{(+p)2\pi i/3} e^{(-q)2\pi i/3} e^{2\pi i/3} \times |\Phi_+\rangle Q_+^p Q_-^q \langle\Phi_-| \tag{A.32}$$

$$= e^{(p-q)2\pi i/3} \times |\Phi_+\rangle Q_+^p Q_-^q \langle\Phi_-|. \tag{A.33}$$

In the above equation, $|(p-q)|$= 0,3,6..., fulfill the invariance condition, because only in these cases the phase factor of Eq. (A.33) is unity. The same procedure is repeated for the remaining elements of the Hamiltonian [cf., Eq. (A.31)], resulting in ten nonvanishing diagonal and nine nonvanishing off-diagonal terms. These terms are summarized in Table A.1 The obtained Hamiltonian matrix will be transformed back to the real representation

TABLE A.1: Nonvanishing terms of the Hamiltonian matrix in complex representation.

Order	Diagonal $H_{++} = H_{--}$	Off-diagonal $H_{+-} = (H_{-+})^*$
0	$Q_+^0 Q_-^0$	-
1	-	$Q_+^0 Q_-^1$
2	$Q_+^1 Q_-^1$	$Q_+^2 Q_-^0$
3	$Q_+^3 Q_-^0$ and $Q_+^0 Q_-^3$	$Q_+^1 Q_-^2$
4	$Q_+^2 Q_-^2$	$Q_+^0 Q_-^4$ and $Q_+^3 Q_-^1$
5	$Q_+^4 Q_-^1$ and $Q_+^1 Q_-^4$	$Q_+^2 Q_-^3$ and $Q_+^5 Q_-^0$
6	$Q_+^6 Q_-^0$ and $Q_+^3 Q_-^3$ and $Q_+^0 Q_-^6$	$Q_+^1 Q_-^5$ and $Q_+^4 Q_-^2$

using the above Eq. (A.24). In continuation of $E\otimes e$ higher-order JT couplings, one can also derive higher-order $(E+A)\otimes e$-PJT coupling terms. For more details readers are referred to the Refs. [114, 115].

Appendix B

Supplementary material for Chapter 3

TABLE B1: The linear intrastate (κ) and second-order (γ) coupling parameters of PFBz derived from the EOM-CCSD electronic structure data. Excitation strengths ($\kappa_i^2/2\omega_i^2$) are given in the parentheses.

	S_1		S_2		S_3	
	κ	γ	κ	γ	κ	γ
ν_1	-0.0232 (0.0016)	-0.0003	0.0161 (0.0008)	-0.0194	0.0214 (0.0014)	-0.0202
ν_2	-0.0019 (0.0000)	0.0141	-0.1527 (0.2679)	-0.0069	0.1416 (0.2305)	-0.0198
ν_3	-0.0830 (0.0952)	-0.0031	0.0778 (0.0837)	-0.0547	0.0622 (0.0534)	-0.0636
ν_4	-0.1270 (0.2596)	0.0000	0.0077 (0.0009)	-0.0324	-0.0077 (0.0009)	-0.0239
ν_5	0.0340 (0.0234)	-0.0017	-0.0070 (0.0010)	-0.0286	0.0277 (0.0155)	-0.0317
ν_6	-0.0216 (0.0134)	-0.0032	-0.0355 (0.0362)	-0.0175	0.0258 (0.0191)	-0.0268
ν_7	0.0809 (0.4145)	-0.0023	0.0636 (0.2565)	-0.0139	0.0008 (0.0000)	-0.0130
ν_8	-0.0854 (0.7208)	0.0007	-0.0413 (0.1684)	-0.0122	-0.0279 (0.0769)	-0.0139
ν_9	0.0047 (0.0032)	-0.0139	0.0652 (0.6341)	-0.0111	-0.0671 (0.6717)	-0.0123
ν_{10}	-0.0090 (0.0225)	-0.0002	-0.0247 (0.1696)	-0.0053	-0.0250 (0.1729)	-0.0072
ν_{11}	0.0125 (0.0715)	-0.0024	0.0428 (0.8365)	-0.0014	-0.0132 (0.0796)	-0.0040
	S_4		S_5		S_6	
	κ	γ	κ	γ	κ	γ
ν_1	-0.0168 (0.0009)	0.0008	0.0665 (0.0135)	-0.0374	0.0771 (0.0182)	-0.0531
ν_2	0.0279 (0.0090)	-0.1948	-0.2220 (0.5663)	-0.0172	-0.0760 (0.0663)	-0.0871
ν_3	-0.0823 (0.0937)	-0.0100	-0.0872 (0.1051)	-0.0087	-0.0676 (0.0632)	-0.0240
ν_4	-0.1196 (0.2300)	-0.0088	-0.1094 (0.1927)	-0.0128	-0.0799 (0.1026)	-0.0361
ν_5	0.0291 (0.0171)	-0.0077	-0.0086 (0.0015)	-0.0155	-0.0056 (0.0006)	-0.0114
ν_6	-0.0144 (0.0060)	-0.0108	0.0070 (0.0014)	-0.0079	-0.0195 (0.0110)	-0.0107
ν_7	0.0559 (0.1983)	-0.0060	0.0521 (0.1722)	-0.0063	0.0345 (0.0756)	-0.0130
ν_8	-0.0546 (0.2953)	-0.0012	0.0005 (0.0000)	-0.0022	-0.0185 (0.0339)	-0.0083
ν_9	-0.0227 (0.0766)	-0.0096	0.0790 (0.9307)	-0.0023	0.0230 (0.0791)	-0.0122
ν_{10}	-0.0021 (0.0013)	-0.0011	0.0027 (0.0002)	0.0044	0.0005 (0.0001)	-0.0014
ν_{11}	-0.0029 (0.0038)	-0.0027	0.0366 (0.6111)	0.0071	-0.0173 (0.1367)	-0.0020
	S_7		S_8			
	κ	γ	κ	γ		
ν_1	-0.0024 (0.0000)	0.0014	-0.0130 (0.0005)	0.0006		
ν_2	-0.0855 (0.0839)	0.2155	-0.0003 (0.0000)	-0.0012		
ν_3	-0.0833 (0.0960)	-0.0131	-0.0934 (0.1207)	-0.0140		
ν_4	-0.1174 (0.2218)	-0.0002	-0.1107 (0.1973)	-0.0054		
ν_5	0.0162 (0.0053)	0.0017	0.0197 (0.0079)	-0.0039		
ν_6	-0.0240 (0.0165)	-0.0000	-0.0411 (0.0485)	-0.0070		
ν_7	0.0593 (0.2228)	-0.0050	0.0753 (0.3592)	-0.0034		
ν_8	-0.0608 (0.3657)	-0.0034	-0.0643 (0.4092)	-0.0017		
ν_9	-0.0251 (0.0943)	-0.0015	-0.0284 (0.1207)	0.0006		
ν_{10}	-0.0024 (0.0002)	-0.0010	-0.0039 (0.0042)	-0.0016		
ν_{11}	-0.0006 (0.0001)	-0.0004	-0.0025 (0.0030)	-0.0012		

TABLE B2: Second-order (γ) coupling parameter (in eV) of PFBz neutral molecule derived from EOM-CCSD electronic structure data.

Symmetry	Mode	γ^{S_1}	γ^{S_2}	γ^{S_3}	γ^{S_4}	γ^{S_5}	γ^{S_6}	γ^{S_7}	γ^{S_8}
a_2	ν_{12}	-0.0888	-0.0792	-0.0082	0.0072	-0.0260	-0.0360	-0.0024	-0.0264
	ν_{13}	-0.0446	0.0454	0.0050	-0.0678	-0.0354	-0.0812	-0.1092	0.0216
	ν_{14}	-0.0157	-0.0282	-0.0070	0.0004	-0.0238	-0.0082	0.0214	-0.0610
b_1	ν_{15}	-0.0822	0.0290	-0.0552	0.0078	-0.0408	-0.0032	-0.0430	-0.0550
	ν_{16}	-0.0922	-0.0008	-0.0588	-0.0200	-0.0154	-0.0984	0.0192	-0.0930
	ν_{17}	-0.0814	0.0237	-0.0424	-0.0266	-0.0426	-0.0718	-0.0084	-0.0430
	ν_{18}	-0.0496	-0.0046	-0.0162	-0.0338	-0.0296	-0.1062	0.0730	-0.0634
	ν_{19}	-0.0128	-0.0077	-0.0136	-0.0094	0.0090	-0.0030	-0.0084	-0.0204
	ν_{20}	-0.0285	-0.0006	-0.0458	0.0118	-0.0144	-0.0158	-0.0112	-0.0014
b_2	ν_{21}	0.0102	-0.1154	0.0796	-0.1542	-0.1188	-0.0812	-0.0218	0.1706
	ν_{22}	-0.0086	-0.0530	-0.0480	-0.0096	-0.1032	0.0772	-0.0176	-0.0154
	ν_{23}	0.1522	0.0404	0.0544	0.0678	0.0516	0.0418	0.0586	0.0672
	ν_{24}	0.0016	-0.0154	0.0066	-0.0170	-0.0092	-0.0248	-0.0034	0.0154
	ν_{25}	-0.0014	-0.0298	-0.0160	-0.0118	-0.0172	-0.0278	-0.0070	0.0108
	ν_{26}	-0.0050	-0.0166	-0.0136	-0.0054	-0.0322	0.0278	-0.0070	-0.0064
	ν_{27}	-0.0052	-0.0088	-0.0092	-0.0050	-0.0054	-0.0068	-0.0076	-0.0062
	ν_{28}	-0.0118	-0.0368	0.0186	-0.0112	-0.0340	-0.0234	-0.0216	0.0146
	ν_{29}	-0.0004	-0.0072	-0.0054	-0.0014	-0.0044	0.0050	-0.0026	0.0008
	ν_{30}	-0.0010	-0.0052	-0.0010	-0.0008	-0.0014	-0.0036	-0.0036	0.0036

TABLE B3: Third-order coupling parameter (η) (in eV) of the Hamiltonian [Eq. 3.7] of symmetrical modes of PFBz.

Symmetry	Mode	η^{S_1}	η^{S_2}	η^{S_3}	η^{S_4}	η^{S_5}	η^{S_6}	η^{S_7}	η^{S_8}
a_1	ν_1	-0.00003	0.01340	0.01726	0.00044	0.00444	0.02134	0.00029	0.00048
	ν_2	-0.00184	0.00103	0.00051	-0.02651	0.14556	0.06407	0.04221	-0.01435
	ν_3	0.00084	0.00349	0.00034	0.00028	-0.00297	0.00436	-0.00026	0.00060
	ν_4	0.00000	0.00154	-0.00064	-0.00048	0.00054	0.00339	0.00054	0.00000
	ν_5	-0.00009	-0.00038	-0.00034	0.00010	0.00089	0.00049	-0.00048	-0.00032
	ν_6	0.00002	0.00103	0.00174	0.00063	-0.00043	0.00323	-0.00088	-0.00004
	ν_7	-0.00004	0.00123	0.00127	-0.00022	-0.00074	0.00179	-0.00038	-0.00015
	ν_8	-0.00006	-0.00133	-0.00126	-0.00001	-0.00008	-0.00062	0.00047	0.00022
	ν_9	0.00092	-0.00068	-0.00074	-0.00151	-0.00664	-0.00484	0.00132	0.00166
	ν_{10}	0.00008	0.00045	0.00052	0.00006	0.00004	-0.00019	-0.00004	0.00000
	ν_{11}	-0.00026	0.00005	0.00022	-0.00013	-0.00210	-0.00067	-0.00011	0.00013

TABLE B4: Fourth-order coupling parameter (ζ) (in eV) of the Hamiltonian [Eq. 3.7] of both symmetric and unsymmetrical modes of PFBz.

Mode	ζ^{S_1}	ζ^{S_2}	ζ^{S_3}	ζ^{S_4}	ζ^{S_5}	ζ^{S_6}	ζ^{S_7}	ζ^{S_8}
a_1								
ν_2	0.00007	-0.00160	-0.00075	0.12777	-0.13970	0.03813	-0.19144	-0.01624
ν_3	0.00003	0.00355	0.00373	-0.00007	0.00015	-0.00177	0.00068	0.00017
ν_4	0.00000	0.00098	0.00045	-0.00006	0.00004	0.00142	-0.00024	-0.00004
ν_7	-0.00003	-0.00008	-0.00016	-0.00004	0.00016	-0.00041	-0.00001	-0.00011
ν_8	-0.00000	0.00003	0.00008	-0.00005	0.00002	-0.00046	-0.00015	-0.00020
ν_9	0.00012	-0.00015	-0.00015	-0.00008	-0.00579	-0.00130	0.00007	-0.00217
ν_{11}	0.00001	-0.00024	-0.00019	0.00009	-0.00231	-0.00018	-0.00011	0.00004
a_2								
ν_{12}	0.00739	0.00875	-0.00268	-0.00797	0.00419	0.00423	0.01115	0.00304
ν_{13}	0.00000	-0.02360	-0.00486	0.02233	-0.00699	0.01147	0.24613	-0.00188
ν_{14}	-0.00019	0.00062	0.00030	-0.00026	0.00529	-0.00032	-0.01088	0.05182
b_1								
ν_{15}	0.01122	-0.00849	-0.00697	-0.00328	-0.01126	0.01426	0.00748	-0.00191
ν_{16}	0.00943	-0.00650	0.00345	-0.00561	-0.03829	0.04598	-0.01872	0.07242
ν_{17}	0.00904	-0.00647	-0.00061	0.00402	-0.00252	0.00824	0.00132	0.00954
ν_{18}	0.00342	-0.00243	-0.00346	0.00098	-0.00069	0.06840	-0.06235	0.03665
ν_{19}	0.00014	-0.00187	-0.00174	0.00014	-0.00049	-0.00722	0.00687	-0.00061
ν_{20}	0.00069	-0.00071	0.00349	-0.00318	0.00091	0.00048	0.00352	0.00006
b_2								
ν_{21}	-0.00008	0.04708	-0.03609	0.06390	0.04911	0.01656	-0.00220	-0.14277
ν_{22}	0.00012	0.00051	0.00066	-0.00039	0.04729	-0.14858	0.00093	0.00046
ν_{24}	-0.00006	-0.00078	-0.00295	0.00116	-0.00882	0.00012	0.00002	-0.00204
ν_{28}	0.00007	0.00415	-0.00432	-0.00057	0.00433	0.00042	0.00542	-0.00497
ν_{29}	-0.00006	-0.00011	-0.00024	0.00006	0.00058	-0.00069	0.00020	-0.02656
ν_{30}	-0.00003	-0.00027	-0.00069	0.00004	0.00013	-0.00011	0.00050	-0.00058

TABLE B5: Higher-order coupling parameters θ, δ, ρ and ξ (in eV) of the Hamiltonian [Eq. 3.7] of ν_2 vibrational mode of PFBz.

	S_1	S_2	S_3	S_4	S_5	S_6	S_7	S_8
θ_2	-0.00002	0.00143	-0.00048	0.02939	-0.13323	-0.07395	0.02147	0.00015
δ_2	-	-	-	-0.14866	0.26099	-0.02868	0.19964	0.02057
ρ_2	-	-	-	-0.02276	0.09385	0.06006	-0.04071	0.00411
ξ_2	-	-	-	0.12776	-0.27149	0.01615	-0.15208	-0.01528

TABLE B6: Diagonal bilinear γ_{ij}^{n} parameters (in eV) along the totally symmetric vibrational modes ν_2, ν_4, ν_7, ν_8, ν_9, ν_{11} of the lowest eight electronic states of PFBz.

	S_1	S_2	S_3	S_4	S_5	S_6	S_7	S_8
γ_{22}	0.0141	-0.0069	-0.0198	-0.1948	-0.0171	-0.0871	0.2155	-0.0012
γ_{24}	-0.0027	-0.0220	-0.0186	0.0533	-0.0040	0.0163	-0.0582	-0.0033
γ_{27}	-0.0044	-0.0179	-0.0067	0.0328	0.0154	0.0089	-0.0256	-0.0023
γ_{28}	0.0034	0.0103	-0.0014	-0.0172	0.0056	-0.0154	0.0052	0.0111
γ_{29}	-0.0126	-0.0117	-0.0179	0.0406	0.0516	0.0540	-0.0462	0.0158
γ_{211}	-0.0059	0.0069	0.0065	0.0259	0.0380	0.0113	-0.0276	0.0035
γ_{44}	0.0001	-0.0324	-0.0239	-0.0088	-0.0128	-0.0361	-0.0002	-0.0054
γ_{47}	-0.0065	-0.0179	-0.0121	-0.0096	-0.0004	-0.0083	0.0011	-0.0067
γ_{48}	0.0026	0.0172	0.0187	0.0103	0.0016	0.0294	0.0034	0.0034
γ_{49}	0.0034	0.0042	0.0055	-0.0086	0.0007	0.0061	0.0099	-0.0018
γ_{411}	-0.0009	0.0021	0.0009	-0.0072	0.0010	0.0085	0.0051	-0.0026
γ_{77}	-0.0023	-0.0139	-0.0130	-0.0060	-0.0063	-0.0130	-0.0050	-0.0034
γ_{78}	-0.0023	-0.0123	-0.0066	-0.0017	-0.0110	-0.0081	-0.0034	-0.0043
γ_{79}	-0.0094	0.0089	0.0028	-0.0110	0.0001	-0.0002	0.0007	0.0008
γ_{711}	-0.0046	0.0054	0.0024	-0.0063	0.0028	0.0053	0.0011	-0.0009
γ_{88}	0.0007	-0.0122	-0.0139	-0.0012	-0.0022	-0.0083	-0.0034	-0.0017
γ_{89}	0.0014	0.0050	0.0133	0.0059	0.0019	0.0049	0.0002	-0.0022
γ_{811}	0.0007	-0.0009	0.0028	0.0026	-0.0011	-0.0042	-0.0011	-0.00002
γ_{99}	-0.0139	-0.0111	-0.0123	-0.0096	-0.0023	-0.0122	-0.0015	0.0006
γ_{911}	-0.0117	0.0043	0.0030	-0.0091	-0.0083	-0.0027	-0.0007	0.0001
γ_{1111}	-0.0024	-0.0014	-0.0040	-0.0028	0.0072	-0.0020	-0.0004	-0.0012

TABLE B7: Same as B6 along the b_1 symmetry vibrational modes ν_{15}, ν_{16}, ν_{16}, ν_{17}, ν_{18}, ν_{19} and ν_{20} of the lowest four electronic states of PFBz.

	S_1	S_2	S_3	S_4
γ_{1515}	-0.0822	0.0290	-0.0552	0.0078
γ_{1516}	0.0222	-0.0155	0.0447	-0.0135
γ_{1517}	0.0029	-0.0382	-0.0396	-0.0202
γ_{1518}	-0.0069	-0.0083	-0.0410	-0.0074
γ_{1519}	-0.0053	0.0072	-0.0212	-0.0012
γ_{1520}	-0.0173	0.0214	-0.0307	0.0213
γ_{1616}	-0.0922	-0.0008	-0.0588	-0.0200
γ_{1617}	-0.0235	0.0127	-0.0360	0.0323
γ_{1618}	0.0164	-0.0254	0.0065	-0.0272
γ_{1619}	0.0053	-0.0136	0.0054	-0.0065
γ_{1620}	0.0096	-0.0008	0.0374	-0.0118
γ_{1717}	-0.0814	0.0237	-0.0424	-0.0266
γ_{1718}	0.0207	-0.0235	0.0015	-0.0101
γ_{1719}	-0.0103	-0.0080	-0.0045	-0.0039
γ_{1720}	0.0013	-0.0121	0.0208	-0.0284
γ_{1818}	-0.0496	-0.0046	-0.0162	-0.0338
γ_{1819}	-0.0136	0.0076	-0.0099	-0.0037
γ_{1820}	-0.0249	0.0292	-0.0182	0.0134
γ_{1919}	-0.0128	-0.0077	-0.0136	-0.0094
γ_{1920}	-0.0094	0.0167	-0.0037	0.0158

TABLE B8: Third-order diagonal bilinear η and η' (in eV) parameters along the a_1 symmetry vibrational modes of PFBz.

	S_4	S_5	S_6	S_7	S_8
η_{24}	0.01304	0.01941	-0.03088	-0.02974	-
η'_{24}	-0.00018	0.00925	0.00648	0.00119	-
η_{27}	-0.00291	-0.02810	-0.02096	-0.02374	-0.01160
η'_{27}	0.00118	0.00730	-0.00037	0.00919	-0.00443
η_{28}	0.00602	0.00161	0.02420	0.02326	0.01590
η'_{28}	0.00113	0.00318	0.00120	0.01025	-0.00629
η_{29}	0.00454	-0.06925	-0.01201	-0.01747	0.01776
η'_{29}	0.00640	0.01468	0.00219	-0.00537	-0.01118
η_{211}	0.00292	-0.05814	0.00526	-0.01345	0.00190
η'_{211}	0.00065	0.01501	-0.00026	-0.00130	0.00136

TABLE B9: Fourth-order diagonal bilinear ζ, ζ' and ζ'' (in eV) parameters along the a_1 symmetry vibrational modes of PFBz.

	S_4	S_5	S_6	S_7	S_8
ζ_{24}	0.00741	-0.01412	0.01929	-0.01156	-
ζ'_{24}	-0.03821	-0.02335	0.00012	0.05688	-
ζ''_{24}	-0.00026	-0.00037	-0.02162	0.00127	-
ζ_{27}	0.00030	-0.00688	0.01041	-0.01669	-0.00675
ζ'_{27}	-0.02470	0.00232	-0.00353	0.05246	-0.01398
ζ''_{27}	0.00068	-0.00061	-0.00080	-0.00208	-0.00019
ζ_{28}	-0.00094	-0.00498	0.01024	-0.01925	-0.00891
ζ'_{28}	0.01034	0.00291	0.00787	-0.03197	0.01294
ζ''_{28}	-0.00020	0.00025	0.00189	0.00309	0.00202
ζ_{29}	0.00606	0.00716	0.01356	-0.00991	-0.01174
ζ'_{29}	-0.02841	0.01501	-0.03882	0.04337	0.01161
ζ''_{29}	-0.00019	-0.00563	-0.00100	0.00052	0.00378
ζ_{211}	0.00192	-0.00578	0.00615	-0.00124	0.00211
ζ'_{211}	-0.01764	0.01397	-0.00955	0.03012	0.00316
ζ''_{211}	-0.00061	0.00056	-0.00019	-0.00002	-0.00065

TABLE B10: Same as B9 along the b_1 symmetry vibrational modes of PFBz.

	S_1	S_2	S_3	S_4
ζ_{1516}	0.00417	-0.00105	0.00570	-0.00051
ζ'_{1516}	-0.00052	0.00223	-0.00185	0.00072
ζ''_{1516}	-0.00130	0.00130	-0.00257	0.00197
ζ_{1517}	0.00280	-0.00203	0.00526	0.00062
ζ'_{1517}	-0.00127	0.00524	-0.00013	0.00511
ζ''_{1517}	0.00085	0.00004	0.00310	-0.00015
ζ_{1518}	0.00249	-0.00094	0.00497	0.00077
ζ'_{1518}	-0.00110	0.00061	0.00113	0.00208
ζ''_{1518}	0.00169	-0.00061	0.00354	-0.00051
ζ_{1519}	0.00171	0.00026	0.00290	-0.00065
ζ'_{1519}	0.00113	-0.00021	0.00196	0.00121
ζ''_{1519}	-0.00033	-0.00011	0.00003	0.00019
ζ_{1520}	0.00277	-0.00146	0.00451	-0.00256
ζ'_{1520}	0.00116	-0.00210	0.00261	-0.00238
ζ''_{1520}	0.00046	-0.00040	0.00094	-0.00080
ζ_{1617}	0.00319	-0.00331	0.00133	-0.00030
ζ'_{1617}	0.00036	-0.00382	0.00097	-0.00286
ζ''_{1617}	0.00173	-0.00023	0.00345	-0.00159
ζ_{1618}	0.00348	0.00141	0.00067	0.00250
ζ'_{1618}	-0.00180	0.00260	0.00080	-0.00036
ζ''_{1618}	0.00071	0.00079	-0.00277	0.00472
ζ_{1619}	0.00197	0.00184	0.00243	0.00060
ζ'_{1619}	-0.00054	0.00208	0.00030	0.00155
ζ''_{1619}	0.00017	-0.00042	-0.00061	-0.00014
ζ_{1620}	0.00253	-0.00043	0.00302	-0.00056
ζ'_{1620}	-0.00140	-0.00101	-0.00382	0.00108
ζ''_{1620}	-0.00022	0.00044	-0.00072	0.00091
ζ_{1718}	0.00181	-0.00189	0.00100	-0.00127
ζ'_{1718}	-0.00133	0.00063	-0.00153	0.00019
ζ''_{1718}	-0.00026	0.00128	0.00078	0.00176
ζ_{1719}	0.00110	-0.00080	0.00265	-0.00176
ζ'_{1719}	-0.00009	0.00119	-0.00090	0.00119
ζ''_{1719}	0.00019	0.00013	0.00051	-0.00070
ζ_{1720}	0.00197	-0.00147	0.00213	-0.00134
ζ'_{1720}	-0.00112	0.00180	-0.00259	0.00385
ζ''_{1720}	0.00004	0.00035	-0.00040	0.00074
ζ_{1819}	-0.00074	-0.00026	0.00000	-0.00120
ζ'_{1819}	0.00082	0.00008	0.00095	0.00081
ζ''_{1819}	-0.00047	-0.00026	0.00057	-0.00100
ζ_{1820}	0.00087	-0.00174	0.00120	-0.00205
ζ'_{1820}	0.00087	-0.00051	0.00223	-0.00278
ζ''_{1820}	0.00177	-0.00180	0.00008	0.00184
ζ_{1920}	-0.00022	0.00009	0.00004	-0.00137
ζ'_{1920}	0.00016	0.00018	0.00071	-0.00070
ζ''_{1920}	0.00103	-0.00136	0.00049	-0.00131

TABLE B11: Linear inter-state coupling parameter between the n and m states (λ^{nm}) (in eV) and the corresponding excitation strength $\frac{1}{2}\left(\frac{\lambda^{nm}}{\omega_i}\right)^2$ (given in the parentheses) of PFBz molecule.

Symmetry	Mode	λ^{nm}	λ^{nm}	λ^{nm}
		S_1-S_3	S_1-S_6	S_2-S_4
a_2	ν_{12}	0.1434 (1.6770)	0.1612 (2.1192)	0.1299 (1.3762)
	ν_{13}	0.1091 (2.6267)	-	-
	ν_{14}	0.0436 (3.5774)	0.0533 (5.3463)	0.0789 (11.7152)
		S_1-S_2	S_1-S_5	S_3-S_4
b_1	ν_{15}	0.1511 (1.0494)	0.1552 (1.1070)	0.0859 (0.3391)
	ν_{16}	0.1306 (1.5873)	0.1801 (3.0185)	0.0573 (0.3055)
	ν_{17}	0.1450 (2.4882)	0.1507 (2.6876)	0.0330 (0.1289)
	ν_{18}	0.0880 (2.5069)	0.1005 (3.2697)	-
	ν_{19}	0.0205 (0.3283)	0.0891 (6.2013)	0.0211 (0.3477)
	ν_{20}	0.0705 (6.5355)	0.0792 (8.2480)	0.0760 (7.5950)
		S_2-S_3	S_2-S_6	S_3-S_5
b_2	ν_{21}	0.1494 (0.2575)	0.1216 (0.1706)	-
	ν_{22}	0.0292 (0.0114)	0.2033 (0.5542)	-
	ν_{23}	0.0317 (0.0149)	0.0276 (0.0114)	-
	ν_{24}	0.0401 (0.0373)	0.0317 (0.0233)	-
	ν_{25}	0.0403 (0.0415)	0.0550 (0.0773)	-
	ν_{26}	0.0165 (0.0099)	0.1046 (0.3969)	-
	ν_{27}	0.0147 (0.0150)	0.0377 (0.0988)	0.0242 (0.0407)
	ν_{28}	0.0762 (1.0258)	0.0867 (1.3279)	-
	ν_{29}	0.0130 (0.0614)	0.0665 (1.6064)	-
	ν_{30}	0.0190 (0.1588)	0.0310 (0.4231)	-
		S_2-S_7	S_3-S_8	S_4-S_5
a_2	ν_{12}	0.1879 (2.8792)	-	-
	ν_{13}	-	0.0559 (0.6881)	0.1026 (2.3230)
	ν_{14}	0.1464 (40.3345)	-	-
		S_3-S_7	S_4-S_6	S_5-S_8
b_1	ν_{15}	0.0817 (0.3068)	-	-
	ν_{16}	0.1575 (2.3085)	-	-
	ν_{17}	-	-	-
	ν_{18}	0.1847 (11.3690)	-	-
	ν_{19}	0.0470 (1.7255)	0.0315 (0.7751)	-
	ν_{20}	0.0945 (11.7426)	-	0.0330 (1.4319)
		S_4-S_8	S_5-S_6	S_7-S_8
b_2	ν_{21}	0.2711 (0.8477)	0.0390 (0.0175)	0.0725 (0.0606)
	ν_{22}	-	0.0869 (0.1012)	0.0039 (0.0002)
	ν_{23}	-	-	0.0089 (0.0012)
	ν_{24}	0.0810 (0.1520)	0.1610 (0.6006)	0.0157 (0.0057)
	ν_{25}	0.0708 (0.1281)	-	0.0154 (0.0061)
	ν_{26}	-	0.0427 (0.0661)	0.0017 (0.0001)
	ν_{27}	-	-	0.0029 (0.0006)
	ν_{28}	0.0823 (1.1966)	0.0200 (0.0707)	0.0286 (0.1445)
	ν_{29}	0.0169 (0.1037)	0.0151 (0.0828)	0.0047 (0.0080)
	ν_{30}	0.0262 (0.3022)	0.0262 (0.3022)	0.0084 (0.0311)
		S_5-S_7	S_6-S_8	
a_2	ν_{12}	0.0387 (0.1221)	-	
	ν_{13}	-	0.0722 (1.1480)	
	ν_{14}	0.0527 (5.2266)	-	
		S_6-S_7		
b_1	ν_{15}	-		
	ν_{16}	0.0725 (0.4891)		
	ν_{17}	0.0394 (0.1837)		
	ν_{18}	0.0990 (3.1728)		
	ν_{19}	-		
	ν_{20}	-		

TABLE B12: The number of harmonic oscillator (HO) basis functions along the totally symmetric vibrational modes and the dimension of the secular matrix used in the calculation of the stick vibrational spectra of the uncoupled S_1 to S_8 and coupled S_1-S_2 electronic states of PFBz shown in various figures.

Electronic states	Vibrational modes	No. of HO basis	Dimension of secular matrix	Figure(s)
S_1	ν_2, ν_3, ν_4 ν_7, ν_8, ν_9, ν_{11}	(6,8,10) (12,14,6,8)	3870720	Figs. 3.6(c)
S_3	ν_2, ν_3, ν_4 ν_7, ν_8, ν_9, ν_{11}	(12,10,8) (6,10,14,10)	8064000	Fig. 3.8(a)
S_4	ν_2, ν_3, ν_4 ν_7, ν_8, ν_9, ν_{11}	(6,10,12) (12,14,10,6)	7257600	Fig. 3.8(b)
S_6	ν_2, ν_3, ν_4 ν_7, ν_8, ν_9, ν_{11}	(10,10,14) (12,10,12,14)	28224000	Fig. 3.8(c)
S_7	ν_2, ν_3, ν_4 ν_7, ν_8, ν_9, ν_{11}	(10,10,12) (12,14,8,8)	12902400	Fig. 3.8(d)
S_8	ν_2, ν_3, ν_4 ν_7, ν_8, ν_9, ν_{11}	(8,10,12) (14,14,10,8)	15052800	Fig. 3.8(e)
coupled S_1-S_2	ν_2, ν_3, ν_4 ν_7, ν_8, ν_9, ν_{11} ν_{15}, ν_{16}, ν_{17} ν_{18}, ν_{19}, ν_{20}	(6,2,2) (6,2,6,6) (4,4,6) (6,2,6)	95551488	Fig. 3.6(d)

TABLE B13: Vibrational energy levels (in cm^{-1}) of the S_1, S_3, S_4, S_6, S_7 and S_8 electronic states of PFBz obtained from the uncoupled state calculations using the EOM-CCSD energy data. The assignment of the levels carried out by examining the nodal pattern of the wave functions is included in the table.

S_1		S_3		S_4	
Energy	Assignment	Energy	Assignment	Energy	Assignment
0	0_0^0	0	0_0^0	0	0_0^0
257	$\nu_{11}{}_0^1$	250	$\nu_{11}{}_0^1$	255	$\nu_{11}{}_0^1$
407	$\nu_9{}_0^1$	408	$\nu_9{}_0^1$	423	$\nu_9{}_0^1$
514	$\nu_{11}{}_0^2$	501	$\nu_{11}{}_0^2$	511	$\nu_{11}{}_0^2$
576	$\nu_8{}_0^1$	512	$\nu_8{}_0^1$	568	$\nu_8{}_0^1$
664	$\nu_9{}_0^1+\nu_{11}{}_0^1$	659	$\nu_9{}_0^1+\nu_{11}{}_0^1$	678	$\nu_9{}_0^1+\nu_{11}{}_0^1$
707	$\nu_7{}_0^1$	661	$\nu_7{}_0^1$	692	$\nu_7{}_0^1$
771	$\nu_{11}{}_0^3$	751	$\nu_{11}{}_0^3$	767	$\nu_{11}{}_0^3$
814	$\nu_9{}_0^2$	762	$\nu_8{}_0^1+\nu_{11}{}_0^1$	824	$\nu_8{}_0^1+\nu_{11}{}_0^1$
833	$\nu_8{}_0^1+\nu_{11}{}_0^1$	816	$\nu_9{}_0^2$	846	$\nu_9{}_0^2$
921	$\nu_9{}_0^1+\nu_{11}{}_0^2$	909	$\nu_9{}_0^1+\nu_{11}{}_0^2$	934	$\nu_9{}_0^1+\nu_{11}{}_0^2$
964	$\nu_7{}_0^1+\nu_{11}{}_0^1$	920	$\nu_8{}_0^1+\nu_9{}_0^1$	948	$\nu_7{}_0^1+\nu_{11}{}_0^1$
983	$\nu_8{}_0^1+\nu_9{}_0^1$	1000	$\nu_{11}{}_0^4$	991	$\nu_8{}_0^1+\nu_9{}_0^1$
1029	$\nu_{11}{}_0^4$	1012	$\nu_8{}_0^1+\nu_{11}{}_0^2$	1022	$\nu_{11}{}_0^4$
1071	$\nu_9{}_0^2+\nu_{11}{}_0^1$	1023	$\nu_8{}_0^2$	1079	$\nu_8{}_0^1+\nu_{11}{}_0^2$
1090	$\nu_8{}_0^1+\nu_{11}{}_0^2$	1067	$\nu_9{}_0^2+\nu_{11}{}_0^1$	1101	$\nu_9{}_0^2+\nu_{11}{}_0^1$
1114	$\nu_7{}_0^1+\nu_9{}_0^1$	1159	$\nu_9{}_0^1+\nu_{11}{}_0^3$	1115	$\nu_7{}_0^1+\nu_9{}_0^1$
1152	$\nu_8{}_0^2$	1224	$\nu_9{}_0^3$	1137	$\nu_8{}_0^2$
1178	$\nu_9{}_0^1+\nu_{11}{}_0^3$	1258	$\nu_3{}_0^1$	1190	$\nu_9{}_0^1+\nu_{11}{}_0^3$
1221	$\nu_7{}_0^1+\nu_{11}{}_0^2$	1262	$\nu_8{}_0^1+\nu_{11}{}_0^3$	1203	$\nu_7{}_0^1+\nu_{11}{}_0^2$
1283	$\nu_7{}_0^1+\nu_8{}_0^1$	1274	$\nu_8{}_0^2+\nu_{11}{}_0^1$	1260	$\nu_7{}_0^1+\nu_8{}_0^1$
1328	$\nu_9{}_0^2+\nu_{11}{}_0^2$	1317	$\nu_9{}_0^2+\nu_{11}{}_0^2$	1269	$\nu_9{}_0^3$
1347	$\nu_8{}_0^1+\nu_{11}{}_0^3$	1322	$\nu_4{}_0^1$	1278	$\nu_{11}{}_0^5$
1390	$\nu_8{}_0^1+\nu_9{}_0^2$	1328	$\nu_8{}_0^1+\nu_9{}_0^2$	1335	$\nu_8{}_0^1+\nu_{11}{}_0^3$
1409	$\nu_8{}_0^2+\nu_{11}{}_0^1$	1432	$\nu_8{}_0^2+\nu_9{}_0^1$	1357	$\nu_9{}_0^2+\nu_{11}{}_0^2$
1414	$\nu_7{}_0^2$	1475	$\nu_9{}_0^3+\nu_{11}{}_0^1$	1384	$\nu_7{}_0^2$
1422	$\nu_4{}_0^1$	1524	$\nu_8{}_0^2+\nu_{11}{}_0^2$	1384	$\nu_4{}_0^1$
1521	$\nu_7{}_0^1+\nu_9{}_0^2$	1524	$\nu_8{}_0^2+\nu_{11}{}_0^2$	1392	$\nu_8{}_0^2+\nu_{11}{}_0^1$
1522	$\nu_3{}_0^1$	1535	$\nu_8{}_0^3$	1414	$\nu_8{}_0^1+\nu_9{}_0^2$
1559	$\nu_8{}_0^2+\nu_9{}_0^1$	1598	$\nu_2{}_0^1$	1459	$\nu_7{}_0^1+\nu_{11}{}_0^3$
1585	$\nu_9{}_0^2+\nu_{11}{}_0^3$	1632	$\nu_9{}_0^4$	1493	$\nu_3{}_0^1$
1666	$\nu_8{}_0^2+\nu_{11}{}_0^2$	1725	$\nu_9{}_0^3+\nu_{11}{}_0^2$	1524	$\nu_9{}_0^3+\nu_{11}{}_0^1$
1671	$\nu_7{}_0^2+\nu_{11}{}_0^1$				
1679	$\nu_4{}_0^1+\nu_{11}{}_0^1$				
1738	$\nu_2{}_0^1$				
1779	$\nu_3{}_0^1+\nu_{11}{}_0^1$				
1829	$\nu_4{}_0^1+\nu_9{}_0^1$				
1928	$\nu_7{}_0^2+\nu_{11}{}_0^2$				

TABLE B.13: contd.

S_6		S_7		S_8	
Energy	Assignment	Energy	Assignment	Energy	Assignment
0	0_0^0	0	0_0^0	0	0_0^0
256	$\nu_{11}{}_0^1$	265	$\nu_{11}{}_0^1$	262	$\nu_{11}{}_0^1$
422	$\nu_9{}_0^1$	463	$\nu_9{}_0^1$	469	$\nu_9{}_0^1$
513	$\nu_{11}{}_0^2$	530	$\nu_{11}{}_0^2$	523	$\nu_{11}{}_0^2$
537	$\nu_8{}_0^1$	561	$\nu_8{}_0^1$	566	$\nu_8{}_0^1$
657	$\nu_7{}_0^1$	697	$\nu_7{}_0^1$	703	$\nu_7{}_0^1$
679	$\nu_9{}_0^1+\nu_{11}{}_0^1$	728	$\nu_9{}_0^1+\nu_{11}{}_0^1$	785	$\nu_{11}{}_0^3$
768	$\nu_{11}{}_0^3$	826	$\nu_8{}_0^1+\nu_{11}{}_0^1$	936	$\nu_9{}_0^2$
794	$\nu_8{}_0^1+\nu_{11}{}_0^1$	927	$\nu_9{}_0^2$	993	$\nu_9{}_0^1+\nu_{11}{}_0^2$
842	$\nu_9{}_0^2$	962	$\nu_7{}_0^1+\nu_{11}{}_0^1$	1036	$\nu_8{}_0^1+\nu_9{}_0^1$
914	$\nu_7{}_0^1+\nu_{11}{}_0^1$	994	$\nu_9{}_0^1+\nu_{11}{}_0^2$	1090	$\nu_8{}_0^1+\nu_{11}{}_0^2$
935	$\nu_9{}_0^1+\nu_{11}{}_0^2$	1024	$\nu_8{}_0^1+\nu_9{}_0^1$	1133	$\nu_8{}_0^2$
960	$\nu_8{}_0^1+\nu_9{}_0^1$	1091	$\nu_8{}_0^1+\nu_{11}{}_0^2$	1172	$\nu_7{}_0^1+\nu_9{}_0^1$
1024	$\nu_{11}{}_0^4$	1122	$\nu_8{}_0^2$	1198	$\nu_9{}_0^2+\nu_{11}{}_0^1$
1050	$\nu_8{}_0^1+\nu_{11}{}_0^2$	1160	$\nu_7{}_0^1+\nu_9{}_0^1$	1226	$\nu_7{}_0^1+\nu_{11}{}_0^2$
1074	$\nu_8{}_0^2$	1192	$\nu_9{}_0^2+\nu_{11}{}_0^1$	1255	$\nu_9{}_0^1+\nu_{11}{}_0^3$
1080	$\nu_7{}_0^1+\nu_9{}_0^1$	1227	$\nu_7{}_0^1+\nu_{11}{}_0^2$	1269	$\nu_7{}_0^1+\nu_8{}_0^1$
1099	$\nu_9{}_0^2+\nu_{11}{}_0^1$	1258	$\nu_7{}_0^1+\nu_8{}_0^1$	1352	$\nu_8{}_0^1+\nu_{11}{}_0^3$
1170	$\nu_7{}_0^1+\nu_{11}{}_0^2$	1387	$\nu_8{}_0^2+\nu_{11}{}_0^1$	1394	$\nu_8{}_0^2+\nu_{11}{}_0^1$
1191	$\nu_9{}_0^1+\nu_{11}{}_0^3$	1390	$\nu_9{}_0^3$	1400	$\nu_4{}_0^1$
1260	$\nu_9{}_0^3$	1394	$\nu_7{}_0^2$	1401	$\nu_9{}_0^3$
1279	$\nu_4{}_0^1$	1422	$\nu_4{}_0^1$	1405	$\nu_7{}_0^2$
1306	$\nu_8{}_0^1+\nu_{11}{}_0^3$	1457	$\nu_9{}_0^2+\nu_{11}{}_0^2$	1460	$\nu_9{}_0^2+\nu_{11}{}_0^2$
1314	$\nu_7{}_0^2$	1480	$\nu_3{}_0^1$	1478	$\nu_3{}_0^1$
1331	$\nu_8{}_0^2+\nu_{11}{}_0^1$	1488	$\nu_8{}_0^1+\nu_9{}_0^2$	1488	$\nu_7{}_0^1+\nu_{11}{}_0^3$
1355	$\nu_9{}_0^2+\nu_{11}{}_0^1$	1585	$\nu_8{}_0^2+\nu_9{}_0^1$	1503	$\nu_8{}_0^1+\nu_9{}_0^2$
1380	$\nu_8{}_0^1+\nu_9{}_0^2$	1623	$\nu_7{}_0^1+\nu_9{}_0^2$	1602	$\nu_8{}_0^2+\nu_9{}_0^1$
1426	$\nu_7{}_0^1+\nu_{11}{}_0^3$	1652	$\nu_8{}_0^2+\nu_{11}{}_0^2$	1639	$\nu_7{}_0^1+\nu_9{}_0^2$
1438	$\nu_3{}_0^1$	1659	$\nu_9{}_0^3+\nu_{11}{}_0^1$	1656	$\nu_8{}_0^2+\nu_{11}{}_0^2$
1447	$\nu_9{}_0^1+\nu_{11}{}_0^4$	1687	$\nu_4{}_0^1+\nu_{11}{}_0^1$	1663	$\nu_9{}_0^3+\nu_{11}{}_0^1$
1497	$\nu_8{}_0^2+\nu_9{}_0^1$	1721	$\nu_9{}_0^2+\nu_{11}{}_0^3$	1667	$\nu_7{}_0^2+\nu_{11}{}_0^1$
1500	$\nu_7{}_0^1+\nu_9{}_0^2$	1745	$\nu_3{}_0^1+\nu_{11}{}_0^3$	1699	$\nu_8{}_0^3$
1516	$\nu_9{}_0^3+\nu_{11}{}_0^1$	1818	$\nu_8{}_0^2+\nu_7{}_0^1$	1835	$\nu_7{}_0^1+\nu_8{}_0^2$
1535	$\nu_4{}_0^1+\nu_7{}_0^1$			1863	$\nu_9{}_0^4$
1570	$\nu_7{}_0^2+\nu_{11}{}_0^1$			1869	$\nu_4{}_0^1+\nu_9{}_0^1$
1587	$\nu_8{}_0^2+\nu_{11}{}_0^2$			1874	$\nu_7{}_0^2+\nu_9{}_0^1$
1611	$\nu_8{}_0^3$			1923	$\nu_4{}_0^1+\nu_{11}{}_0^2$
1675	$\nu_9{}_0^4$			1947	$\nu_3{}_0^1+\nu_9{}_0^1$
1681	$\nu_7{}_0^1+\nu_{11}{}_0^4$			1966	$\nu_4{}_0^1+\nu_8{}_0^1$

TABLE B.13: Normal mode combination, sizes of the primitive and single particle functions (SPFs) used in the coupled states dynamics calculations of PFBz using MCTDH suite of programs. [a] The primitive basis is the number of Harmonic oscillator DVR functions for the relevant mode. The primitive basis for each particle is the product of the one-dimensional bases. [b] The SPF basis is the number of single-particle functions used.

Electronic state	Normal modes	Primitive basis[a]	SPF basis[b]	Figure
coupled S_1 to S_8	ν_2, ν_3, ν_4, ν_{21}, ν_{22}, ν_{24}	(10,6,8,6,6,6)	[6,8,8,8,6,8,8,8]	panel b of Figs. 3.9 and 3.10
	ν_7, ν_8, ν_{12}, ν_{15}, ν_{16}, ν_{17}	(10,12,8,6,6,8)	[6,6,8,6,8,6,8,8]	
	ν_9, ν_{13}, ν_{18}, ν_{28}, ν_{29}	(12,8,8,8,8)	[8,6,6,8,8,6,6,8]	
	ν_{11}, ν_{14}, ν_{19}, ν_{20}, ν_{30}	(10,10,10,10,6)	[8,8,6,8,8,8,6,6]	

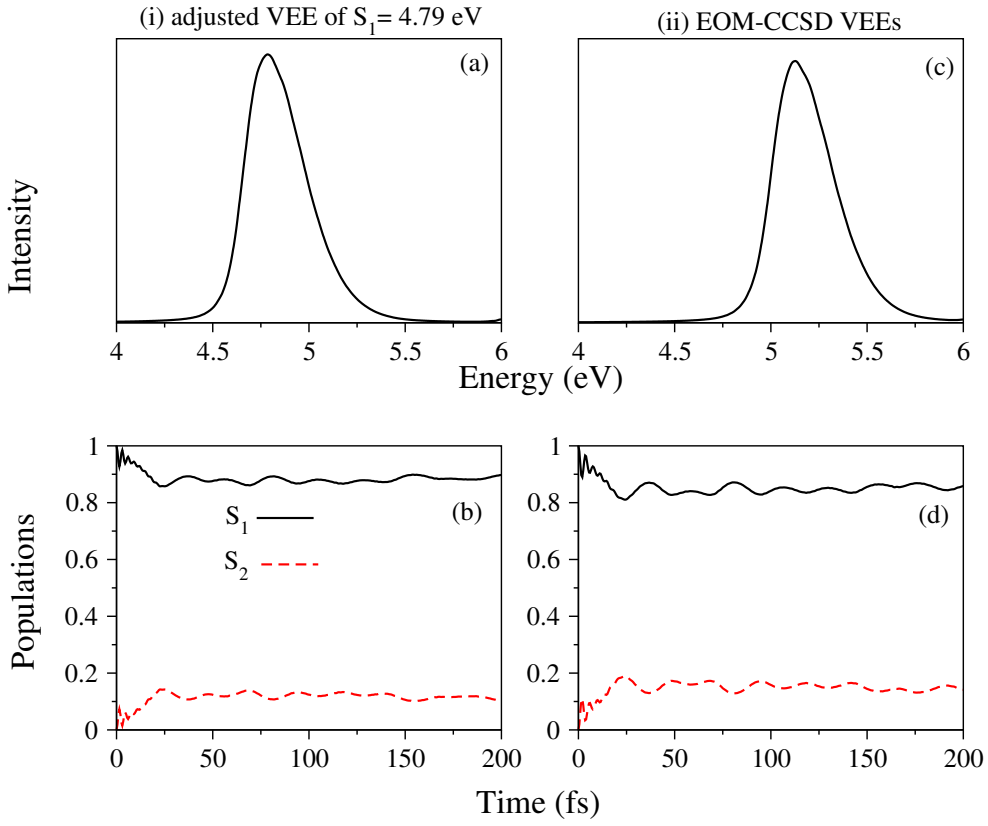

FIGURE B1: Absorption spectrum and time-dependence of corresponding diabatic electronic populations in the coupled S_1-S_2 states dynamics obtained with (panels a and b, respectively) and without (panels c and d, respectively) adjusted VEE of the S_1 state.

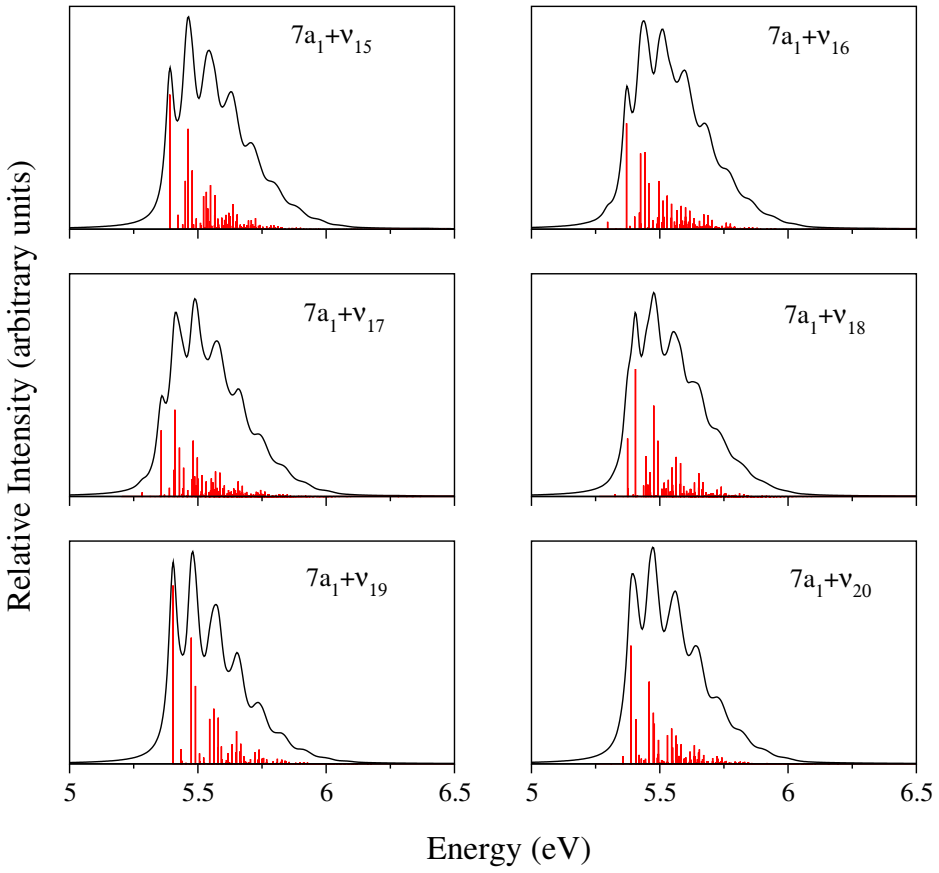

FIGURE B2: Stick spectrum and its convoluted envelope of the S_1 state when one b_1 mode is included at a time with seven totally symmetric modes.

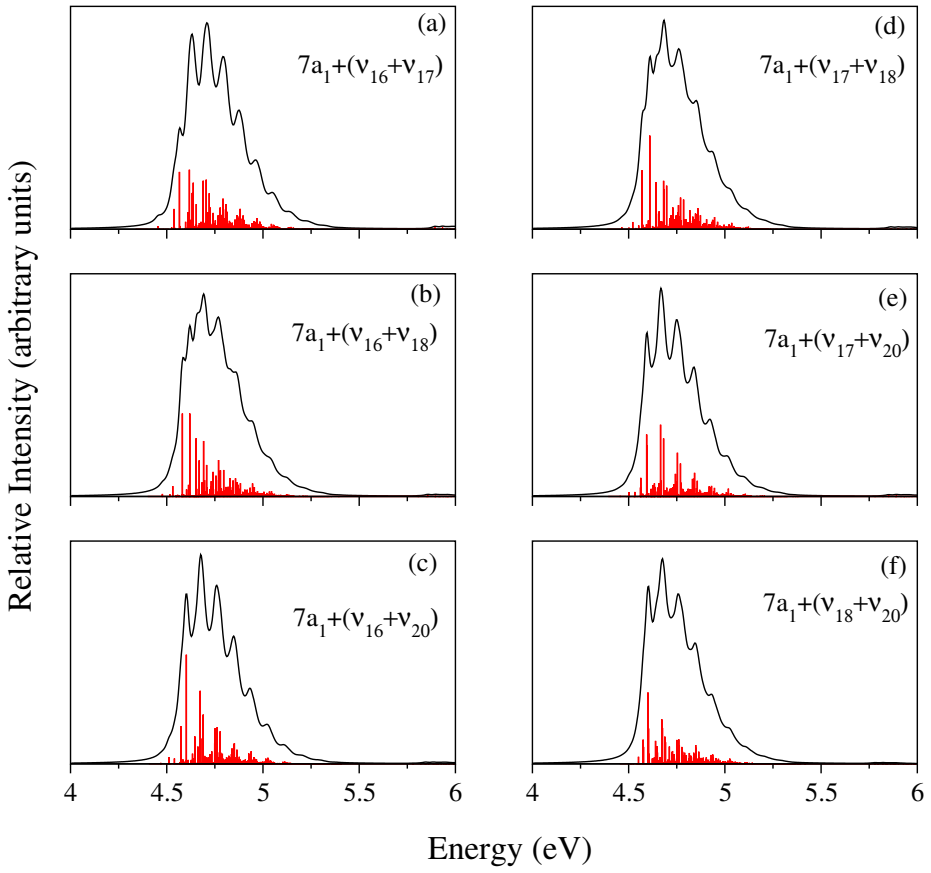

FIGURE B3: Stick spectrum and its convoluted envelope of the S_1 state when two b_1 modes are included at a time with seven totally symmetric modes.

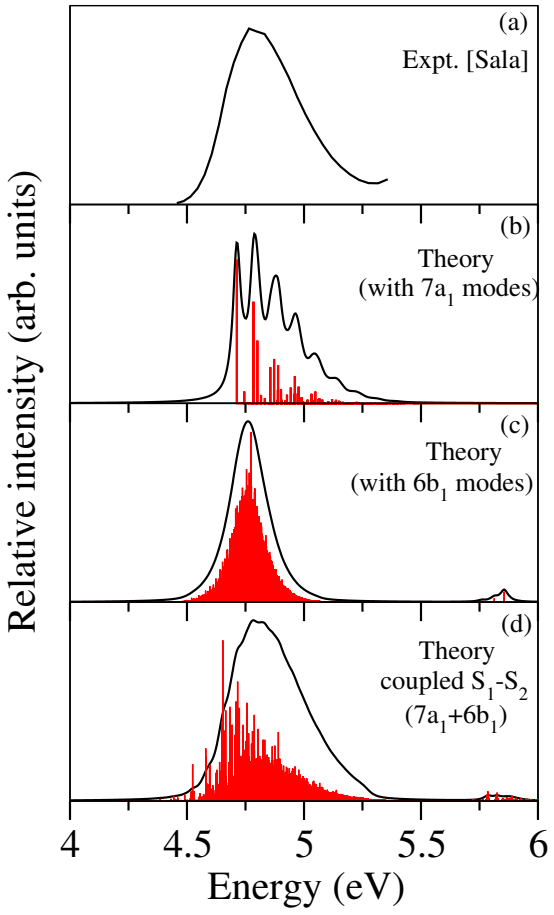

FIGURE B4: Vibronic energy level spectra of the S_1 electronic state of PFBz. The S_1 band structure computed with seven totally symmetric modes (ν_2-ν_4, ν_7-ν_9 and ν_{11}) only is shown in panel b and with all six b_1 modes (ν_{15}-ν_{20}) only is shown in panel c. The coupled S_1-S_2 states spectrum with $7a_1$+$6b_1$ modes is shown in panel d. The experimental S_1 band reproduced from Ref. [22] is shown in panel a.

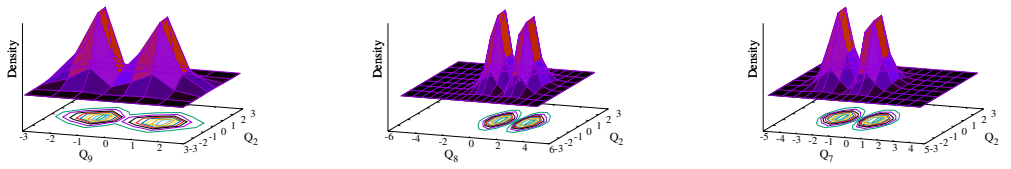

(a) 407 cm^{-1} (b) 576 cm^{-1} (c) 707 cm^{-1}

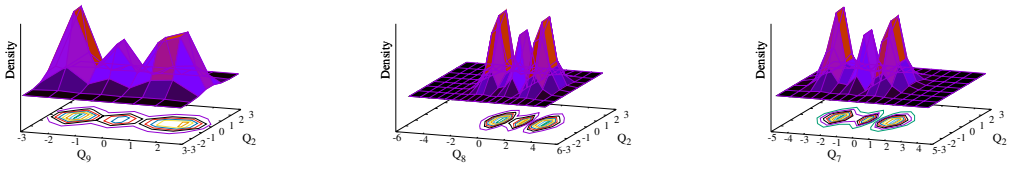

(d) 814 cm^{-1} (e) 1152 cm^{-1} (f) 1414 cm^{-1}

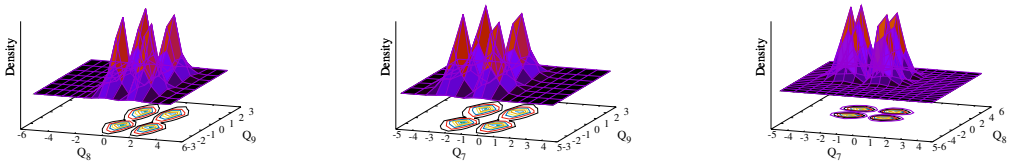

(g) 983 cm^{-1} (h) 1114 cm^{-1} (i) 1283 cm^{-1}

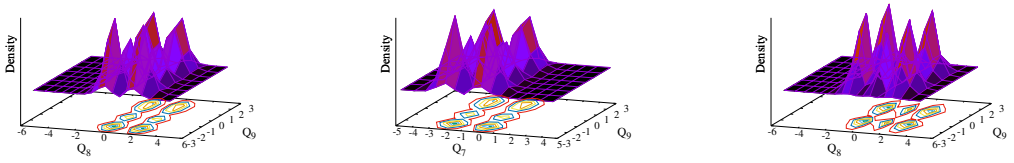

(j) 1390 cm^{-1} (k) 1521 cm^{-1} (l) 1559 cm^{-1}

FIGURE B5: Reduced density plots of the vibronic wave functions of the fundamental of ν_9, ν_8 and ν_7 (panels a, b and c, respectively) and first overtone of ν_9, ν_8, and ν_7 (panels d-f, respectively) excited in the S_1 ($\pi\pi^*$) state (uncoupled) of PFBz. The wave functions in panels g-l represent the combination peaks $\nu_8 + \nu_9$, $\nu_7 + \nu_9$, $\nu_7 + \nu_8$, $\nu_8 + \nu_{9_0^2}$, $\nu_7 + \nu_{9_0^2}$ and $\nu_{8_0^2} + \nu_9$. The Q_i in the abscissa represents the dimensionless normal displacement coordinate of the ith vibrational mode.

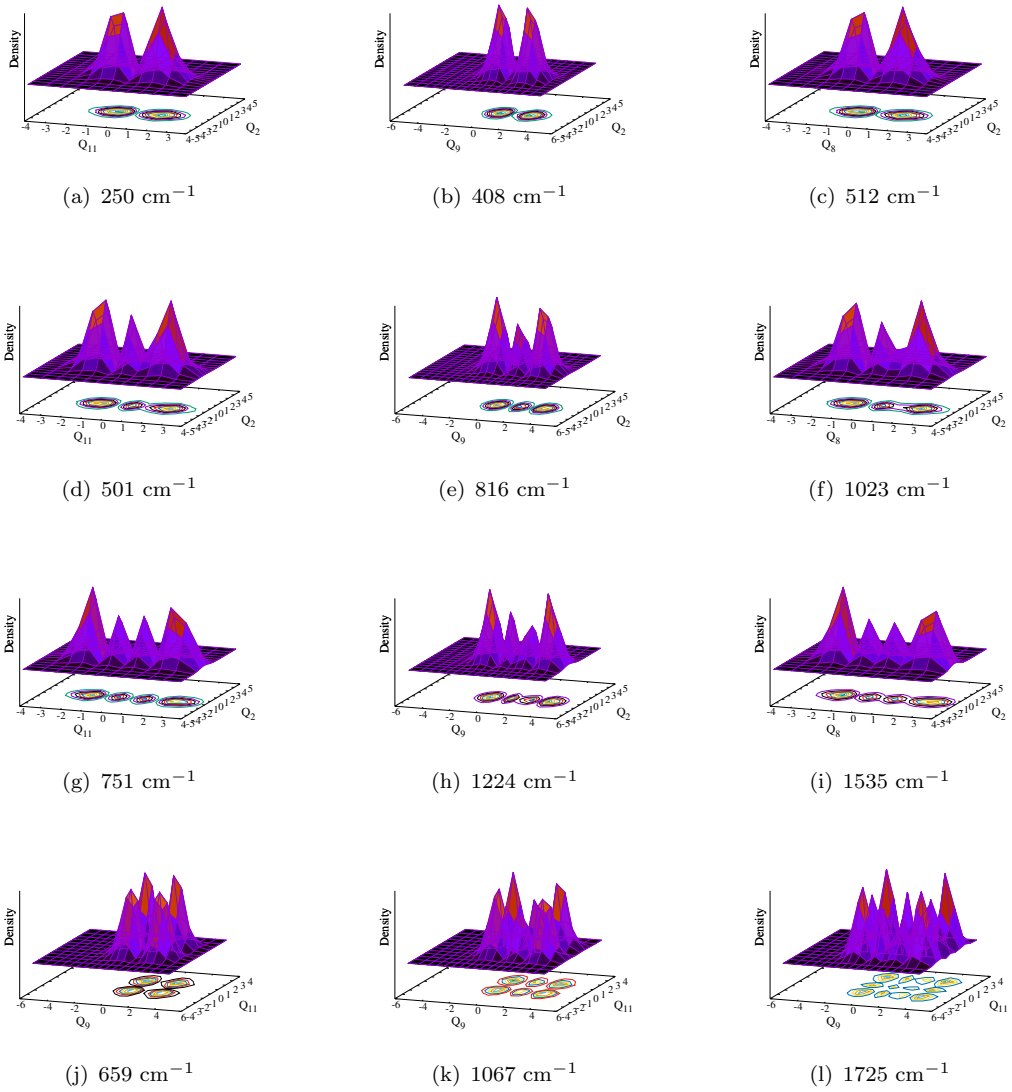

(a) 250 cm^{-1} (b) 408 cm^{-1} (c) 512 cm^{-1}

(d) 501 cm^{-1} (e) 816 cm^{-1} (f) 1023 cm^{-1}

(g) 751 cm^{-1} (h) 1224 cm^{-1} (i) 1535 cm^{-1}

(j) 659 cm^{-1} (k) 1067 cm^{-1} (l) 1725 cm^{-1}

FIGURE B6: Reduced density plots of the vibronic wave functions of the fundamental of ν_{11}, ν_9 and ν_8 (panels a, b and c, respectively) and first and second overtone of ν_{11}, ν_9, and ν_8 (panels d-i, respectively) excited in the S_3 ($\pi\sigma^*$) state (uncoupled) of PFBz. The wave functions in panels j-l represent the combination peaks $\nu_9+\nu_{11}$, $\nu_9{}_0^2+\nu_{11}$, and $\nu_9{}_0^3+\nu_{11}{}_0^2$. The Q_i in the abscissa represents the dimensionless normal displacement coordinate of the ith vibrational mode.

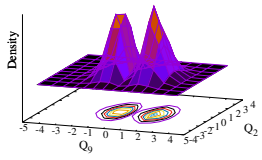

(a) 423 cm^{-1}

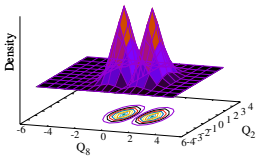

(b) 568 cm^{-1}

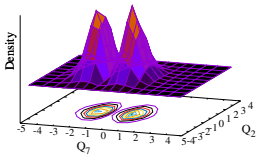

(c) 692 cm^{-1}

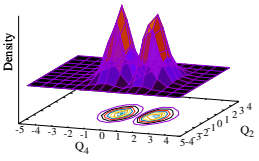

(d) 1384 cm^{-1}

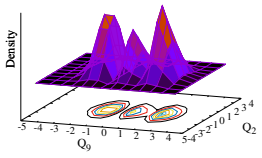

(e) 846 cm^{-1}

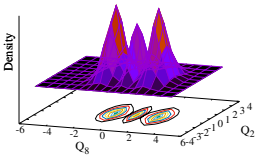

(f) 1137 cm^{-1}

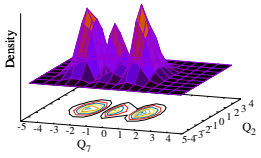

(g) 1384 cm^{-1}

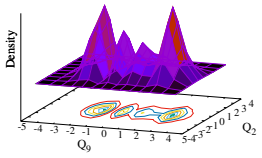

(h) 1269 cm^{-1}

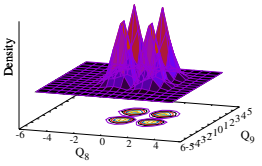

(i) 961 cm^{-1}

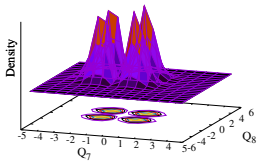

(j) 1260 cm^{-1}

FIGURE B7: Reduced density plots of the vibronic wave functions of the fundamental of ν_9, ν_8, ν_7, and ν_4 (panels a, b, c, and d, respectively) and first overtone of ν_9, ν_8, and ν_7 (panels e-g, respectively), and second overtone of ν_9 (panel h) excited in the S_4 ($\pi\pi^*$) state (uncoupled) of PFBz. The wave functions in panels i and j represent the combination peaks $\nu_8 + \nu_9$, and $\nu_7 + \nu_8$. The Q_i in the abscissa represents the dimensionless normal displacement coordinate of the ith vibrational mode.

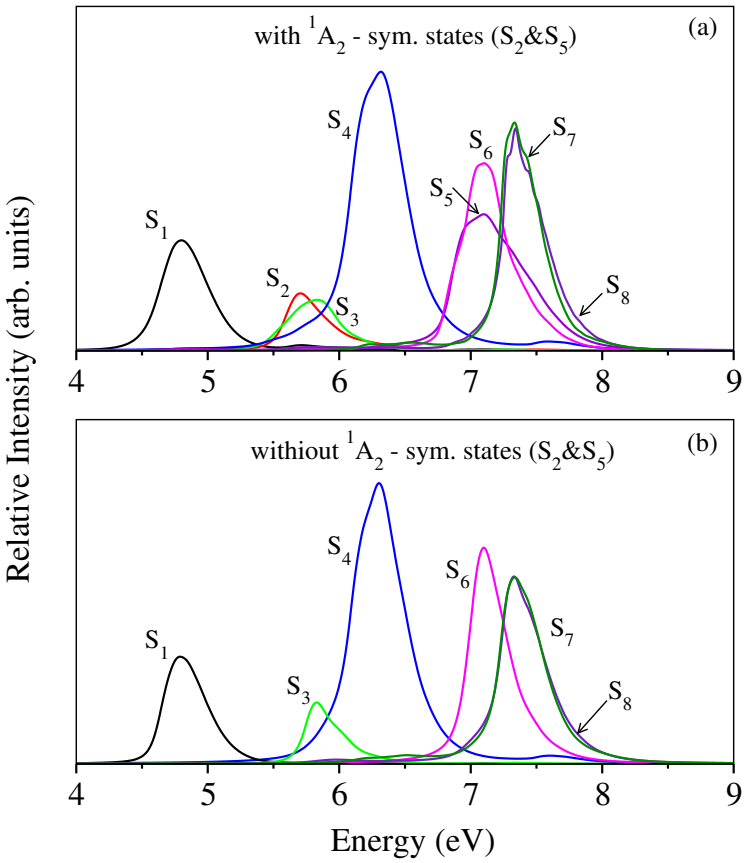

FIGURE B8: The absorption band structure of the individual states in the coupled states dynamics of PFBz obtained with (panel a) and without (panel b) the $^1A_2$ states (S_2 and S_5).

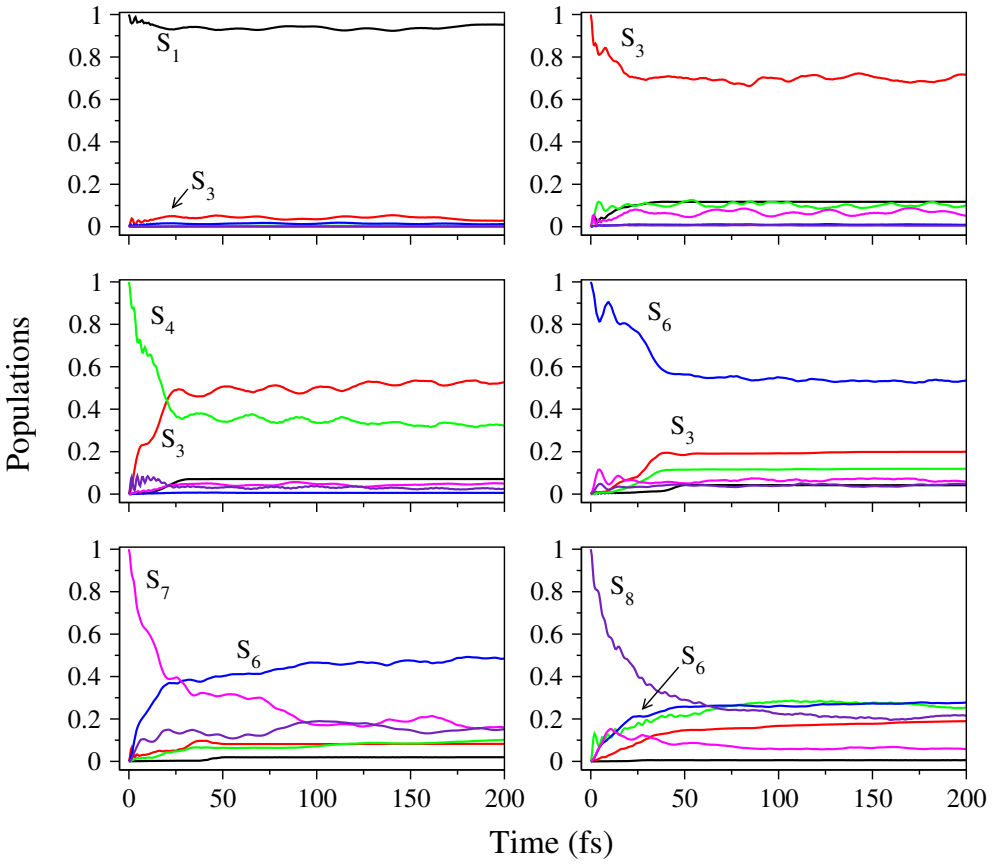

FIGURE B9: Time-dependence of diabatic electronic populations during the evolution of the WP in the coupled electronic states of PFBz without inclusion of $^1A_2$ symmetry (S_2 and S_5) states.

Appendix C

Supplementary material for Chapter 4

TABLE C1: The coupling parameters κ and γ (in eV) of the Hamiltonian [Eq. (4.5)] of totally symmetric vibrational modes of PFBz derived from the CASSCF-MRCI electronic energy data. Excitation strength, $\frac{1}{2}\left(\frac{\kappa_i}{\omega_i}\right)^2$ is given in the parentheses.

	$\widetilde{\mathrm{X}}\ ^2\mathrm{A}_2$		$\widetilde{\mathrm{A}}\ ^2\mathrm{B}_1$		$\widetilde{\mathrm{B}}\ ^2\mathrm{B}_1$	
	κ	γ	κ	γ	κ	γ
ν_1	0.0095 (0.0003)	-0.0019	-0.0021 (0.0000)	-0.0003	-0.0195 (0.0012)	0.0005
ν_2	-0.2436 (0.6819)	0.0155	0.1464 (0.2465)	-0.0013	-0.0096 (0.0011)	-0.0055
ν_3	-0.1889 (0.4936)	-0.0048	-0.1970 (0.5371)	-0.0201	-0.2270 (0.7130)	0.0269
ν_4	-0.2076 (0.6933)	-0.0055	-0.2361 (0.8968)	-0.0040	-0.2997 (1.4457)	0.0129
ν_5	0.0130 (0.0034)	-0.0058	0.0333 (0.0225)	-0.0069	0.0528 (0.0564)	-0.0009
ν_6	-0.0206 (0.0121)	-0.0020	0.0133 (0.0051)	-0.0070	-0.0073 (0.0015)	-0.0038
ν_7	0.0210 (0.0280)	-0.0045	-0.0325 (0.0668)	-0.0016	0.0349 (0.0770)	-0.0052
ν_8	0.0137 (0.0185)	-0.0014	0.0368 (0.1335)	-0.0029	-0.0230 (0.0525)	-0.0017
ν_9	0.0833 (1.0360)	-0.0023	-0.0542 (0.4391)	-0.0039	-0.0022 (0.0007)	-0.0040
ν_{10}	-0.0005 (0.0001)	0.0079	0.0089 (0.0219)	0.0042	0.0000 (0.0000)	0.0086
ν_{11}	0.0320 (0.4682)	0.0088	-0.0271 (0.3343)	0.0039	0.0041 (0.0076)	0.0028
	$\widetilde{\mathrm{C}}\ ^2\mathrm{B}_2$		$\widetilde{\mathrm{D}}\ ^2\mathrm{A}_1$		$\widetilde{\mathrm{E}}\ ^2\mathrm{B}_2$	
	κ	γ	κ	γ	κ	γ
ν_1	-0.0630 (0.0122)	0.0106	0.2943 (0.2656)	-0.1388	-0.0333 (0.0034)	0.0026
ν_2	-0.0320 (0.0117)	-0.0313	-0.2712 (0.8452)	-0.0364	0.2571 (0.7597)	-0.0303
ν_3	-0.2528 (0.8838)	-0.0803	-0.1087 (0.1633)	-0.0151	-0.0840 (0.0977)	0.0227
ν_4	-0.2068 (0.6884)	-0.0422	-0.2297 (0.8488)	-0.0309	-0.1387 (0.3097)	-0.0228
ν_5	0.0555 (0.0623)	-0.0220	-0.0990 (0.1982)	-0.0331	0.0504 (0.0514)	-0.0391
ν_6	0.0020 (0.0001)	-0.0192	0.0711 (0.1453)	-0.0064	-0.0789 (0.1792)	-0.0006
ν_7	0.0365 (0.0843)	-0.0085	-0.1352 (1.1581)	-0.0282	0.0394 (0.0986)	-0.0060
ν_8	0.0298 (0.0879)	-0.0076	-0.0171 (0.0290)	-0.0032	0.0235 (0.0545)	-0.0057
ν_9	0.0248 (0.0917)	-0.0116	-0.0685 (0.6997)	0.0010	0.0703 (0.7382)	-0.0151
ν_{10}	0.0009 (0.0002)	0.0012	0.0193 (0.1037)	0.0043	-0.0313 (0.2709)	0.0016
ν_{11}	-0.0036 (0.0058)	0.0102	0.0164 (0.1220)	0.0079	-0.0133 (0.0801)	-0.0042

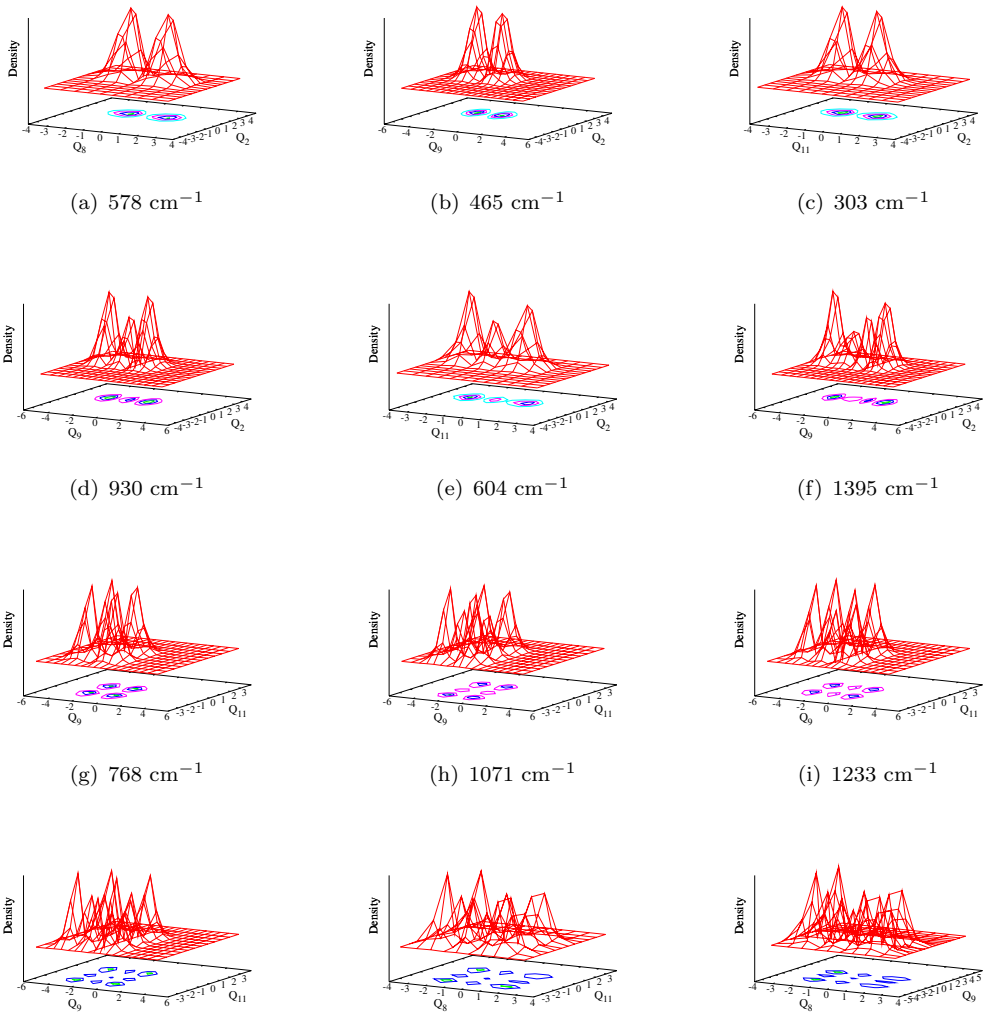

(a) 578 cm^{-1} (b) 465 cm^{-1} (c) 303 cm^{-1}

(d) 930 cm^{-1} (e) 604 cm^{-1} (f) 1395 cm^{-1}

(g) 768 cm^{-1} (h) 1071 cm^{-1} (i) 1233 cm^{-1}

(j) 1536 cm^{-1} (k) 1762 cm^{-1} (l) 2086 cm^{-1}

FIGURE C1: Reduced density plots of the vibronic wavefunctions of the fundamental of ν_8, ν_9 and ν_{11} (panels a, b and c, respectively) and first overtone of ν_9 and ν_{11} and second overtone of ν_9 (panels d-f, respectively) excited in the $\widetilde{X}\ ^2A_2$ state (uncoupled) of $PFBz^+$ calculated with the CASSCF-MRCI data. The wavefunctions in panels g-l represent the combination peaks $\nu_9+\nu_{11}$, $\nu_9+\nu_{11}{}_0^2$, $\nu_9{}_0^2+\nu_{11}$, $\nu_9{}_0^2+\nu_{11}{}_0^2$, $\nu_8{}_0^2+\nu_{11}{}_0^2$ and $\nu_8{}_0^2+\nu_9{}_0^2$. The Q_i in the abscissa represents the dimensionaless normal displacement coordinate of the i^{th} vibrational mode.

TABLE C2: The coupling parameter γ (in eV) of the Hamiltonian [Eq. (4.5)] of non-totally symmetric vibrational modes of PFBz derived from the CASSCF-MRCI electronic energy data.

Sym.	Mode	$\gamma^{(\widetilde{X})}$	$\gamma^{(\widetilde{A})}$	$\gamma^{(\widetilde{B})}$	$\gamma^{(\widetilde{C})}$	$\gamma^{(\widetilde{D})}$	$\gamma^{(\widetilde{E})}$
a_2	ν_{12}	0.0082	-0.0026	-0.0199	-0.0204	-0.0799	-0.0945
	ν_{13}	0.0286	-0.0057	-0.0105	-0.0009	0.0151	-0.0398
	ν_{14}	0.0026	0.0037	0.0014	0.0047	0.0024	-0.0146
b_1	ν_{15}	0.0002	0.0108	-0.0303	0.0439	-0.0642	-0.1449
	ν_{16}	0.0062	0.0033	-0.0185	-0.0449	-0.0772	-0.0769
	ν_{17}	-0.0010	-0.0074	-0.0225	-0.0176	-0.0670	-0.0075
	ν_{18}	-0.0058	0.0127	-0.0095	0.0021	-0.0439	0.0033
	ν_{19}	0.0187	0.0174	0.0170	0.0228	0.0063	0.0133
	ν_{20}	0.0025	0.0010	-0.00005	0.0033	-0.0140	0.0046
b_2	ν_{21}	-0.1597	0.1989	-0.0556	-0.0483	-0.1744	0.0846
	ν_{22}	-0.0213	-0.0068	0.0459	-0.3362	0.2588	-0.0499
	ν_{23}	0.0922	0.0594	0.1126	0.0223	-0.0423	-0.0701
	ν_{24}	-0.0112	0.0095	0.0014	-0.0578	-0.0787	-0.0182
	ν_{25}	-0.0021	-0.0006	0.0088	-0.0078	-0.0214	-0.0183
	ν_{26}	-0.0020	-0.0021	0.0018	-0.0263	0.0051	-0.0170
	ν_{27}	0.0004	0.0002	-0.0017	-0.0108	-0.0146	-0.0087
	ν_{28}	-0.0479	0.0368	-0.0024	-0.0115	-0.0153	0.0017
	ν_{29}	0.0050	0.0076	0.0059	0.0012	0.0095	-0.0021
	ν_{30}	0.0062	0.0072	0.0037	0.0135	0.0021	-0.0034

TABLE C3: Same as in Table C1, derived from the EOMIP-CCSD electronic energy data.

	$\widetilde{X}\ ^2A_2$		$\widetilde{A}\ ^2B_1$		$\widetilde{B}\ ^2B_1$	
	κ	γ	κ	γ	κ	γ
ν_1	0.0042 (0.00005)	0.0016	0.0093 (0.0003)	0.0028	-0.0034 (0.00003)	0.0019
ν_2	-0.2050 (0.4835)	0.0106	0.1261 (0.1828)	-0.0027	-0.0197 (0.0045)	0.0023
ν_3	-0.1628 (0.3666)	-0.0062	-0.1809 (0.4529)	-0.0189	-0.1503 (0.3126)	0.0057
ν_4	-0.1736 (0.4852)	-0.0069	-0.1964 (0.6209)	-0.0058	-0.2238 (0.8069)	-0.0039
ν_5	0.0098 (0.0019)	-0.0057	0.0311 (0.0196)	-0.0065	0.0389 (0.0307)	-0.0039
ν_6	-0.0203 (0.0118)	-0.0021	0.0129 (0.0048)	-0.0064	-0.0201 (0.0116)	-0.0028
ν_7	0.0190 (0.0230)	-0.0026	-0.0346 (0.0760)	0.0029	0.0282 (0.0504)	-0.0013
ν_8	0.0193 (0.0367)	-0.0016	0.0393 (0.1524)	-0.0028	-0.0063 (0.0039)	-0.0017
ν_9	0.0815 (0.9936)	-0.0031	-0.0486 (0.3529)	-0.0038	0.0034 (0.0017)	-0.0017
ν_{10}	0.0006 (0.0001)	0.0066	0.0063 (0.0112)	0.0041	-0.0001 (0.0000)	0.0040
ν_{11}	0.0332 (0.5045)	0.0076	-0.0275 (0.3447)	0.0041	0.0013 (0.0008)	0.0050
	$\widetilde{C}\ ^2B_2$		$\widetilde{D}\ ^2A_1$		$\widetilde{E}\ ^2B_2$	
	κ	γ	κ	γ	κ	γ
ν_1	0.0047 (0.00006)	0.0020	0.1139 (0.0398)	-0.0365	-0.0098 (0.0003)	0.0018
ν_2	-0.0237 (0.0066)	-0.0226	-0.2136 (0.5247)	-0.0278	0.1574 (0.2848)	-0.0244
ν_3	-0.1804 (0.4504)	-0.0505	-0.0848 (0.0994)	-0.0177	-0.0500 (0.0346)	0.0030
ν_4	-0.1351 (0.2941)	-0.0304	-0.1338 (0.2883)	-0.0262	-0.0498 (0.0399)	-0.0254
ν_5	0.0256 (0.0132)	-0.0275	-0.0456 (0.0421)	-0.0324	0.0493 (0.0492)	-0.0309
ν_6	0.0000 (0.0000)	-0.0193	0.0353 (0.0359)	-0.0074	-0.0795 (0.1821)	-0.0071
ν_7	0.0186 (0.0220)	-0.0070	-0.0696 (0.3069)	-0.0191	0.0264 (0.0442)	-0.0045
ν_8	0.0266 (0.0504)	-0.0065	0.0009 (0.0001)	-0.0038	0.0149 (0.0218)	-0.0043
ν_9	0.0166 (0.0410)	-0.0038	-0.0395 (0.2333)	0.0010	0.0601 (0.5397)	-0.0107
ν_{10}	-0.0033 (0.0029)	-0.0015	0.0196 (0.1069)	0.0018	-0.0291 (0.2361)	-0.0001
ν_{11}	-0.0103 (0.0484)	0.0082	0.0197 (0.1767)	0.0081	0.0073 (0.0242)	-0.0096

TABLE C4: Same as in Table C2, derived from the EOMIP-CCSD electronic energy data.

Sym.	Mode	$\gamma^{(\widetilde{X})}$	$\gamma^{(\widetilde{A})}$	$\gamma^{(\widetilde{B})}$	$\gamma^{(\widetilde{C})}$	$\gamma^{(\widetilde{D})}$	$\gamma^{(\widetilde{E})}$
a_2	ν_{12}	0.0053	-0.0037	-0.0154	-0.0111	-0.0238	0.0016
	ν_{13}	0.0271	-0.0067	-0.0101	0.0052	0.0129	-0.0026
	ν_{14}	0.0023	0.0031	0.0019	0.0029	0.0016	0.0040
b_1	ν_{15}	0.0043	0.0066	-0.0335	0.0009	-0.0415	-0.0048
	ν_{16}	0.0032	0.0009	-0.0090	-0.0307	-0.0121	-0.0182
	ν_{17}	-0.0016	-0.0094	-0.0151	-0.0108	0.0047	-0.0196
	ν_{18}	-0.0066	0.0119	-0.0064	0.0025	0.0018	0.0027
	ν_{19}	0.0171	0.0156	0.0139	0.0157	0.0109	0.0056
	ν_{20}	0.0021	0.0009	0.0010	0.0021	0.0042	0.0010
b_2	ν_{21}	-0.1146	0.1197	0.0019	-0.0307	-0.1192	0.0408
	ν_{22}	-0.0208	-0.0021	0.0084	-0.1295	0.0621	-0.0477
	ν_{23}	0.0558	0.0505	0.0237	0.0022	-0.0309	-0.0328
	ν_{24}	-0.0076	0.0076	0.0000	-0.0144	-0.0347	-0.0118
	ν_{25}	-0.0095	-0.0035	-0.0060	-0.0112	-0.0218	-0.0200
	ν_{26}	-0.0027	-0.0017	-0.0021	-0.0197	0.0041	-0.0162
	ν_{27}	0.0005	-0.0003	-0.0028	-0.0105	-0.0118	-0.0092
	ν_{28}	-0.0307	0.0236	-0.0020	-0.0092	-0.0119	0.0010
	ν_{29}	0.0048	0.0063	0.0044	0.0019	0.0050	-0.0053
	ν_{30}	0.0027	0.0098	-0.0001	0.0112	-0.0001	0.0002

TABLE C5: Third-order coupling parameter (η) (in eV) of the Hamiltonian [Eqs. (4.5)] of symmetrical modes of PFBz derived from CASSCF-MRCI electronic structure data.

Sym.	Mode	$\eta^{(\widetilde{X})}$	$\eta^{(\widetilde{A})}$	$\eta^{(\widetilde{B})}$	$\eta^{(\widetilde{C})}$	$\eta^{(\widetilde{D})}$	$\eta^{(\widetilde{E})}$
	ν_1	-0.000030	0.000060	0.000092	0.000319	0.000162	0.000042
	ν_2	0.000000	0.000000	0.000201	-0.000205	0.000115	-0.000507
	ν_3	0.000004	-0.000014	0.000132	0.000285	-0.000000	0.000372
	ν_4	0.000000	0.000000	0.000000	-0.000088	0.000145	0.000362
	ν_5	0.000010	0.000002	0.000025	-0.000129	0.000172	-0.000080
a_1	ν_6	-0.000002	-0.000009	0.000020	-0.000083	-0.000032	-0.000027
	ν_7	0.000049	-0.000032	0.000091	-0.000019	0.000028	-0.000007
	ν_8	-0.000008	-0.000005	-0.000013	0.000000	0.000008	0.000009
	ν_9	-0.000003	-0.000016	-0.000003	0.000033	-0.000007	0.000032
	ν_{10}	-0.000001	-0.000017	-0.000038	-0.000052	0.000003	-0.000004
	ν_{11}	0.000013	0.000004	0.000122	0.000000	-0.000022	0.000049

TABLE C6: Fourth-order coupling parameter (ζ) (in eV) of the Hamiltonian [Eqs. (4.5)] of unsymmetrical modes of PFBz derived from CASSCF-MRCI electronic structure data.

Sym.	Mode	$\zeta^{(\widetilde{X})}$	$\zeta^{(\widetilde{A})}$	$\zeta^{(\widetilde{B})}$	$\zeta^{(\widetilde{C})}$	$\zeta^{(\widetilde{D})}$	$\zeta^{(\widetilde{E})}$
a_2	ν_{12}	0.000001	0.000002	0.000000	0.000073	-0.000012	-0.000048
	ν_{13}	-0.000002	0.000000	0.000000	0.000057	0.000007	-0.000056
	ν_{14}	-0.000000	0.000000	0.000000	0.000000	-0.000003	0.000000
b_1	ν_{15}	-0.000008	-0.000023	-0.000007	-0.000096	0.000022	-0.000066
	ν_{16}	0.000001	0.000002	0.000002	0.000043	-0.000025	0.000711
	ν_{17}	0.000001	0.000002	0.000002	0.000054	-0.000045	0.000105
	ν_{18}	-	0.000000	0.000000	-0.000013	0.000016	0.000018
	ν_{19}	-	0.000000	0.000000	-0.000001	0.000000	-0.000001
	ν_{20}	-	0.000000	0.000000	0.000003	-0.000005	0.000000
b_2	ν_{21}	0.000234	-0.000402	0.000164	-0.000065	0.000131	-0.000123
	ν_{22}	0.000000	0.000006	-0.000073	0.000783	-0.000800	-0.000032
	ν_{23}	-0.000147	0.000025	-0.000253	-0.000082	-0.000088	0.000031
	ν_{24}	-0.000002	0.000000	-0.000019	-0.000090	0.000221	0.000018
	ν_{25}	-0.000028	-0.000026	-0.000089	-0.000002	-0.000011	-0.000001
	ν_{26}	-0.000009	0.000012	-0.000065	0.000010	-0.000033	0.000004
	ν_{27}	-0.000003	0.000000	-0.000003	0.000001	0.000001	0.000000
	ν_{28}	0.000086	-0.000056	0.000000	0.000000	0.000002	-0.000007
	ν_{29}	0.000000	0.000000	0.000000	0.000000	0.000000	0.000000
	ν_{30}	-0.000011	0.000028	0.000005	0.000000	0.000010	0.000042

TABLE C7: Same as in Table C6, derived from the EOMIP-CCSD electronic structure data.

Sym.	Mode	$\zeta^{(\widetilde{X})}$	$\zeta^{(\widetilde{A})}$	$\zeta^{(\widetilde{B})}$	$\zeta^{(\widetilde{C})}$	$\zeta^{(\widetilde{D})}$	$\zeta^{(\widetilde{E})}$
a_2	ν_{12}	0.00071	0.00069	0.00111	0.00094	0.00109	0.00062
	ν_{13}	-0.00153	0.00009	0.00026	-0.00029	-0.00073	-0.00007
	ν_{14}	-	-	-	-	-	-
b_1	ν_{15}	0.00013	-0.00197	-0.00209	-0.00041	-0.01120	0.00125
	ν_{16}	0.00108	0.00148	0.00057	0.00003	0.00112	0.00241
	ν_{17}	0.00022	0.00135	0.00095	0.00044	-0.00058	0.00079
	ν_{18}	0.00022	-0.00022	0.00010	-0.00016	-0.00023	-0.00021
	ν_{19}	-0.00039	-0.00034	-0.00042	-0.00063	-0.00052	-0.00071
	ν_{20}	-0.00004	0.00000	0.00000	-0.00002	-0.00012	-0.00002
b_2	ν_{21}	0.05305	-0.05288	-0.00023	-0.00614	0.04064	-0.03059
	ν_{22}	0.00076	-0.00035	-0.00089	0.04191	-0.04247	0.00908
	ν_{23}	-0.00684	-0.00679	-0.00468	-0.00388	0.00378	0.00185
	ν_{24}	0.00015	-0.00085	-0.00018	-0.00745	0.00181	-0.00095
	ν_{25}	0.00012	-0.00003	0.00000	-0.00006	0.00024	-0.00094
	ν_{26}	0.00000	0.00000	0.00000	0.00166	-0.00175	0.00026
	ν_{27}	-0.00006	-0.00007	-0.00004	-0.00008	0.00012	-0.00027
	ν_{28}	0.00659	-0.00651	0.00005	0.00009	0.00017	-0.00010
	ν_{29}	0.00000	0.00000	0.00000	0.00000	0.00000	0.00000
	ν_{30}	0.00012	-0.00037	-0.00007	-0.00018	-0.00092	-0.00036

TABLE C8: Diagonal bilinear γ_{ij}^{α} (in eV) parameters (in eV) along the totally symmetric vibrational modes $\nu_2, \nu_3, \nu_4, \nu_9, \nu_{11}$ of the lowest six electronic states of $PFBz^+$ and these are derived from the EOMIP-CCSD electronic structure data.

Mode	$\widetilde{X}^2A_2$	$\widetilde{A}^2B_1$	$\widetilde{B}^2B_1$	$\widetilde{C}^2B_2$	$\widetilde{D}^2A_1$	$\widetilde{E}^2B_2$
γ_{22}	0.0106	-0.0027	0.0023	-0.0226	-0.0278	-0.0244
γ_{23}	0.0033	-0.0062	0.0054	0.0043	-0.0152	0.0342
γ_{24}	-0.0012	-0.0059	-0.0095	-0.0085	-0.0099	-0.0137
γ_{29}	-0.0001	-0.0064	-0.0048	-0.0230	-0.0114	-0.0229
γ_{211}	-0.0066	-0.0059	-0.0064	-0.0024	0.0012	-0.0084
γ_{33}	-0.0062	-0.0189	0.0057	-0.0505	-0.0177	0.0030
γ_{34}	-0.0007	0.0130	-0.0272	0.0290	0.0103	-0.0130
γ_{39}	-0.0016	0.0045	0.0010	0.0021	-0.0013	0.0082
γ_{311}	0.0011	0.0005	0.0001	0.0010	0.0039	-0.0043
γ_{44}	-0.0070	-0.0058	-0.0039	-0.0304	-0.0262	-0.0254
γ_{49}	0.0017	0.0035	0.0019	0.0052	0.0017	0.0028
γ_{411}	0.0009	-0.0006	-0.0001	-0.0008	0.0067	-0.0160
γ_{99}	-0.0031	-0.0038	-0.0017	-0.0096	0.0010	-0.0107
γ_{911}	-0.0016	-0.0019	0.0001	0.0036	0.0053	-0.0022
γ_{1111}	0.0076	0.0041	0.0050	0.0082	0.0081	-0.0096

TABLE C9: Linear inter-state coupling parameter between the α and α' state ($\lambda^{\alpha\alpha'}$) (in eV) and corresponding excitation strength $\frac{1}{2}\left(\frac{\lambda^{\alpha\alpha'}}{\omega_i}\right)^2$ (given in the parentheses) derived from the CASSCF-MRCI electronic energy data.

Sym.	Mode	$\lambda^{\alpha\alpha'}$	$\lambda^{\alpha\alpha'}$
		$\widetilde{A}$-$\widetilde{C}$	$\widetilde{B}$-$\widetilde{C}$
a_2	ν_{12}	0.0000 (0.0000)	0.0000 (0.0000)
	ν_{13}	0.1233 (3.3549)	0.0823 (1.4947)
	ν_{14}	0.0404 (3.0715)	0.0481 (4.3540)
		$\widetilde{X}$-$\widetilde{C}$	$\widetilde{X}$-$\widetilde{E}$
b_1	ν_{15}	0.2797 (3.5957)	0.0000 (0.0000)
	ν_{16}	0.0000 (0.0000)	0.0000 (0.0000)
	ν_{17}	0.0000 (0.0000)	0.0000 (0.0000)
	ν_{18}	0.0924 (2.7639)	0.1163 (4.3787)
	ν_{19}	0.1055 (8.6943)	0.0000 (0.0000)
	ν_{20}	0.0354 (1.6478)	0.0631 (5.2355)
		$\widetilde{X}$-$\widetilde{A}$	$\widetilde{X}$-$\widetilde{B}$
b_2	ν_{21}	0.1769 (0.3610)	0.2474 (0.7060)
	ν_{22}	0.0387 (0.0201)	0.2114 (0.5993)
	ν_{23}	0.0000 (0.0000)	0.1052 (0.1647)
	ν_{24}	0.0387 (0.0347)	0.1086 (0.2733)
	ν_{25}	0.0128 (0.0042)	0.0681 (0.1185)
	ν_{26}	0.0126 (0.0058)	0.0000 (0.0000)
	ν_{27}	0.0000 (0.0000)	0.0000 (0.0000)
	ν_{28}	0.0756 (1.0097)	0.1756 (5.4475)
	ν_{29}	0.0128 (0.0595)	0.0297 (0.3204)
	ν_{30}	0.0199 (0.1743)	0.0000 (0.0000)
		$\widetilde{C}$-$\widetilde{D}$	$\widetilde{D}$-$\widetilde{E}$
b_2	ν_{21}	0.0000 (0.0000)	0.2332 (0.6273)
	ν_{22}	0.2328 (0.7267)	0.0000 (0.0000)
	ν_{23}	0.0000 (0.0000)	0.0000 (0.0000)
	ν_{24}	0.0894 (0.1852)	0.0965 (0.2158)
	ν_{25}	0.0000 (0.0000)	0.0289 (0.0213)
	ν_{26}	0.0526 (0.1004)	0.0000 (0.0000)
	ν_{27}	0.0000 (0.0000)	0.0369 (0.0947)
	ν_{28}	0.0000 (0.0000)	0.0639 (0.7213)
	ν_{29}	0.0252 (0.2307)	0.0000 (0.0000)
	ν_{30}	0.0000 (0.0000)	0.0000 (0.0000)

TABLE C10: Same as in Table C9 derived from the EOMIP-CCSD electronic energy data.

Sym.	Mode	$\lambda^{\alpha\alpha'}$	$\lambda^{\alpha\alpha'}$	$\lambda^{\alpha\alpha'}$	$\lambda^{\alpha\alpha'}$
		$\widetilde{A}$-$\widetilde{C}$	$\widetilde{A}$-$\widetilde{E}$	$\widetilde{B}$-$\widetilde{C}$	$\widetilde{B}$-$\widetilde{E}$
a_2	ν_{12}	0.0000 (0.0000)	0.0773 (0.4873)	0.0309 (0.0779)	0.0886 (0.6402)
	ν_{13}	0.1047 (2.4191)	0.0690 (1.0506)	0.0589 (0.7656)	0.0587 (0.7604)
	ν_{14}	0.0000 (0.0000)	0.0346 (2.2529)	0.0149 (0.4178)	0.0323 (1.9633)
		$\widetilde{X}$-$\widetilde{C}$	$\widetilde{X}$-$\widetilde{E}$	$\widetilde{A}$-$\widetilde{D}$	$\widetilde{B}$-$\widetilde{D}$
b_1	ν_{15}	0.0000 (0.0000)	0.0000 (0.0000)	0.0000 (0.0000)	0.0000 (0.0000)
	ν_{16}	0.0000 (0.0000)	0.0000 (0.0000)	0.0000 (0.0000)	0.0000 (0.0000)
	ν_{17}	0.0000 (0.0000)	0.0000 (0.0000)	0.1187 (1.6674)	0.0805 (0.7669)
	ν_{18}	0.0954 (2.9463)	0.1074 (3.7342)	0.0000 (0.0000)	0.0519 (0.8270)
	ν_{19}	0.0000 (0.0000)	0.0000 (0.0000)	0.0000 (0.0000)	0.0000 (0.0000)
	ν_{20}	0.0063 (0.0522)	0.0000 (0.0000)	0.0589 (4.5617)	0.0326 (1.3974)
		$\widetilde{X}$-$\widetilde{A}$	$\widetilde{X}$-$\widetilde{B}$	$\widetilde{C}$-$\widetilde{D}$	$\widetilde{D}$-$\widetilde{E}$
b_2	ν_{21}	0.1693 (0.3306)	0.3079 (1.0935)	0.0000 (0.0000)	0.1531 (0.2704)
	ν_{22}	0.0412 (0.0228)	0.1514 (0.3074)	0.1562 (0.3272)	0.0000 (0.0000)
	ν_{23}	0.0000 (0.0000)	0.0000 (0.0000)	0.0000 (0.0000)	0.0000 (0.0000)
	ν_{24}	0.0370 (0.0317)	0.0768 (0.1367)	0.0000 (0.0000)	0.0547 (0.0693)
	ν_{25}	0.0230 (0.0135)	0.0524 (0.0701)	0.0000 (0.0000)	0.0142 (0.0052)
	ν_{26}	0.0097 (0.0034)	0.0220 (0.0176)	0.0499 (0.0903)	0.0000 (0.0000)
	ν_{27}	0.0000 (0.0000)	0.0000 (0.0000)	0.0000 (0.0000)	0.0179 (0.0223)
	ν_{28}	0.0713 (0.8981)	0.1482 (3.8801)	0.0000 (0.0000)	0.0416 (0.3057)
	ν_{29}	0.0115 (0.0480)	0.0000 (0.0000)	0.0183 (0.1217)	0.0000 (0.0000)
	ν_{30}	0.0250 (0.2752)	0.0407 (0.7293)	0.0000 (0.0000)	0.0082 (0.0296)

TABLE C11: The number of HO basis functions along the totally symmetric vibrational modes and the dimension of the secular matrix used in the calculation of the stick vibrational spectra of the uncoupled electronic states of $PFBz^+$ shown in various figures.

Electronic states	Vibrational modes	No. of HO basis	Dimension of secular matrix	Figure(s)
CASSCF-MRCI				
$\widetilde{X}$	ν_2, ν_3, ν_4, ν_6,	12, 10, 12, 8,	69672960	Fig. 4.3(a)
	ν_7, ν_8, ν_9, ν_{11}	6, 6, 14, 12		
$\widetilde{A}$	ν_2, ν_3, ν_4, ν_5,	12, 10, 12, 4,	69672960	Fig. 4.3(a)
	ν_7, ν_8, ν_9, ν_{11}	6, 6, 14, 12		
$\widetilde{B}$	ν_2, ν_3, ν_4, ν_5, ν_6	4, 10, 12, 6, 4,	19906560	Fig. 4.3(a)
	ν_7, ν_8, ν_9, ν_{10}, ν_{11}	6, 6, 4, 2, 6		
$\widetilde{C}$	ν_2, ν_3, ν_4, ν_5, ν_6	6, 10, 12, 6, 4,	70778880	Fig. 4.3(a)
	ν_7, ν_8, ν_9, ν_{10}, ν_{11}	8, 8, 8, 2, 4		
$\widetilde{D}$	ν_2, ν_3, ν_4, ν_5, ν_6	10, 8, 10, 8, 6,	117964800	Fig. 4.3(a)
	ν_7, ν_8, ν_9, ν_{10}, ν_{11}	12, 2, 8, 4, 4		
$\widetilde{E}$	ν_2, ν_3, ν_4, ν_5, ν_6	10, 4, 8, 4, 6,	58982400	Fig. 4.3(a)
	ν_7, ν_8, ν_9, ν_{10}, ν_{11}	6, 4, 10, 8, 4		
EOMIP-CCSD				
$\widetilde{X}$	ν_2, ν_3, ν_4, ν_5, ν_6,	6, 6, 6, 3, 4,	5971968	Fig. 4.3(b)
	ν_7, ν_8, ν_9, ν_{10}, ν_{11}	4, 4, 8, 3, 6		
$\widetilde{A}$	ν_2, ν_3, ν_4, ν_5, ν_6,	4, 6, 8, 3, 3,	2985984	Fig. 4.3(b)
	ν_7, ν_8, ν_9, ν_{10}, ν_{11}	4, 4, 6, 3, 6		
$\widetilde{B}$	ν_2, ν_3, ν_4, ν_5, ν_6,	3, 6, 8, 4, 4,	746496	Fig. 4.3(b)
	ν_7, ν_8, ν_9, ν_{10}, ν_{11}	4, 3, 3, 3, 3		
$\widetilde{C}$	ν_2, ν_3, ν_4, ν_5, ν_6,	3, 8, 6, 3, 3,	746496	Fig. 4.3(b)
	ν_7, ν_8, ν_9, ν_{10}, ν_{11}	3, 4, 4, 3, 4		
$\widetilde{D}$	ν_2, ν_3, ν_4, ν_5, ν_6,	8, 4, 6, 3, 3,	199065	Fig. 4.3(b)
	ν_7, ν_8, ν_9, ν_{10}, ν_{11}	6, 3, 4, 4, 4		
$\widetilde{E}$	ν_2, ν_3, ν_4, ν_5, ν_6,	6, 4, 4, 4, 6,	3981312	Fig. 4.3(b)
	ν_7, ν_8, ν_9, ν_{10}, ν_{11}	4, 3, 8, 6, 3		

TABLE C12: Energy eigenvalue (in cm^{-1}) of the low-lying vibrational levels of the $\widetilde{X}\ ^2A_2$ and $\widetilde{A}\ ^2B_1$ electronic states of $PFBz^+$ obtained from the uncoupled state calculations using the set of parameters derived from the CASSCF-MRCI energy data [cf., Table C1]. The assignment of the levels carried out by examining the nodal pattern of the wave functions are included in the table.

$\widetilde{X}\ ^2A_2$		$\widetilde{A}\ ^2B_1$	
Energy	Assignment	Energy	Assignment
0	0_0^0	0	0_0^0
303	$\nu_{11}{}_0^1$	285	$\nu_{11}{}_0^1$
465	$\nu_9{}_0^1$	458	$\nu_9{}_0^1$
578	$\nu_8{}_0^1$	570	$\nu_{11}{}_0^2$
606	$\nu_{11}{}_0^2$	572	$\nu_8{}_0^1$
711	$\nu_7{}_0^1$	722	$\nu_7{}_0^1$
768	$\nu_9{}_0^1+\nu_{11}{}_0^1$	743	$\nu_9{}_0^1+\nu_{11}{}_0^1$
881	$\nu_8{}_0^1+\nu_{11}{}_0^1$	857	$\nu_8{}_0^1+\nu_{11}{}_0^1$
930	$\nu_9{}_0^2$	917	$\nu_9{}_0^2$
1014	$\nu_7{}_0^1+\nu_{11}{}_0^1$	1008	$\nu_7{}_0^1+\nu_{11}{}_0^1$
1043	$\nu_8{}_0^1+\nu_9{}_0^1$	1028	$\nu_9{}_0^1+\nu_{11}{}_0^2$
1071	$\nu_9{}_0^1+\nu_{11}{}_0^2$	1063	$\nu_6{}_0^1$
1084	$\nu_6{}_0^1$	1142	$\nu_8{}_0^1+\nu_{11}{}_0^2$
1157	$\nu_8{}_0^2$	1145	$\nu_8{}_0^2$
1177	$\nu_7{}_0^1+\nu_9{}_0^1$	1181	$\nu_7{}_0^1+\nu_9{}_0^1$
1184	$\nu_8{}_0^1+\nu_{11}{}_0^1$	1202	$\nu_9{}_0^2+\nu_{11}{}_0^1$
1233	$\nu_9{}_0^2+\nu_{11}{}_0^1$	1295	$\nu_7{}_0^1+\nu_8{}_0^1$
1288	$\nu_7{}_0^1+\nu_8{}_0^1$	1348	$\nu_6{}_0^1+\nu_{11}{}_0^1$
1317	$\nu_7{}_0^1+\nu_{11}{}_0^2$	1375	$\nu_9{}_0^3$
1387	$\nu_6{}_0^1+\nu_{11}{}_0^1$	1428	$\nu_4{}_0^1$
1395	$\nu_9{}_0^3$	1445	$\nu_7{}_0^2$
1421	$\nu_4{}_0^1$	1468	$\nu_3{}_0^1$
1460	$\nu_8{}_0^2+\nu_{11}{}_0^1$	1486	$\nu_9{}_0^2+\nu_{11}{}_0^2$
1508	$\nu_8{}_0^1+\nu_9{}_0^2$	1489	$\nu_8{}_0^1+\nu_9{}_0^2$
1532	$\nu_3{}_0^1$	1522	$\nu_6{}_0^1+\nu_9{}_0^1$
1536	$\nu_9{}_0^2+\nu_{11}{}_0^2$	1635	$\nu_6{}_0^1+\nu_8{}_0^1$
1549	$\nu_6{}_0^1+\nu_9{}_0^1$	1639	$\nu_7{}_0^1+\nu_9{}_0^2$
1622	$\nu_8{}_0^2+\nu_9{}_0^1$	1677	$\nu_2{}_0^1$
1641	$\nu_7{}_0^1+\nu_9{}_0^2$	1712	$\nu_4{}_0^1+\nu_{11}{}_0^1$
1690	$\nu_6{}_0^1+\nu_{11}{}_0^2$	1715	$\nu_8{}_0^3$
1744	$\nu_2{}_0^1$	1731	$\nu_7{}_0^2+\nu_{11}{}_0^1$
1835	$\nu_3{}_0^1+\nu_{11}{}_0^1$	1753	$\nu_3{}_0^1+\nu_{11}{}_0^1$
1997	$\nu_3{}_0^1+\nu_9{}_0^1$	1786	$\nu_6{}_0^1+\nu_7{}_0^1$
2000	$\nu_7{}_0^2+\nu_8{}_0^1$	1868	$\nu_7{}_0^1+\nu_8{}_0^2$
2027	$\nu_4{}_0^1+\nu_{11}{}_0^2$	1886	$\nu_4{}_0^1+\nu_9{}_0^1$
2047	$\nu_2{}_0^1+\nu_{11}{}_0^1$	1904	$\nu_7{}_0^2+\nu_9{}_0^1$
2087	$\nu_8{}_0^2+\nu_9{}_0^2$	1962	$\nu_2{}_0^1+\nu_{11}{}_0^1$
		2000	$\nu_4{}_0^1+\nu_8{}_0^1$

TABLE C13: Same as in Table C12, obtained with the set of parameters derived from the EOMIP-CCSD energy data [cf., Table C3].

$\bar{X}\ ^2A_2$		$\bar{A}\ ^2B_1$	
Energy	Assignment	Energy	Assignment
0	0_0^0	0	0_0^0
298	$\nu_{11}{}_0^1$	285	$\nu_{11}{}_0^1$
355	$\nu_{10}{}_0^1$	345	$\nu_{10}{}_0^1$
488	$\nu_9{}_0^1$	460	$\nu_9{}_0^1$
577	$\nu_8{}_0^1$	570	$\nu_{11}{}_0^2$
597	$\nu_{11}{}_0^2$	572	$\nu_8{}_0^1$
653	$\nu_{10}{}_0^1+\nu_{11}{}_0^1$	631	$\nu_{10}{}_0^1+\nu_{11}{}_0^1$
710	$\nu_{10}{}_0^2$	690	$\nu_{10}{}_0^2$
718	$\nu_7{}_0^1$	741	$\nu_7{}_0^1$
786	$\nu_9{}_0^1+\nu_{11}{}_0^1$	745	$\nu_9{}_0^1+\nu_{11}{}_0^1$
876	$\nu_8{}_0^1+\nu_{11}{}_0^1$	805	$\nu_9{}_0^1+\nu_{10}{}_0^1$
895	$\nu_{11}{}_0^3$	858	$\nu_8{}_0^1+\nu_{11}{}_0^1$
932	$\nu_8{}_0^1+\nu_{10}{}_0^1$	916	$\nu_{10}{}_0^1+\nu_{11}{}_0^2$
952	$\nu_{10}{}_0^1+\nu_{11}{}_0^2$	916	$\nu_{10}{}_0^1+\nu_{11}{}_0^2$
1008	$\nu_{10}{}_0^2+\nu_{11}{}_0^1$	918	$\nu_9{}_0^2$
1017	$\nu_7{}_0^1+\nu_{11}{}_0^1$	976	$\nu_{10}{}_0^2+\nu_{11}{}_0^1$
1061	$\nu_9{}_0^1+\nu_{11}{}_0^2$	1026	$\nu_7{}_0^1+\nu_{11}{}_0^1$
1066	$\nu_{10}{}_0^3$	1029	$\nu_9{}_0^1+\nu_{11}{}_0^2$
1083	$\nu_6{}_0^1$	1032	$\nu_8{}_0^1+\nu_9{}_0^1$
1154	$\nu_8{}_0^2$	1035	$\nu_{10}{}_0^3$
1174	$\nu_8{}_0^1+\nu_{11}{}_0^2$	1066	$\nu_6{}_0^1$
1287	$\nu_5{}_0^1$	1086	$\nu_7{}_0^1+\nu_{10}{}_0^1$
1296	$\nu_7{}_0^1+\nu_8{}_0^1$	1141	$\nu_{11}{}_0^4$
1383	$\nu_6{}_0^1+\nu_{11}{}_0^1$	1143	$\nu_8{}_0^1+\nu_{11}{}_0^2$
1416	$\nu_4{}_0^1$	1150	$\nu_9{}_0^1+\nu_{10}{}_0^2$
1437	$\nu_7{}_0^2$	1200	$\nu_7{}_0^1+\nu_9{}_0^1$
1438	$\nu_6{}_0^1+\nu_{10}{}_0^1$	1277	$\nu_5{}_0^1$
1529	$\nu_3{}_0^1$	1313	$\nu_7{}_0^1+\nu_8{}_0^1$
1726	$\nu_2{}_0^1$	1351	$\nu_6{}_0^1+\nu_{11}{}_0^1$
		1411	$\nu_6{}_0^1+\nu_{10}{}_0^1$
		1525	$\nu_6{}_0^1+\nu_9{}_0^1$
		1563	$\nu_5{}_0^1+\nu_{11}{}_0^1$
		1620	$\nu_5{}_0^1+\nu_9{}_0^1$
		1672	$\nu_2{}_0^1$

TABLE C14: Same as in Table C12, for the coupled $\widetilde{\text{X}}\ ^2\text{A}_2$-$\widetilde{\text{A}}\ ^2\text{B}_1$, states of PFBz^+.

$\bar{X}^2A_2$		$\bar{A}^2B_1$	
Energy	Assignment	Energy	Assignment
0	0_0^0	0	0_0^0
300	$\nu_{11}{}_0^1$	284	$\nu_{11}{}_0^1$
333	$\nu_{29}{}_0^1$	301	$\nu_{30}{}_0^1$
460	$\nu_9{}_0^1$	460	$\nu_9{}_0^1$
593	$\nu_{11}{}_0^2$	586	$\nu_{11}{}_0^1+\nu_{30}{}_0^1$
623	$\nu_{29}{}_0^1+\nu_{30}{}_0^1$	621	$\nu_{11}{}_0^1+\nu_{29}{}_0^1$
624	$\nu_{11}{}_0^1+\nu_{29}{}_0^1$	743	$\nu_9{}_0^1+\nu_{11}{}_0^1$
763	$\nu_9{}_0^1+\nu_{30}{}_0^1$	758	$\nu_9{}_0^1+\nu_{30}{}_0^1$
765	$\nu_9{}_0^1+\nu_{11}{}_0^1$	870	$\nu_{28}{}_0^1+\nu_{30}{}_0^1$
787	$\nu_9{}_0^1+\nu_{29}{}_0^1$	887	$\nu_{11}{}_0^1+\nu_{30}{}_0^2$
898	$\nu_{11}{}_0^1+\nu_{30}{}_0^2$	911	$\nu_9{}_0^2$
918	$\nu_{29}{}_0^1+\nu_{30}{}_0^2$	928	$\nu_{29}{}_0^1+\nu_{30}{}_0^2$
930	$\nu_9{}_0^2$	1201	$\nu_9{}_0^2+\nu_{11}{}_0^1$
		1375	$\nu_9{}_0^3$
		1428	$\nu_4{}_0^1$
		1460	$\nu_3{}_0^1$

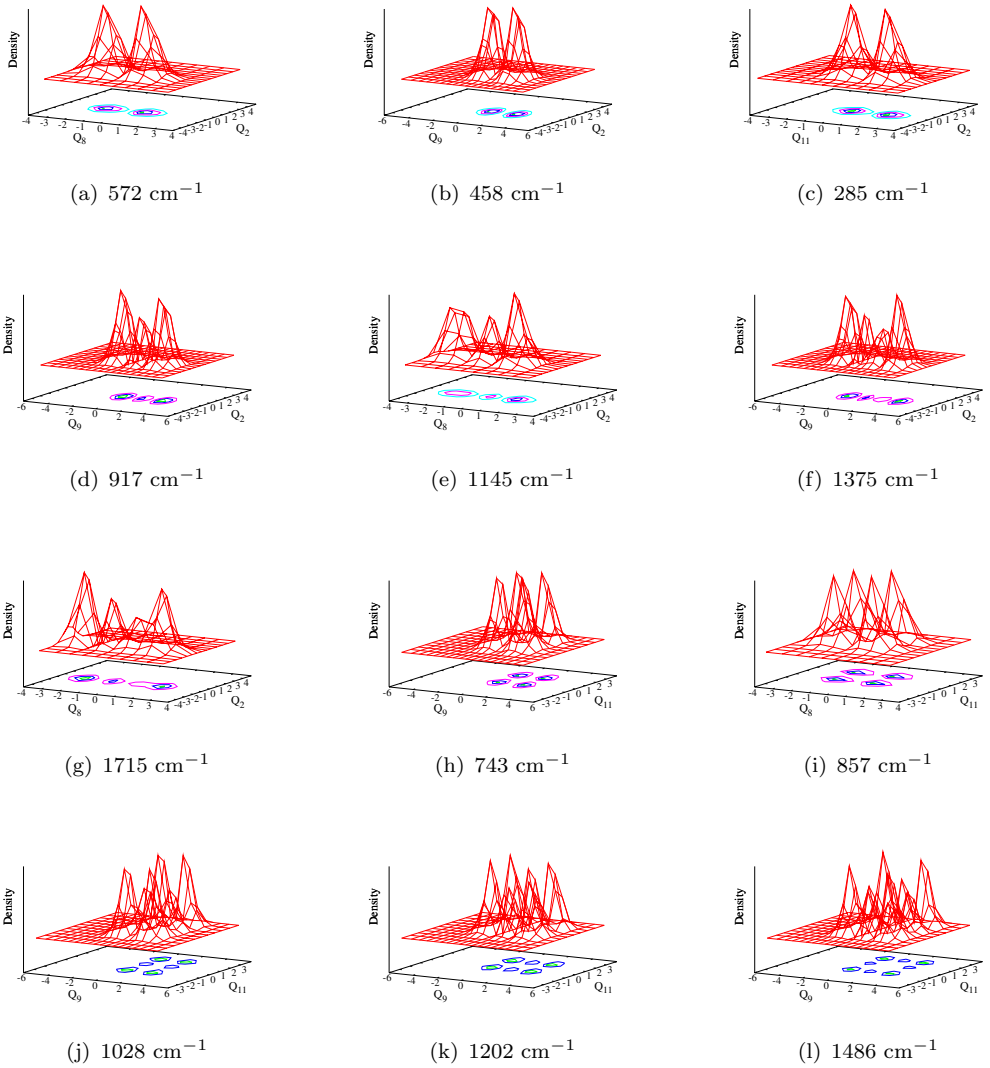

(a) 572 cm^{-1} (b) 458 cm^{-1} (c) 285 cm^{-1}

(d) 917 cm^{-1} (e) 1145 cm^{-1} (f) 1375 cm^{-1}

(g) 1715 cm^{-1} (h) 743 cm^{-1} (i) 857 cm^{-1}

(j) 1028 cm^{-1} (k) 1202 cm^{-1} (l) 1486 cm^{-1}

FIGURE C2: Reduced density plots of the vibronic wavefunctions of the fundamental of ν_8, ν_9 and ν_{11} (panels a, b and c, respectively). First and second overtones of ν_9 and ν_8 (panels d-g, respectively) excited in the $\widetilde{A}\ ^2B_1$ state (uncoupled) of $PFBz^+$ calculated with the CASSCF-MRCI data. The wavefunctions in panels h-l represent the combination peaks $\nu_9 + \nu_{11}$, $\nu_8 + \nu_{11}$, $\nu_9 + \nu_{11}{}_0^2$, $\nu_9{}_0^2 + \nu_{11}$ and $\nu_9{}_0^2 + \nu_{11}{}_0^2$. The Q_i in the abscissa represents the dimensionaless normal displacement coordinate of the i^{th} vibrational mode.

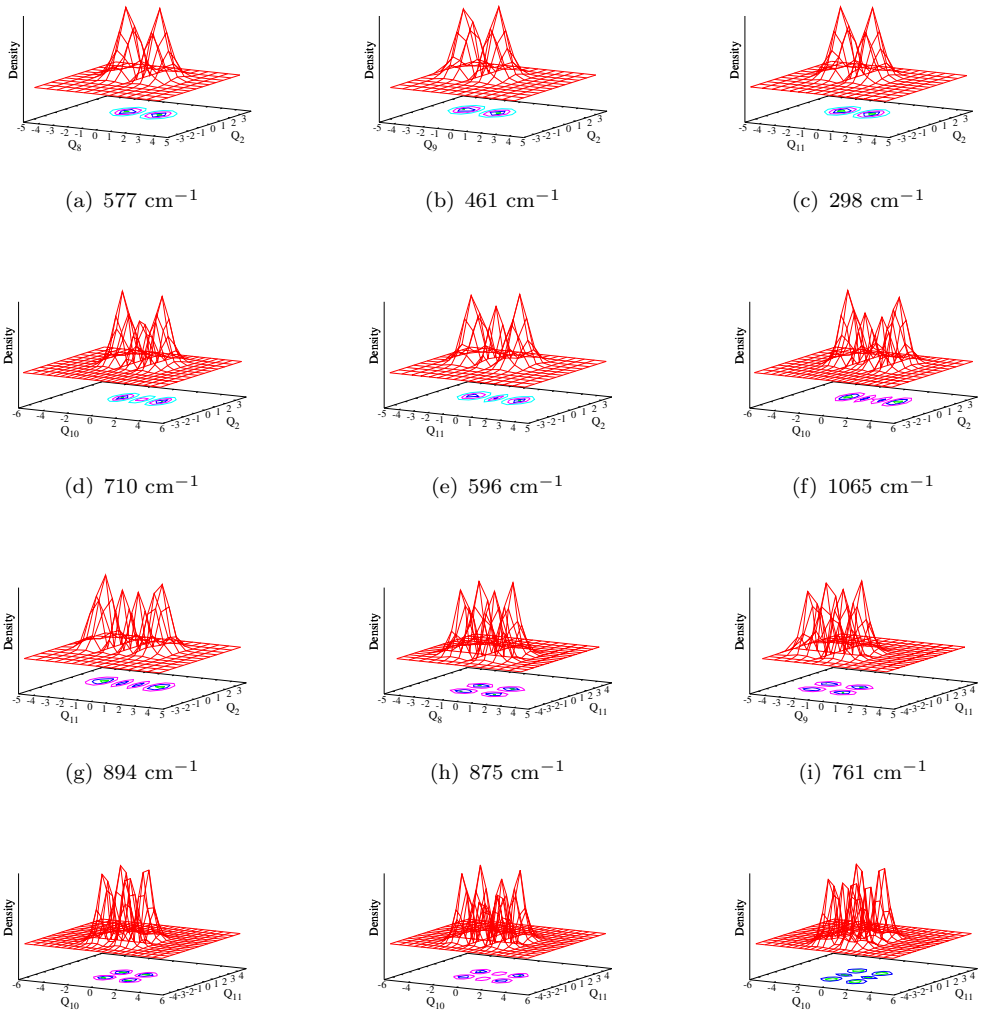

(a) 577 cm^{-1} (b) 461 cm^{-1} (c) 298 cm^{-1}

(d) 710 cm^{-1} (e) 596 cm^{-1} (f) 1065 cm^{-1}

(g) 894 cm^{-1} (h) 875 cm^{-1} (i) 761 cm^{-1}

(j) 653 cm^{-1} (k) 1008 cm^{-1} (l) 951 cm^{-1}

FIGURE C3: Reduced density plots of the vibronic wavefunctions of the fundamental of ν_9, ν_{10} and ν_{11} (panels a, b and c, respectively) and first and second overtones of ν_{10} and ν_{11} (panels d-g, respectively) excited in the $\widetilde{X}\ ^2A_2$ state (uncoupled) of $PFBz^+$ calculated with the EOMIP-CCSD data. The wavefunctions in panels h-l represent the combination peaks $\nu_8 + \nu_{11}$, $\nu_9 + \nu_{11}$, $\nu_{10} + \nu_{11}$, $\nu_{10}{}_0^2 + \nu_{11}$ and $\nu_{10} + \nu_{11}{}_0^2$. The Q_i in the abscissa represents the dimensionless normal displacement coordinate of the i^{th} vibrational mode.

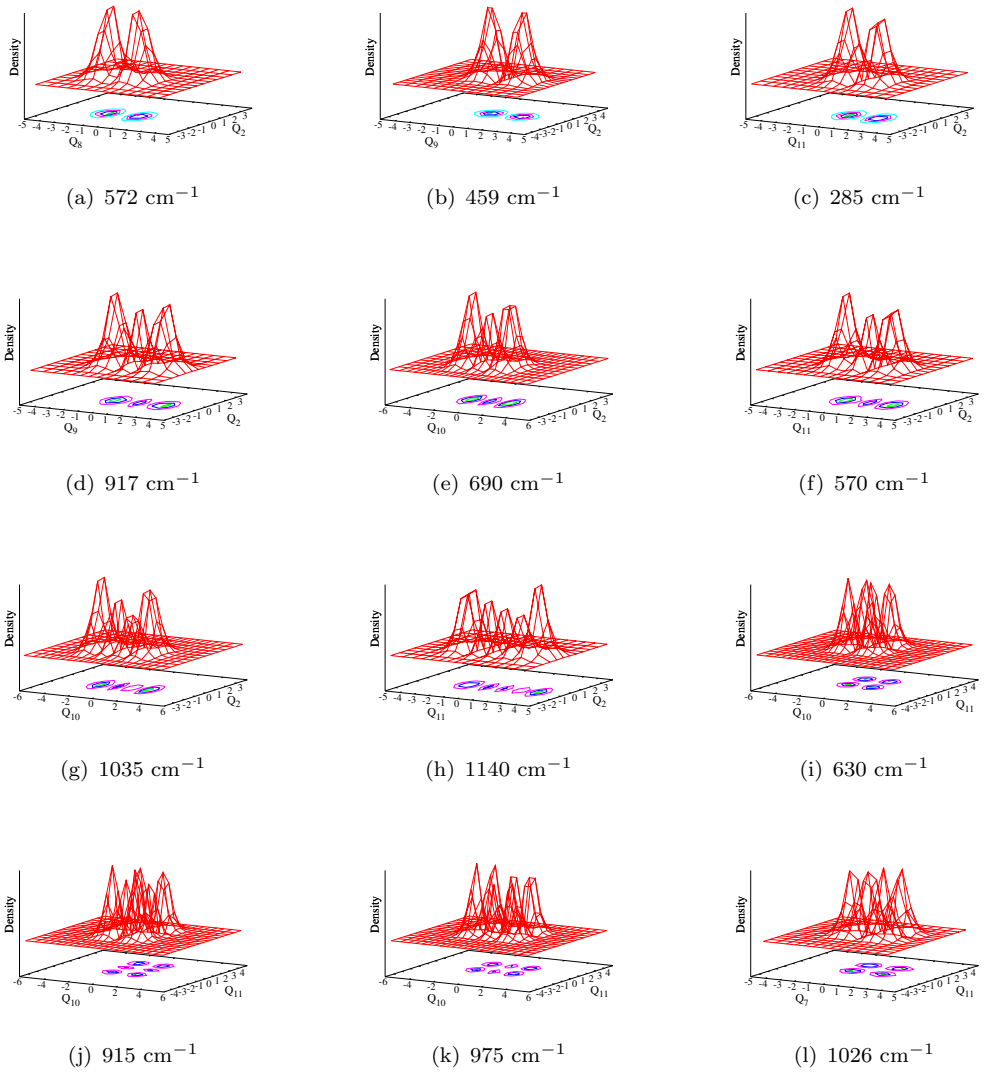

(a) 572 cm^{-1} (b) 459 cm^{-1} (c) 285 cm^{-1}

(d) 917 cm^{-1} (e) 690 cm^{-1} (f) 570 cm^{-1}

(g) 1035 cm^{-1} (h) 1140 cm^{-1} (i) 630 cm^{-1}

(j) 915 cm^{-1} (k) 975 cm^{-1} (l) 1026 cm^{-1}

FIGURE C4: Reduced density plots of the vibronic wavefunctions of the fundamental of ν_9, ν_{10} and ν_{11} (panels a, b and c, respectively) and first overtones of ν_9, ν_{10} and ν_{11} (panels d-f, respectively). Second and third overtones of $\nu_{10}{}_0^3$ and $\nu_{11}{}_0^4$ (panels g and h, respectively) excited in the $\widetilde{A}\ ^2B_1$ state (uncoupled) of $PFBz^+$ calculated with the EOMIP-CCSD data. The wavefunctions in panels i-l, represents, the combination peaks $\nu_{10} + \nu_{11}$, $\nu_{10} + \nu_{11}{}_0^2$, $\nu_{10}{}_0^2 + \nu_{11}$, and $\nu_7 + \nu_8$. The Q_i in the abscissa represents the dimensionaless normal displacement coordinate of the i^{th} vibrational mode.

TABLE C15: Same as in Table C13, for the coupled $\widetilde{X}\ ^2A_2$-$\widetilde{A}\ ^2B_1$, states of $PFBz^+$.

$\widetilde{X}^2A_2$		$\widetilde{A}^2B_1$	
Energy	Assignment	Energy	Assignment
0	0_0^0	0	0_0^0
297	$\nu_{11}{}_0^1$	296	$\nu_{11}{}_0^1$
462	$\nu_9{}_0^1$	453	$\nu_9{}_0^1$
594	$\nu_{11}{}_0^2$	592	$\nu_{11}{}_0^1+\nu_{30}{}_0^1$
611	$\nu_{29}{}_0^1+\nu_{30}{}_0^1$	613	$\nu_{11}{}_0^1+\nu_{29}{}_0^1$
644	$\nu_{29}{}_0^2$	630	$\nu_{30}{}_0^2$
759	$\nu_9{}_0^1+\nu_{11}{}_0^1$	647	$\nu_{29}{}_0^2$
932	$\nu_9{}_0^2$	749	$\nu_9{}_0^1+\nu_{11}{}_0^1$
1030	$\nu_9{}_0^1+\nu_{30}{}_0^2$	790	$\nu_9{}_0^1+\nu_{30}{}_0^1$
1055	$\nu_9{}_0^1+\nu_{11}{}_0^2$	798	$\nu_{11}{}_0^1+\nu_{28}{}_0^1$
1204	$\nu_9{}_0^2+\nu_{11}{}_0^1$	907	$\nu_{11}{}_0^1+\nu_{30}{}_0^2$
		915	$\nu_9{}_0^2$
		950	$\nu_{29}{}_0^1+\nu_{30}{}_0^2$
		970	$\nu_{29}{}_0^2+\nu_{30}{}_0^1$
		1032	$\nu_9{}_0^1+\nu_{11}{}_0^2$
		1203	$\nu_9{}_0^2+\nu_{11}{}_0^1$
		1374	$\nu_9{}_0^3$
		1422	$\nu_4{}_0^1$
		1473	$\nu_{30}{}_0^1$

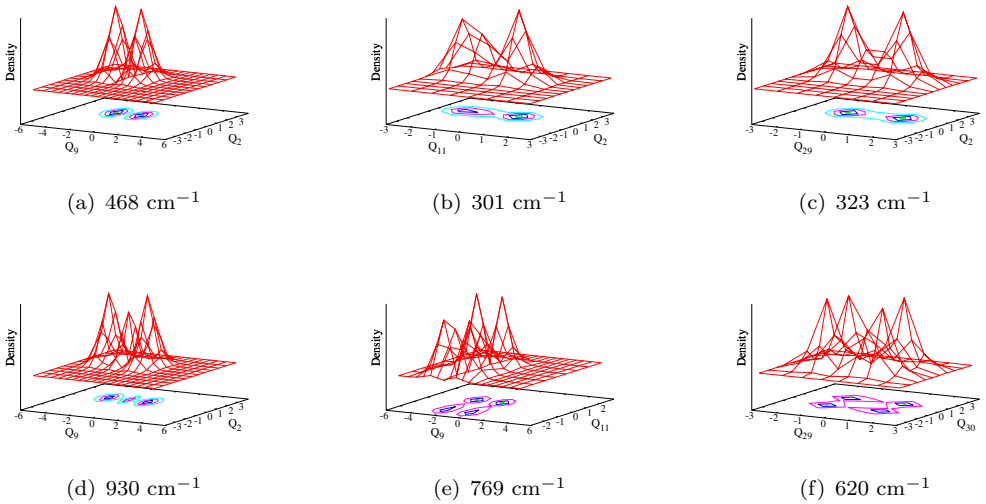

(a) 468 cm^{-1} (b) 301 cm^{-1} (c) 323 cm^{-1}

(d) 930 cm^{-1} (e) 769 cm^{-1} (f) 620 cm^{-1}

FIGURE C5: Reduced density plots of the vibronic wave functions of the fundamental of ν_9, ν_{11} and ν_{29} (panels a, b and c, respectively) and first overtone of ν_9 (panel d) excited in the $\widetilde{X}\ ^2A_2$ state (coupled with the $\widetilde{A}\ ^2B_1$ state) of $PFBz^+$ calculated with the CASSCF-MRCI data. The wave function in panels e and f represents the combination peaks $\nu_9+\nu_{11}$ and $\nu_{29}+\nu_{30}$. The Q_i in the abscissa represents the dimensionaless normal displacement coordinate of the i^{th} vibrational mode.

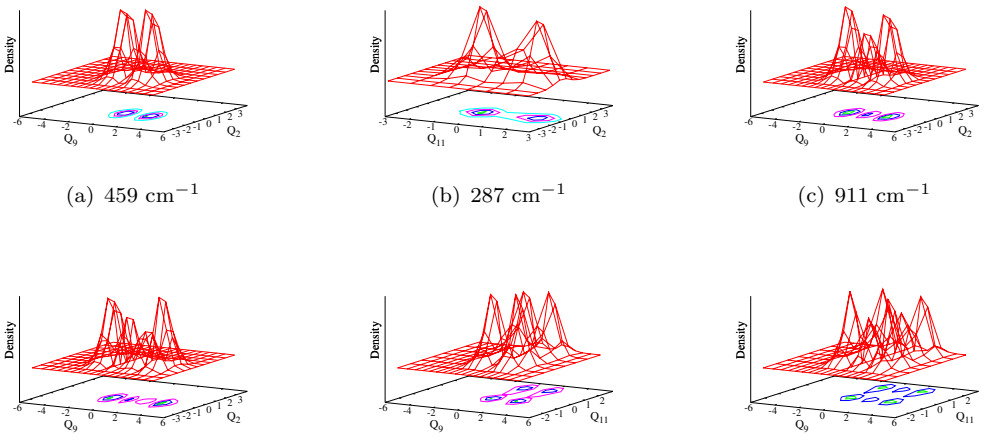

(a) 459 cm^{-1} (b) 287 cm^{-1} (c) 911 cm^{-1}

(d) 1375 cm^{-1} (e) 747 cm^{-1} (f) 1203 cm^{-1}

FIGURE C6: Reduced density plots of the vibronic wavefunctions of the fundamental of ν_9 and ν_{11} (panels a and b, respectively) and first and second overtone of ν_9 (panels c-d, respectively) excited in the $\widetilde{A}\ ^2B_1$ state (coupled with the $\widetilde{X}\ ^2A_2$ state) of $PFBz^+$ calculated with the CASSCF-MRCI data. The wave function in panels e and f represent the combination peaks $\nu_9 + \nu_{11}$, $\nu_9^2 + \nu_{11}$. The Q_i in the abscissa represents the dimensionaless normal displacement coordinate of the i^{th} vibrational mode.

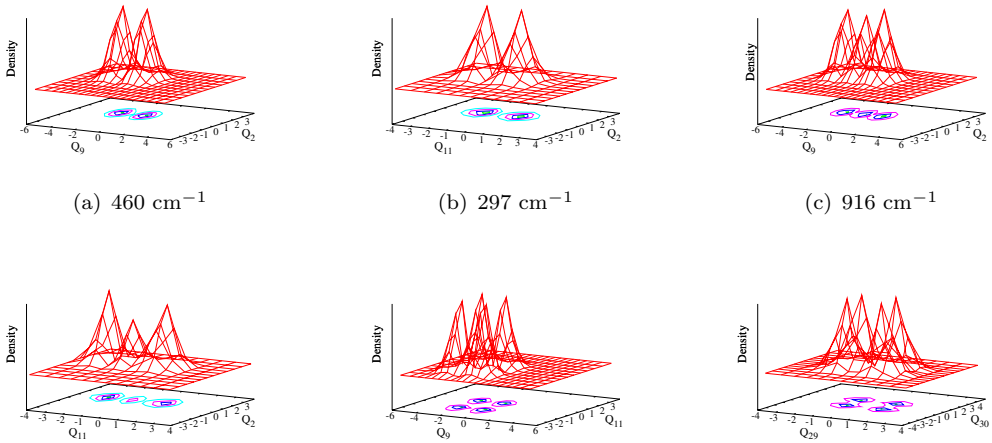

(a) 460 cm^{-1} (b) 297 cm^{-1} (c) 916 cm^{-1}

(d) 594 cm^{-1} (e) 757 cm^{-1} (f) 611 cm^{-1}

FIGURE C7: Reduced density plots of the vibronic wavefunctions of the fundamental of ν_9 and ν_{11} (panels a and b, respectively) and overtone of ν_9 and ν_{11} (panels c-d, respectively) excited in the $\widetilde{X}\ ^2A_2$ state (coupled with the $\widetilde{A}\ ^2B_1$ state) of $PFBz^+$ calculated with the EOMIP-CCSD data. The wave function in panels e and f represent the combination peaks $\nu_9 + \nu_{11}$, $\nu_{29} + \nu_{30}$. The Q_i in the abscissa represents the dimensionaless normal displacement coordinate of the i^{th} vibrational mode.

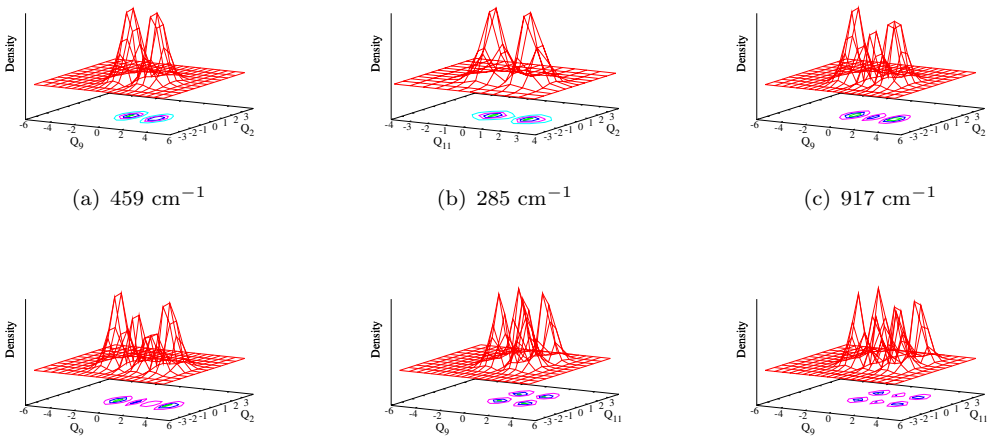

(a) 459 cm^{-1} (b) 285 cm^{-1} (c) 917 cm^{-1}

(d) 1376 cm^{-1} (e) 744 cm^{-1} (f) 1203 cm^{-1}

FIGURE C8: Reduced density plots of the vibronic wavefunctions of the fundamental of ν_9 and ν_{11} (panels a and b, respectively) and first and second overtone of ν_9 (panels c-d, respectively) excited in the $\widetilde{A}\ ^2B_1$ state (coupled with the $\widetilde{X}\ ^2A_2$ state) of $PFBz^+$ calculated with the EOMIP-CCSD data. The wave function in panels e and f represent the combination peaks $\nu_9 + \nu_{11}$, $\nu_9^2 + \nu_{11}$. The Q_i in the abscissa represents the dimensionaless normal displacement coordinate of the i^{th} vibrational mode.

TABLE C16: Normal mode combination, sizes of the primitive and single particle functions (SPFs) used in the coupled states dynamics calculations of $PFBz^+$ using MCTDH suite of programmes. [a] The primitive basis is the number of Harmonic oscillator DVR functions for the relevant mode. The primitive basis for each particle is the product of the one-dimensional bases. [b] The SPF basis is the number of single-particle functions used.

CASSCF-MRCI				
Electronic states	Normal modes	Primitive basis [a]	SPF basis [b]	Figure(s)
$\widetilde{X}$-$\widetilde{A}$-$\widetilde{B}$	(ν_2, ν_3, ν_{21}, ν_{22})	(14, 12, 40, 12)	[12, 10, 6]	Fig. 4.9(b)
	(ν_4, ν_{23})	(12, 8)	[8, 8, 6]	
	(ν_6, ν_{24}, ν_{25}, ν_{26})	(8, 12, 12, 12)	[10, 12, 8]	
	(ν_7, ν_9, ν_{28})	(10, 22, 40)	[12, 12, 8]	
	ν_{11}, ν_{29}, ν_{30})	(12, 12, 10)	[10, 10, 6]	
$\widetilde{B}$-$\widetilde{C}$-$\widetilde{D}$-$\widetilde{E}$	(ν_2, ν_3, ν_4, ν_{21}, ν_{22})	(12, 8, 12, 14, 28)	[6, 6, 8, 6]	Fig. 4.9(b)
	(ν_6, ν_{24}, ν_{25})	(10, 16, 12)	[6, 6, 6, 6]	
	(ν_7, ν_{27}	(16, 8)	[6, 8, 8, 6]	
	(ν_9, ν_{13}, ν_{28})	(12, 12, 12)	[8, 6, 6, 6]	
	(ν_{11}, ν_{14}, ν_{29})	(10, 8, 12)	[6, 6, 6, 6]	
EOMIP-CCSD				
$\widetilde{X}$-$\widetilde{A}$-$\widetilde{B}$	(ν_2, ν_3, ν_{21}, ν_{22})	(14, 14, 16, 12)	[12, 12, 8]	Fig. 4.9(c)
	(ν_4, ν_{24})	(16, 10)	[10, 12, 8]	
	(ν_6, ν_{25}, ν_{26})	(10, 10, 10)	[10, 12, 12]	
	(ν_7, ν_8, ν_9, ν_{28})	(10, 10, 22, 26)	[10, 8, 8]	
	(ν_{11}, ν_{29}, ν_{30})	(14, 8, 14)	[12, 10, 8]	
$\widetilde{B}$-$\widetilde{C}$-$\widetilde{D}$-$\widetilde{E}$	(ν_2, ν_3, ν_4, ν_{21}, ν_{22})	(10, 10, 10, 8, 8)	[6, 8, 8, 6]	Fig. 4.9(c)
	(ν_6, ν_{24}, ν_{25}, ν_{26})	(8, 10, 8, 8)	[8, 6, 8, 6]	
	(ν_7, ν_8, ν_{12}, ν_{17}, ν_{27}	(10, 10, 8, 18, 8)	[6, 8, 8, 8]	
	(ν_9, ν_{10}, ν_{13}, ν_{18}, ν_{28}, ν_{29})	(8, 10, 10, 24, 10, 8)	[6, 6, 8, 8]	
	(ν_{11}, ν_{14}, ν_{20}, ν_{30})	(8, 12, 8, 8)	[6, 6, 8, 8]	

Appendix D

Derivation for energetic minimum and saddle points of doubly degenerate electronic states

Steps to arrive at the energetic minimum and saddle points of doubly degenerate electronic state

The diabatic quadratic $E\otimes e$-JT electronic Hamiltonian of the degenerate electronic state is given by

$$\Delta\mathcal{H} = \begin{bmatrix} u^{x} & u^{xy} \\ u^{xy} & u^{y} \end{bmatrix}, \tag{D1a}$$

with

$$u^{x/y} = E^{0} + \sum_{i\epsilon a_1}\kappa_i Q_i + \frac{1}{2}\sum_{i\epsilon a_1}\gamma_i Q_i^2 \pm \sum_{i\epsilon e}\lambda_i Q_{ix} + \frac{1}{2}\sum_{i\epsilon e}\gamma_i(Q_{ix}^2 + Q_{iy}^2) \pm \frac{1}{2}\sum_{i\epsilon e}\eta_i(Q_{ix}^2 - Q_{iy}^2), \tag{D1b}$$

and

$$u^{xy} = \sum_{i\epsilon e}\left[\lambda_i Q_{iy} - 2\eta_i Q_{ix}Q_{iy}\right]. \tag{D1c}$$

Upon diagonalization of Eq. D1a, the adiabatic potential energy surfaces are obtained

$$V_{\pm} = \frac{(u^{x} + u^{y})}{2} \pm \left[\left(\frac{u^{x} - u^{y}}{2}\right)^{2} + (u^{xy})^{2}\right]^{1/2}. \tag{D2a}$$

Substitution of Eqs. D1b and D1c into Eq. D2a and add addition of the harmonic potential of reference state $\mathcal{V}_0$ (Eq. 6.6 of the text) yields

$$V_{\pm} + \mathcal{V}_0 = \mathcal{V}_{\pm} = E^0 + \sum_{i\epsilon a_1} \kappa_i Q_i + \frac{1}{2}\sum_{i\epsilon a_1}\left[\gamma_i Q_i^2 + \omega_i Q_i^2\right] + \frac{1}{2}\sum_{i\epsilon e}\left[\gamma_i(Q_{ix}^2 + Q_{iy}^2) + \omega_i(Q_{ix}^2 + Q_{iy}^2)\right] \pm \left[\left(\sum_{i\epsilon e}\lambda_i Q_{ix} + \frac{1}{2}\sum_{i\epsilon e}\eta_i\left(Q_{ix}^2 - Q_{iy}^2\right)\right)^2 + \sum_{i\epsilon e}\left(\lambda_i Q_{iy} - 2\eta_i Q_{ix}Q_{iy}\right)^2\right]^{1/2}. \tag{D2b}$$

The minimum of the seam of CIs occurs at the minimum of $\mathcal{V}_+$ in the space of symmetric vibrational modes. Upon minimization of $\mathcal{V}_+$ with respect to Q_i one obtains Eq. 6.15 (see text). Next the location of the minimum and saddle points of the lower adiabatic sheet are obtained by setting the first derivative of $\mathcal{V}_-$ with respect to the symmetric modes and degenerate modes to zero separately. Upon substitution of the results into $\mathcal{V}_-$ one obtains Eqs. 6.13 and 6.14 (see text). Note that absolute value of η_i distinguishes between minimum and saddle point. Finally the JT stabilization energy (Eq. 6.16) is obtained by subtracting Eq. 6.13 from Eq. 6.14.

A detailed derivation of the above mentioned critical points are given bellow. The position of the minimum with respect to the Q_i (i.e., stationary points along the symmetric modes),

$$\begin{aligned} \frac{\partial \mathcal{V}_+}{\partial Q_i} = \sum_{i\epsilon a_1}\kappa_i + \sum_{i\epsilon a_1}\gamma_i Q_i + \sum_{i\epsilon a_1}\omega_i Q_i = 0 \\ \Rightarrow \sum_{i\epsilon a_1}\left[\kappa_i + (\gamma_i + \omega_i)Q_i\right] = 0 \\ \therefore Q_i = \frac{-\kappa_i}{(\gamma_i + \omega_i)}. \end{aligned} \tag{D2c}$$

Due to vibronic coupling, the lower adiabatic potential surface $\mathcal{V}_-$ exhibits minima at nuclear geometries that differ from the equilibrium geometry of the molecule in its neutral ground state. Therefore, the adiabatic potential energies [cf., Eq. D2b] along the a_1 symmetry, at CI configuration (i.e., $u^x = u^y$ and $u^{xy} = 0$; these lead to the the

terms under the square root goes to zero)

$$\begin{aligned}\mathcal{V}_{\pm} &= E^0 + \sum_{i\epsilon a_1}\kappa_i Q_i + \frac{1}{2}\sum_{i\epsilon a_1}\gamma_i Q_i^2 + \frac{1}{2}\sum_{i\epsilon a_1}\omega_i Q_i^2 \\ &= E^0 + \sum_{i\epsilon a_1}\kappa_i Q_i + \frac{1}{2}\sum_{i\epsilon a_1}(\gamma_i+\omega_i) Q_i^2 \\ &= E^0 + \sum_{i\epsilon a_1}\kappa_i \left(\frac{-\kappa_i}{\gamma_i+\omega_i}\right) + \frac{1}{2}\sum_{i\epsilon a_1}(\gamma_i+\omega_i)\left(\frac{-\kappa_i}{\gamma_i+\omega_i}\right)^2 \\ &= E^0 - \sum_{i\epsilon a_1}\left(\frac{\kappa_i^2}{\gamma_i+\omega_i}\right) + \frac{1}{2}\sum_{i\epsilon a_1}\left(\frac{\kappa_i^2}{\gamma_i+\omega_i}\right)\end{aligned} \tag{D2d}$$

The minimum of the energy along the a_1 symmetric modes is,

$$\mathcal{V}_{-} = E^0 - \frac{1}{2}\sum_{i\epsilon a_1}\left(\frac{\kappa_i^2}{\gamma_i+\omega_i}\right). \tag{D2e}$$

The position of the stationary points along the degenerate modes (i.e., minimum with respect to Q_{ix}),

$$\begin{aligned}\frac{\partial \mathcal{V}_{\pm}}{\partial Q_{ix}} &= \sum_{i\epsilon e}(\gamma_i+\omega_i)\,Q_{ix} \\ &\pm \frac{1}{2}\sum_{i\epsilon e}\frac{2\left[\lambda_i Q_{ix} + \frac{1}{2}\eta_i\left(Q_{ix}^2 - Q_{iy}^2\right)\right](\lambda_i + \eta_i Q_{ix}) + 2\left[\lambda_i Q_{iy} - 2\eta_i Q_{ix} Q_{iy}\right](-2\eta_i Q_{iy})}{\sqrt{\left[\lambda_i Q_{ix} + \frac{1}{2}\eta_i\left(Q_{ix}^2 - Q_{iy}^2\right)\right]^2 + \left[\lambda_i Q_{iy} - 2\eta_i Q_{ix} Q_{iy}\right]^2}}\end{aligned} \tag{D3a}$$

Let's say, $Q_{iy} = 0$.

$$\frac{\partial \mathcal{V}_{\pm}}{\partial Q_{ix}} = \sum_{i\epsilon e}(\gamma_i+\omega_i)\,Q_{ix} \pm \sum_{i\epsilon e}\frac{\left(\lambda_i Q_{ix} + \frac{1}{2}\eta_i Q_{ix}^2\right)(\lambda_i + \eta_i Q_{ix})}{\sqrt{\left(\lambda_i Q_{ix} + \frac{1}{2}\eta_i Q_{ix}^2\right)^2}} \tag{D3b}$$

$$\Rightarrow \sum_{i\epsilon e}\left[(\gamma_i+\omega_i)\,Q_{ix} \pm \lambda_i \pm \eta_i Q_{ix}\right] \tag{D3c}$$

$$\Rightarrow \sum_{i\epsilon e}(\gamma_i+\omega_i \pm \eta_i)\,Q_{ix} \pm \sum_{i\epsilon e}\lambda_i = 0 \tag{D3d}$$

$$Q_{ix} = \frac{\mp\lambda_i}{(\gamma_i+\omega_i \pm \eta_i)} \tag{D3e}$$

The adiabatic potential energies along the degenerate (e) modes is (at CI geometry),

$$\begin{aligned}\mathcal{V}_{\pm} &= E^0 \pm \sum_{i\epsilon e} \lambda_i Q_{ix} + \frac{1}{2}\sum_{i\epsilon e} \gamma_i Q_{ix}^2 \pm \frac{1}{2}\eta_i Q_{ix}^2 + \frac{1}{2}\omega_i Q_{ix}^2 \\ &= E^0 \pm \sum_{i\epsilon e} \lambda_i Q_{ix} + \frac{1}{2}\sum_{i\epsilon e} \left(\gamma_i + \omega_i \pm \eta_i\right) Q_{ix}^2.\end{aligned} \tag{D4a}$$

Substituting Q_{ix} in Eq. D4a, the minimum of the energy along the e mode obtained as

$$\begin{aligned}\mathcal{V}_{-} &= E^0 - \sum_{i\epsilon e} \lambda_i \left(\frac{\mp\lambda_i}{\gamma_i + \omega_i \pm \eta_i}\right) + \frac{1}{2}\sum_{i\epsilon e} \left(\gamma_i + \omega_i \pm \eta_i\right) \left(\frac{\mp\lambda_i}{\gamma_i + \omega_i \pm \eta_i}\right)^2 \\ &= E^0 - \sum_{i\epsilon e} \frac{\lambda_i^2}{\left(\gamma_i + \omega_i \pm \eta_i\right)} + \frac{1}{2}\sum_{i\epsilon e} \frac{\lambda_i^2}{\left(\gamma_i + \omega_i \pm \eta_i\right)} \\ &= E^0 - \frac{1}{2}\sum_{i\epsilon e} \frac{\lambda_i^2}{\left(\gamma_i + \omega_i \pm \eta_i\right)}.\end{aligned} \tag{D4b}$$

So, finally we will have the following quantities along a_1 and e vibrational modes, $Q_i = \frac{-\kappa_i}{(\gamma_i+\omega_i)}$, $Q_{ix} = \frac{\mp\lambda_i}{(\gamma_i+\omega_i\pm\eta_i)}$ and $Q_{iy} = 0$.
The original eigenvalue equation along both a_1 and e vibrational modes is,

$$\mathcal{V}_{-}^0 = E^0 + \sum_{i\epsilon a_1}\left[\kappa_i Q_i + \frac{1}{2}\left(\gamma_i + \omega_i\right) Q_i^2\right] + \sum_{i\epsilon e}\left[-\lambda_i Q_{ix} + \frac{1}{2}\left(\gamma_i + \omega_i \pm \eta_i\right) Q_{ix}^2\right]. \tag{D4c}$$

Substituting the position of the stationary points along a_1 and e modes of Q_i and Q_{ix} in Eq. D4c one obtains

$$\begin{aligned}\mathcal{V}_{-}^0 = E^0 &+ \sum_{i\epsilon a_1}\left[\kappa_i\left(\frac{-\kappa_i}{\gamma_i + \omega_i}\right) + \frac{1}{2}\left(\gamma_i + \omega_i\right)\left(\frac{-\kappa_i}{\gamma_i + \omega_i}\right)^2\right] \\ &+ \sum_{i\epsilon e}\left[-\lambda_i\left(\frac{\mp\lambda_i}{\left(\gamma_i + \omega_i \pm \eta_i\right)}\right) + \frac{1}{2}\left(\gamma_i + \omega_i \pm \eta_i\right)\left(\frac{\mp\lambda_i}{\left(\gamma_i + \omega_i \pm \eta_i\right)}\right)^2\right]\end{aligned} \tag{D4d}$$

$$\mathcal{V}_{-}^0 = E^0 + \sum_{i\epsilon a_1}\left[-\frac{\kappa_i^2}{\left(\gamma_i + \omega_i\right)} + \frac{1}{2}\frac{\kappa_i^2}{\left(\gamma_i + \omega_i\right)}\right] + \sum_{i\epsilon e}\left[-\frac{\lambda_i^2}{\left(\gamma_i + \omega_i \pm \eta_i\right)} + \frac{1}{2}\frac{\lambda_i^2}{\left(\gamma_i + \omega_i \pm \eta_i\right)}\right] \tag{D4e}$$

$$\mathcal{V}_{-}^0 = E^0 - \frac{1}{2}\sum_{i\epsilon a_1}\frac{\kappa_i^2}{\left(\gamma_i + \omega_i\right)} - \frac{1}{2}\sum_{i\epsilon e}\frac{\lambda_i^2}{\left(\gamma_i + \omega_i \pm \eta_i\right)} \tag{D5a}$$

From Eq. D5a, we can write the energetic minimum of the JT split lower adiabatic sheet and saddle points of degenerate electronic state as follows,

$$\mathcal{V}_{-}^{min} = E^0 - \frac{1}{2}\sum_{i\epsilon a_1}\frac{\kappa_i^2}{\left(\gamma_i + \omega_i\right)} - \frac{1}{2}\sum_{i\epsilon e}\frac{\lambda_i^2}{\left(\gamma_i + \omega_i - |\eta_i|\right)} \tag{D5b}$$

$$\mathcal{V}_{-}^{sp} = E^0 - \frac{1}{2}\sum_{i\epsilon a_1}\frac{\kappa_i^2}{(\gamma_i+\omega_i)} - \frac{1}{2}\sum_{i\epsilon e}\frac{\lambda_i^2}{(\gamma_i+\omega_i+|\eta_i|)} \tag{D5c}$$

Bibliography

[1] B. M. Wong, M. Piacenza, and F. Della Sala, Phys. Chem. Chem. Phys. **11**, 4498 (2009).

[2] O. Tagit and N. Hildebrandt, ACS Sensors **2**, 31 (2017), PMID: 28722447.

[3] S. Perun, A. L. Sobolewski, and W. Domcke, Chem. Phys. **313**, 107 (2005).

[4] S. Perun, A. L. Sobolewski, and W. Domcke, J. Am. Chem. Soc. **127**, 6257 (2005).

[5] D. Zhong, Ann. Rev. Phys. Chem. **66**, 691 (2015), PMID: 25830375.

[6] H. Wang, X. Chen, and W. Fang, Phys. Chem. Chem. Phys. **16**, 25432 (2014).

[7] M. Hariharan and P. Kamat, ACS Energy Lett. **7**, 2114 (2022).

[8] S. Hahn and G. Stock, J. Phys. Chem. B **104**, 1146 (2000).

[9] T. V. Tscherbul and P. Brumer, J. Phys. Chem. A **118**, 3100 (2014), PMID: 24684415.

[10] M. Chattoraj, B. A. King, G. U. Bublitz, and S. G. Boxer, Proc. Natl. Acad. Sci. **93**, 8362 (1996).

[11] D. Stoner-Ma et al., J. Am. Chem. Soc. **127**, 2864 (2005).

[12] X. Shu et al., Protein Sci. **16**, 2703 (2007).

[13] M. Born and R. Oppenheimer, Ann. Phys. **389**, 457 (1927).

[14] H. Köppel, W. Domcke, and L. S. Cederbaum, Adv. Chem. Phys. **57**, 59 (1984).

[15] W. Domcke, D. Yarkony, and H. Köppel, *Conical Intersections: Electronic Structure, Dynamics and Spectroscopy*, World Scientific, Singapore, 2004.

[16] E. Teller, J. Phys. Chem. **41**, 109 (1937).

[17] G. Herzberg and H. C. Longuet-Higgins, Discuss. Faraday Soc. **35**, 77 (1963).

[18] T. Carrington, Faraday Discuss. Chem. Soc. **53**, 27 (1972).

[19] D. R. Yarkony, Acc. Chem. Res. **31**, 511 (1998).

[20] F. Bernardi, M. Olivucci, and M. A. Robb, Chem. Soc. Rev. **25**, 321 (1996).

[21] S. Mahapatra, Acc. Chem. Res. **42**, 1004 (2009).

[22] I. Prigogine and S. A. Rice, *The role of degenerate states in chemistry*, volume 150, John Wiley & Sons, 2003.

[23] C. J. Ballhausen and A. E. Hansen, Ann. Rev. Phys. Chem. **23**, 15 (1972).

[24] G. Fisher, *Vibronic coupling*, Academic press, London, 1984.

[25] G. Bieri, L. Åsbrink, and W. V. Niessen, J. Electron. Spectrosc. Relat. Phenom. **23**, 281 (1981).

[26] D. W. Turner, C. Baker, A. D. Becker, and C. R. Brundle, *Molecular Photoelectron Spectroscopy*, Wiley, New York, 1970.

[27] A. W. Potts, W. C. Price, D. G. Streets, and T. A. Williams, Faraday Discuss. Chem. Soc. **54**, 168 (1972).

[28] M. Klessinger, Angew. Chem. **84**, 544 (1972).

[29] K. Walter, K. Scherm, and U. Boesl, J. Phys. Chem. **95**, 1188 (1991).

[30] R. Anand, J. E. LeClaire, and P. M. Johnson, J. Phys. Chem. A **103**, 2618 (1999).

[31] C. H. Kwon, H. L. Kim, and M. S. Kim, J. Chem. Phys. **116**, 10361 (2002).

[32] C. H. Kwon, H. L. Kim, and M. S. Kim, J. Chem. Phys. **118**, 6327 (2003).

[33] W. C. Price, A. W. Potts, and T. A. Williams, Chem. Phys. Lett. **37**, 17 (1976).

[34] C. R. Brundle, M. B. Robin, and N. A. Kuebler, J. Am. Chem. Soc. **94**, 1466 (1972).

[35] D. W. Davis, D. A. Shirley, and T. D. Thomas, J. Am. Chem. Soc. **94**, 6565 (1972).

[36] D. T. Clark, D. Kilcast, D. Adams, and W. K. R. Musgrave, J. Electron Spectrosc. Relat. Phenom. **1**, 227 (1972).

[37] R. Gilbert and C. Sandorfy, Chem. Phys. Lett. **27**, 457 (1974).

[38] B. Narayan and J. Murrell, Mol. Phys. **19**, 169 (1970).

[39] M. Allan, J. P. Maier, and O. Marthaler, Chem. Phys. **26**, 131 (1977).

[40] C. Cossart-Magos, D. Cossart, and S. Leach, Mol. Phys. **37**, 793 (1979).

[41] C. Cossart-Magos, D. Cossart, and S. Leach, Chem. Phys. **41**, 363 (1979).

[42] V. E. Bondybey, T. A. Miller, and J. H. English, J. Chem. Phys. **71**, 1088 (1979).

[43] Y. Tsuchiya, M. Fujii, and M. Ito, J. Chem. Phys. **90**, 6965 (1989).

[44] G. Dujardin, S. Leach, O. Dutuit, T. Govers, and P. M. Guyon, J. Chem. Phys. **79**, 644 (1983).

[45] B. E. Applegate and T. A. Miller, J. Chem. Phys. **117**, 10654 (2002).

[46] D. Klapstein et al., Mol. Phys. **51**, 413 (1984).

[47] H. Köppel, M. Döscher, I. Bâldea, H.-D. Meyer, and P. G. Szalay, J. Chem. Phys. **117**, 2657 (2002).

[48] I. Bâldea, J. Franz, P. G. Szalay, and H. Köppel, Chem. Phys. **329**, 65 (2006).

[49] E. Gindensperger, I. Bâldea, J. Franz, and H. Köppel, Chem. Phys. **338**, 207 (2007).

[50] S. Faraji and H. Köppel, J. Chem. Phys. **129**, 074310 (2008).

[51] S. Faraji, H.-D. Meyer, and H. Köppel, J. Chem. Phys. **129**, 074311 (2008).

[52] T. Mondal and S. Mahapatra, J. Chem. Phys. **133**, 084304 (2010).

[53] T. Mondal and S. Mahapatra, J. Chem. Phys. **133**, 084305 (2010).

[54] T. Mondal, S. R. Reddy, and S. Mahapatra, J. Chem. Phys. **137**, 054311 (2012).

[55] T. Mondal and S. Mahapatra, Phys. Chem. Chem. Phys. **11**, 10867 (2009).

[56] J. G. Philis, T. Mondal, and S. Mahapatra, Chem. Phys. Lett. **495**, 187 (2010).

[57] A. K. Kanakati and S. Mahapatra, J. Chem. Phys. **154**, 054313 (2021).

[58] A. K. Kanakati, V. Jhansi Rani, R. Sarkar, and S. Mahapatra, J. Chem. Phys. **157**, 204304 (2022).

[59] A. Hitchcock, P. Fischer, A. Gedanken, and M. Robin, J. Phys. Chem. **91**, 531 (1987).

[60] O. Hüter et al., J. Chem. Phys. **145**, 014302 (2016).

[61] D. Phillips, J. Chem. Phys. **46**, 4679 (1967).

[62] G. Loper and E. Lee, Chem. Phys. Lett. **13**, 140 (1972).

[63] J. Philis, A. Bolovinos, G. Andritsopoulos, E. Pantos, and P. Tsekeri, J. Phys. B: At. Mol. Phys. **14**, 3621 (1981).

[64] D. V. O'Connor, M. Sumitani, J. M. Morris, and K. Yoshihara, Chem. Phys. Lett. **93**, 350 (1982).

[65] M. Z. Zgierski, T. Fujiwara, and E. C. Lim, J. Chem. Phys. **122**, 144312 (2005).

[66] H. Studzinski, S. Zhang, Y. Wang, and F. Temps, J. Chem. Phys. **128**, 164314 (2008).

[67] M. Sala and D. Egorova, Photochem. Photobiol. Sci. **17**, 1036 (2018).

[68] S. Karmakar, D. P. Mukhopadhyay, and T. Chakraborty, J. Chem. Phys. **142**, 184303 (2015).

[69] K. Rajak, A. Ghosh, and S. Mahapatra, J. Chem. Phys. **148**, 054301 (2018).

[70] A. Coustenis et al., Icarus **161**, 383 (2003).

[71] R. I. Kaiser, Chem. Rev. **102**, 1309 (2002).

[72] R. I. Kaiser, D. S. Parker, and A. M. Mebel, Annu. Rev. Phys. Chem. **66**, 43 (2015).

[73] M. J. McEwan et al., Astrophys. J. **513**, 287 (1999).

[74] N. Hansen et al., Combust. flame **156**, 2153 (2009).

[75] H. A. Jahn and E. Teller, Pro. R. Soc. London. Ser. A **161**, 220 (1937).

[76] I. B. Bersuker, Chem. Rev. **101**, 1067 (2001).

[77] I. B. Bersuker, *The Jahn-Teller Effect*, Cambridge University Press, Cambridge, UK, 2006.

[78] W. Von Niessen, G. Diercksen, L. S. Cederbaum, and W. Domcke, Chem. Phys. **18**, 469 (1976).

[79] L. Cederbaum, W. Domcke, and H. Köppel, Chem. Phys. **33**, 319 (1978).

[80] C. Woywod and W. Domcke, Chem. Phys. **162**, 349 (1992).

[81] S. Mahapatra, L. S. Cederbaum, and H. Köppel, J. Chem. Phys. **111**, 10452 (1999).

[82] G. A. Worth and L. S. Cederbaum, Chem. Phys. Lett. **348**, 477 (2001).

[83] S. Mahapatra, G. A. Worth, H.-D. Meyer, L. S. Cederbaum, and H. Köppel, J. Phys. Chem. A **105**, 5567 (2001).

[84] A. M. Schulenburg and F. Merkt, J. Chem. Phys. **130**, 034308 (2009).

[85] S. Sardar, A. K. Paul, and S. Adhikari, Mol. Phys. **107**, 2467 (2009).

[86] P. Baltzer et al., Chem. Phys. **196**, 551 (1995).

[87] R. K. Thomas and H. W. Thompson, Proc. R. Soc. London A **339**, 29 (1974).

[88] F. J. Leng and G. L. Nyberg, J. Chem. Soc., Faraday Trans. 2 **73**, 1719 (1977).

[89] G. Bieri, F. Burger, E. Heilbronner, and J. P. Maier, Helv. Chim. Acta **60**, 2213 (1977).

[90] A. C. Parr, A. J. Jason, and R. Stockbauer, Int. J. Mass Spectrom. Ion Phys. **26**, 23 (1978).

[91] Z. Z. Yang et al., Chem. Phys. Lett. **171**, 9 (1990).

[92] E. B. Wilson, J. C. Decius, and P. C. Cross, *Molecular Vibrations*, McGraw-Hill, New York, 1955.

[93] B. H. Lengsfield III and D. R. Yarkony, *Nonadiabatic Interactions Between Potential Energy Surfaces: Theory and Applications*, pages 1–71, John Wiley & Sons, Ltd, 1992.

[94] M. Born and K. Huang, *Dynamical theory of crystal lattices*, Oxford University press, New York, 1954.

[95] W. Pauli jr, Ann. Phys. **373**, 177 (1922).

[96] Güttinger P., Z. Phys. **73**, 169 (1932).

[97] Hellmann H., Z. Phys. **85**, 180 (1933).

[98] R. P. Feynman, Phys. Rev. **56**, 340 (1939).

[99] R. Englman, *The Jahn-Teller effect in Molecules and Crystals*, Wiley-Interscience, New York, 1972.

[100] W. Lichten, Phys. Rev. **164**, 131 (1967).

[101] F. T. Smith, Phys. Rev. **179**, 111 (1969).

[102] T. F. O'Malley, Adv. At. Mol. Phys. **7**, 223 (1971).

[103] W. Domcke and G. Stock, Adv. Chem. Phys. **100**, 1 (1997).

[104] M. Baer, Chem. Phys. **15**, 49 (1976).

[105] M. Baer, Chem. Phys. Lett. **35**, 112 (1975).

[106] M. Baer, Mol. Phys. **40**, 1011 (1980).

[107] Z. H. Top and M. Baer, J. Chem. Phys. **66**, 1363–1371 (1977).

[108] J. von Neumann and E. Wigner, Physik. Z. **30**, 467 (1929).

[109] Renner R., Z. Physik **92**, 172 (1934).

[110] H. A. Jahn, Proc. R. Soc. London. Ser. A **164**, 117 (1938).

[111] I. B. Bersuker and V. Z. Polinger, *Vibronic Interactions in Molecules and Crystals*, Springer Series in Chem. Phys., Springer Berlin Heidelberg, 1987.

[112] H. C. Longuet-Higgins, Some Recent Developments in the Theory of Molecular Energy Levels, in *Advances in Spectroscopy*, edited by H. W. Thompson, page 429, 1961.

[113] I. B. Bersuker and P. V. Z., *Vibronic Interactions in Molecules and Crystals*, Springer, Berlin, 1989.

[114] A. Viel and W. Eisfeld, J. Chem. Phys. **120**, 4603 (2004).

[115] W. Eisfeld and A. Viel, J. Chem. Phys. **122**, 204317 (2005).

[116] H. Köppel, D. R. Yarkony, and H. Barentzen, *The Jahn-Teller Effect: Fundamentals and Implications for Physics and Chemistry*, volume 97, Springer Science & Business Media, 2009.

[117] H. Köppel, and L. S. Cederbaum, and S. Mahapatra, *Theory of the Jahn–Teller Effect in Handbook of high-resolution spectroscopy*, volume 3, edited by M. Quack, and F. Merkt, (Wiley, Chichester, 2011), Quack, Martin and Merkt, Frédéric (Eds.).

[118] J. C. Tully, J. Chem. Phys. **93**, 1061 (1990).

[119] H.-D. Meyer, U. Manthe, and L. S. Cederbaum, Chem. Phys. Lett. **165**, 73 (1990).

[120] E. J. Heller, J. Chem. Phys. **68**, 3891 (1978).

[121] W. Domcke, H. Köppel, and L. S. Cederbaum, Mol. Phys. **43**, 851 (1981).

[122] J. Cullum and R. A. Willoughby, *Lanczos Algorithms for Large Symmetric Eigenvalue Computations*, Vol. I and II, Birkhäuser Boston, 1985.

[123] H. Köppel and W. Domcke, *Encyclopedia in Computational Chemistry*, edited by P. von Ragué (Wiley, New York, 1998), p. 3166.

[124] P. A. M. Dirac, Note on exchange phenomena in the thomas atom, volume 26, pages 376–385, 1930.

[125] J. Frenkel, *Waves Mechanics: Advanced General Theory*, volume 18, Clarendon Press, Oxford, 1934, 1934.

[126] J. Kucar, H.-D. Meyer, and L. Cederbaum, Chem. Phys. Lett. **140**, 525 (1987).

[127] U. Manthe, H. Meyer, and L. S. Cederbaum, J. Chem. Phys. **97**, 3199 (1992).

[128] M. H. Beck, A. Jäckle, G. A. Worth, and H.-D. Meyer, Phys. Rep. **324**, 1 (2000).

[129] H.-D. Meyer and G. A. Worth, Theor. Chem. Acc. **109**, 251 (2003).

[130] H.-D. Meyer, F. Gatti, and G. A. Worth, *Multidimensional Quantum Dynamics: MCTDH Theory and Applications*, Wiley-VCH, Weinheim, 2009.

[131] G. A. Worth, M. H. Beck, A. Jackle, and H.-D. Meyer, The MCTDH package, version 8.2, (2000), University of Heidelberg, Heidelberg, Germany. H.-D. Meyer, version 8.3 (2002), version 8.4 (2007). O. Vendrell and H.-D. Meyer, version 8.5 (2011)., See http://mctdh.uni-hd.de.

[132] H. Sponer, J. Chem. Phys. **22**, 234 (1954).

[133] C. D. Cooper, J. Chem. Phys. **22**, 503 (1954).

[134] K. N. Rao and H. Sponer, Can. J. Phys. **35**, 332 (1957).

[135] R. Gilbert, P. Sauvageau, and C. Sandorfy, Can. J. Chem. **50**, 543 (1972).

[136] J. Metcalfe, M. G. Rockley, and D. Phillips, J. Chem. Soc., Faraday Trans. 2 **70**, 1660 (1974).

[137] C. B. Duke, K. L. Yip, G. P. Ceasar, A. W. Potts, and D. G. Streets, J. Chem. Phys. **66**, 256 (1977).

[138] R. P. Frueholz, W. M. Flicker, O. A. Mosher, and A. Kuppermann, J. Chem. Phys. **70**, 3057 (1979).

[139] O. Plashkevych, L. Yang, O. Vahtras, H. Ågren, and L. G. Petterson, Chem. Phys. **222**, 125 (1997).

[140] C. D. Keefe, J. Barrett, and L. L. Jessome, J. Mol. Struct. **734**, 67 (2005).

[141] S.-H. Lee, C.-Y. Wu, S.-K. Yang, and Y.-P. Lee, J. Chem. Phys. **125**, 144301 (2006).

[142] I. Pugliesi, N. M. Tonge, and M. C. R. Cockett, J. Chem. Phys. **129**, 104303 (2008).

[143] M. Döscher, H. Köppel, and P. G. Szalay, J. Chem. Phys. **117**, 2645 (2002).

[144] V. P. Vysotsky, G. E. Salnikov, and L. N. Shchegoleva, Int. J. Quantum Chem. **100**, 469 (2004).

[145] K. Levenberg, Quart. Appl. Math. **2**, 164 (1944).

[146] D. W. Marquardt, J. Appl. Math. **11**, 431 (1963).

[147] M. O. Toolbox, Matlab optimization toolbox, version 9.8.0.1323502 (R2020a), The MathWorks, Natick, MA, USA.

[148] C. Møller and M. S. Plesset, Phys. Rev. **46**, 618 (1934).

[149] T. H. Dunning, J. Chem. Phys. **90**, 1007 (1989).

[150] M. J. Frisch et al., Gaussian 09 Revision E.01, Gaussian Inc. Wallingford CT 2009.

[151] H. Sekino and R. J. Bartlett, Int. J. Quantum Chem. **26**, 255 (1984).

[152] J. Geertsen, M. Rittby, and R. J. Bartlett, Chem. Phys. Lett. **164**, 57 (1989).

[153] J. F. Stanton and R. J. Bartlett, J. Chem. Phys. **98**, 7029 (1993).

[154] H.-J. Werner et al., MOLPRO, version 2010.1, a package of ab initio programs, see https://www.molpro.net/.

[155] S. G. Frankiss and D. J. Harrison, Spectrochim. Acta A Mol. Spectrosc. **31**, 1839 (1975).

[156] D. Steele and D. H. Whiffen, Trans. Faraday Soc. **55**, 369 (1959).

[157] Wolfram Research Inc., Mathematica Version 11.1, Champaign, Illinois, 2017.

[158] I. B. Bersuker, Chem. Rev. **113**, 1351 (2013), doi: 10.1021/cr300279n.

[159] H.-D. Meyer, F. L. Quéré, and C. Léonard, Chem. Phys. **329**, 179 (2006).

[160] L. J. Doriol, F. Gatti, C. Iung, and H.-D. Meyer, J. Chem. Phys. **129**, 224109 (2008).

[161] H.-J. Werner and P. J. Knowles, J. Chem. Phys. **82**, 5053 (1985).

[162] P. J. Knowles and H.-J. Werner, Chem. Phys. Lett. **115**, 259 (1985).

[163] H.-J. Werner and P. J. Knowles, J. Chem. Phys. **89**, 5803 (1988).

[164] P. J. Knowles and H.-J. Werner, Theoret. Chim. Acta **84**, 95 (1992).

[165] M. Musiał, S. A. Kucharski, and R. J. Bartlett, J. Chem. Phys. **118**, 1128 (2003).

[166] Y. J. Bomble et al., J. Chem. Phys. **122**, 154107 (2005).

[167] A. Schäfer, C. Huber, and R. Ahlrichs, J. Chem. Phys. **100**, 5829 (1994).

[168] F. Weigend and R. Ahlrichs, Phys. Chem. Chem. Phys. **7**, 3297 (2005).

[169] D. Rappoport and F. Furche, J. Chem. Phys. **133**, 134105 (2010).

[170] B. C. Trudell and S. J. W. Price, Can. J. Chem. **57**, 2256 (1979).

[171] J. F. Stanton et al., Cfour, coupled-cluster techniques for computational chemistry, a quantum-chemical program package, With contributions from A.A. Auer, R.J. Bartlett, U. Benedikt, C. Berger, D.E. Bernholdt, Y.J. Bomble, O. Christiansen, F. Engel, R. Faber, M. Heckert, O. Heun, M. Hilgenberg, C. Huber, T.-C. Jagau, D. Jonsson, J. Jusélius, T. Kirsch, K. Klein, W.J. Lauderdale, F. Lipparini, T. Metzroth, L.A. Mück, D.P. O'Neill, D.R. Price, E. Prochnow, C. Puzzarini, K. Ruud, F. Schiffmann, W. Schwalbach, C. Simmons, S. Stopkowicz, A. Tajti, J. Vázquez, F. Wang, J.D. Watts and the integral packages MOLECULE (J. Almlöf and P.R. Taylor), PROPS (P.R. Taylor), ABACUS (T. Helgaker, H.J. Aa. Jensen, P. Jørgensen, and J. Olsen), and ECP routines by A. V. Mitin and C. van Wüllen. For the current version, see http://www.cfour.de.

[172] I. D. Clark and D. C. Frost, J. Am. Chem. Soc. **89**, 244 (1967), PMID: 22175957.

[173] T. kobayashi, S. Nagakura, and C. McDowell, J. Electron Spectrosc. Relat. Phenom. **7**, 187 (1975).

[174] J. A. Sell, D. M. Mintz, and A. Kuppermann, Chem. Phys. Lett. **58**, 601 (1978).

[175] T. Kobayoshi, Physics Letters A **69**, 105 (1978).

[176] J. Bastide, D. Hall, E. Heilbronner, J. Maier, and R. Plevey, J. Electron Spectrosc. Relat. Phenom. **16**, 205 (1979).

[177] J. P. Maier and F. Thommen, Chem. Phys. **57**, 319 (1981).

[178] C. Motch et al., Chem. Phys. **328**, 183 (2006).

[179] V. E. Bondybey and T. A. Miller, J. Chem. Phys. **70**, 138 (1979).

[180] T. Sears, T. A. Miller, and V. E. Bondybey, J. Am. Chem. Soc. **103**, 326 (1981).

[181] P. Decleva, M. Stener, D. M. P. Holland, A. W. Potts, and L. Karlsson, J. Phys. B: At. Mol. Opt. Phys. **40**, 2939 (2007).

[182] D. M. P. Holland, D. A. Shaw, M. Stener, and P. Decleva, J. Phys. B: At. Mol. Opt. Phys. **42**, 245201 (2009).

[183] A. ALMENNINGEN, O. BASTIANSEN, R. SEIP, and H. M. SEIP, Acta Chem. Scand **18** (1964).

[184] D. A. Braden and B. S. Hudson, J. Phys. Chem. A **104**, 982 (2000).

[185] S. Mahapatra, V. Vallet, C. Woywod, H. Köppel, and W. Domcke, Chem. Phys. **304**, 17 (2004).

[186] A. K. Kanakati, V. Jhansi Rani, and S. Mahapatra, Phys. Chem. Chem. Phys. **24**, 16522 (2022).

[187] C. Baker and D. W. Turner, Pro. R. Soc. London. Ser. A **308**, 19 (1968).

[188] A. C. Parr, A. J. Jason, R. Stockbauer, and K. McCulloh, Int. J. Mass Spectrum. **30**, 319 (1979).

[189] G. H. Ho, M. S. Lin, Y. L. Wang, and T. W. Chang, J. Chem. Phys. **109**, 5868 (1998).

[190] G. Bieri and L. Åsbrink, J. Electron Spectrosc. Relat. Phenom. **20**, 149 (1980).

[191] J.-C. Shieh et al., J. Chem. Phys. **112**, 7384 (2000).

[192] X. Xing et al., J. Chem. Phys. **128**, 094311 (2008).

[193] H. Matsui, Y.-F. Zhu, and E. R. Grant, Laser Chem. **16**, 151 (1996).

[194] S. Marquez, J. Dillon, and D. R. Yarkony, J. Phys. Chem. A **117**, 12002 (2013).

[195] U. Jacovella et al., J. Chem. Phys. **141**, 114303 (2014).

[196] U. Jacovella and F. Merkt, Mol. Phys. **116**, 3602 (2018).

[197] S. T. Pratt, P. M. Dehmer, and J. L. Dehmer, J. Chem. Phys. **99**, 6233 (1993).

[198] W. Ensslin, H. Bock, and G. Becker, J. Am. Chem. Soc. **96**, 2757 (1974).

[199] M. Hamermesh, *Group Theory and Its Application to Physical Problems*, Addison Wesley Series in Physics, Dover Publications, 1989.

[200] T. Pacher, L. S. Cederbaum, and H. Köppel, Adv. Chem. Phys. **84**, 293 (1993).

[201] T. Zeng and I. Seidu, Phys. Chem. Chem. Phys. **19**, 11098 (2017).

[202] M. H. Palmer, C. C. Ballard, and I. C. Walker, Chem. Phys. **249**, 129 (1999).

[203] D. Frost, F. Herring, C. McDowell, and I. Stenhouse, Chem. Phys. Lett. **4**, 533 (1970).

[204] J. Duncan, D. McKean, P. Mallinson, and R. McCulloch, J. Mol. Spectrosc. **46**, 232 (1973).

[205] L. S. Cederbaum and W. Domcke, *Theoretical Aspects of Ionization Potentials and Photoelectron Spectroscopy: A Green's Function Approach*, pages 205–344, John Wiley & Sons, Ltd, 1977.

[206] R. Sarkar, S. Rajagopala Reddy, S. Mahapatra, and H. Köppel, Chem. Phys. **482**, 39 (2017).

List of publications

[1] **Arun Kumar Kanakati**, V. Jhansi Rani, R. Sarkar and S. Mahapatra, "*Elucidation of vibronic structure and dynamics of first eight excited electronic states of Pentafluorobenzene*", J. Chem. Phys. **157**, 204304 (2022).

[2] V. Jhansi Rani[†], **Arun Kumar Kanakati**[†] and S. Mahapatra, "*Multi-state and multi-mode vibronic coupling effects in the photo-ionization spectroscopy of acetaldehyde*", J. Phys. Chem. A **126**, 6581 (2022)([†] equal contribution).

[3] **Arun Kumar Kanakati**, V. Jhansi Rani and S. Mahapatra, "*Impact of Jahn-Teller and pseudo-Jahn-Teller effect in Propyne radical cation*", Phys. Chem. Chem. Phys. **24**, 16522 (2022).

[4] S. Barik, **Arun Kumar Kanakati**, S. Dutta, N. R. Behera, R. K. Kushawaha and G. Aravind, "*Low-lying Dipole Resonances in $FeCN^-$: A Viable Formation Pathway for $FeCN^-$ in Space*", Astrophys. J. **931**, 47 (2022).

[5] **Arun Kumar Kanakati** and S. Mahapatra, "*Vibronic coupling in the first six electronic states of Pentafluorobenzene radical cation: Radiative emission and non-radiative decay*", J. Chem. Phys. **154**, 054313 (2021).

[6] V. Madhu and **Arun Kumar Kanakati** and Samar K. Das, "*Serendipitous isolation of a triazinone-based air stable organic radical: synthesis, crystal structure, and computation*", New. J. Chem. **44**, 10781 (2020).

[7] K. R. Nandipati, **Arun Kumar Kanakati**, H. Singh, and S. Mahapatra, "*Controlled intramolecular H-transfer in Malonaldehyde in the electronic ground state mediated through the conical intersection of $^1n\pi^*$ and $^1\pi\pi^*$ excited electronic states*", Phys. Chem. Chem. Phys. **21**, 20018 (2019).

[8] Arpita Ghosh, K Rajak, **Arun Kumar Kanakati** and S. Mahapatra, "*Renner-Teller and pseudo-Renner-Teller interactions in the electronic ground and excited states of the dicyanoacetylene radical cation: Assignment of vibronic spectrum and elucidation of nonradiative and radiative decay mechanisms*", Comput. Theor. Chem. **1155**, 109 (2019).

[9] K. R. Nandipati, **Arun Kumar Kanakati**, H. Singh, Z. Lan, and S. Mahapatra, "*Initial state-specific photodissociation dynamics of pyrrole via* $^1\pi\sigma^*/S_0$ *conical intersections initiated with optimally controlled UV-laser pulses*", Eur. Phys. J. D. **71**, 222 (2017).

[10] K. R. Nandipati and **Arun Kumar Kanakati**, "*Optimal Control of Vibrational Transitions in HCl molecule*", Pramana -J. Phys. **87**, 50 (2016).

[11] R. Bodapati, Monima Sarma, **Arun Kumar Kanakati** and Samar K. Das, "*Asymmetrically Substituted and* π*-Conjugated 2,2′-Bipyridine Derivatives: Synthesis, Spectroscopy, Computation, and Crystallography*", J. Org. Chem. **80**, 12482 (2015).

[12] K. R. Nandipati, H. Singh, S. N. Reddy, **Arun Kumar Kanakati** and S. Mahapatra, "*Optimal Initiation of Electronic Excited State Mediated Intramolecular H-transfer in Malonaldehyde by UV-laser Pulses*", Eur. Phys. J. D. **68**, 355 (2014).

[13] M. Rani†, **Arun Kumar Kanakati**† and S. Mahapatra, "*Photoionization bands of Cyanogen: Multi-mode vibronic coupling and Renner-Teller effects*", Chem. Phys. Chem. (2022)(under review, † equal contribution).

[14] **Arun Kumar Kanakati** and S. Mahapatra, "*The Jahn-Teller and pseudo-Jahn-Teller effects in Hexafluorobenzene radical cation: Radiative emission and nonradiative decay*", (manuscript under preparation).

[15] V. Jhansi Rani, **Arun Kumar Kanakati** and S. Mahapatra, "*Vibronic coupling effects in the six low-lying electronic states of Oxirane radical cation: Theoretical photoelectron spectrum of Oxirane*", (manuscript under preparation).

Posters and Oral presentations in conferences/Symposia

[1] Poster presented in "A Tributary Symposium on 100 Years of Chemical Bonding-2016, 4-5 August, 2016, at CSIR-Indian Institute of Chemical Technology, Hyderabad, India".

[2] Poster presented in "15^{th} Indian Theoretical Chemistry Symposium (TCS-2016), 14-17 December, 2016, at University of Hyderabad, Hyderabad, India".

[3] Poster presented in "8^{th} International Collaborative and Cooperative Chemistry Symposium, 18-19 December, 2017, at University of Hyderabad, Hyderabad, India".

[4] Poster presented in "16^{th} Indian Theoretical Chemistry Symposium (TCS-2019), 13-16 February, 2019, at BITS Pilani, Pilani campus, Rajasthan, India".

[5] Poster presented in "Chemfest 2016 to 2020 an in-house symposium held at School of Chemistry, University of Hyderabad, India".

[6] Oral presentation in "Chemfest 2020 an in-house symposium held at School of Chemistry, University of Hyderabad, India".